Optical Excitation of Electromagnetic Modes Using Grating Coupling

submitted by

Guy Peter Bryan-Brown

to the University of Exeter
as a thesis for the degree of
Doctor of Philosophy
in the Faculty of Science

March 1991

I certify that all material in this thesis which is not my own work has been identified and that no material is included for which a degree has previously been conferred upon me.

To Mum,
for all her support.

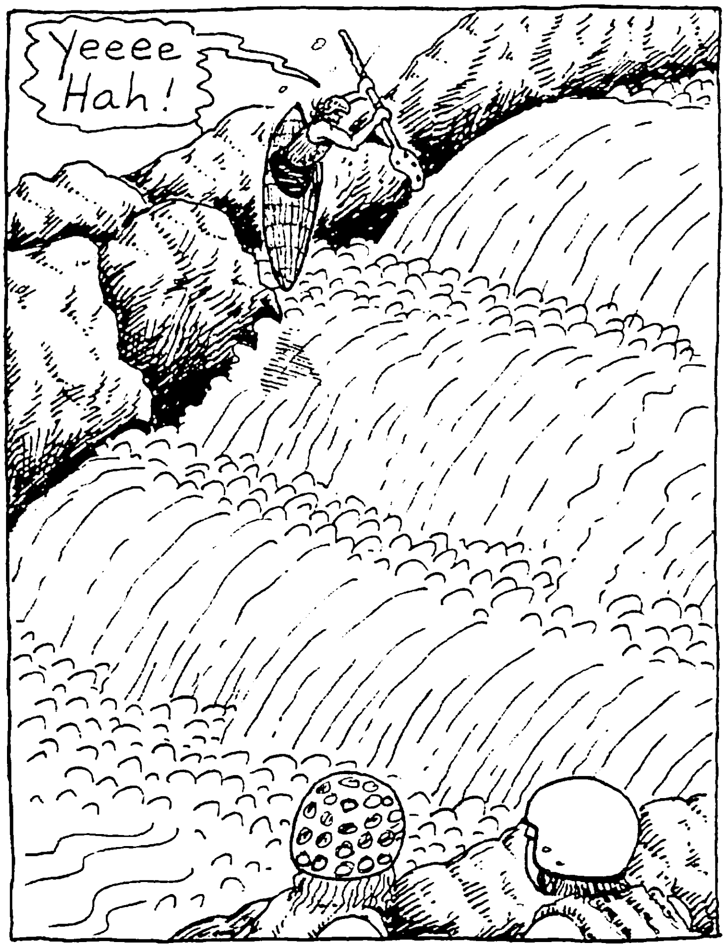
Yeeee Hah!

Contents

Acknowledgements

Abstract

Acknowledgements

I would like to express my thanks to all the people who have helped me with this work during the past three years and have made it enjoyable.

Principally to my supervisor at Exeter, Dr Roy Sambles, for his enthusiasm, motivation and guidance. To my external supervisor at NPL, Dr Mike Hutley and also Mrs Silvia Wilson for their help in grating manufacture and characterisation.

To Dr Stephen Elston and Dr Trevor Preist for their involvement in the development of theoretical modelling programs.

To all past and present members of Thin Film and Interface Research Group for providing an enjoyable working environment (Dave Gleed, Norman Geddes, Ori Robinson, Martin Tillin, Chris Lavers, Simon Cowen, Alistair Scott-Martin, Emma Wood, Chris Lawrence, Pete Vukusic, Rob Crook, Tim Watson, Paul Gass, Yang Fuzi, Bill Parker and Geoff Bradberry).

To Pete Cann for making things (and making things work!) and Dave Jarvis for evaporating many films. (ie. Depositing thin layers!)

To the members of the mechanical workshop.

To Frank Miners and others in the electronics workshop.

To Margaret Cornish and the secretarial staff.

To Dr Trevor Preist and Prof John Inkson (sucessive heads of department) for the use of departmental resources to carry out the research.

SERC and NPL for the provision of a CASE studentship.

Abstract

The recent developments in the manufacture and theoretical modelling of diffraction gratings have lead to much interest in the physics and applications of electromagnetic modes that may be excited on a grating surface.

In this work, grating surfaces are used to enhance photon momentum and so allow coupling of photons into electromagnetic resonances. The excitation of surface plasmon polaritons (SPPs) on gratings has been studied both experimentally and theoretically. Accurate fitting of theory to reflectivity data has shown that SPP excitation is an excellent method of characterising metal films and also shows that our holographically produced gratings have a well defined groove profile.

Thin silver films have been used to demonstrate the excitation of long range surface plasmons (LRSPs) and short range surface plasmons. The dispersion of these modes has been examined theoretically and experimentally. Theory has been fitted to reflectivity data with an accuracy never before seen for this configuration. A recently discovered optical mode, the long range surface exciton polariton (LRSEP) has been observed on thin chromium films at infra red wavelengths. The dispersion of this mode with film thickness is examined along with the different perturbations on the mode due to grating coupling and prism coupling. Excitation of long range modes on palladium films has been used to optically characterise the metal and has shown that effective medium theories may be used as a qualitative description of film porosity.

Further work reports the discovery of a new phenomenon called p to s conversion which occurs when an optical mode is excited on a suitably orientated grating. This phenomenon is studied in detail for surface plasmon polaritons, long range surface plasmons and guided modes. Conversion efficiencies of up to 66% have been observed for lightly modulated gratings via the excitation of SPPs and guided modes have also shown high efficiencies. A new differential theory applicable to conical diffraction has been developed and shows excellent agreement with p to s conversion data. Applications of polarisation conversion to gas sensing are also studied.

Finally results are shown concerning nonlinear work carried out using grating coupled electromagnetic modes.

Chapter 1

Introduction and Review

1.1 Aim of this work

Diffraction gratings have a large number of applications in many areas of optics. In spectroscopy their large dispersion combined with high diffraction efficiency has made them more attractive than traditional prism devices. Since their discovery over 150 years ago, grating technology has taken two major steps forward. Namely, the improvement in fabrication using 'holographic' techniques and also the ability to theoretically model the optical response of a grating surface which until now has been limited by lack of computing power.

It is the aim of the work in this thesis to use diffraction gratings to enhance photon momentum and so allow coupling into resonant electromagnetic modes that exist in suitable grating structures. The phyical origin and behaviour of these modes is studied for various grating configurations and many useful applications to material characterisation and sensing are demonstrated.

1.2 Outline of Thesis

The remainder of this chapter introduces the three types of mode studied in this thesis: Surface plasmon polaritons, coupled surface plasmon polaritons and resonant guided modes. Three different configurations for coupling to these modes are discussed and finally theoretical modelling methods applicable to grating coupling are reviewed. In chapter 2, a differential grating theory is described in detail and then extended to a more general case which allows modelling of virtually all the data shown in this thesis. Chapter 3 describes the experimental procedures for grating manufacture and characterisation and also reflectivity measurements. Chapter 4 shows that grating coupling to surface plasmon polaritons is as reliable as the more traditional prism coupling for the determination of the dielectric constants of metals. In chapter 5, thin silver films are shown to support long range and short range surface plasmon polaritons. Comparison of theory with reflectivity measurements show a thickness dependent dielectric constant for these films. Chapter 6 reports studies on thin chromium films (in the infra-red) which support a new resonant mode called the long range surface exciton polariton. This resonance is obtained using both grating coupling and prism coupling. In chapter 7, results from palladium films are fitted and also reveal a thickness dependent dielectric constant which is explained in terms of film porosity using effective medium theory. Chapter 8 presents a new grating phenomenon called p to s conversion which is produced via all electromagnetic modes when the grating grooves are not parallel or perpendicular to the plane of incidence. Chapter 9 discusses applications of p to s conversion in gas sensing, biosensing and spectroscopy. Results from a prototype gas sensor are also presented. The conclusions of the thesis along with suggestions for future work are contained in chapter 10. Appendix A reports on nonlinear studies carried out using resonant modes in semiconductor films, semiconductor doped glass and Langmuir Blodgett films.

1.3 Surface Plasmon Polaritons

At the interface between two media, the normal component of the electric displacement (D) is continuous. Also

$$D = \epsilon\epsilon_0 E \tag{1.1}$$

ϵ is usually a complex quantity but if it has a real part that is positive in one media and negative in the other, then equation 1.1 dictates that the normal component of the electric field (E) will reverse direction across the interface. The change of E leads to trapped charge at the interface. If we now consider electromagnetic waves instead of static fields then we can derive the dispersion equation of the oscillating trapped charge (following the method of H Raether, 1988).

Figure 1.1 shows a p-polarised (TM) wave passing from a medium with $\epsilon = \epsilon_2$ (a dielectric) into a medium with $\epsilon = \epsilon_1$ (a metal). For non-radiative surface modes we may set E_2^+ to zero and so the fields above and below the interface may be

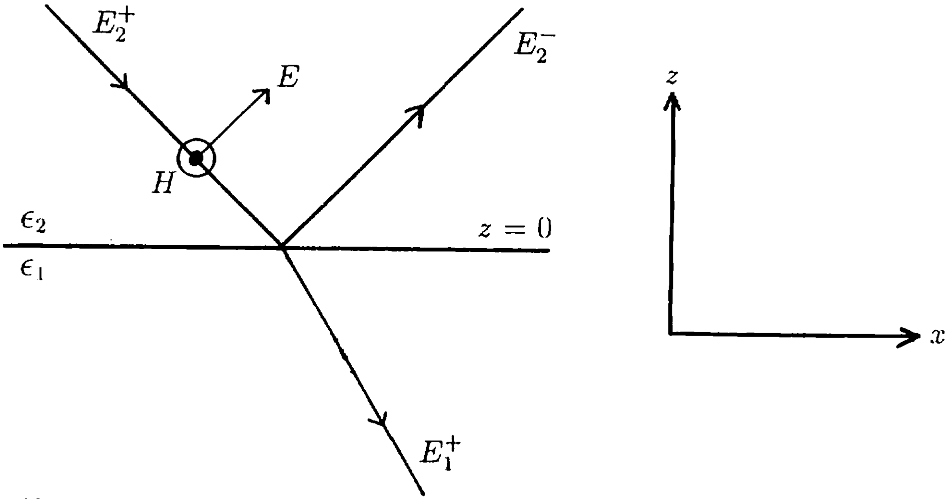

Figure 1.1: A TM polarised wave passing from medium 2 to medium 1.

written as

$$\begin{aligned} z > 0 \quad \mathbf{H_2} &= (0, H_{y2}, 0) \exp i(k_{x2}x + k_{z2}z - \omega t) \\ \mathbf{E_2} &= (E_{x2}, 0, E_{z2}) \exp i(k_{x2}x + k_{z2}z - \omega t) \end{aligned} \tag{1.2}$$

$$\begin{aligned} z < 0 \quad \mathbf{H_1} &= (0, H_{y1}, 0) \exp i(k_{x1}x - k_{z1}z - \omega t) \\ \mathbf{E_1} &= (E_{x1}, 0, E_{z1}) \exp i(k_{x1}x - k_{z1}z - \omega t) \end{aligned} \tag{1.3}$$

If we substitute these into one of Maxwell's equations;

$$\nabla \times \mathbf{H} = \epsilon \frac{\partial \mathbf{E}}{\partial t}$$

then we obtain

$$k_{z1} H_{y1} = \omega \epsilon_1 E_{x1} \tag{1.4}$$

$$k_{z2} H_{y2} = -\omega \epsilon_1 E_{x2} \tag{1.5}$$

but boundary conditions dictate that $E_{x1} = E_{x2}$ and $H_{y1} = H_{y2}$, hence equations 1.4 and 1.5 may be combined to give

$$\frac{k_{z1}}{\epsilon_1} = -\frac{k_{z2}}{\epsilon_2} \tag{1.6}$$

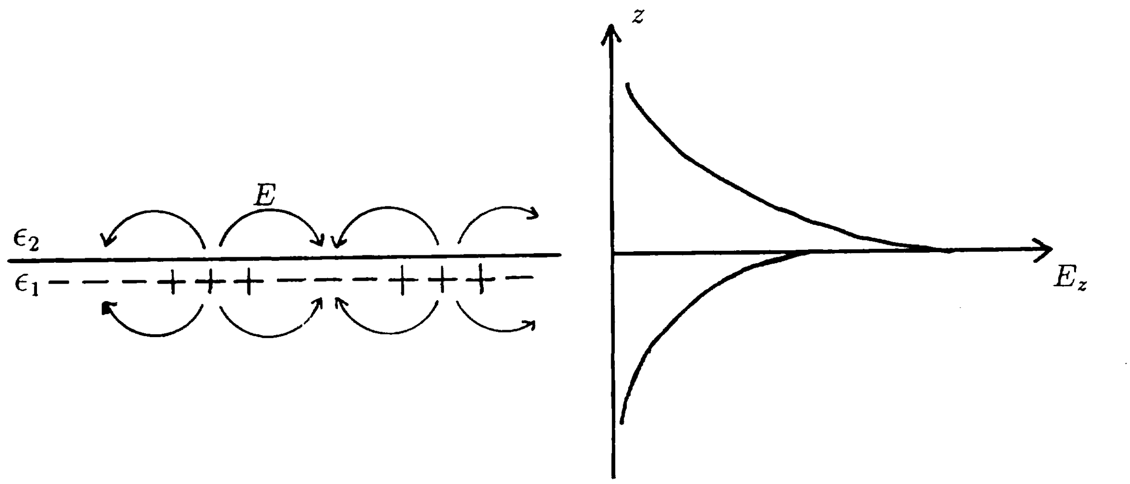

Figure 1.2: Charge distribution and field profiles associated with the SPP.

The above boundary conditions also dictate that

$$k_{x1} = k_{x2} = k_x$$

Also for the electromagnetic waves

$$k^2 = \epsilon\left(\frac{\omega}{c}\right)^2$$

or

$$k_x^2 + k_z^2 = \epsilon\left(\frac{\omega}{c}\right)^2 \tag{1.7}$$

The x component of the wavevector (which is continuous across the interface) is obtained from equations 1.6 and 1.7;

$$k_x = \frac{\omega}{c}\left(\frac{\epsilon_1\epsilon_2}{\epsilon_1 + \epsilon_2}\right)^{1/2} \tag{1.8}$$

It is this dispersion equation that describes the charge oscillation at the interface. This is a longitudinal oscillation trapped at the interface with associated electromagnetic fields which decrease exponentially into each medium. (The charge distribution and the field profiles associated with this oscillation are sketched in figure 1.2). The surface plasmon polariton (SPP) is the electromagnetic oscillation coupled to this charge oscillation. Since the required k_x is greater than ω/c, some form of momentum enhancement is required for excitation by photons. (various ways of achieving this are listed in section 1.4). The SPP can only be coupled to via TM radiation as TE radiation has no electric field component in the z direction and so cannot trap charge at the interface.

As medium 1 is a metal, then $\epsilon_1 = \epsilon_{1r} + i\epsilon_{1i}$ and the SPP wavevector is then written $k_x = k_{xr} + ik_{xi}$ where

$$k_{xr} = \frac{\omega}{c}\left(\frac{\epsilon_{1r}\epsilon_2}{\epsilon_{1r}+\epsilon_2}\right)^{1/2} \tag{1.9}$$

$$k_{xi} = \frac{\omega}{c}\left(\frac{\epsilon_{1r}\epsilon_2}{\epsilon_{1r}+\epsilon_2}\right)^{3/2} \frac{\epsilon_{1i}}{2(\epsilon_{1r})^2} \tag{1.10}$$

It can be seen from equation 1.9 that the SPP will only propagate (real k_{xr}) when $|\epsilon_{1r}| > \epsilon_2$, assuming that $\epsilon_{1r} < 0$ (a metal). k_{xi} determines the damping of the mode and scales linearly with ϵ_{1i}.

It is of interest to calculate how far the SPP fields extend into each medium. These fields decrease exponentially as $\exp(-|k_{zi}||z|)$ normal to the surface. The value of the SPP skin depth at which the fields fall to 1/e is therefore given by

$$\hat{z} = \frac{1}{|k_{zi}|}$$

which, using equation 1.7 can be written as

$$\hat{z} = \left(\epsilon\left(\frac{\omega}{c}\right)^2 - k_x^2\right)^{-1/2} \tag{1.11}$$

Using equation 1.11 along with 1.8 gives expressions for the SPP skin depth in each medium;

$$\hat{z}_2 = \frac{c}{\omega}\left|\frac{\epsilon_{1r}+\epsilon_2}{\epsilon_2^2}\right|^{1/2} \tag{1.12}$$

$$\hat{z}_1 = \frac{c}{\omega}\left|\frac{\epsilon_{1r}+\epsilon_2}{\epsilon_{1r}^2}\right|^{1/2} \tag{1.13}$$

For a silver/air interface at $632.8nm$ ($\epsilon_2 = 1.0$, $\epsilon_1 = -17.12{+}0.623i$), $\hat{z}_2 = 404nm$ and $\hat{z}_1 = 24nm$. Hence the fields extend much further into the air than into the metal . (For a perfectly conducting metal, $\epsilon = -\infty + 0.0i$ and $\hat{z}_1$ is zero).

The SPP also decays exponentially during its propagation along the interface (x direction). This decay goes as $\exp(-2k_{xi}x)$. Hence the length L after which the intensity decreases to $1/e$ is given by

$$L = \frac{1}{2k_{xi}} \tag{1.14}$$

For silver at a wavelength of $632.8nm$, L is $43.3\mu m$, whereas at a wavelength of $3.391\mu m$ ($\epsilon = -657.6 + 87.1i$), L is $2.68mm$. The energy lost by the SPP is absorbed as heat in the metal film. This local heating can be fairly substantial if the propagation length is short.

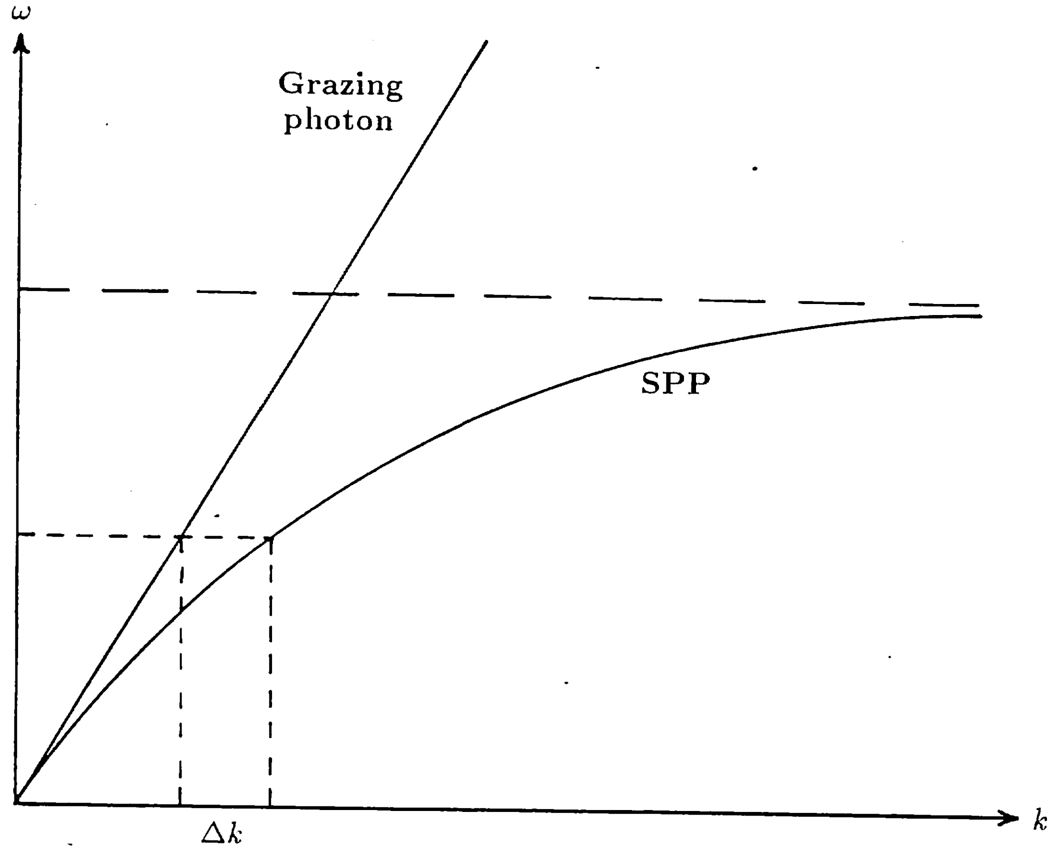

Figure 1.3: Dispersion of a SPP.

If we consider an ideal metal, its dielectric constant is described by the Drude equation which may be substituted into equation 1.8 to give an idealised form of the SPP dispersion (this is plotted in figure 1.3). The dispersion of a grazing photon (with a gradient c) is also shown. This demonstrates that at a particular wavelength ω, there is a mismatch in momentum (Δk) between the photon and the SPP. Hence a photon cannot couple into the SPP without some form of momentum enhancement.

1.4 Methods of Coupling to SPPs

There are in general two methods of coupling light into a SPP mode; prism coupling (Otto and Kretschmann configurations) and grating coupling. These are shown in figure 1.4 (a), (b) and (c) respectively.

The Otto and Kretschmann configurations both rely on the fact that when a photon passes from air into the prism its momentum is increased from k to nk where n is the refractive index of the prism. The component of photon momentum along the prism/air interface is therefore $nk \sin\theta$ and so coupling to the SPP occurs when

$$nk \sin\theta_{spp} = k\left(\frac{\epsilon_1 \epsilon_2}{\epsilon_1 + \epsilon_2}\right)^{1/2} = k_{spp} \tag{1.15}$$

For the prism/air interface, $n \sin\theta_c = 1$, where θ_c is the critical angle, but equation 1.15 implies that $n \sin\theta_{spp} > 1$ and hence $\theta_{spp} > \theta_c$. When $\theta > \theta_c$, no real beams propagate downwards from the prism (total internal reflection) and so it is the evanescent field below the prism that couples energy to the SPP. The excitation of the SPP removes energy from the incident beam and can therefore be detected as a drop in reflectivity. The configuration shown in figure 1.4(a) was first demonstrated by A Otto (1968). In this case, an air gap separates the metal surface from the prism and the SPP is excited on the top metal surface. Adjusting the air gap will vary the amount of light that is coupled to the SPP. An optimum gap exists for which 100% of the incident radiation is absorbed and hence zero reflectivity is seen (at an angle where the reflectivity would usually be unity). The configuration in figure 1.4(b) was first shown by E Kretschmann *et al* (1968) and in this case a thin metal film is deposited directly onto the prism. The evanescent field from the incident beam passes through the metal and excites a SPP on the bottom surface of the metal. Adjustment of coupling is achieved by changing the thickness of the metal film. For silver at 632.8nm the optimum thickness is about 40nm. The Otto configuration is more difficult to set up correctly as the air gap must not be

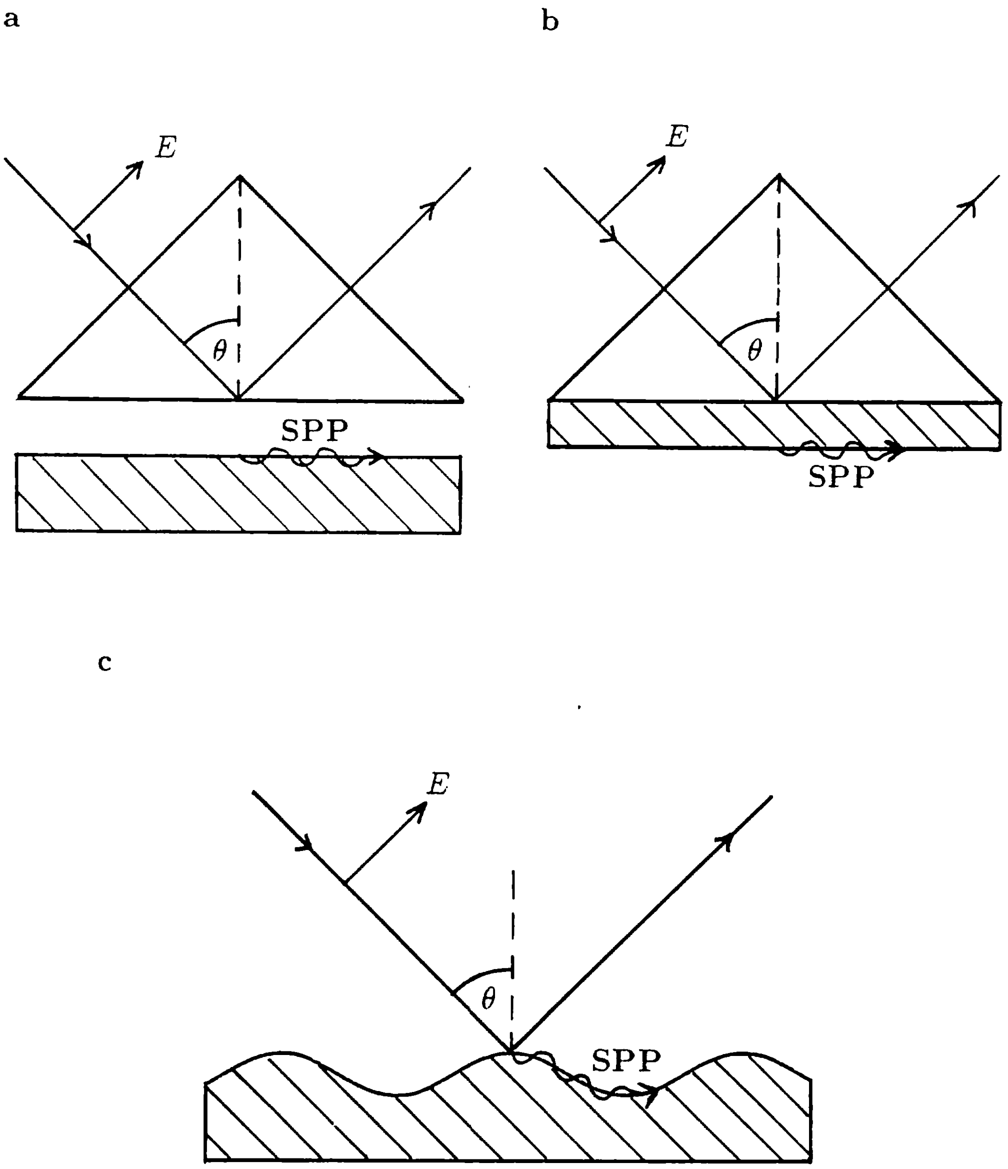

Figure 1.4: Three methods of coupling radiation to SPPs; (a) Otto configuration, (b) Kretschmann configuration and (c) Grating configuration.

wedged but it does have the advantage over the Kretschmann method in that it allows the probing of bulk metal samples such as polished crystals.

The evanescent fields due to the SPP are enhanced with respect to the incoming electromagnetic wave. This is a useful property of the SPP which has been exploited in many areas such as surface enhanced raman scattering (W Knoll *et al*, 1982) and second harmonic generation (JL Coutaz *et al*, 1985). For the Kretschmann configuration we can calculate this enhancement using the following expression (from H Raether, 1988);

$$T^{el}_{max} = \frac{1}{\epsilon_2} \frac{2|\epsilon_{1r}|^2}{\epsilon_{1i}} \frac{\left[|\epsilon_{1r}|(\epsilon_0 - 1) - \epsilon_0\right]^{1/2}}{1 + |\epsilon_{1r}|} \tag{1.16}$$

T^{el}_{max} is the ratio of the electric field intensity on the metal surface at the air side divided by the incident field intensity (ϵ_0 refers to the dielectric constant of the prism). If the prism is made of quartz ($\epsilon_0 = 2.2$) and $\epsilon_2 = 1$ (air) then, for a silver surface at $632.8nm$, T^{el}_{max} is 106. If instead, we use silver at $3.391\mu m$ then T^{el}_{max} is now 202.

The grating configuration shown in figure 1.4(c) was the first configuration to be practically demonstrated (RW Wood, 1902), but due to difficulties in theoretical modelling this method was not widely used until much later. When radiation is incident on the grating, reflected, diffracted and evanescent fields are produced. The last of these are diffracted beams which do not propagate as they have wavevectors greater than ω/c. It is these evanescent fields that may couple radiation to the SPP. The coupling equation in this case is

$$k \sin\theta = \pm k_{spp} \pm nG \tag{1.17}$$

Where G is the grating momentum vector (equal to 2π/groove pitch). The grating can add or subtract momenta from the incident photon in multiples of G and hence excite a SPP which may travel in either direction along the grating surface ($\pm x$ direction). The strength of coupling to the SPP is adjusted by varying the grating groove depth. With an optimum groove depth, a grating will absorb 100% of p-polarised incident radiation via SPP excitation (MC Hutley *et al*, 1976).

Due to its compatibility with thin film optics, the grating configuration has recently received much attention. The effect of grating grooves on k_{spp} has been studied both theoretically and experimentally by I Pockrand *et al* (1976). V Celli *et al* (1988) showed that two SPPs may exist simultaneously by appropriate choice of grating pitch. These SPPs were found to repel each other forming a momentum gap in the SPP dispersion. Other workers (ES Koteles *et al*, 1984) have instead found energy gaps between counterpropagating SPPs and RW Gruhlke *et al* (1989) found both energy gaps and momentum gaps from the same sample. I Pockrand (1976) coated a metallised grating with thin dielectric overlayers to demonstrate the sensitivity of SPPs to changes occurring at the metal surface. Grating coupling to SPPs has also been used to enhance the efficiency of infra red Schottky photodetectors (SRJ Bruek *et al*, 1985), and RJ Seymour *et al* (1984) showed that radiation from a $119\mu m$ laser may be coupled into a SPP via a grating.

The coupling methods discussed above may also be used to couple radiation into coupled surface plasmon polaritons and resonant guided modes. (These modes are discussed in the following sections).

1.5 Coupled Surface Plasmon Polaritons

If an optically thin metal film is bounded by dielectrics of equal permittivity then SPP modes excited on each metal/dielectric interface can interfere with each other across the metal film. This interference of fields leads to the formation of two coupled modes. One mode is symmetric (in H field) and the other is antisymmetric.

Figure 1.5(a) and (b) show the real and imaginary parts of the wavevectors associated with allowed modes on a gold film at a wavelength of $3.391\mu m$ ($\epsilon = -440 + 84i$). When the film is thick ($300nm$) a single allowed mode exists with k_r and k_i given by equations 1.9 and 1.10 (this is the single interface SPP). However when the film thickness is decreased, two branches appear. These have different k_r and so in a practical configuration, they are excited at different angles of incidence. They also have different k_i and so the modes have a different damping. One mode has damping that decreases with decreasing film thickness and the other mode has damping that increases. The former therefore has a longer propagation length and so is called the long range surface plasmon (LRSP). The mode with higher damping is called the short range surface plasmon (SRSP). It can be seen from figure 1.5(a) that below a certain thickness, the SRSP wavevector becomes very

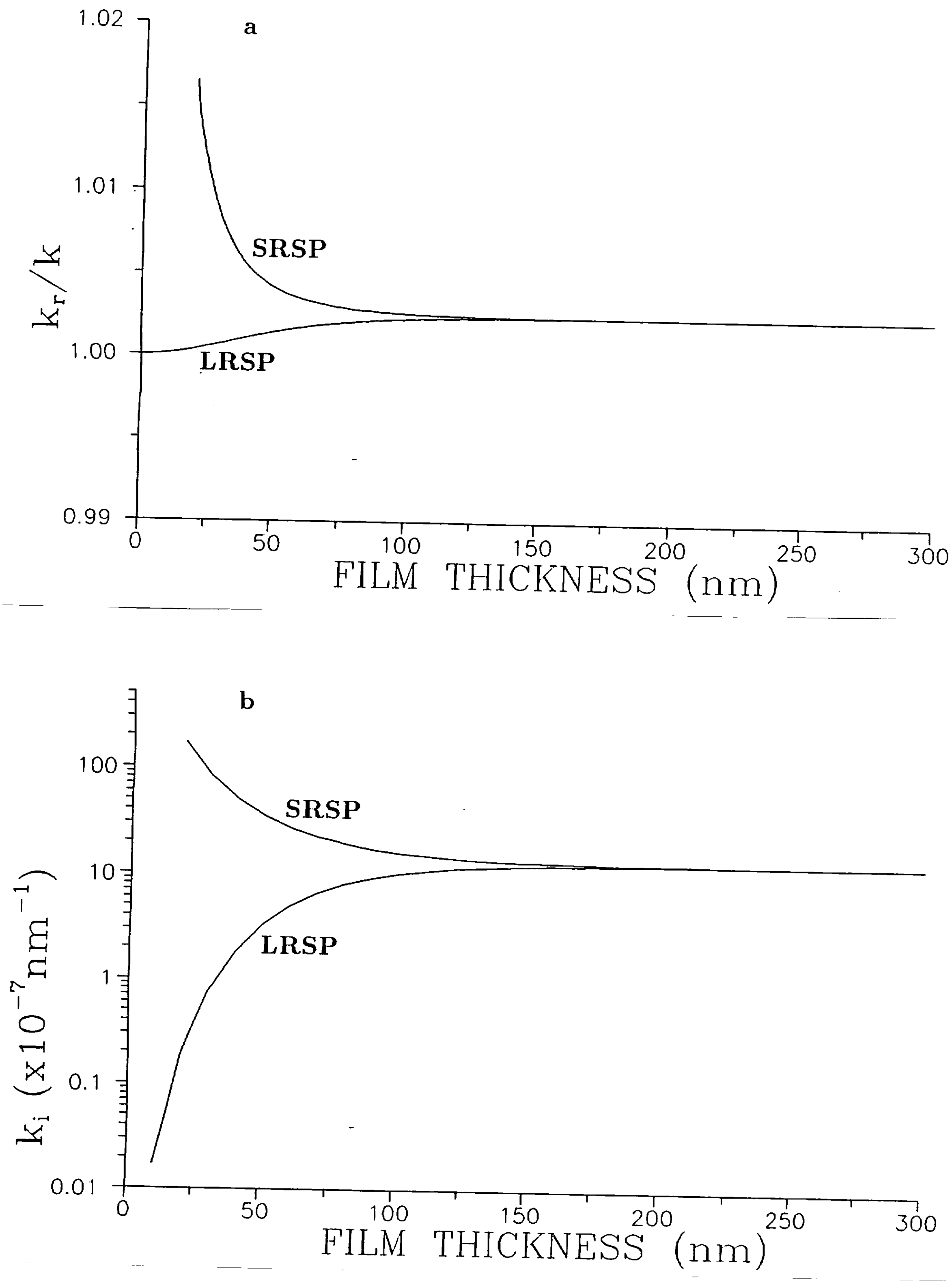

Figure 1.5: Mode dispersion curves showing (a) the real and (b) the imaginary components of the wavevectors verses film thickness for the LRSP and the SRSP on a gold film.

large and so in practice it cannot be excited at a suitable angle.

These modes were originally discovered by A Otto (1969) soon after his demonstration of single interface SPPs. D Sarid (1981) calculated mode dispersion curves (similar to those shown in figure 1.5) and also calculated H field profiles. Figure 1.6 shows sketches of E and H field profiles and also the Poynting vector (power flow) magnitudes as a function of z for the LRSP and the SRSP. The LRSP has an antisymmetric E field and a symmetric H field. The power plots also show that the proportion of the power flow in the metal is less for the LRSP than the SRSP. For a $17nm$ silver film at $\lambda = 632.8nm$, only 0.34% of the power flow associated with the LRSP is contained in the metal (L Wendler *et al*, 1986). It is the exclusion of the power flow from the absorbing metal that leads to a reduction in mode damping and hence k_i. This implies that as the film becomes thinner, the LRSP has an increased range and hence lifetime. For a $15nm$ silver film (at $632.8nm$) the range is $\sim 0.5mm$ compared to $43.3\mu m$ for the single interface SPP (see section 1.3). The decreased damping also leads to an increased field enhancement. D Sarid *et al* (1982) calculated the ratio of the square of the magnetic field at the metal surface to that inside the prism used to couple to the modes. For a $70nm$ silver film at a wavelength of $632.8nm$, the ratio was 40 whereas for a $10nm$ film with the same ϵ values, the ratio was 600. These large enhancements have prompted many workers to examine the LRSP with respect to possible nonlinear applications (see for example GI Stegeman *et al*, 1982 and RK Hickernell *et al*, 1986).

Experimental observations of these modes are contained in chapters 5,6 and 7.

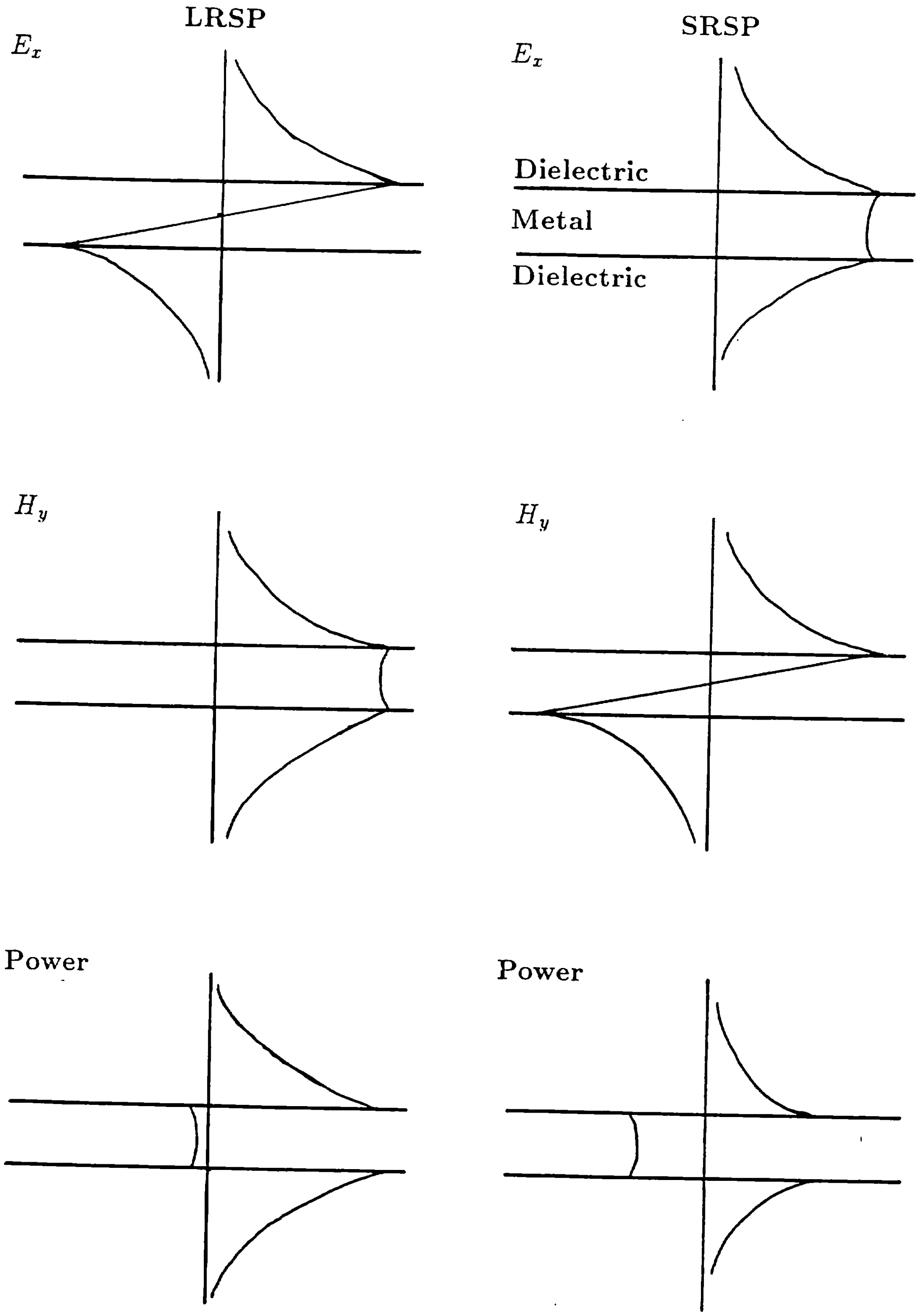

Figure 1.6: Field profiles and power flow magnitudes as a function of z for the LRSP and the SRSP.

1.6 Guided Modes

If a dielectric overlayer of a thickness greater than $\sim \lambda/4n$ is bounded by media with lower refractive indices then it may support a resonant guided mode. This is the optical equivalent to a microwave cavity and may be modelled as a wavefront zigzagging inside the dielectric layer (PK Tien, 1977). If the dielectric layer is made thicker then more than one guided mode may exist. The zigzag photon paths and the associated field profiles are sketched in figure 1.7 for 4 different guided modes. For isotropic layers guided modes may be transverse magnetic (TM) or transverse electric (TE) (the first transverse magnetic mode is called the TM_0 mode *etc.*). A TM_0 mode will always have a different propagation wavevector to a TE_0 mode even in an isotropic film due to different phase shifts that are encountered during the reflection of the zigzag wave. The field profiles sketched in figure 1.6 show that the TM_0 mode has one antinode in the film, the TM_1 has two antinodes *etc.*. Also the zigzag photon paths show that there is an upper limit on allowed mode number. Higher order modes are not strictly guided if their zigzag angle (θ_1) is less than the critical angles at either interface, as they then become leaky.

If we consider a three layer system with refractive indices n_0, n_1 and n_2 (n_1 refers to the waveguide refractive index), then the dispersion equation for both TM and TE modes may be written (PK Tien, 1977) as

$$k_\perp d + \Phi_{10} + \Phi_{12} = m\pi \tag{1.18}$$

where

$$\Phi_{10} = -\tan^{-1}(p_0/k_\perp), \quad \Phi_{12} = -\tan^{-1}(p_2/k_\perp) \quad \text{For a TE wave.} \tag{1.19}$$

$$\Phi_{10} = -\tan^{-1}(n_1^2 p_0/n_0^2 k_\perp), \quad \Phi_{12} = -\tan^{-1}(n_1^2 p_2/n_2^2 k_\perp) \quad \text{For a TM wave.} \tag{1.20}$$

with

$$p_{0,2}^2 = k_\parallel^2 - k^2 n_{0,2}^2,$$

$$k_\parallel = n_1 k \sin\theta_1, \quad k_\perp = n_1 k \cos\theta_1$$

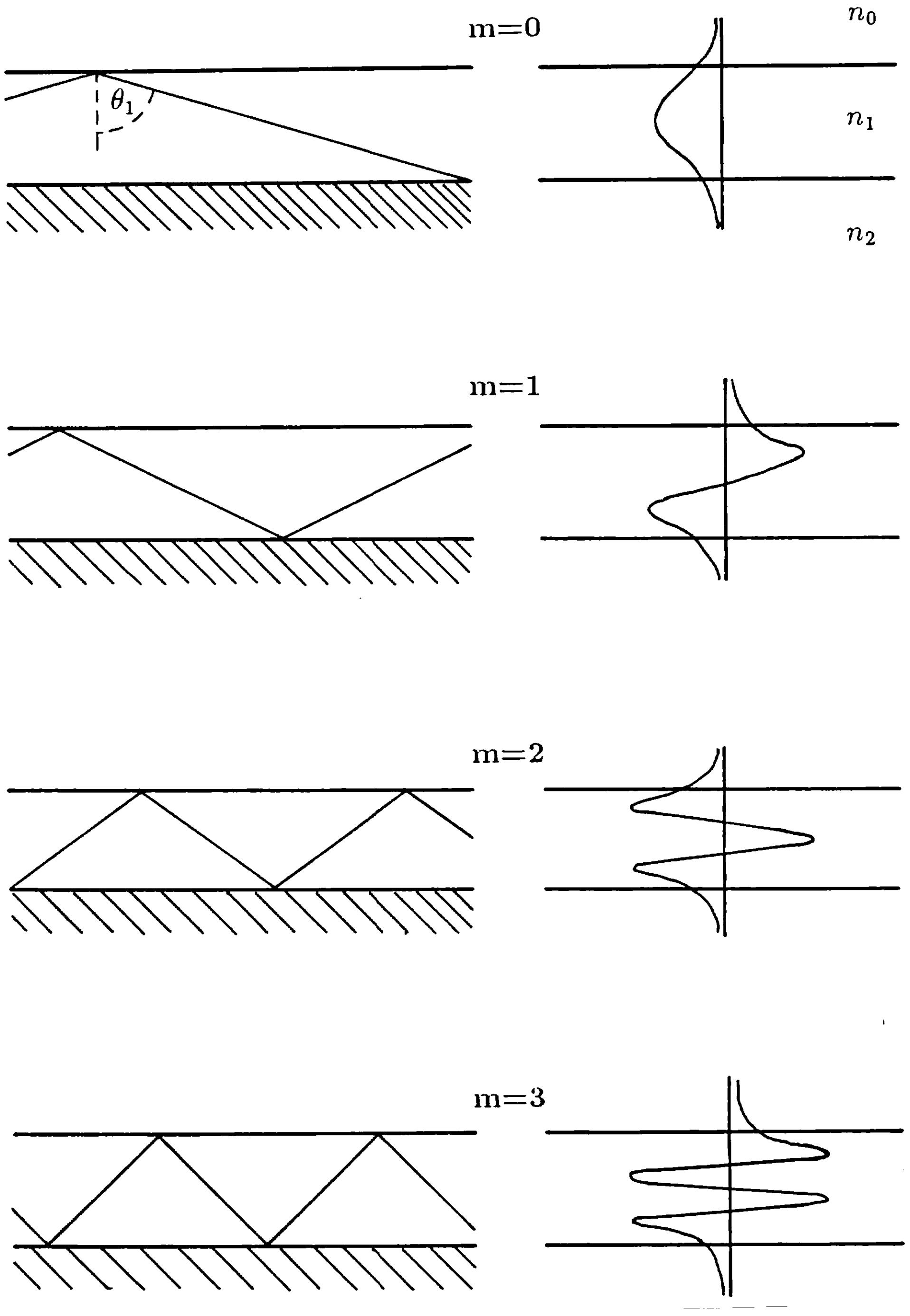

Figure 1.7: The zigzag photon paths and the H field profiles associated with the first four TM guided modes.

d is the film thickness, θ_1 is the zigzag angle (sown in figure 1.7) and $k = \omega/c$. Φ_{10} and Φ_{12} are the phase changes that occur when the wave reflects off each interface and $k_{\|}$ and $k_{\perp}$ are the wavevector components parallel and perpendicular to the interfaces. Equation 1.18 may be computed for any mode number m to produce the dispersion of the TM_m or TE_m mode. For a particular film thickness a TE mode will always have a larger $k_{\|}$ than the corresponding TM mode. The dispersion equation is most usefully solved in terms of $k_{\|}$ as this quantity is continuous across each interface (see section 1.3).

If this waveguide structure is on a grating surface then we may couple to a waveguide mode when

$$k \sin\theta = \pm k_{\|} \pm nG$$

Where θ is the external angle of incidence. By careful choice of grating depth, pitch and profile, over 35% of incident radiation may be coupled into a guided mode (SL Chuang *et al*, 1983) which can propagate many cm in a purely dielectric waveguide. The process of coupling to the guided mode will of course perturb the dispersion equation (1.18) by a small amount.

So far we have only dealt with purely dielectric waveguides but the structure made up of air/dielectric/metal will also act as a waveguide. In this case the metal has significant absorption so n_2^2 is replaced by ϵ_2 (relative permittivity) and Φ_{12} becomes complex. Metal clad guided modes therefore have a significant imaginary part (k_i) to their propagation wavevector and typically will only propagate a few μm. However when coupled to by a prism or a grating they do appear as narrow resonances and by correct choice of Otto gap or groove depth, 100% of the incident radiation may be coupled into a mode. This is useful in nonlinear optics as it can lead to significant heating of the film (see appendix A). Metal clad waveguides are also of interest with respect to p to s conversion (chapter 8).

1.7 Review of Theoretical Modelling

Theoretical modelling of the optical response of gratings has been historically limited by the lack of powerful computers. Unlike planar interface systems, grating systems cannot be solved to give analytic solutions. Instead, the obtained solution is always an infinite series which must be truncated at a suitable point.

The improvement of computers in the last 25 years has allowed more and more calculations to be carried out and nowadays very complex grating structures can be accurately modelled with moderate computation times. Two main methods exist for solving the grating problem; integral methods and differential methods (described by R Petit *et al*, 1980). The former is considered to be the only rigorous method but is of sufficient complexity to encourage many workers (including ourselves) to use the differential method.

A Hessel *et al* (1965) used a simple differential method which produced results similar to our data in short computation times. Unfortunately they modelled their grating as a periodic surface impedance which was impossible to express in terms of realistic parameters. H Numata (1982) used a differential technique in which the electromagnetic fields and the permittivity were described as Fourier sums. These were substituted into modified Maxwell equations which were then integrated up through the system to reveal the scattered mode amplitudes at the top of the grating. However, we found that the results depended strongly on the integration method and on the number of integration steps and so for our modelling this method was dropped in favour of the more elaborate differential technique of J Chandezon *et al* (1982) (described in detail in the next chapter). JJ Greffet *et al* (1990) have developed an iterative series solution to solve the grating problem. Their formulation is simple and applicable to any azimuthal angle but it appears to be limited to very shallow gratings (depth to pitch ratio of ~ 0.04). HA Yueh *et al* (1988) used a very complex formulation which was solved by a second order perturbation technique. This formulation allowed random roughness to be added to a grating surface and is perhaps unique in being able to describe both grating diffraction and roughness backscatter from the same surface. Many workers (such as E Kretschmann *et al*, 1975 and A Marvin *et al*, 1975) have studied SPPs on rough surfaces which are effectively gratings with many Fourier components and directions. However, these are only approximate theories and can only model small roughness. The most rigorous method for modelling gratings is perhaps that of D Maystre (1978) who uses the integral method which is applicable to multilayered gratings of any depth to pitch ratio and allows different groove profiles on each interface. However this method is conceptually and numerically complex and is probably only understood by a limited number of experts.

Theoretical modelling has also been extended to model particular applications. SD Gupta *et al* (1987) used a Rayleigh expansion method to solve a double interface grating system and hence modelled coupled SPPs occurring across a thin metal film. Two papers by E Popov *et al* (1990 and 1990a) show the exact energy flow contours within a grating groove. The first paper uses these to explain SPP losses in deep gratings, The second shows that shallow and deep gratings may appear similar in terms of energy flow lines over the tops of the grooves. This was used to explain the quasi periodicity in diffraction efficiency (with groove depth) that is observed in the Littrow configuration. P Halevi *et al* (1989) have theoretically modelled the form of minigaps that occur when two electromagnetic modes propagate simultaneously on a grating. They showed that the observed gap may be a momentum gap, an energy gap or both.

Other applications of grating theory include the modelling of second harmonic generation (SHG) which is enhanced by the presence of a grating. HJ Simon *et al* (1988) successfully used a Rayleigh method to compare with SHG data taken from a modulated silver/quartz interface. A differential method (M Nevière *et al*, 1988) and an integral method (D Maystre *et al*, 1988) have been found to produce almost identical results (within 1%) when used to describe SHG from a shallow silver grating (depth to pitch ratio of 0.05). Finally R Petit *et al* (1987) have used both differential and integral theories to describe the response of gratings which include an anisotropic layer. This final application is still in its early stages due to complexity of computation.

1.8 Summary

In this chapter the properties of SPPs, LRSPs and guided modes have been discussed. All these modes have been shown to have propagation wavevectors greater than k ($= \omega/c$) and the common methods of exciting these modes by enhancing photon momentum have been outlined. In the next chapter, we describe in detail the theoretical modelling method that was eventually used to describe the experimental results in this thesis.

Chapter 2

Electromagnetic Theory of Gratings

2.1 Introduction

In this chapter, the effect of a grating surface on incident photons is modelled theoretically. The primary objective is to be able to calculate the angular dependent zeroth order (specular) reflectivity from a grating to compare with experimental data. In section 2.2, we describe in detail the method of J Chandezon *et al* (1982) for achieving this objective. This is a differential method which allows for multiple interfaces and assumes that the incidence radiation lies in a plane of incidence which is normal to the grating grooves. In this configuration, all the diffracted beams propagate in the plane of incidence and so it is referred to as the planar geometry. We define an azimuthal angle ϕ which is zero in this case.

In section 2.3 we present a new formulation which is a more complex form of Chandezon's method and allows for conical diffraction ($\phi \neq 0°$). This theory is required to explain the newly discovered phenomenon of p to s conversion via optical modes on gratings (described in chapter 8).

2.2 Planar Diffraction

2.2.1 Presentation of the problem

The configuration to be modelled is shown in figure 2.1. Here a surface modulated substrate has a complex relative permittivity of ϵ_1 ($\epsilon = \epsilon_r + i\epsilon_i$). This is orientated such that the surface modulation is only a function of the variable x, and is described by $y = a(x)$. This structure is periodic, with period L, and a basis scattering vector of magnitude $K = 2\pi/L$. On top of this substrate can be deposited a series of overlayers with permittivities ϵ_2, ϵ_3 *etc.* and thicknesses of d_2, d_3 *etc.* (the total thickness being d). It is assumed that the surface form of any

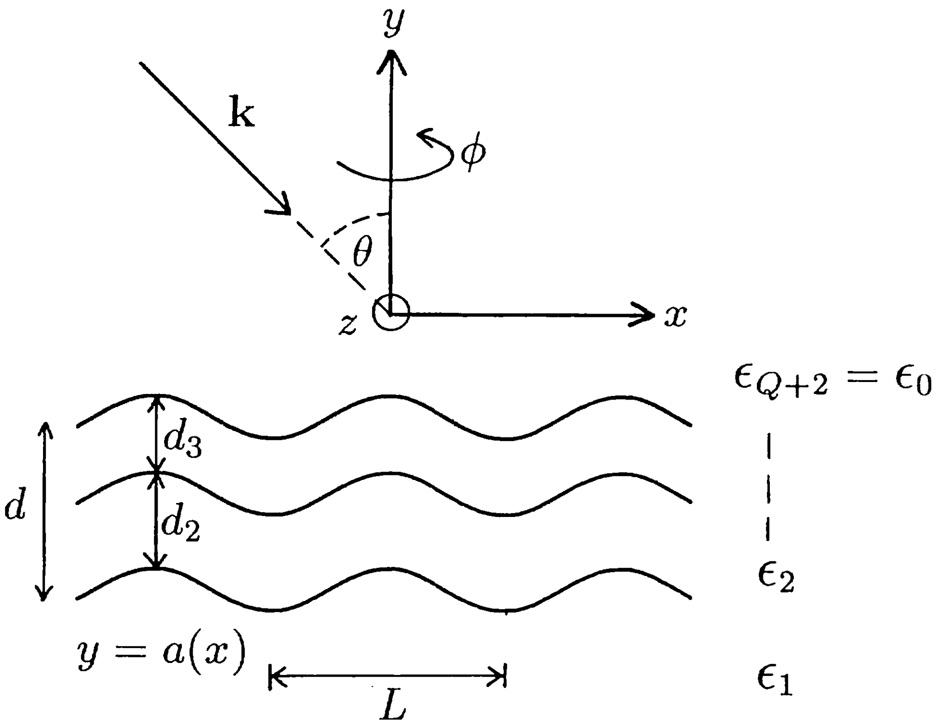

Figure 2.1: Presentation of the problem and notation.

overlayers on the grating is the same as that of the grating surface itself, and hence these are described by $y = a(x) + c$, where c is the sum thickness from the grating surface. The grating is illuminated through the top semi-infinite, non-absorbing medium with light of free space wave vector $\mathbf{k}$ (which has magnitude k in free space). The radiation is incident at an angle θ to the y-axis and lies in the x–y plane, which contains the grating scattering vector. Although the development can allow for general polarization of incoming light, for our purposes this will be limited to the cases of Transverse Electric (TE, or s-polarised with E-field perpendicular to the plane of incidence), or Transverse Magnetic (TM, or p-polarised with the H-field perpendicular to the plane of incidence). To simplify the notation we call F^i the complex amplitude of the incident field equal to E_z^i in the TE case or $\mathrm{H}_z^i(\mu_0/\epsilon_0)^{1/2}$ in the TM case. E_z^i and H_z^i are the only components (parallel to 0z) of the electric and magnetic field. The normalised incident field can be written as

$$F^i = \exp(ikx\sin\theta - iky\cos\theta) \tag{2.1}$$

The time dependence $\exp(-i\omega t)$ has been dropped for the sake of convenience. Above the grating, the diffracted field may be written as

$$F^d = \sum_n \mathrm{B_n} \exp\left[i(\alpha_n x + \beta_n y)\right] \tag{2.2}$$

where

$$\alpha_n = k\sin\theta + nK \tag{2.3}$$

$$\beta_n = (k^2 - \alpha_n^2)^{1/2}$$

When $k^2 > \alpha_n^2$, β_n is real and then F^d represents real propagating waves which are finite when $y \longrightarrow \infty$. When $k^2 < \alpha_n^2$, β_n is imaginary and F^d then represents the evanescent diffracted field which is bound to the grating and can be neglected as $y \longrightarrow \infty$. These two contributions are called F^{ad} and F^{ed} respectively.

We now translate the coordinate system in the following manner

$$v = y - a(x)$$

$$u = x, \quad w = z$$

This new coordinate system is one in which the grating modulation has been flattened out and the layers are now separated by plane interfaces. This allows a simpler description of field continuity as the normal to each interface no longer oscillates in the x (or u) direction. In this new coordinate system the expression for the incident field becomes

$$F^i = \exp(-ikv\cos\theta)\exp[-ika(u)\cos\theta]\exp(iku\sin\theta)$$

The second term of the right hand side contains the grating profile and may be developed as a Fourier series. Hence

$$F^i = \sum_m L_m(\beta_0)\exp\left[i(\alpha_m u - \beta_0 v)\right] \tag{2.4}$$

with

$$L_m(\beta_0) = \frac{1}{L}\int_0^L \exp\{-i[a(u)\beta_0 + mKx]\}dx \tag{2.5}$$

In a similar way, the propagating diffracted field can be written as

$$F^{ad} = \sum_{n\subset U}\sum_m B_n L_{m-n}(-\beta_n)\exp\left[i(\alpha_m u + \beta_n v)\right] \tag{2.6}$$

In this case we have a double sum over m Fourier components and n diffracted beams that are contained in the set U (where U is the set of integers which correspond to beams that are finite at $y \longrightarrow \infty$).

We may now state Maxwell's equations in the new coordinate system in terms of F and also another covariant component G which are defined in the jth medium as

$$F = E_w, \qquad G = kZ_0H_u \qquad \text{for TE polarisation}$$

$$F = Z_0H_w \qquad G = -k\epsilon_j E_u \qquad \text{for TM polarisation}$$

with $Z_0 = (\mu_0/\epsilon_0)^{1/2}$. The new Maxwell's equations are stated without proof as

$$\frac{\partial F}{\partial v} = \frac{a'}{1+a'^2}\frac{\partial F}{\partial u} + \frac{i}{1+a'^2}G \tag{2.7}$$

$$\frac{\partial G}{\partial v} = \frac{\partial}{\partial u}\left(\frac{i}{1+a'^2}\frac{\partial F}{\partial u}\right) + i\epsilon k^2 F + \frac{\partial}{\partial u}\left(\frac{a'}{1+a'^2}G\right) \tag{2.8}$$

where a' denotes the derivative of $a(u)$ with respect to u.

2.2.2 Formation of the solution

We now wish to solve the problem. Maxwell's equations have been formulated in the transformed coordinate frame in terms of the two field variables F and G, where these fields are functions of u and v. Also the incoming and scattered fields have been re-expressed in terms of a Fourier expansion in the u-direction momentum (that is α_m). It is now necessary to add in the appropriate boundary conditions. These are:-

(1) The continuity of the tangential fields at each interface.

(2) The outgoing wave condition (OWC), that is all fields remain finite when $y \longrightarrow \pm\infty$.

To do this we note that in the Maxwell's equations (2.7 and 2.8) the grating profile only enters the problem through a pair of periodic functions.

$$C(u) = \frac{1}{1+a'^2}\ , \qquad D(u) = \frac{a'}{1+a'^2}$$

We expand these as Fourier series in the grating scattering vector magnitude K, giving-

$$C(u) = \sum_n C_n \exp(inKu) \tag{2.9}$$

$$D(u) = \sum_n D_n \exp(inKu) \tag{2.10}$$

We then look for a similar expansions in terms of the u-component of momentum (α_m) for a solution of Maxwell's equations . These have the following form:-

$$\mathbf{F}(u,v) = \sum_m \mathbf{F}_m(v) \exp(i\alpha_m u) \tag{2.11}$$

$$\mathbf{G}(u,v) = \sum_m \mathbf{G}_m(v) \exp(i\alpha_m u)$$

Introducing these expansions for the profile of the grating surface, and for the fields into equations (2.7 and 2.8) and matching momenta leads to an infinite series of linear differential equations for each medium of the form:-

$$-i\frac{\partial F_m}{\partial v} = \sum_n (\alpha_n D_{m-n} F_n + C_{m-n} G_n) \tag{2.12}$$

$$-i\frac{\partial G_m}{\partial v} = \sum_n (\alpha_n \left[(-\alpha_m \alpha_n C_{m-n} + k^2 \epsilon_j \delta_{mn}) F_n + \alpha_m D_{m-n} G_n\right] \tag{2.13}$$

where δ_{mn} denotes the Kronecker symbol. Now in order to solve this infinite system numerically, it is necessary to introduce some cut-off in the scattered orders taken into account in the calculations. Hence a limit must be placed on the range over which n is summed, and the m components of the fields are evaluated. Here we allow each of the field components (F and G) to be expanded in a range of $\pm N$ in equations 2.12 and 2.13. We then write a new generalised field vector ξ containing the expanded field components:-

$$\xi(v) = (F_{-N}, F_{-N+1}, \cdots, F_N, G_{-N}, G_{-n+1}, \cdots, G_N) \text{ for TE polarisation} \tag{2.14}$$

$$\xi(v) = [F_{-N}, F_{-N+1}, \cdots, F_N, G_{-N}/\epsilon(v), \cdots, G_N/\epsilon(v)] \text{ for TM polarisation} \tag{2.15}$$

where the function $\epsilon(v)$ is equal to the value of ϵ at the ordinate v.

With the above expansions, equations 2.12 and 2.13 may be combined to form a convenient eigenequation:

$$-i\frac{d\xi(v)}{dv} = \{[R(v)]^{-1}\mathbf{T}(v)R(v)\}\xi(v) \tag{2.16}$$

where the matrix $\mathbf{T}$ is $4N+2$ by $4N+2$, made from 4 smaller $2N+1$ by $2N+1$ matrices expanded to $\pm N$. This is given by:-

$$\mathbf{T} = \begin{pmatrix} A & B \\ C & D \end{pmatrix}$$

where A to D are square matrices defined from equations (2.12) to (2.13) as follows:-

$$A_{m,n} = \alpha_n D_{m-n}$$

$$B_{m,n} = C_{m-n}$$

$$C_{m,n} = \alpha_m \alpha_n C_{m-n} + k^2 \epsilon_j(v)\delta_{mn}$$

$$D_{m.n} = \alpha_m D_{m-n}$$

R is a generalised diagonal matrix

$$\begin{pmatrix} R_1 & 0 \\ 0 & R_2 \end{pmatrix}$$

which is made up of two zero matrices, an R_1 matrix and an R_2 matrix each of size $2N+1$. The R_1 matrix contains terms δ_{mn} for the TE case or $\delta_{mn}/\epsilon^{1/2}$ for the TM case. The R_2 matrix contains terms δ_{mn} for the TE case or $\delta_{mn}\epsilon^{1/2}$ for the TM case. $(R)^{-1}$ is obtained simply by interchanging R_2 and R_1 in R.

$R^{-1}TR$ contained in the right hand side of equation 2.16 is constant in each medium j, therefore we may expand $\xi(v)$ as a sum of exponentials

$$\xi^j(v) = \sum_{q=1}^{2N+1} \xi_q^j \exp(ir_q^j v) \tag{2.17}$$

where r_q^j are the eigenvalues of the matrix T (the same as those of $R^{-1}TR$) and ξ_q^j are proportional to the eigenvectors $R^{-1}V_q^j$ of the matrix $R^{-1}TR$. If $\mathbf{V}_q^j$ are the eigenvectors of T then we may write

$$\xi_q^j = b_q^j(R^{-1}\mathbf{V}_q^j) \tag{2.18}$$

Finally from equation 2.17 and 2.18 we may state the form of $\xi(v)$ in each medium j

$$\xi^j = \mathbf{M}^j \phi^j(v) \mathbf{b}^j \tag{2.19}$$

where $\phi^j(v)$ is a diagonal matrix of components ϕ_{qp} $(= \exp(ir_q^j v)\delta_{qp})$ and M is a matrix whose columns are made from the eigenvectors $R^{-1}\mathbf{V}_q^j$. The amplitude vectors $\mathbf{b}^j$ need to be found in order to evaluate the field in each medium. ξ is continuous at each interface hence when $v = v^j$, $\xi^j = \xi^{j+1}$ or

$$\mathbf{M}^j \phi^j(v_j) \mathbf{b}^j = \mathbf{M}^{j+1} \phi^{j+1}(v_j) \mathbf{b}^{j+1} \tag{2.20}$$

From the above relationships we may prove two useful equations

$$\phi^j(v_j)[\phi^j(v_{j-1})]^{-1} = \phi^j(v_j - v_{j-1}) = \phi^j(d_j)$$

$$\phi^{Q+2}(v_{Q+1}) = \phi^{Q+2}(0) = 1$$

Where d_j is the thickness of the layer j and Q+2 is the top (semi-infinite) medium. Using these equations along with equation 2.20 we may finally deduce a relationship between the field at the bottom of the system (of magnitude $\mathbf{b}^1$) and the field at the top of the system (of magnitude $\mathbf{b}^{Q+2}$);

$$\begin{aligned} \mathbf{M}^{Q+2}\mathbf{b}^{Q+2} = & \left[\mathbf{M}^{Q+1}\phi^{Q+1}(d_{Q+1})(\mathbf{M}^{Q+1})^{-1}\right] \cdots \left[\mathbf{M}^j \phi^j(d_j)(\mathbf{M}^j)^{-1}\right] \\ & \cdots \left[\mathbf{M}^2 \phi^2(d_2)(\mathbf{M}^2)^{-1}\right] \mathbf{M}^1 \phi^1(-d) \mathbf{b}^1 \end{aligned} \tag{2.21}$$

For an uncoated (single interface) grating, $Q = 0$ and equation 2.21 may be written in the form

$$\mathbf{M}^1\mathbf{b}^1 = \mathbf{M}^2\mathbf{b}^2$$

For a multilayer grating, we note that each medium j is represented in equation 2.21 by the matrix $\mathbf{H^j} = \mathbf{M^j}\phi^j(d_j)(\mathbf{M}^j)^{-1}$, hence equation 2.21 may be written in the form

$$\mathbf{Hb^1} = \mathbf{M^{Q+2}b^{Q+2}} \tag{2.22}$$

where

$$\mathbf{H} = \mathbf{H^{Q+1}H^{Q}}\cdots\mathbf{H^1M^1}\phi^1(-d)$$

We are interested in the field above the grating represented by the vector $\mathbf{b}^{Q+2}$. To find this vector we must now apply the outgoing wave condition to the fields at the bottom and top of the grating structure.

At the bottom of the grating we must keep only the terms $\mathbf{b}_q^1$ for which r_q^1 corresponds to waves whose amplitudes decrease as $v \longrightarrow \infty$ (evanescent waves) or waves that propagate downwards. These waves have a v dependence that is contained in $\exp(ir_q^1 v)$ hence we must keep terms such that

$$\mathrm{Im}(r_q^1) < 0 \quad \text{or} \quad \mathrm{Im}(r_q^1) = 0 \ \text{ and } \ \mathrm{Re}(r_q^1) < 0 \tag{2.23}$$

For the ease of calculation we now separate the incident and real diffracted beams from the evanescent diffracted field. The former are given by equations 2.4 and 2.6 and the latter is left as a sum of exponentials as in equation 2.17. Therefore equation 2.19 is replaced for $j = Q + 2$ by

$$\xi = \mathbf{M}^{Q+2}\phi^{Q+2}(v)\mathbf{b}^{Q+2} + \exp(-i\beta_0 v)\mathbf{l} + \mathbf{M}'\phi'(v)\mathbf{B} \tag{2.24}$$

where $\mathbf{l}$ is a generalised vector having two components

$$\begin{pmatrix} \mathbf{l}' \\ \mathbf{l}'' \end{pmatrix}$$

given by

$$\mathbf{l}'_{\mathbf{m}} = L_m(\beta_0)$$

$$\mathbf{l}''_{\mathbf{m}} = -\left(\beta_0 - mK\frac{\alpha_0}{\beta_0}\right)L_m(\beta_0)$$

$\mathbf{B}$ is a vector of components $\mathbf{B}_\mathrm{n}$ $(n \subset U)$ and of size P. $\phi'(v)$ is a diagonal matrix of size P and components $\exp(i\beta_n v)\delta_{mn}$. M' is a generalised matrix

$$\begin{pmatrix} \mathrm{M}'' \\ \mathrm{M}''' \end{pmatrix}$$

where M$''$ and M$'''$ are rectangular matrices of size (4N+2)×P given by

$$\mathbf{M}''_{\mathbf{mn}} = L_{m-n}(-\beta_n)$$

$$\mathbf{M}'''_{\mathbf{mn}} = [\beta_n - (m-n)K\alpha_n/\beta_n]L_{m-n}(-\beta_n)$$

Since the term $\mathbf{M}^{Q+2}\mathbf{b}^{Q+2}$ represents only the evanescent diffracted field, we must only keep the components of $\mathbf{b}^{Q+2}$ corresponding to r_q^{Q+2} which decay in the positive v direction i.e.

$$\mathrm{Im}(r_q^{Q+2}) > 0 \tag{2.25}$$

Equation 2.19 has therefore been modified to equation 2.24 and so equation 2.22 now becomes

$$\mathbf{Hb^1} = \mathbf{M^{Q+2}b^{Q+2}} + \mathbf{l} + \mathbf{M'B} \tag{2.26}$$

It is this equation which must be solved in order to derive the scattered field amplitudes but we may simplify it further by noting the size of each quantity. b^1 contains 2N+1 terms, b^{Q+2} contains 2N+1-P terms and B contains P terms (where P is the number of real propagating diffracted beams). Hence if b^1, b^{Q+1} and B are stacked on top of each other we obtain a vector of 4N+2 terms. Similarly, the matrix H contains (4N+2)×(2N+1) terms, M^{Q+2} contains (4N+2)×(2N+1-P) terms and M' contains (4N+2)×P terms. Hence if H, M^{Q+2} and M' are stacked side by side they form a matrix of (4N+2)×(4N+2) terms. We can represent the new equation with the stacked vectors and matrices as

$$\mathbf{M} \quad \mathbf{b} = \mathbf{l} \tag{2.27}$$

where M contains the matrices stacked side by side and b contains the field amplitudes stacked one on top of the other. Therefore

$$\mathbf{b} = \mathbf{l}[\mathrm{M}]^{-1}$$

Hence we can obtain the evanescent fields and the real scattered fields from b which is convenently arranged due to the sorting of terms carried out earlier. The real scattered field amplitudes occur at the bottom of b and may typically be

$$\mathrm{b} = \begin{pmatrix} \vdots \\ B_1 \\ B_0 \\ B_{-1} \\ B_{-2} \end{pmatrix}$$

The position of the required result B_0 (specular reflectivity) in the column will change depending on the number of diffracted beams and so we must be careful to pick off the correct term.

2.2.3 Discussion

In this method of J Chandezon *et al* (1982), the incident and scattered beams along with the Maxwell's equations are converted into a non-orthogonal curvilinear coordinate system. The field components and the grating profile functions are expanded in Fourier series to give a system of 4N+2 linear differential equations which are combined into an eigen equation. The eigenvalues and eigenvectors of this equation are then sorted into different quantities depending on whether they are evanescent or propagating. The final matrix equation is then inverted to yield the scattered field intensities.

This theory was programmed in Fortran and run on a PC 386 with maths coprocessor. For a single interface system the computation time is 22 seconds per point. For a two interface system this rises to 34 seconds (over 90% of this time is spent solving the eigenequation). The value N is carefully chosen in order to evaluate reflectivities to high accuracy while still retaining workable computing times (the times given above are for N=5). If N=10, the single interface system takes 180 seconds to compute but in virtually all cases accurate convergence was achieved with N=5.

To check that our computations are correct we compared theoretical results to those shown by RA Depine *et al* (1987) who used the differential method of M Neviere *et al* (1974) and the integral method of D Maystre (1978). Figure 2.2(a) plots specular reflectivity verses angle showing our results (crosses) along with Neviere's method (solid line) and Maystre's method (dashed line). The system is

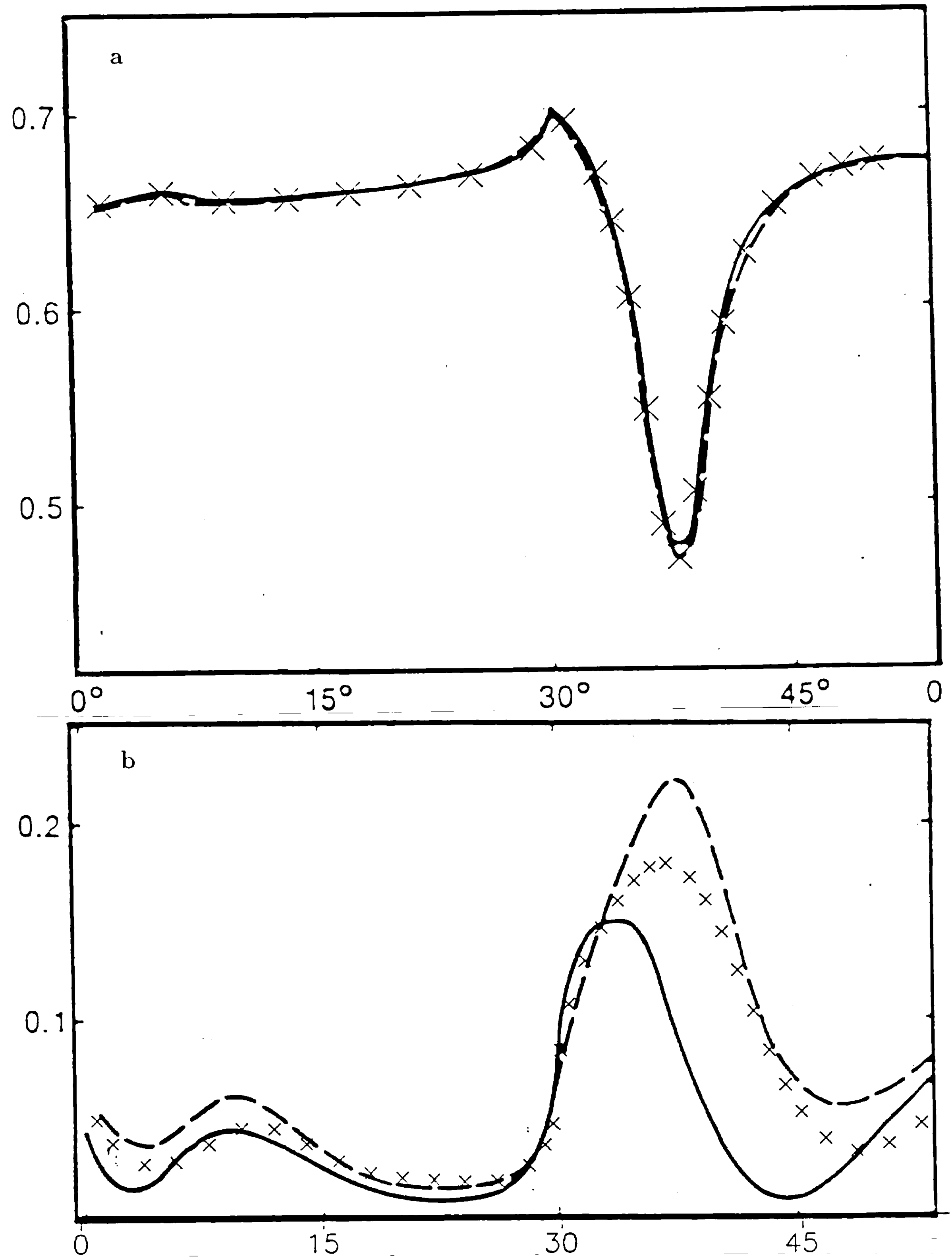

Figure 2.2: Specular reflectivity verses angle of incidence for a air/metal interface with $\epsilon_{metal} = -5.28 + 1.48i$. The grating is sinusoidal with $\lambda/L = 0.5$ and (a) $h/L = 0.05$, (b) $h/L = 0.2$. The crosses are our calculations, the solid line is the differential technique of Neviere *et al* and the dashed line is the integral method of Maystre.

a single interface between air and a metal, the latter having $\epsilon = -5.48+1.48i$. The grating has h/L=0.05 (h is groove depth) and λ/L=0.5. The agreement between all three methods is very good. Our points were calculated with N=10 but an N=3 calculation also converged very well (to within ±0.001%). Figure 2.2(b) shows reflectivity verses angle results using similar parameters but now with h/L=0.2. Our results lie between the other differential method and the integral method. In this regime (deep grooves) the integral method is the only rigorous method as all differential methods represent the electromagnetic fields as a plane wave expansion which is not realistic within the region close to the grooves. Therefore figure 2.3(b) shows the failure of differential methods when h/L=0.2 (they are only considered to be accurate when h/L<0.07). However the results seem to show that our calculations (using the differential method of J Chandezon) are more accurate than those using the method of M Neviere. For the gratings used in this thesis (with shallow grooves), the differential method is preferable to the integral method as the latter involves considerable mathematical and numerical complexity.

2.3 Conical Diffraction

We now present a new differential formulation applicable to conical diffraction. This method is a more general case of that used by J Chandezon *et al* (1982) and so the presentation and solution of the problem is carried out in a similar way to section 2.2.

2.3.1 Presentation of the problem

The configuration used in this section is the same as that shown in figure 2.1. The incoming field is again incident at an angle θ to the y axis but is now also at an angle ϕ to the $x-y$ plane. This incoming beam may be either TM or TE polarised and can be written as

$$\mathbf{F} = \mathbf{F}^i \exp\left[ik(x \sin\theta\cos\phi - y\cos\theta + z\sin\theta\sin\phi)\right] \tag{2.28}$$

where the time dependence $\exp(-i\omega t)$ has been dropped for convenience. The field components represented by $\mathbf{F}$ are dependent on the polarisation. The diffracted field above the grooves may be written as

$$\mathbf{F}^d = \sum_n \mathbf{B}_n \exp\left[i(\alpha_n x + \beta_n y + \gamma z)\right] \tag{2.29}$$

where

$$\alpha_n = k \sin\theta \cos\phi + nK$$

$$\beta_n = \left(k^2 - \alpha_n^2 - \gamma^2\right)^{1/2} \tag{2.30}$$

$$\gamma = k \sin\theta \sin\phi$$

When β_n is real, $\mathbf{B}_n$ represent propagating scattered fields (the observed reflected and diffracted beams). Comparing 2.30 to equation 2.3 shows that we now have an extra component γ which represents the azimuthal twist.

In order to model the system and match the boundary conditions at the interfaces we use the same coordinate transformation as J Chandezon;

$$v = y - a(x)$$

$$u = x \ , \quad w = z$$

Then as before we wish to express Maxwell's equations, and the incoming and scattered fields, in this new coordinate frame.

The transformed Maxwell's equations in this case will now be derived as opposed to the last section where they were merely stated without proof. We start with Maxwell's equations in the form

$$\nabla \wedge \mathbf{E} = -\frac{\partial \mathbf{B}}{\partial t}$$

$$\nabla \wedge \mathbf{H} = \frac{\partial \mathbf{D}}{\partial t}$$

Now in a transformed coordinate system we can write the curl part (of say **E**) as

$$\nabla \wedge \mathbf{E} = (\underline{\epsilon}^1 \frac{\partial}{\partial u} + \underline{\epsilon}^2 \frac{\partial}{\partial v} + \underline{\epsilon}^3 \frac{\partial}{\partial w}) \times (E_u \underline{\epsilon}_1 + E_v \underline{\epsilon}_2 + E_w \underline{\epsilon}_3)$$

where the $\underline{\epsilon}$'s are the contravariant and covariant vectors in the new coordinate frame, given for the system here by

$$\underline{\epsilon}^1 = \underline{i} \qquad \underline{\epsilon}^2 = \underline{j} - a'\underline{i} \qquad \underline{\epsilon}^3 = \underline{k} \tag{2.31}$$

$$\underline{\epsilon}_1 = \underline{i} + a'\underline{j} \qquad \underline{\epsilon}_2 = \underline{j} \qquad \underline{\epsilon}_3 = \underline{k}$$

where $\underline{i}$, $\underline{j}$ and $\underline{k}$ are the unit basis vectors in the original coordinate frame, and a' is the differential of $a(u)$ with respect to u.

Expanding this gives us the curl as

$$\begin{aligned} \nabla \wedge \mathbf{E} =& a' \frac{\partial E_u}{\partial u} \underline{k} + a'' E_u \underline{k} + \frac{\partial E_v}{\partial u} \underline{k} - \frac{\partial E_w}{\partial u} \underline{j} \\ & - (1 + a'^2) \frac{\partial E_u}{\partial v} \underline{k} - a' \frac{\partial E_v}{\partial v} \underline{k} + \frac{\partial E_w}{\partial v} \underline{i} + a' \frac{\partial E_w}{\partial v} \underline{j} \\ & + \frac{\partial E_u}{\partial w} \underline{j} - a' \frac{\partial E_u}{\partial w} \underline{i} - \frac{\partial E_v}{\partial w} \underline{i} \end{aligned} \tag{2.32}$$

together with a similar expression for $\nabla \wedge \mathbf{H}$. To transform the right hand sides of Maxwell's equations (the partial derivatives) we re-introduce a time dependence of $\exp(-i\omega t)$ to give

$$\frac{\partial \mathbf{B}}{\partial t} = -i\omega \mathbf{B} = -ikZ_0 \mathbf{H}$$

where Z_0 is the impedence of free space, defined as $Z_0 = (\mu_0/\epsilon_0)^{1/2}$. Once again we can express **H** in the new coordinate frame. This gives

$$\frac{\partial \mathbf{B}}{\partial t} = -ikZ_0 \left[H_u(\underline{i} + a'\underline{j}) + H_v \underline{j} + H_w \underline{k})\right] \tag{2.33}$$

with a similar form for $\partial \mathbf{D}/\partial t$.

This set of equations, 2.32 and 2.33 together with the corresponding expressions for $\nabla \wedge \mathbf{H}$ and $\partial\mathbf{D}/\partial t$, can be put into Maxwell's equations to lead to the new coordinate frame expressions. This is a set of six equations in six variables (the E-field and H-field components) which requires solution. It is convenient to write this in a matrix form. To do this we use a general field vector, containing the E and H components, in the form:-

$$\mathbf{G} = \begin{pmatrix} E_u \\ E_v \\ E_w \\ H_u \\ H_v \\ H_w \end{pmatrix}$$

We can then write Maxwell's equations as

$$\begin{pmatrix} \mathbf{0} & \mathbf{C} \\ \mathbf{C} & \mathbf{0} \end{pmatrix} \mathbf{G} = \frac{ik}{Z_0} \begin{pmatrix} -\epsilon\mathbf{T} & \mathbf{0} \\ \mathbf{0} & Z_0^2\mathbf{T} \end{pmatrix} \mathbf{G} \tag{2.34}$$

Where $\mathbf{0}$ is a 3×3 matrix of zeros (null matrix), ϵ is the relative permittivity, and $\mathbf{C}$ and $\mathbf{T}$ define the transformed curl and transformed field components respectively. They are defined from equations 2.32 and 2.33 as

$$\mathbf{C} = \begin{pmatrix} -a'\frac{\partial}{\partial w} & \frac{-\partial}{\partial w} & \frac{\partial}{\partial v} \\ \frac{\partial}{\partial w} & 0 & \frac{-\partial}{\partial u} + a'\frac{\partial}{\partial v} \\ a'\frac{\partial}{\partial u} + a'' - (1 + a'^2)\frac{\partial}{\partial v} & \frac{\partial}{\partial u} - a'\frac{\partial}{\partial v} & 0 \end{pmatrix}$$

and

$$\mathbf{T} = \begin{pmatrix} 1 & 0 & 0 \\ a' & 1 & 0 \\ 0 & 0 & 1 \end{pmatrix}$$

This then is a 6×6 system which defines Maxwell's equations in our new coordinate frame, and these require solution to find the fields as functions of u, v and w.

It is helpful to notice that terms in $\partial/\partial w$ can be replaced. Since the only z dependance is that due to the component of incoming light wave vector in the z-direction (that is all z components go as $\exp(i\gamma z)$) we can write:-

$$\frac{\partial}{\partial w} = i\gamma$$

This conveniently removes one of the differentials from the definition of the **C** matrix above, and we can write all fields in the form

$$\mathbf{F}(u,v,w) = \mathbf{F}(u,v)\exp(i\gamma w)$$

It should also be noted at this point that we can then rearrange our equations into a form involving four variables, and always find the additional field components by substitution if required. This is very useful, as reduction to a four variable system (two E-fields and two H-fields) will allow faster and more efficient numerical evaluation. More importantly, by use of field components which are parallel to the grating surface it will be convenient to match the continuity of the tangential components of **E** and **H** required at interfaces in the system. Therefore here we reduce to a 4×4 system involving the components $E_{\|}$, E_w, $H_{\|}$ and H_w, where the $\|$ components are those tangential to the grating surface in the x–y plane, given by

$$H_{\|} = (1 + a'^2)H_u + a'H_v$$

$$E_{\|} = (1 + a'^2)E_u + a'E_v$$

and the w components are those tangential to the surface along the grating grooves:-

$$H_w \equiv H_z$$

$$E_w \equiv E_z$$

We can then after some algebraic manipulation write equation 2.34 as

$$\begin{aligned} \frac{\partial E_{\|}}{\partial v} = & - ikZ_0 H_w + \frac{\partial}{\partial u}\left[\frac{a'}{1 + a'^2}E_{\|}\right] \\ & - \frac{\partial}{\partial u}\left[\frac{\gamma Z_0}{k\epsilon(1 + a'^2)}H_{\|} + \frac{iZ_0}{k\epsilon(1 + a'^2)}\frac{\partial H_w}{\partial u}\right] \end{aligned} \qquad (2.35)$$

$$\begin{aligned}\frac{\partial E_w}{\partial v} =& \left[ikZ_0 - \frac{i\gamma^2 Z_0}{k\epsilon}\right]\frac{H_{\parallel}}{1+a'^2} \\ &+ \frac{a'}{1+a'^2}\frac{\partial E_w}{\partial u} + \frac{Z_0\gamma}{k\epsilon(1+a'^2)}\frac{\partial H_w}{\partial u}\end{aligned} \tag{2.36}$$

$$\begin{aligned}\frac{\partial H_{\parallel}}{\partial v} =& \frac{ik\epsilon}{Z_0}E_w + \frac{\partial}{\partial u}\left[\frac{a'}{1+a'^2}H_{\parallel}\right] \\ &+ \frac{\partial}{\partial u}\left[\frac{\gamma}{kZ_o(1+a'^2)}E_{\parallel} + \frac{i}{kZ_o(1+a'^2)}\frac{\partial E_w}{\partial u}\right]\end{aligned} \tag{2.37}$$

$$\begin{aligned}\frac{\partial H_w}{\partial v} =& \left[-\frac{ik\epsilon}{Z_0} + \frac{i\gamma^2}{kZ_0}\right]\frac{E_{\parallel}}{1+a'^2} \\ &+ \frac{a'}{1+a'^2}\frac{\partial H_w}{\partial u} - \frac{\gamma}{kZ_0(1+a'^2)}\frac{\partial E_w}{\partial u}\end{aligned} \tag{2.38}$$

These are the off-axis (conical diffraction) analogues of equations 2.7 and 2.8 in section 2.2. These then are the reduced form of Maxwell's equations for each layer in the new coordinate frame, and the solution of these is now required.

Having developed the Maxwell equations we now require the development of the incoming and scattered fields in the new coordinate frame. In order to do this the w-component of the incident field is written in the new frame as

$$F_w = F_w^i \exp(i\gamma w - i\beta_0 v)\exp(i\alpha_0 u - i\beta_0 a(u))$$

This can be developed as a Fourier series around the second right hand term $\exp(i\alpha_m u)$:

$$F_w = F_w^i \sum_m L_m(\beta_0)\exp\left[i(\alpha_m u - \beta_0 v + \gamma w)\right]$$

where

$$L_m(\beta_0) = \frac{1}{L}\int_0^L \exp\left[-i\big(a(u)\beta_0 + mKu\big)\right]du$$

Now the incident field can be expressed primarily in terms of the z-components (w-components in the new frame) of $\mathbf{E}$ and $\mathbf{H}$ for plane polarized waves. So we then write

$$H_w^i = \mathrm{TM}\cos\phi - \mathrm{TE}\sin\phi\cos\theta$$

$$E_w^i = \mathrm{TM}\sin\phi\cos\theta Z_0 + \mathrm{TE}\cos\phi Z_0 \tag{2.39}$$

In these, the values of TM and TE define the magnitudes of the H components of the incoming p-polarized and s-polarized light respectively. Now we can derive the form of the $\|$-components of these incident fields. This is done using equation (2.38) (for the E-field component) and equation (2.36) (for the H-field component), together with the useful identities:

$$\frac{\partial F_w}{\partial v} = -i\beta_0 F_w$$

and

$$\beta_0 a' F_w = -F_w^i \sum_m (mK) L_m(\beta_0) \exp\left[i(\alpha_m u - \beta_0 v + \gamma w)\right]$$

This then leads to the definitions of the incoming fields as

$$E_{\|} = \frac{i}{fac} \sum_m \left[\frac{\alpha_0}{\beta_0} H_w^i mK - \beta_0 H_w^i + \frac{\gamma}{kZ_0} \alpha_0 E_w^i + \frac{\gamma}{kZ_0} E_w^i mK \right] L_m(\beta_0) \exp(i\alpha_m u) \tag{2.40}$$

$$fac = \frac{-ik\epsilon}{Z_0} + \frac{i\gamma^2}{kZ_0}$$

$$H_{\|} = \frac{i}{fac2} \sum_m \left[\frac{\alpha_0}{\beta_0} E_w^i mK - \beta_0 E_w^i - \frac{Z_0\gamma}{k\epsilon} \alpha_0 H_w^i - \frac{Z_0\gamma}{k\epsilon} H_w^i mK \right] L_m(\beta_0) \exp(i\alpha_m u) \tag{2.41}$$

$$fac2 = ikZ_0 - \frac{i\gamma^2 Z_0}{k\epsilon} = \frac{-Z_0^2}{\epsilon} fac$$

and

$$E_w = \sum_m E_w^i L_m(\beta_0) \exp(i\alpha_m u) \tag{2.42}$$

$$H_w = \sum_m H_w^i L_m(\beta_0) \exp(i\alpha_m u) \tag{2.43}$$

Where the $\exp(i\gamma w - i\beta_0 v)$ terms have been dropped from the expressions.

We wish to derive similar expansions for the propagating scattered fields, in order to calculate the reflectivites from the grating structure. We expand these as

$$F_w^d = \sum_n \sum_m F_w^{nd} L_{m-n}(-\beta_n) \exp\left[i(\alpha_m u + \beta_n v + \gamma w)\right]$$

In this we use the further identity:

$$\beta_n a' \sum_m L_{m-n}(-\beta_n) \exp\left[i(\alpha_m u + \beta_0 v + \gamma w)\right] =$$

$$\sum_m (m-n) K L_{m-n}(-\beta_n) \exp\left[i(\alpha_m u + \beta_0 v + \gamma w)\right]$$

Again substitution into equations (2.38) and (2.36) yields expressions for the scattered electric and magnetic fields. These are

$$\begin{aligned} E_{\parallel}^{d} = \frac{i}{fac} \sum_{n} \sum_{m} \Bigg[& \beta_n H_w^{nd} - \frac{\alpha_n}{\beta_n} H_w^{nd} (m-n) K + \frac{\gamma}{k Z_0} \alpha_n E_w^{nd} \\ & + \frac{\gamma}{k Z_0} E_w^{nd} (m-n) K \Bigg] L_{m-n}(-\beta_n) \exp(i\alpha_m u) \end{aligned} \tag{2.44}$$

$$\begin{aligned} H_{\parallel}^{d} = \frac{i}{fac2} \sum_{n} \sum_{m} \Bigg[& \beta_n E_w^{nd} - \frac{\alpha_n}{\beta_n} E_w^{nd} (m-n) K - \frac{Z_0 \gamma}{k \epsilon} \alpha_n H_w^{nd} \\ & - \frac{Z_0 \gamma}{k \epsilon} H_w^{nd} (m-n) K \Bigg] L_{m-n}(-\beta_n) \exp(i\alpha_m u) \end{aligned} \tag{2.45}$$

and

$$E_w^d = \sum_n \sum_m E_w^{nd} L_{m-n}(-\beta_n) \exp(i\alpha_m u) \tag{2.46}$$

$$H_w^d = \sum_n \sum_m H_w^{nd} L_{m-n}(-\beta_n) \exp(i\alpha_m u) \tag{2.47}$$

where the $\exp(i\gamma w + i\beta_n v)$ terms have been dropped.

Here we write the outgoing (scattered) field components in the w-direction as:

$$H_w^{nd} = \mathrm{TM}^n \cos\phi' + \mathrm{TE}^n \sin\phi' \cos\theta'$$

$$E_w^{nd} = -\mathrm{TM}^n \sin\phi' \cos\theta' Z_0 + \mathrm{TE}^n \cos\phi' Z_0 \tag{2.48}$$

Notice the change of signs for the components of the field parallel to the plane of incidence and the dashes which indicate that it is the scattered field directions which are involved. The values of TE^n and TM^n are the scattered field amplitudes which we wish to find.

2.3.2 Formation of the solution

In equations 2.35 to 2.38 the grating profile enters the problem through two periodic functions

$$C(u) = \frac{1}{1+a'^2}\,, \quad D(u) = \frac{a'}{1+a'^2}$$

Hence we may expand these as a fourier series in exactly the same way as section 2.2.2 giving

$$C(u) = \sum_n C_n \exp(inKu)$$

$$D(u) = \sum_n D_n \exp(inKu)$$

A similar expansion for the field components has the form

$$\mathbf{F}(u,v) = \sum_m \mathbf{F}_m(v) \exp(i\alpha_m u)$$

where **F** represents any of the four field components in this problem.

Introducing these expansions into equations 2.35 to 2.38 and matching momenta leads to a series of equations for each medium of the form

$$\begin{aligned} -i\frac{\partial E^{\|}_m}{\partial v} = \sum_p \Big[\Big(\frac{Z_0\alpha_m\alpha_p}{k\epsilon_j}C_{m-p} - kZ_0\delta_{mp}\Big)H^w_p \\ + \alpha_m D_{m-p}E^{\|}_p - \frac{\gamma Z_0}{k\epsilon_j}\alpha_m C_{m-p}H^{\|}_p\Big] \end{aligned} \tag{2.49}$$

$$\begin{aligned} -i\frac{\partial E^w_m}{\partial v} = \sum_p \Big[\alpha_p D_{m-p}E^w_p + \Big(kZ_0 - \frac{\gamma Z_0}{k\epsilon_j}\Big)C_{m-p}H^{\|}_p \\ + \frac{Z_0\gamma}{k\epsilon_j}\alpha_p C_{m-p}H^w_p\Big] \end{aligned} \tag{2.50}$$

$$\begin{aligned} -i\frac{\partial H^{\|}_m}{\partial v} = \sum_p \Big[\Big(\frac{-\alpha_m\alpha_p}{kZ_0}C_{m-p} + \frac{k\epsilon_j}{Z_0}\delta_{mp}\Big)E^w_p \\ + \alpha_m D_{m-p}H^{\|}_p + \frac{\gamma}{kZ_0}\alpha_m C_{m-p}E^{\|}_p\Big] \end{aligned} \tag{2.51}$$

$$\begin{aligned} -i\frac{\partial H^w_m}{\partial v} = \sum_p \Big[\alpha_p D_{m-p}H^w_p + \Big(\frac{-k\epsilon_j}{Z_0} + \frac{\gamma}{kZ_0}\Big)C_{m-p}E^{\|}_p \\ - \frac{\gamma}{kZ_0}\alpha_p C_{m-p}E^w_p\Big] \end{aligned} \tag{2.52}$$

where δ_{mp} is the Kronecker delta and j is the medium label.

Now in order to solve this infinite system numerically, it is necessary to introduce some cut-off in the scattered orders taken into account in the calculations. That is a limit must be placed on the range over which p is summed, and the m components of the fields are evaluated.

Here we allow each of the components of field ($E_{\|}$, E_w, $H_{\|}$ and H_w) to be expanded in a range of $\pm N$ in equations 2.49 to 2.52. We then write a new generalised field vector ξ containing the expanded field components

$$\xi(v) = \begin{pmatrix} E_{\|} \\ E_w \\ H_{\|} \\ H_w \end{pmatrix}$$

where each of the field components is expanded to $\pm N$. This ξ is therefore a vector of size $8N + 4$. With this expansion for the fields we can write the above set of equations conveniently as an eigenequation.

$$-i\frac{d\xi(v)}{dv} = \mathbf{T}(v)\xi(v) \tag{2.53}$$

where the matrix $\mathbf{T}$ is $8N+4$ by $8N+4$, made from 16 smaller $2N+1$ by $2N+1$ matrices expanded to $\pm N$. This is given by

$$\mathbf{T} = \begin{pmatrix} A & 0 & C & D \\ 0 & F & G & H \\ I & J & A & 0 \\ M & N & 0 & F \end{pmatrix}$$

Where the 0's are $2N + 1$ by $2N + 1$ matrices of zeros, and A to N are similar square matrices defined from equations 2.49 to 2.52 as follows:

$$A = \alpha_m D_{m-p}$$

$$C = \frac{-\gamma Z_0}{k\epsilon_j}\alpha_m C_{m-p}$$

$$D = \frac{Z_0}{k\epsilon_j}\alpha_m\alpha_p C_{m-p} - kZ_0\delta_{mp}$$

$$F = \alpha_p D_{m-p}$$

$$G = \left(kZ_0 - \frac{\gamma^2 Z_0}{k\epsilon_j}\right)C_{m-p}$$

$$H = \frac{Z_0\gamma}{k\epsilon_j}\alpha_p C_{m-p}$$

$$\begin{pmatrix} I & J \\ M & N \end{pmatrix} = \frac{-\epsilon_j}{Z_0^2}\begin{pmatrix} C & D \\ G & H \end{pmatrix}$$

The eigenequation (2.53) can be solved in each medium, leading to a set of $8N+4$ eigenvectors and eigenvalues for each medium. We write these as $\mathbf{V}_q^j$ and r_q^j respectively. Here the subscript q is the eigenvector/value index, and the superscript j is the medium index.

We now expand ξ as a sum in each medium, writing

$$\xi(v) = \sum_q b_q^j \mathbf{V}_q^j \exp(i r_q^j v)$$

and can therefore write

$$\xi(v) = \mathbf{M}^j \phi^j(v) \mathbf{b}^j \qquad (2.54)$$

where $\mathbf{M}^j$ is a matrix whose columns are made from the eigenvectors $\mathbf{V}_q^j$ and ϕ^j is a matrix whose components are $\phi_{qp}^j = \exp(i r_q^j v)\delta_{pq}$. The amplitude vectors $\mathbf{b}^j$ need then to be found in order to evaluate the fields in each medium.

By applying the outgoing wave condition in a similar way to section 2.2.2, equation 2.54 may be written (in the top medium) as

$$\xi = \mathbf{M}^{Q+2} \phi^{Q+2}(v) \mathbf{b}^{Q+2} + \exp(i\gamma w - i\beta_0 v)\mathbf{l} + \mathbf{M}' \phi'(v) \mathbf{B}$$

Where the $\mathbf{M}^{Q+2}$ now contains only the decaying waves, and $\mathbf{l}$ is the vector made up from 4 vectors of size $2N+1$ defining the incoming fields for $E_{\|}$, E_w, $H_{\|}$ and H_w from equations 2.40 to 2.43 (where the vertical index of the vector replaces the summation index m in the equations). $\mathbf{B}$ is the required vector of amplitudes of the propagating scattered modes, being the values of TE^n and TM^n in the scattered field equations earlier. $\phi'(v)$ is then a matrix defined by $\exp(i\gamma w + i\beta_n v)\delta_{nm}$, and $\mathbf{M}'$ is a generalised matrix giving the scattered field expansions as shown in equations 2.44 to 2.47 above. The index m in the summation now becomes the vertical index of the matrix and the index n becomes the horizontal index, chosen only for the subset of propagating scattered modes (when β_n is real).

In the same way as section 2.2.2, boundary conditions link the fields at the bottom and the top of the grating by

$$\mathbf{H}\mathbf{b}^1 = \mathbf{M}^{Q+2}\mathbf{b}^{Q+2} + \mathbf{l} + \mathbf{M}'\mathbf{B} \qquad (2.55)$$

It is this equation which requires final solution in order to derive the scattered field amplitudes.

Using the chosen condition for the top layer ($\mathrm{Im}(r_q^{Q+2}) > 0$) it is found that $\mathbf{b}^{Q+2}$ retains 4N+2-2P unknowns. where P is the number of propagating scattered modes (including the zero order mode). Thus the remaining $2P$ unknowns are the amplitudes of the propagating modes for the two polarizations, TM and TE. They are the unknowns in equations 2.44 to 2.47 above, and form the **B** vector in equation 2.55. We now note that in the bottom medium the field must also satisfy the outgoing wave condition, that is must either be propagating downwards, or decay as $y \longrightarrow -\infty$. This requires that we retain only the components of $\mathbf{b}^1$ such that the eigenvalues r_q^1 are either purely real and negative, or have negative imaginary components. There are 4N+2 such components, which means that if the above equation is to be solved numerically a total of 4N+2 other unknowns are evaluated. Finally therefore for equation 2.55 we have 4N+2 unknowns on the left hand side (in the $\mathbf{b}^1$), 4N+2-2P unknowns in $\mathbf{M}^{Q+2}\mathbf{b}^{Q+2}$ and 2P unknowns in the scattered field vector **B** on the right hand side. This gives a total of 8N+4 unknowns in equation 2.55, where **I** is the known incoming field vector. Now solution of the remaining 8N+4 by 8N+4 system allows the evaluation of these unknowns, and hence the required reflectivities. This is carried out in the same way as in section 2.2.2 by stacking the vectors and matrices into a new matrix equation.

2.3.3. Discussion

This formulation was programmed in Fortran onto a PC386 with maths coprocesser. Computation times were 95 seconds per point for a single interface system and 196 seconds per point for a two interface system (with N=5). These times are considerably longer than those given in section 2.2.3 as we are now solving an 8N+4 system instead of a 4N+2 system. The convergence of this new method was found to be identical to the planar geometry case. Setting $\phi = 0°$ in our method gave very similar results to the planar case and showed the same deviation from the integral method for deep gratings. The accuracy of our new formulation when ϕ is not 0° is tested in chapter 8 by comparison with experimental data taken from gratings with well known parameters.

2.4 Summary

In this chapter we have described in detail the differential method of J Chandezon *et al.* In this method, the surface modulation is flattened out by conversion to a new coordinate system. The incoming and outgoing fields along with Maxwell's equations are expressed in this new system and solved by expanding these as a Fourier series in the grating vector. Our numerical results compare well with other methods for low groove depth to pitch ratios (~ 0.07) but lead to inaccurate predictions for deeper gratings.

The theory programs were also extended to produce automatic fitting routines. These routines take a data set reduced to about 40 points to increase the program speed. Theoretical points are calculated at the same angles as each of the data points. The differences between theory and data are squared and added and the fitting routine then iterates the relevant theory parameters to attempt to reduce this difference. Another set of theory points is then calculated and the process is repeated until an acceptable sum of squares difference is achieved. (The iterations were carried out very efficiently by a NAG routine).

The chapter also describes a new differential method applicable to conical diffraction. This is substantially more complex than the planar diffraction theory and requires the solution of a 8N+4 system rather than a 4N+2 system (leading to far greater computation times). This new theory is required to model the newly discovered phenomenon of p to s conversion (chapter 8).

Chapter 3

Experimental Techniques

3.1 Grating Manufacture

All gratings used in this study were produced at the National Physical Laboratory with the help of Dr M C Hutley and Mrs S J Wilson.

3.1.1 Substrate Preparation

The grating substrates used are all circular with a diameter of $30mm$ and thicknesses ranging from $3mm$ to $6mm$. They are made from either glass or silica with a surface flatness of $\sim \lambda/5$.

The substrates are first coated on one face with black paint (Ebonite) which prevents reflections from the back face of the substrate causing interference during exposure. The unpainted face of the substrate is then cleaned by wiping with a cloth soaked first in acetone then methanol and finally by drag cleaning with methanol on lens tissue. This ensured the removal of grease and dust.

The photoresists used are either Shipley 1350 or Shipley 1400 depending on the application. These are spin coated at 1700 RPM and 2000 RPM respectively. Each coating is spun for 40 seconds after applying a single drop of photoresist at the centre of the substrate. Dust is a major problem in spinning and leads to 'boomerang' shaped streaks in the surface. Therefore the spinning is carried out in a laminar flow hood using photoresist that has been filtered to $1\mu m$. The substrate is also dusted off with filtered air immediately prior to spinning.

After spinning, the substrates are placed in an oven at $60°C$ for 30 minutes to fully dry the photoresist. The photoresist layer obtained is almost as flat as the substrate and is ready for exposure. Between spinning and exposure the substrates are kept in the dark or under yellow light to avoid pre-exposure of the photoresist which is mainly sensitive to light in the range of $300 - 400nm$.

3.1.2 Exposure and Development

The system for grating exposure is illustrated in figure 3.1.

There are many other configurations of interferometer (M C Hutley, 1982), but this system is well tested and is known to produce sinusoidal gratings. The purpose of the system is to produce interference fringes in the vicinity of the photoresist to obtain a grating of pitch d where $\lambda = 2d\sin\theta$ (θ is as shown).

The $457.9nm$ line from an argon ion laser is used as it lies closest to the range of high sensitivity of the photoresist. An intercavity etalon is fitted in the laser to reduce the line width and so increase the laser coherence length to $> 1m$. The maximum power output on this line is $\sim$ 600mW. The mirrors and beam splitter used all have a quoted flatness of $\lambda/20$.

The laser beam is first focused by a short focal length lens L1 onto a diffuser D1 and then passes through a second rotating diffuser D2 placed at the focus of L1. The diffusers each have one optically flat face and one diffuse face produced by grinding and then immersing in 5% hydrofluoric acid for a few hours. The etching results in a much smaller solid angle of scatter and so increases the amount of light collected by the concave mirror. As well as diverging the laser beam, the diffusers also destroy spatial coherence across the beam by producing very small speckles. The latter property is vital for producing good gratings as dust on any of the mirrors is illuminated by an incoherent wavefront and so will not be recorded in the photoresist as a ring pattern. Systems without diffusers have only worked in ultra clean environments. The distance from D2 to the concave mirror is carefully adjusted to give a collimated beam. At the beamsplitter the amplitude is split roughly 50:50 and the two beams eventually fall on the sample. Each beam undergoes the same number of reflections and so the speckles at the sample overlay.

Alignment of the system is carried out without the diffusers and with the sample holder replaced with a mirror on a graduated rotating table. The latter is used to set up the angle θ and to check that reflections back down the system pass back through the aperture. Various tests are carried out to ensure that the beam is collimated and that the two beams overlay perfectly at the sample. Also the path lengths of the two beams need to be within a few centimetres of each other (well within the coherence length). Only when all the tests work simultaneously is the system ready for use.

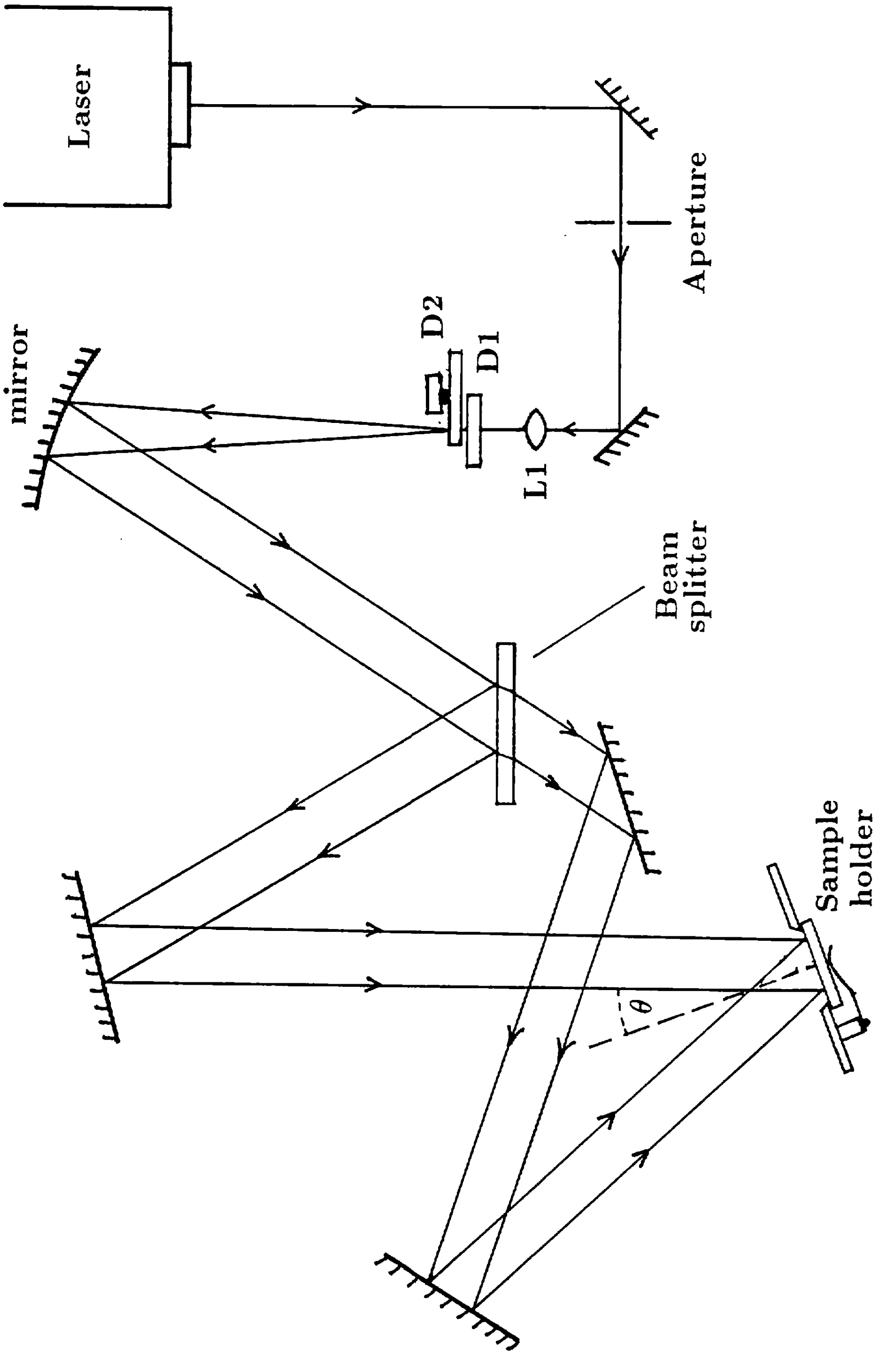

Figure 3.1: The interferometer used in the production of gratings.

After blocking off the laser beam, the grating substrate is placed in the holder. The whole system is then surrounded by foam in order to reduce vibrations from the air and also air currents. The sample is left in the holder for 5 minutes prior to the exposure to allow it to reach thermal equilibrium. Exposure times ranged from 20-200 seconds.

After exposure the photoresist is developed in Shipley Microposit developer for 5 seconds and then immediately rinsed in water for at least 1 minute.(The developer removes the photoresist that has been polymerized by the laser beam and so converts the stored interference profile into grating grooves). The sample was dried with an air blower and finally left under a mercury lamp for 30 minutes to fully harden the photoresist.

This 'holographic' technique is far easier and cheaper than producing ruled gratings and permits excellent control of groove pitch, depth and profile. A total of 63 gratings were produced in this way.

3.1.3 Ion Beam Etching

There are several problems in leaving the grating profile in photoresist. Firstly, the photoresist is very sensitive to vapour attack and cannot be cleaned in most organic solvents. After coating the grating with a metal it cannot be cleaned in acid and recoated without severe loss in quality. Also some experiments require the metal film to be deposited on a dielectric with a well defined refractive index and a very low absorption. Photoresist is not suitable for these applications. It is therefore far more convenient to transfer the grating profile from the photoresist to the silica substrate. This cannot be done by chemical etching as photoresist and silica are chemically dissimilar, and so ion beam etching is used as illustrated in figure 3.2.

The system is initially pumped down to 6.0×10^{-4}Pa then argon gas is admitted until a pressure of 1.2×10^{-2}Pa is obtained. This pressure is regulated automatically throughout the etching. Electrons given off from the heated cathode collide with argon atoms causing ionization. These argon ions are then accelerated through a potential of 600V and are collimated to within $\sim 10°$. The ions collide with the sample knocking out molecules in a controlled, uniform manner. The total etching time required is about 13 minutes but this is split into 1.5 minute

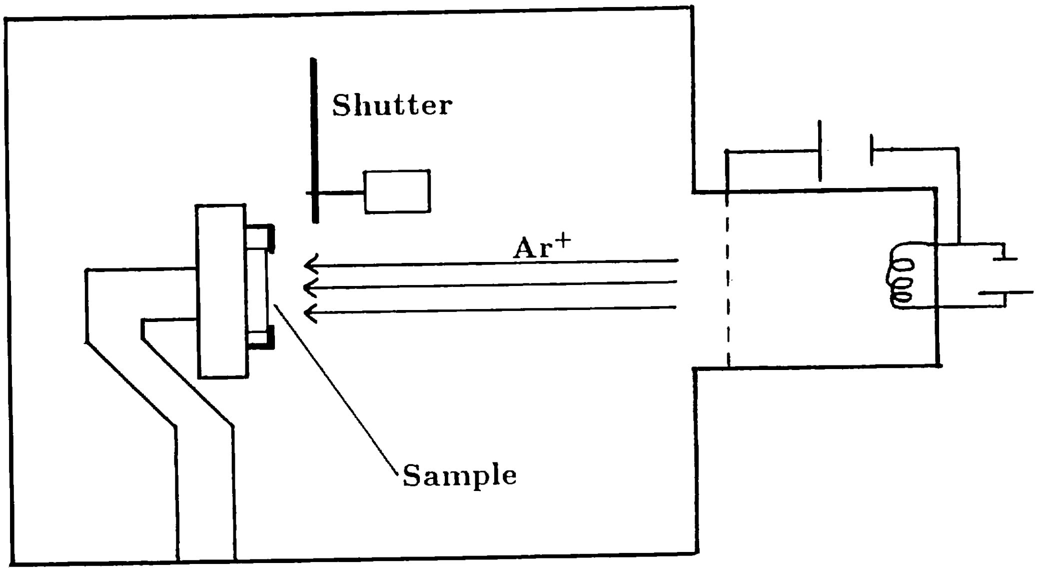

Figure 3.2: Experimental arrangement for ion beam etching.

exposures with 5 minute gaps to prevent the photoresist from melting. The grating is held by earthed metal clips to prevent charging of the sample which would decrease etching efficiency and the sample holder is also constantly rotating to prevent the photoresist from sagging.

When the gratings are to be etched, the photoresist used is Shipley 1350 diluted to 50%. This gives a thinner coating of $\sim 1.3\mu m$ and so long etch times are not required. The argon ions etch faster through silica than photoresist and so the final groove depth in silica is 1.3-1.5 times deeper than the original depth in photoresist. However the profile remains unchanged for shallow gratings (Etching efficiency depends on angle of incidence and so deep gratings with large facet angles will be distorted by etching leading to a more triangular profile).

3.2 Characterisation

Once the grating has been made its groove depth, pitch and profile need to be measured. Several methods are employed to find all of these.

3.2.1 Use of Talystep and S.E.M.

The talystep may be used to measure the groove depth and check the profile. This works by drawing a lightly loaded diamond stylus across the grating surface and electronically monitoring its vertical displacement as the stylus tip moves up and down the grooves. The talystep used (at the National Physical Laboratory) can measure vertical displacements of a few angstroms and is calibrated to ±0.3% (for a typical measurement). Figure 3.3 shows some typical traces from different gratings (only the vertical scale is calibrated). Care must be taken in interpreting these plots as they are the convolution of the groove profile with the profile of the stylus tip. However this is only a significant problem for deep gratings with fine pitches.

Photoresist gratings can only be used with the talystep after coating with metal to prevent the stylus tip cutting into the grooves. Talystep measurements showed that the variation in groove depth across the grating was less than 10% which shows that the illumination of the grating during exposure is fairly uniform.

A scanning electron microscope was also used to check the quality of the grating grooves. Figure 3.4 shows images of grooves from two different gratings.

The images are not particularly high resolution but do show that the grooves are uniform along their length. Much clearer S.E.M. photographs have been obtained by breaking the grating in two and looking at the grooves 'edge on' (M C Hutley, 1982 and T Harada *et al*, 1987).

3.2.2 Determination of Grating Pitch

The best method for determining grating pitch is via reflectivity scans (explained in detail in section 3.3). Figure 3.5 shows a typical experimental scan containing a SPP resonance.

To the left of the resonance at 12.12° is a 'critical' angle seen by a sharp increase in reflectivity. This is due to a diffracted beam 'passing off' or ceasing to

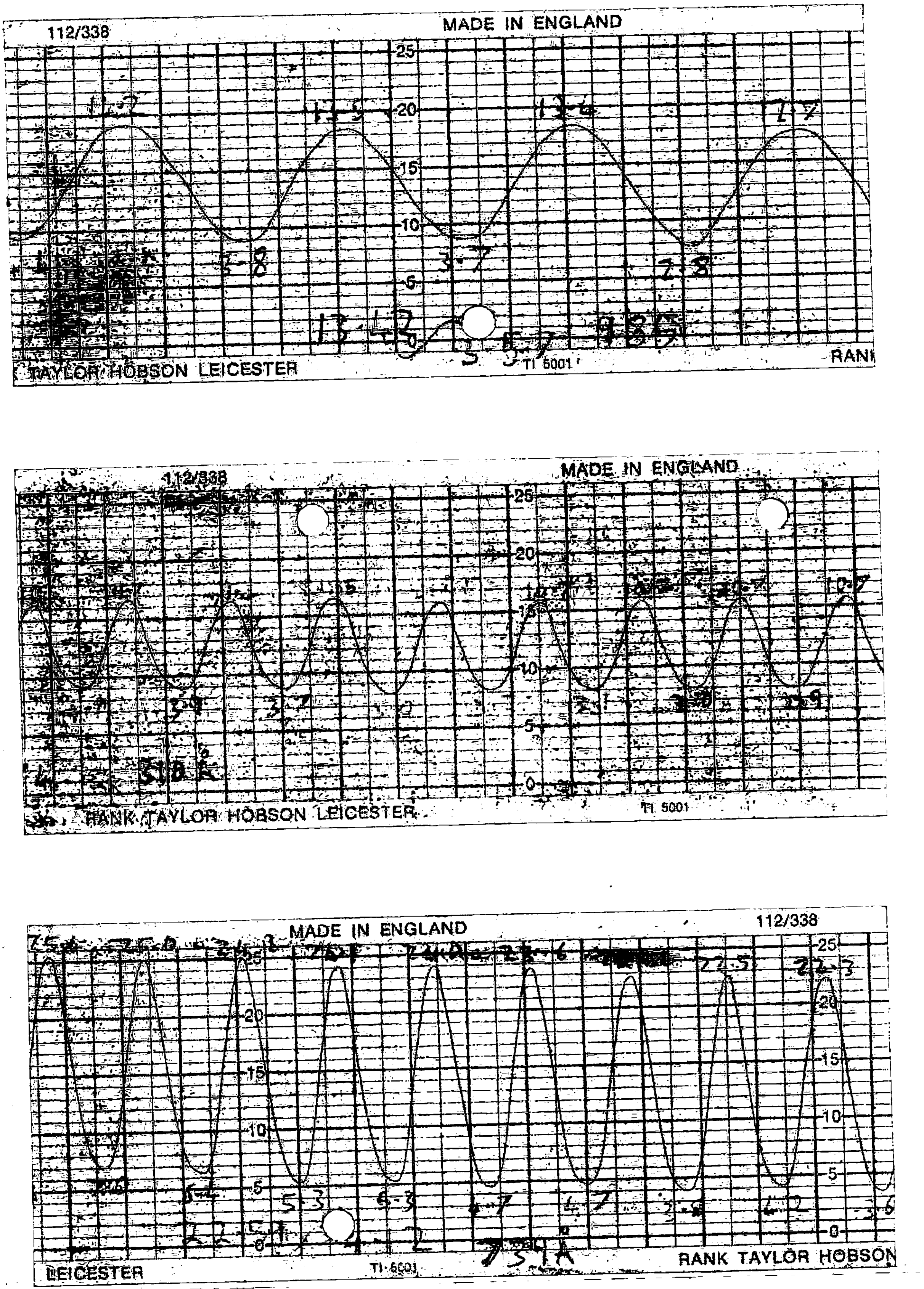

Figure 3.3: Groove profiles measured with the talystep.

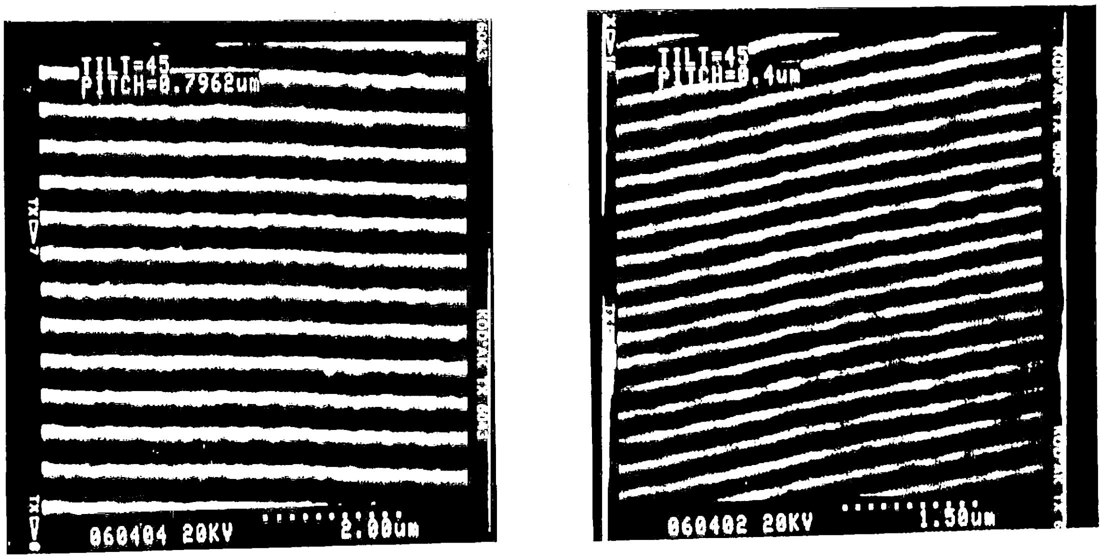

Figure 3.4: Scanning electron microscope pictures of grating grooves from two different gratings.

propagate as a real wave. The light from this diffracted beam is then redistributed amongst the other beams including the specular reflection leading to the observed rise in reflectivity. The 'critical' angle, θ_c is given by;

$$k \sin \theta_c = k - G$$

Where k is the wavevector of light in vacuum and G is the reciprocal grating vector (equal to 2π/grating pitch). Hence from the critical angle, the pitch may be calculated. For the scan shown in figure 3.5;

$$\text{Grating Pitch} = 801.0nm \pm 0.5nm$$

Hence the technique is accurate to better than 0.1%.

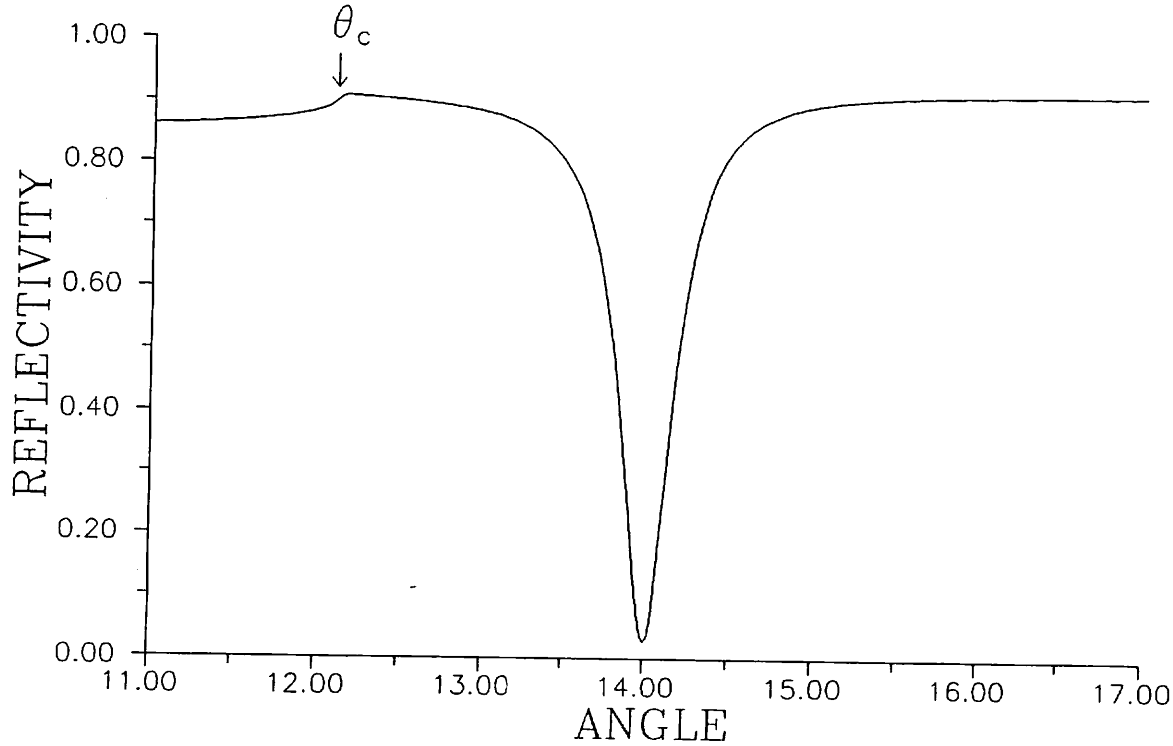

Figure 3.5: Reflectivity scan showing 'critical angle' (θ_c) used in the determination of grating pitch.

3.3 Reflectivity Measurements

All investigations in this thesis involved recording reflectivity verses angle of incidence. This was done at several wavelengths using different sources and detectors.

Figure 3.6 shows a schematic of the experimental arrangement. The sample is illuminated with laser light that has been mechanically chopped at 1.7kHz. The first polariser is used to set the input polarisation to either p or s. The signal detector and sample are mounted on a rotating table that is geared in such a way that the detector moves at twice the angular speed of the sample. A second polariser in front of the signal detector allows either the p or s component of the reflected beam to be monitored. A glass beamsplitter reflects a small percentage of the beam into a reference detector to allow correction for drift in laser intensity.

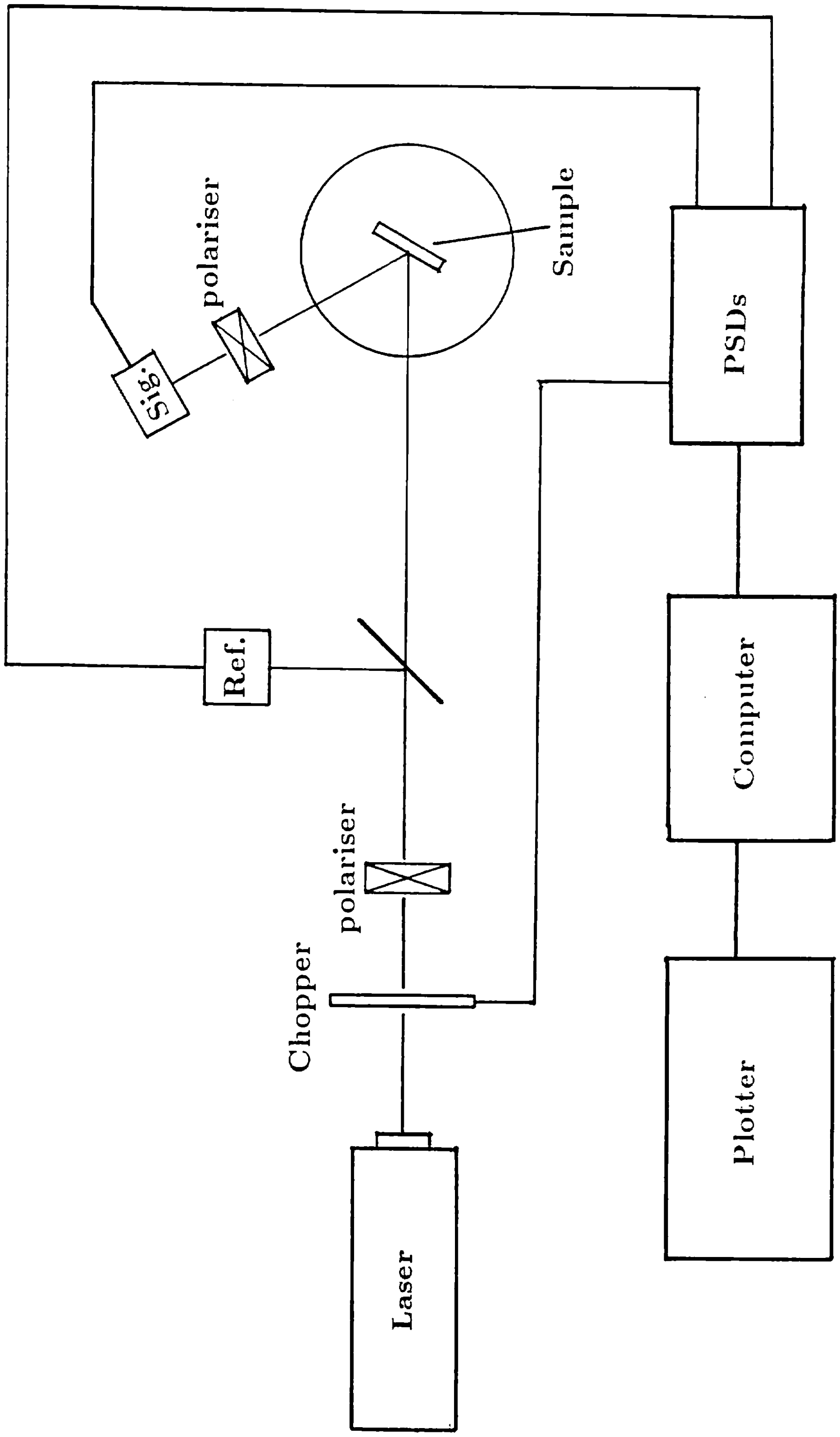

Figure 3.6: Experimental arrangement used in reflectivity measurements.

Both the signal and reference lines are fed into phase sensitive detectors (PSDs) which use the chopper signal as their phase input. The D.C. outputs from these are finally stored on computer after A to D conversion, and an unnormalised reflectivity is obtained by dividing the signal by the reference.

The extinction ratio of the polarisers is better than $200,000:1$ when using red HeNe ($\lambda = 632.8nm$) laser light. Angular scan rates are carefully chosen so that the rate of change of reflectivity with time is always slow compared to the time constants of the PSDs. All data is normalised to the direct signal by removing the sample and directly measuring the laser beam with the signal detector. When this signal is divided by the reference it gives the normalisation signal to be divided into all the other data. The error involved in normalisation is $\pm 0.2\%$, and the signal detector has a large active area compared to the beam width so that slight movement of the spot on the detector does not cause a significant reflectivity error. Noise on the data is of the order of $\pm 0.01\%$ using a red HeNe laser and silicon photodiode detectors.

When studying modes with a small half width, the beam divergence has a measureable effect on the reflectivity measurements and so must be well quantified. For the red HeNe line, the beam divergence is $0.06°$ but this may be reduced to $\sim 0.02°$ by using a spatial filter and a lens to expand and recollimate the beam. Other lasers used were an argon ion laser with a beam divergence of $0.03°$ and an infra red ($\lambda = 1.52\mu m$) HeNe laser with a beam divergence of $0.12°$. The latter was detected with germanium photodiodes.

Experiments were also carried out using a monochromator as a tunable wavelength source. Careful use of optics and apertures produces a beam with a divergence of $0.15°$ and a wavelength spread of less than $0.1nm$ (both these parameters are acceptable values). Due to the weak intensity from the monochromator, photomultiplier tubes are used for signal and reference detection. Acceptable signal to noise ratios were obtained in the wavelength range of $360 - 800nm$ by using slow scan speeds and a longer PSD time constant.

All scans taken in this thesis monitor the specular (zeroth order) reflectivity from the grating. Previous work has dealt with scanning diffracted beams but this requires a more complex rotating table. Also for the experiments in this thesis no extra useful information would be obtained by scanning diffracted beams.

Chapter 4

Surface Plasmon Polaritons on Gratings

4.1 Introduction

As discussed in section 1.4, diffraction gratings have been used by many workers for the excitation of SPPs. The strength of coupling to the mode is dictated by the metal parameters, the groove depth and also the azimuthal angle (discussed in section 4.2).

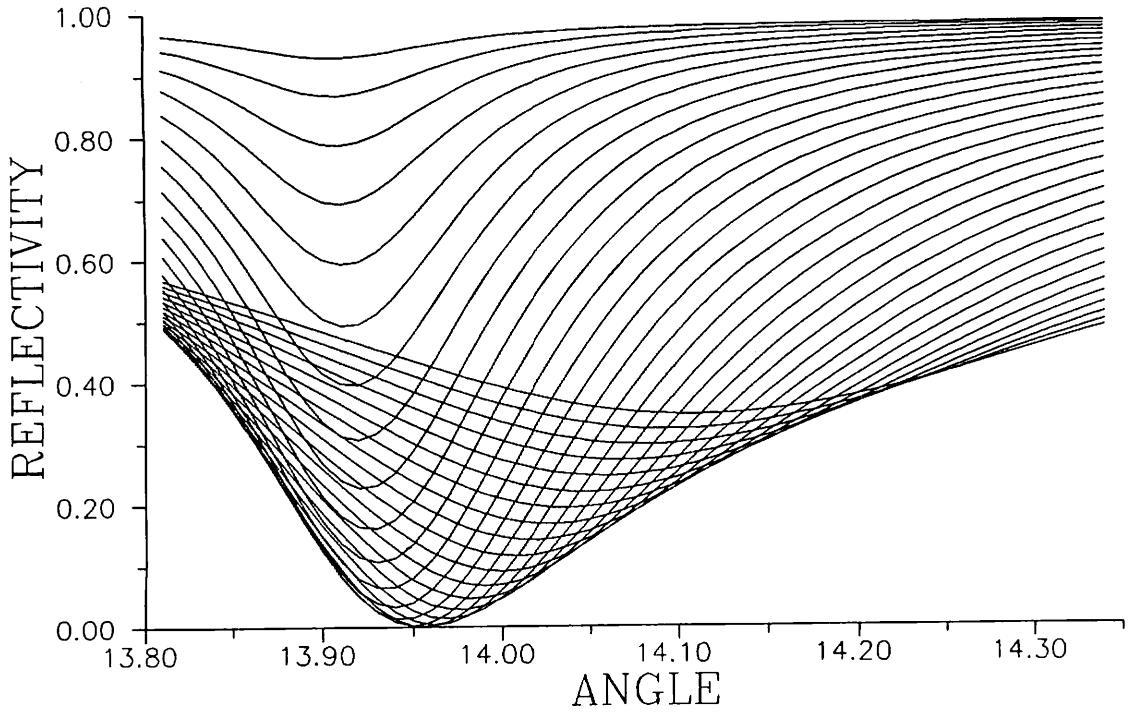

Figure 4.1: Theoretically generated reflectivity scans in the region of a surface plasmon polariton resonance. The groove depth is varied from 4.0nm to 66.0nm in steps of 2.0nm.

Figure 4.1 shows theoretically generated reflectivity scans in the region of a SPP minimum for a variety of groove depths (varying from 4.0*nm* to 66.6*nm* in steps of 2.0*nm*. The grating pitch is 800.8*nm* and the metal parameters are $\epsilon = -17.12 + 0.62i$ (silver at $\lambda = 632.8nm$). As the groove depth is increased, the coupling to the mode changes from being undercoupled to overcoupled. Perfect coupling exists at a groove depth of 34.0*nm*. This shows that SPPs are best excited on gratings with shallow grooves. In this case the optimum depth to pitch ratio is only 0.042 which contrasts with spectroscopic gratings where the depth to pitch ratio may be as large as 0.5.

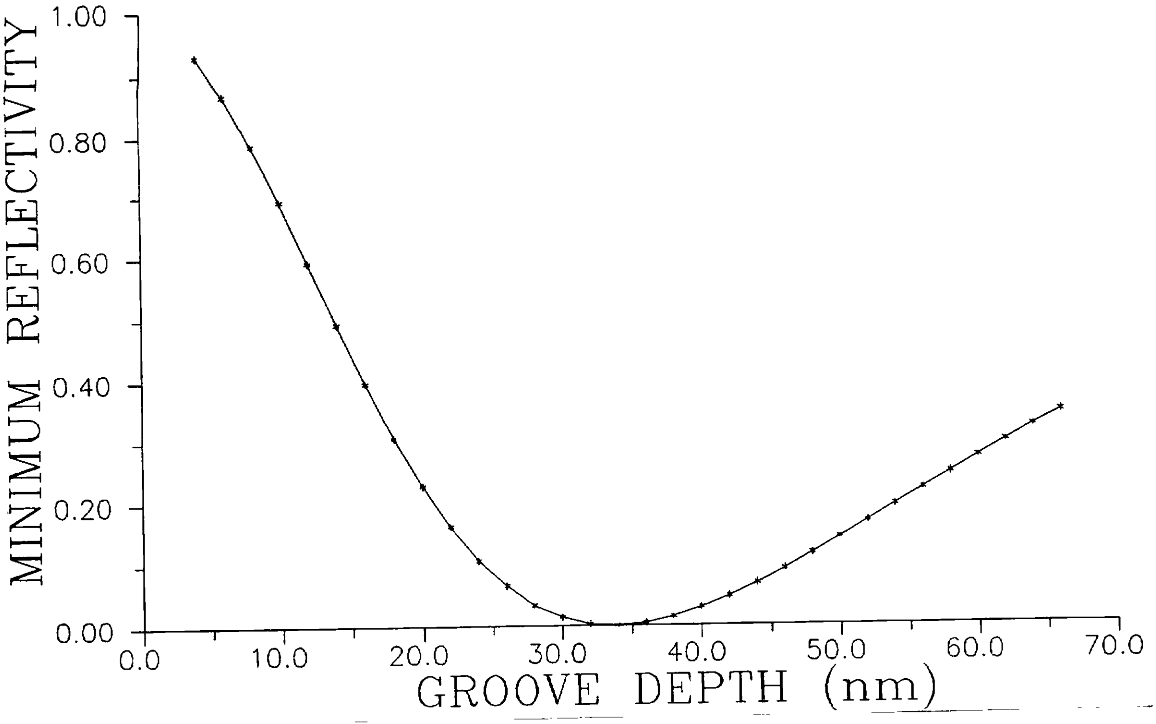

Figure 4.2: Resonance depth as a function of groove depth.

Figure 4.2 shows the minimum reflectivity for each scan in figure 4.1 verses groove depth. The curve itself has a broad minimum showing that a well coupled mode can be obtained from gratings with a range of groove depths. This is a useful property of SPP coupling as exact control of groove depth during manufacture in not possible. The gradient of the curve shows that the resonance depth is more sensitive to groove depth for an undercoupled SPP than for an overcoupled SPP and is especially sensitive for groove depths lying in the range of $\sim 10.0 - 20.0nm$. This sensitivity of the mode to groove depth is important if we wish to find an unknown groove depth using SPP excitation. Avoidance of the minimum in figure 4.2 to enhance this sensitivity can be achieved either by changing the wavelength of study or by using a different metal (both cause a change in ϵ).

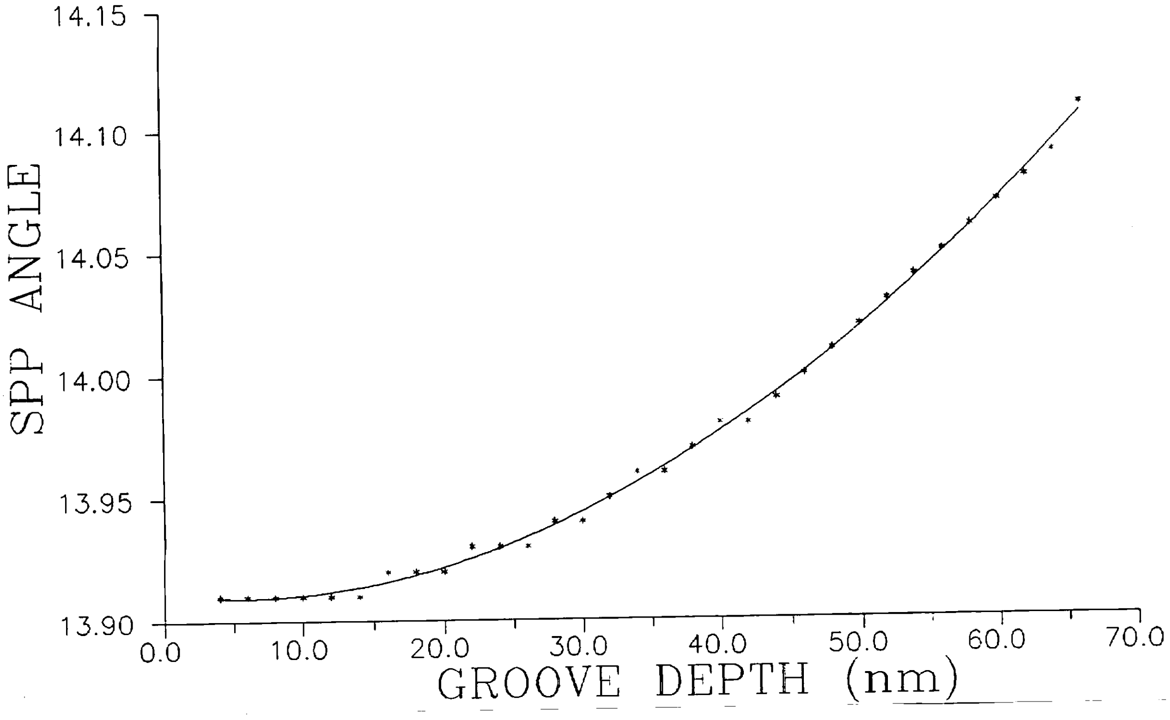

Figure 4.3: Resonance angle (θ_{spp}) verses groove depth.

Figure 4.3 shows the resonance angle of the SPP (θ_{spp}) verses groove depth. The points are obtained from figure 4.1 and the solid line is a polynomial fit. Up to $14.0nm$, the SPP resonance remains at the same angle to within $0.01°$. This shows that shallow grating grooves do not affect the SPP propagation and the equation (1.8) may be used to describe the SPP angle. However for deeper grooves, the resonance moves to higher angles. This can be considered to be due to the fact that the SPP is now running up and down grooves instead of along a flat surface. The extra propagation distance due to the grooves causes a perturbation in the

SPP dispersion equation (1.8). The fitted polynomial curve in figure 4.3 has a dominant quadratic term which is the same form of perturbation seen in previous work (I Pockrand *et al*, 1976 and H Raether, 1982). These authors also found a quadratic dependence of the SPP half width on groove depth.

4.2 Geometric Considerations

Coupling of radiation to the SPP is also dependent on the azimuthal angle (ϕ), defined as the angle between the plane of incidence and the normal to the grating grooves (other authors may have other definitions). All the resonances shown in previous sections deal with p polarised (TM) incident radiation at $\phi = 0°$. When $\phi \neq 0°$, the diffracted beams from the grating no longer lie in the plane of incidence and we therefore need to consider conical diffraction.

Figure 4.4 (a) shows R_{pp} reflectivity (p polarised incident, p polarised detected) verses angle of incidence at $\phi = 0°$. The SPP in this plot is well coupled and has a minimum at $\theta = 14.06°$. If the grating is rotated to an azimuthal angle of $\phi = 45°$ then the plots shown in figure 4.4 (b, c) are obtained for R_{pp} and R_{ss} polarised radiation respectively. The coupling of p radiation to the SPP has decreased and is now similar to the coupling of s radiation. At $\phi = 90°$ there is no coupling of p radiation to the SPP while s radiation couples with maximum efficiency as shown in figure 4.4 (d)). If the SPP had been overcoupled at $\phi = 0°$ then it is possible to tune ϕ to obtain zero R_{pp} reflectivity at the resonance minimum. Figure 4.4 also shows that θ_{spp} is dependent on ϕ. This can be explained with the aid of reciprocal space (k space) diagrams.

Figure 4.5 shows a k space diagram in the plane of the grating surface . The solid circles have radii k and represent the maximum momentum component in the plane available from an incident photon. This corresponds to a photon at grazing incidence. The dotted line has a radius of k_{spp} which is larger than k (see equation 1.8) and hence the SPP cannot be directly excited even by a grazing incidence photon. The grating allows the momentum of the photon to be enhanced or reduced by integral amounts of G and so the k circles may be displaced by these multiples of G. An incident photon with a momentum component $k \sin\theta$ (in the plane of the grating surface) may now couple to a SPP at an azimuthal angle ϕ as

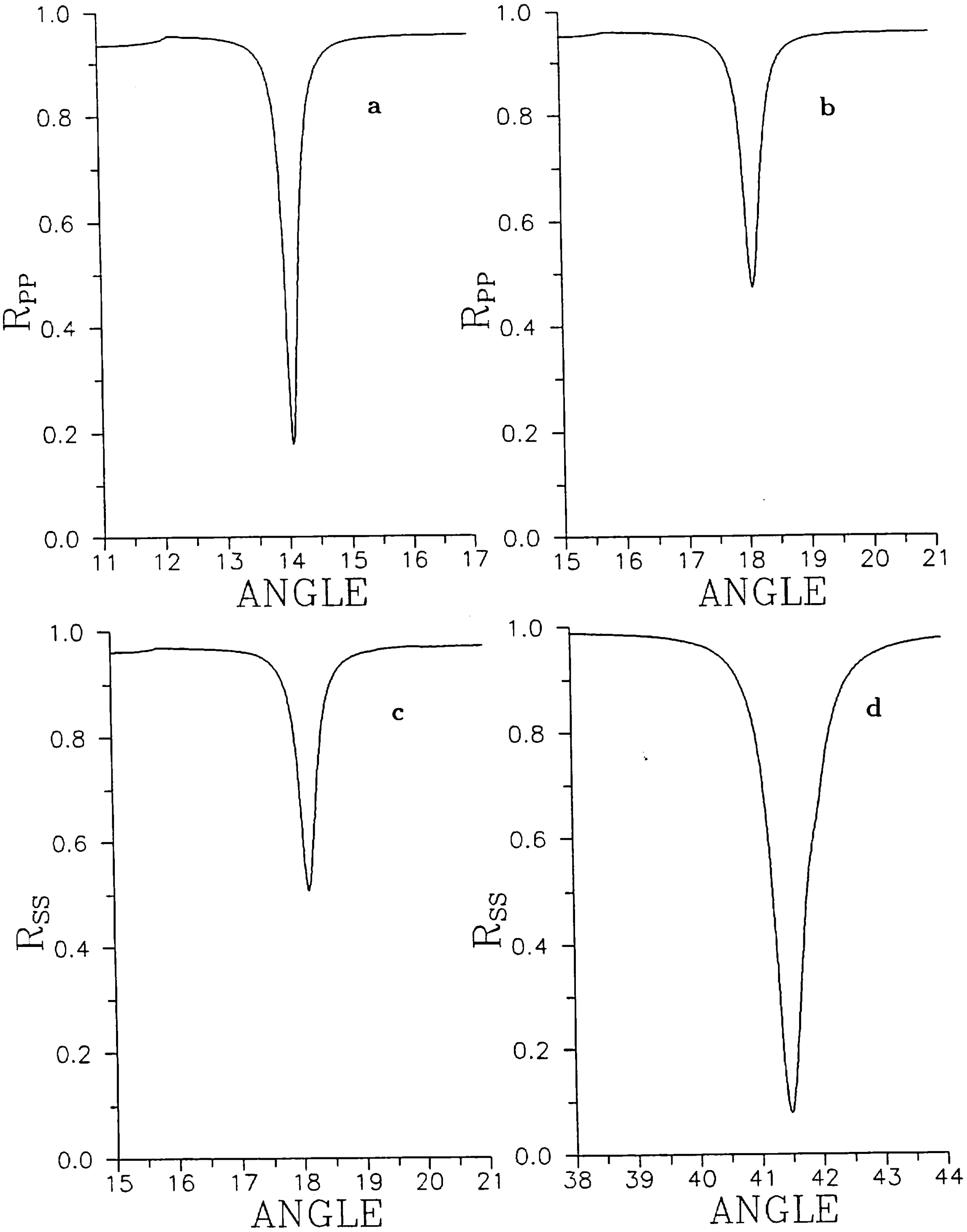

Figure 4.4: Experimental reflectivity scans taken at different azimuths with different polarisations. a, R_{pp} at $\phi = 0°$; b, R_{pp} at $\phi = 45°$; c, R_{ss} at $\phi = 45°$; d, R_{ss} at $\phi = 90°$.

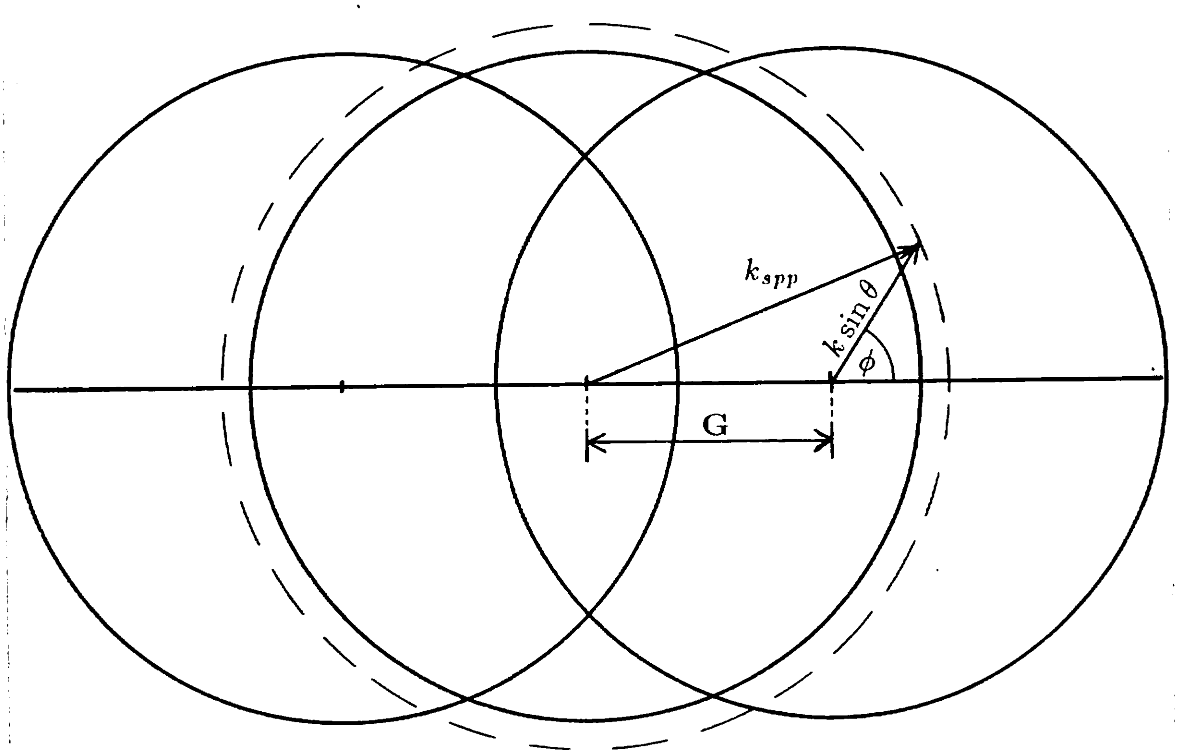

Figure 4.5: K space diagram showing a solution for resonant coupling of a photon to a SPP.

shown. It can clearly be seen that as ϕ is varied, $k\sin\theta$ must vary in magnitude for coupling to be maintained and hence θ must vary. When $\phi = 0°$, coupling is given by;

$$k\sin\theta = k_{spp} - G \tag{4.1}$$

However, when $\phi \neq 0°$ we now have, by simple trigonometry;

$$k_{spp}^2 - G^2 = k^2\sin^2\theta - 2kG\sin\theta\cos\phi \tag{4.2}$$

Equation 4.2 is a quadratic in $\sin\theta$ and so care must be taken in choosing the applicable solution.

Figure 4.5 can be simplified somewhat by only considering one quadrant of a k circle as shown in figure 4.6. The area inside the quadrant represents the total accessible region of k space for an incident photon. If a SPP curve lies within this quadrant then it may be excited by the photon. Due to k space symmetry, figure

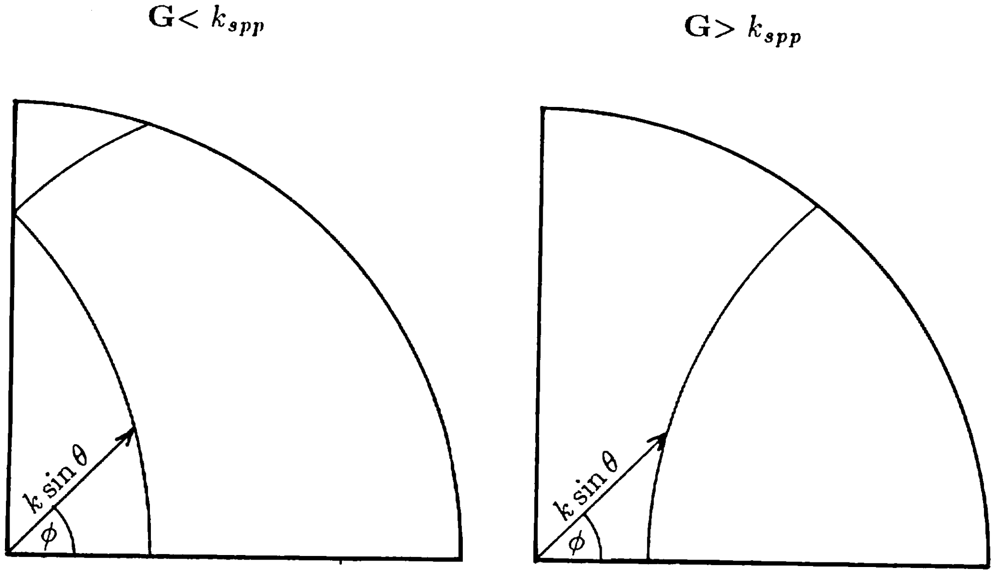

Figure 4.6: K space diagrams with (a) $G < k_{spp}$ and (b) $G > k_{spp}$.

4.6 (a) shows two branches to the SPP curve. These have been shifted in opposite directions by an amount G with respect to the quadrant centre. It can be seen that when ϕ is large an angle scan will reveal two SPP modes which merge at $\phi = 90°$. When $G > k_{spp}$ (figure 4.6 (b)) only one branch exists and there is now a maximum ϕ beyond which no mode can be excited.

In summary, we have shown that unlike a prism coupled SPP, a grating coupled SPP may be excited by s polarised light. The variation of θ_{spp} with ϕ has also been explained with the aid of k space diagrams.

4.3 Experimental Technique

Prism coupling to surface plasmon polaritons is a well established method for determination of the optical constants of metals in the visible and infra red regions. Studies have been made on many metals including silver (A Otto, 1968), aluminium (M D Tillin *et al*, 1989a), gold (R A Innes *et al*, 1987), magnesium (M D Tillin *et al*, 1989b), and nickel, platinum and palladium (Y Fuzi *et al*, 1989). In general, reflectivity data are compared to predictions based on Fresnel theory and parameters for the metal obtained using an iterative least squares fit method. A small range of parameters for the metal are found for different experiments and this is easily justifiable since thermally evaporated films do not have consistent optical properties. In contrast to prism coupling, grating-coupled surface plasmons have never to our knowledge been used to characterize metals. Only approximate fits to theory have been obtained without the adjustment of optical constants.

In this section, we use differential grating theory (section 2) to fit reflectivity data from a grating coated with different metals. Using grating coupling together with prism coupling in the Otto geometry (A Otto, 1968) it is found possible to fit reflectivity data from the same metal surface to both grating and prism theory. This allows a direct comparison of the optical constants of the metal found from each method.

The grating used in this section was ion beam etched to allow cleaning and recoating with different metals. The grating has a sinusoidal profile with a pitch of $800.0nm \pm 0.5nm$ and a groove depth of $24.5nm \pm 0.5nm$. After coating the grating with an optically opaque ($> 150nm$) layer of the metal, reflectivity was recorded as a function of angle of incidence for p polarised light from a HeNe laser ($\lambda = 632.8nm$). For this scan the grating was orientated at $\phi = 0°$ as shown in figure 4.7(a). This scan gives the grating-coupled SPP.

The grating was then rotated to $\phi = 90°$ and an equilateral sapphire prism (cut so that the optic axis is along the three fold symmetry axis) was lightly pressed against the grating surface as shown in figure 4.7(b). With the grating at $\phi = 90°$, there is no grating coupling of p-polarised radiation into a surface plasmon (as discussed in section 4.2). Hence an angle scan will only show a prism coupled surface plasmon in the Otto configuration. By altering the pressure on the prism, the air gap between the prism and the grating could be varied. This changed the strength of coupling of light to the mode and allowed comparison of theory to data for more than one set of data for the same sample. The spread in thickness of the Otto air gap due to the presence of the grating was small and could be ignored in fitting (a typical air gap was $1\mu m$ which is large compared to the groove depth of $24.5nm$).

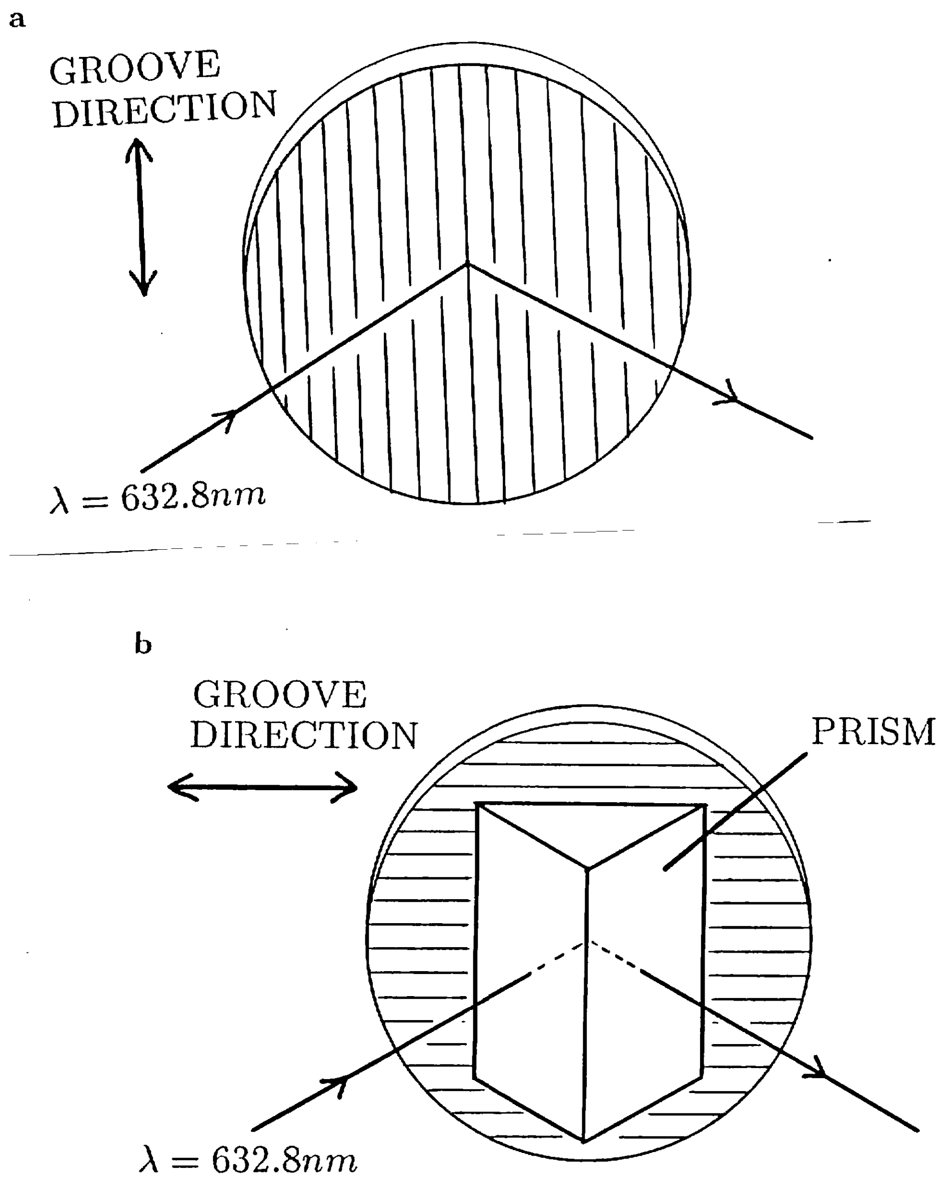

Figure 4.7: Experimental configurations for exciting SPPs via (a) grating coupling and (b) prism coupling.

4.4 Results

Figure 4.8 shows the grating-coupled reflectivity as a function of angle of incidence for a grating coated with a thick silver film using p-polarised light ($\lambda = 632.8nm$) with the grating at $\phi = 0°$.

The theory line has been fitted to the data by adjusting the relevant parameters (ϵ_r, ϵ_i and d) until the best agreement is achieved. Small adjustment in h is justifiable as talystep measurements showed that this varied across the surface by $\pm 3nm$.

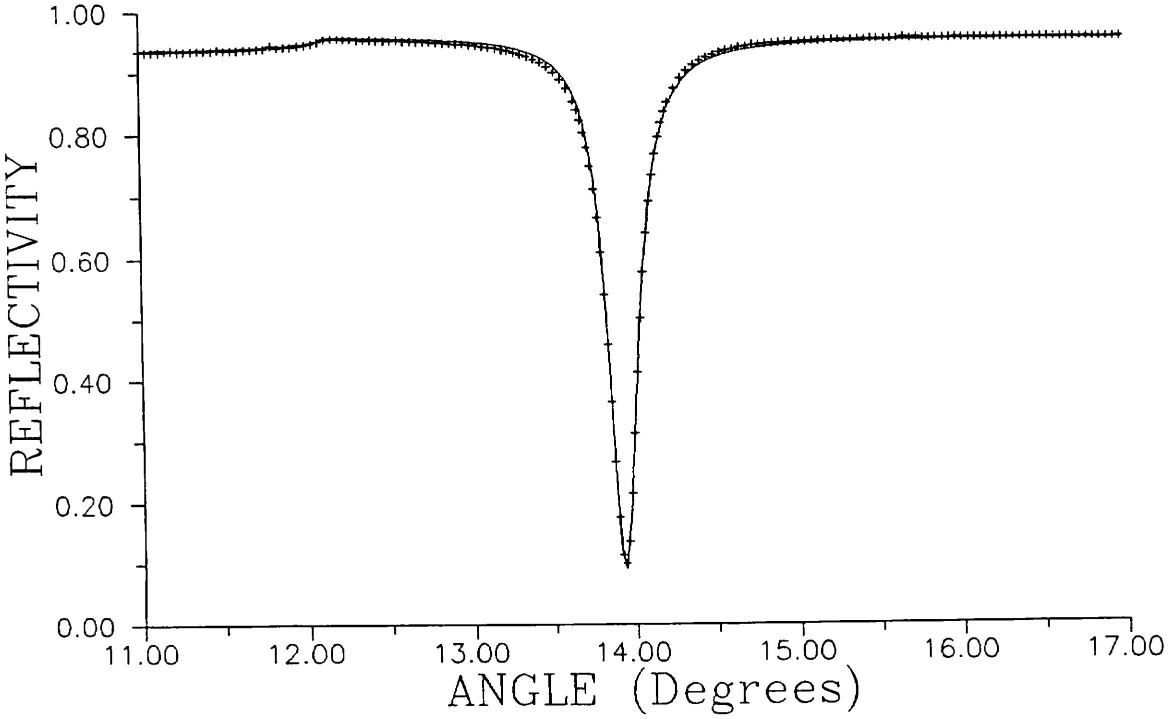

Figure 4.8: Reflectivity (R_{pp}) from a silver coated grating showing a grating-coupled SPP. Crosses are data and the solid line is theory.

Figure 4.9 shows two angle scans obtained from the prism configuration (with the grating at $\phi = 90°$). Again the dip in reflectivity is the SPP resonance now coupled through the air gap. The depth of coupling has been varied by altering the pressure on the prism and hence the air gap thickness. For each curve the points are data and the solid line is fitted theory. The data has been corrected for reflection and refraction on entering the prism and the angle range refers to the internal angle. This requires knowledge of the refractive index of the prism and its facet angles (both were previously determined with high accuracy). Fitting by adjustment of the relevant parameters (ϵ_r, ϵ_i and the air gap thickness) is carried out automatically by the program until the minimum sum of squares deviation is

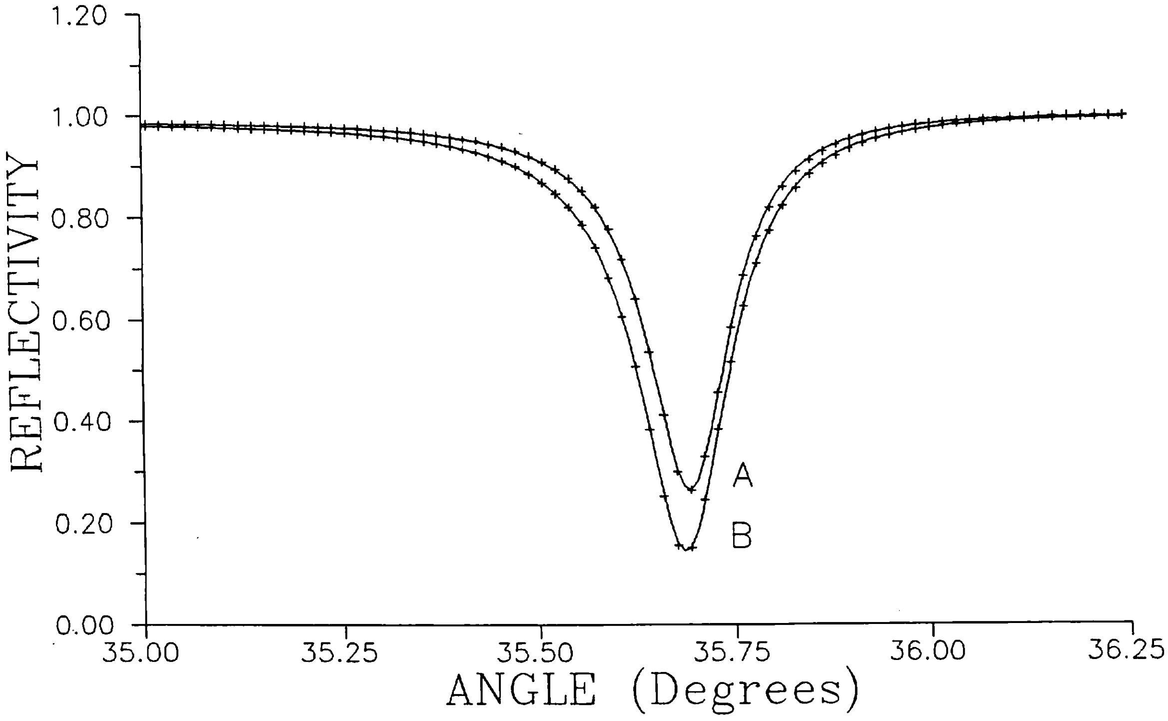

Figure 4.9: Reflectivity curves from the prism configuration with a silver coated sample for two air gaps. A, 1.14μm; B, 1.07μm. Crosses are data and the solid lins is Fresnel theory.

achieved.

This procedure was repeated with the same grating substrate with aluminium and gold coatings. Figures 4.10 (a, b) show the grating-coupled surface plasmons for Al and Au respectively (note reduced reflectivity axes). Both show diminished coupling depth and increased half width compared to the surface plasmon resonance from silver. This is simply due to the increased absorption of both these metals. As with figure 4.9, the points are data and the solid line is theory.

Table 4.1 shows the average parameters obtained from two fits to prism data for each metal (estimated errors have been included). Table 4.2 shows the parameters obtained from fitting theory to grating data. The error for the groove depth (h) in the latter varies between metals for reasons discussed in section 4.1. For all three metals agreement between the two sets of deduced parameters is well within experimental error. The parameters obtained in both cases for silver are in good

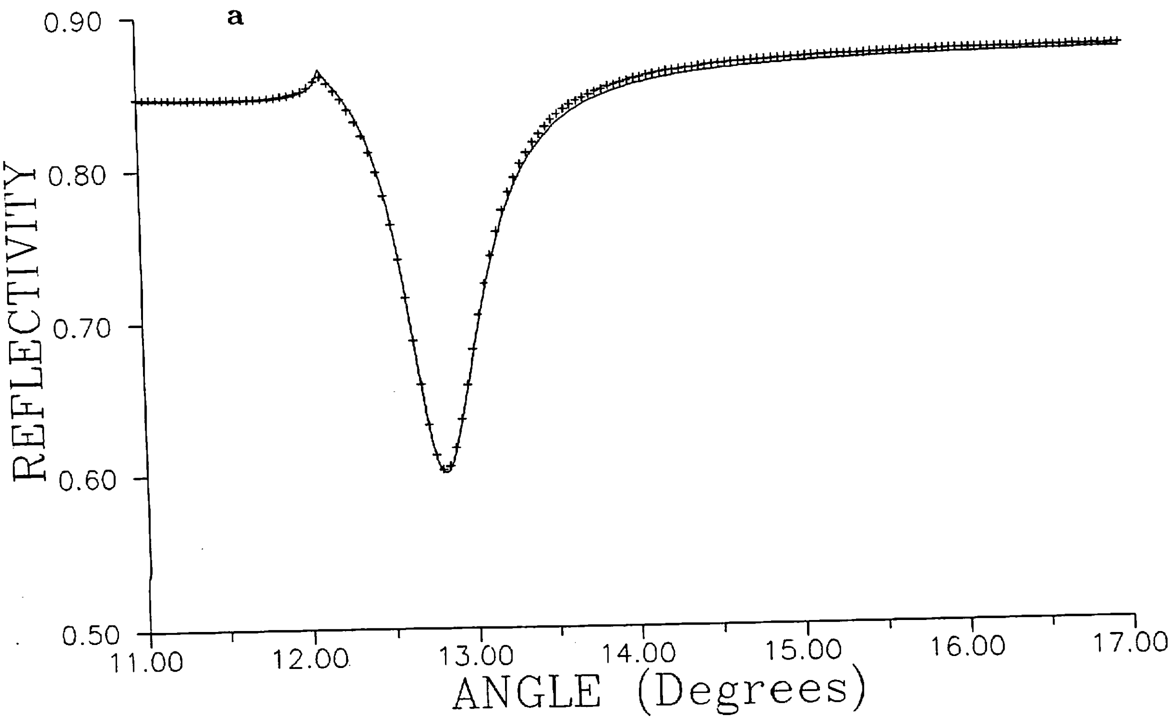

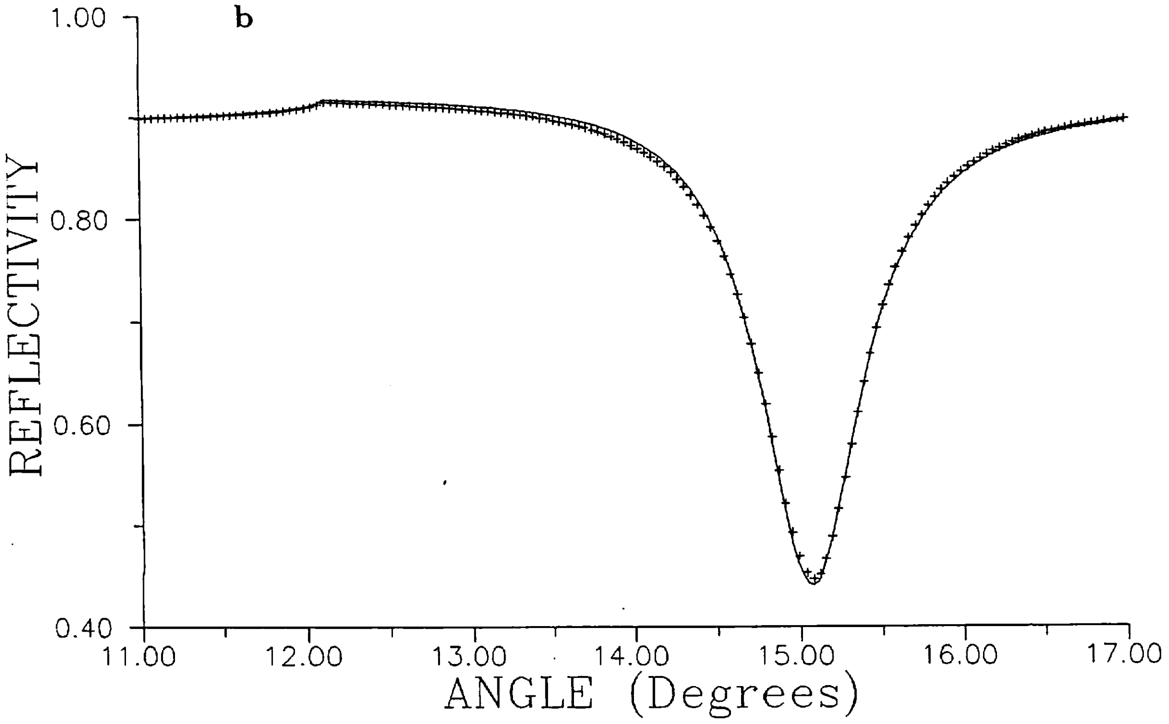

Figure 4.10: Reflectivity curves showing grating-coupled SPPs on samples coated with (a) aluminium and (b) gold. Crosses are data and solid line is theory.

agreement with other values in the literature, for example $\epsilon = -17.8 + 0.67i$ (U Schroder,1981). The reduced imaginary part in our case is almost certainly due to our film being thicker with larger grains and less defects. An experiment was also carried out using a 500.0nm silver film. This produced an almost identical SPP to that shown in figure 4.8 and hence shows that ϵ is not dependent on film thickness for thick films (> 150.0nm). It also shows that the evaporated silver follows the exact profile of the grooves and does not fill them in. For aluminium the results are in reasonable agreement with the value given by M D Tillin *et al* (1988) ($\epsilon = -36.88 + 13.31i$). In this case discrepancies are probably due to the oxidation of the aluminium layer inevitably present in our experiment.

Table 4.1: Parameters obtained from fitting of prism theory to the appropriate data taken from silver, aluminium and gold samples.

Metal	ϵ_r	ϵ_i	$\delta\epsilon_r$	$\delta\epsilon_i$
Silver	-17.14	0.624	0.05	0.005
Aluminium	-39.54	14.96	0.1	0.3
Gold	-10.77	1.067	0.05	0.005

Table 4.2: Parameters obtained from fitting of grating theory to the appropriate data taken from silver, aluminium and gold samples.

Metal	ϵ_r	ϵ_i	h (nm)	$\delta\epsilon_r$	$\delta\epsilon_i$	δh (nm)
Silver	-17.12	0.623	25.0	0.03	0.02	0.5
Aluminium	-39.50	14.45	25.5	0.3	0.3	0.3
Gold	-10.77	1.065	27.1	0.03	0.02	0.3

In the case of gold, our results again show a somewhat reduced ϵ_i value by comparison to other work, for instance R A Innes *et al* (1987) give $\epsilon = -11.84 + 1.358i$. However their films were $45nm$ thick whereas ours will have much less absorption due to the increased grain size in the thicker films. This inevitably leads to a reduced value for ϵ_i.

We have confirmed that the differential grating formulation of Chandezon gives accurate predictions of the form of reflectivity curves for grating -coupled surface plasmons on metal surfaces obtaining optical constants in good agreement with those found from fitting prism-coupled data to the well established Fresnel theory. Hence the differential formulation developed by Chandezon is reliable, and can be used to accurately determine the optical constants of metals and the grating groove depth. In the case of a groove depth to pitch ratio of 1:32 it is sufficiently precise with the retention of only ten scattered modes.

Both the prism coupling and grating coupling techniques provide powerful tools for the determination of the optical constants of metals. Despite the increased complexity of the theory, grating coupling offers a few advantages over prism coupling. For example in the UV / visible region, the Otto coupling gap may be inconveniently small and then grating coupling provides a more suitable method to couple to surface plasmon resonances. Also, the open geometry of the grating system allows many more experiments involving thick overcoatings on 'bulk' metals, or bulk fluids in contact with the metal (the Kretchmann prism configuration may be used in a similar way but requires metal layers of optimized thickness). The fitting to grating data has also demonstrated the high accuracy of the technique in the determination of the grating groove depth (the error is of the order of atomic radii).

4.5 Influence of Groove Distortion

The grating data in section 4.4 fitted well with the assumption of a sinusoidal profile. However, for deeper gratings made by the holographic method the grooves become distorted leading to sharper peaks than troughs. This distortion is due to a nonlinearity in the exposure sensitivity of the photoresist and also maybe a nonlinearity in the development process. It has been found by previous workers that this distortion can be quantified by fitting SPP resonances (E H Rosengart *et al*, 1977). They added higher harmonics to the sine wave profile to improve fits to data. This is probably not a realistic model of the photoresist nonlinearity and lead to failure of fitting for quite modest values of the second harmonic (0.26× the fundamental). Instead it is better to directly distort the sine wave by raising it to a power. The grating profile a(x) now becomes;

$$a(x) \;=\; h\left[\left(\frac{\cos(Gx)+1}{2}\right)^{\gamma} - \frac{1}{2}\right] \tag{4.3}$$

The extra complexity of equation 4.3 is merely to renormalise the profile about $y = 0$. For $\gamma > 1$ the profile is distorted so that the groove peaks are sharper than the troughs and for $\gamma < 1$ the opposite occurs. Figure 4.11(a) shows the effect of varying γ on the SPP resonance (grating and metal parameters are as for silver in the previous section). γ is varied from 0.5 to 1.5 in steps of 0.25 and the insert shows the effect on the profile (not to scale). For such a variation in profile the effect on the SPP is small and so the SPP is not a good measure of γ. A much better feature to scan is the second order SPP excited when;

$$k\sin\theta = -k_{spp} + 2G$$

This feature is much more sensitive to γ as shown in figure 4.11(b) (the parameters and variation are as figure 4.11(a)). The grating used in the previous section produced good fits to SPPs without distortion. However, a scan of the second order SPP clearly shows that a distortion is present as shown in figure 4.12. The theory (solid line) is fitted with the same constants as in the previous section but now with $\gamma = 1.2352$.

For deeper gratings the distortion effect can clearly be seen in both SPPs. Figure 4.13(a, b) shows the first and second order SPPs from a much deeper silver coated grating. The crosses are data and the solid lines are theory curves calculated with and without the distortion factor. The theory curves with distortion fit extremely well using the following parameters for both SPPs;

Groove Pitch = $800.8nm$
Groove Depth = $64.2nm$
$\epsilon = -16.70 + 0.64i$
$\gamma = 1.85$

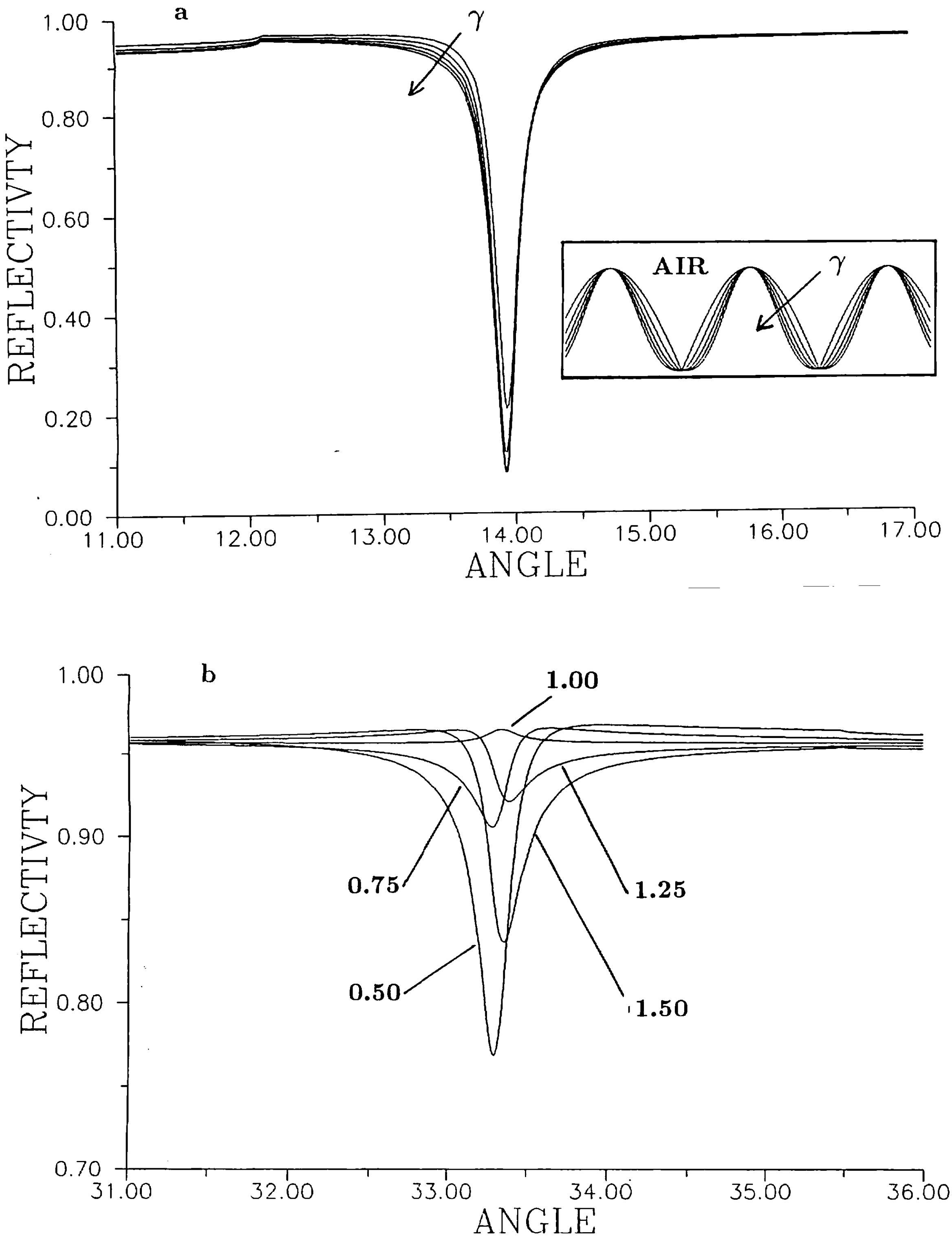

Figure 4.11: Theoretically generated reflectivity scans showing the effect of varying γ from 0.5 to 1.5 in steps of 0.25. Plots are (a) the first order SPP and (b) the second order SPP.

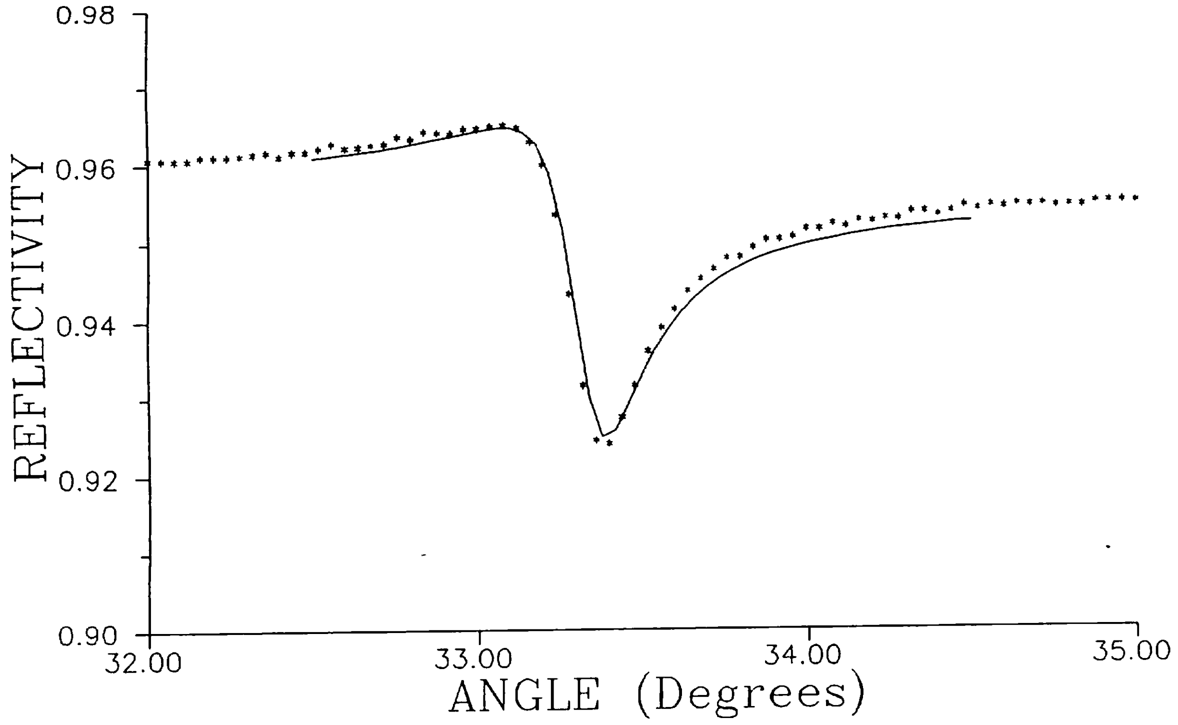

Figure 4.12: Theoretical fit to a second order SPP taken with the grating used in the previous section. The fit is achieved with the same parameters as before but now with $\gamma = 1.2352$.

The distortion in this grating is much larger than those studied by Rosengart *et al* and yet the quality of fitting is excellent. Hence equation 4.3 is a good description of groove distortion due to nonlinearity in photoresist exposure sensitivity. Our results are also confirmed to a certain extent by comparison with plots taken with the Talystep surface profiler. Figure 4.14 shows a Talystep plot of the grating used to obtain the data in figure 4.13 along with the fitted distorted profile having a distortion factor of $\gamma = 1.85$ (not to scale). The Talystep plot shows narrower troughs than the fitted distortion but this is due to the finite radius of the stylus tip which has a significant effect on the traces obtained for this deep grating. The comparison is therefore as good as can be expected. Both the Talystep plot and the fitted distortion show sharper peaks than troughs and so the photoresist sensitivity is decreasing with length of exposure. The developing process may also be nonlinear but it is impossible to isolate the nonlinearity from

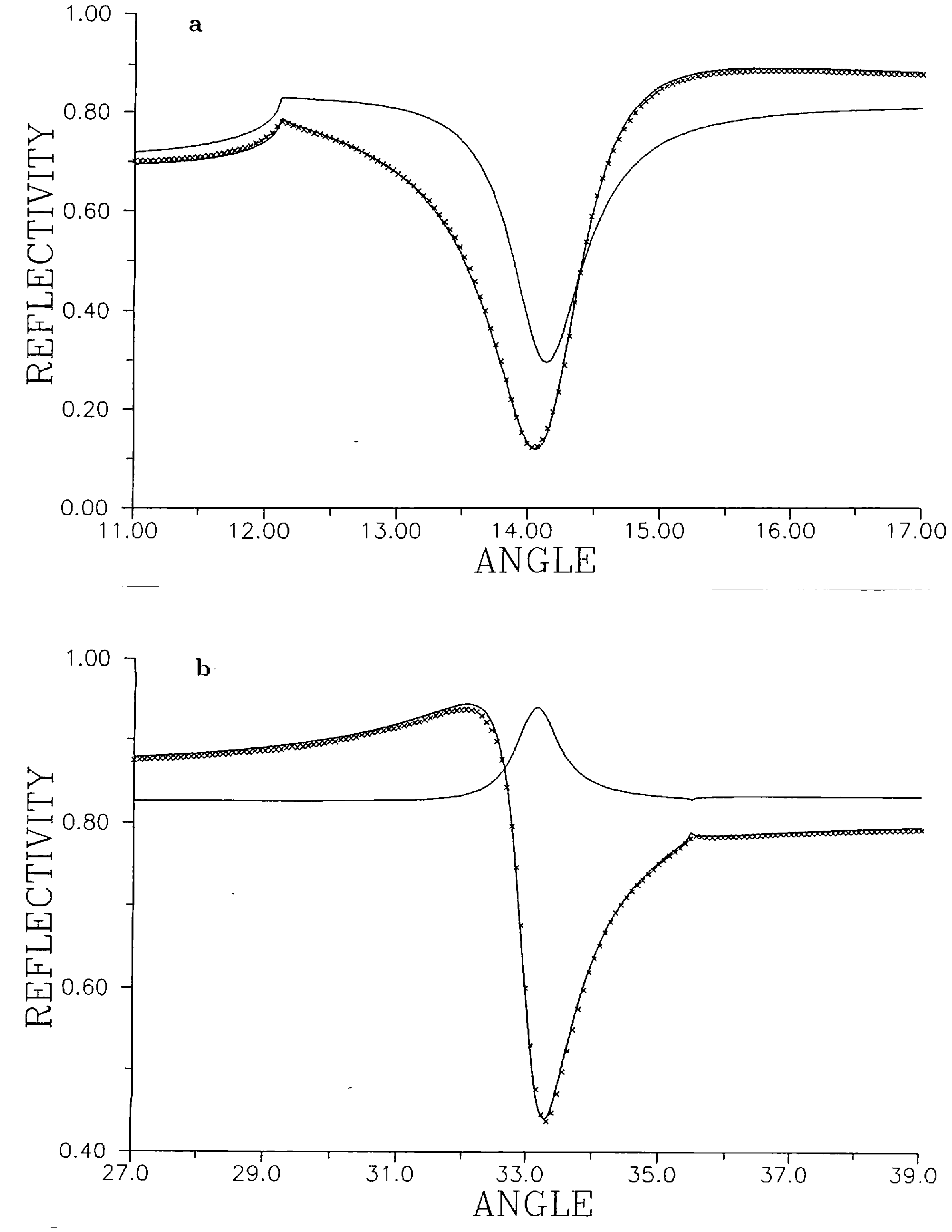

Figure 4.13: Theoretical comparison to data taken on a deeper grating showing (a) the first order SPP and (b) the second order SPP. The theory curves are generated with $\gamma = 1.0$ and 1.85. The latter value produces the best fit in each case.

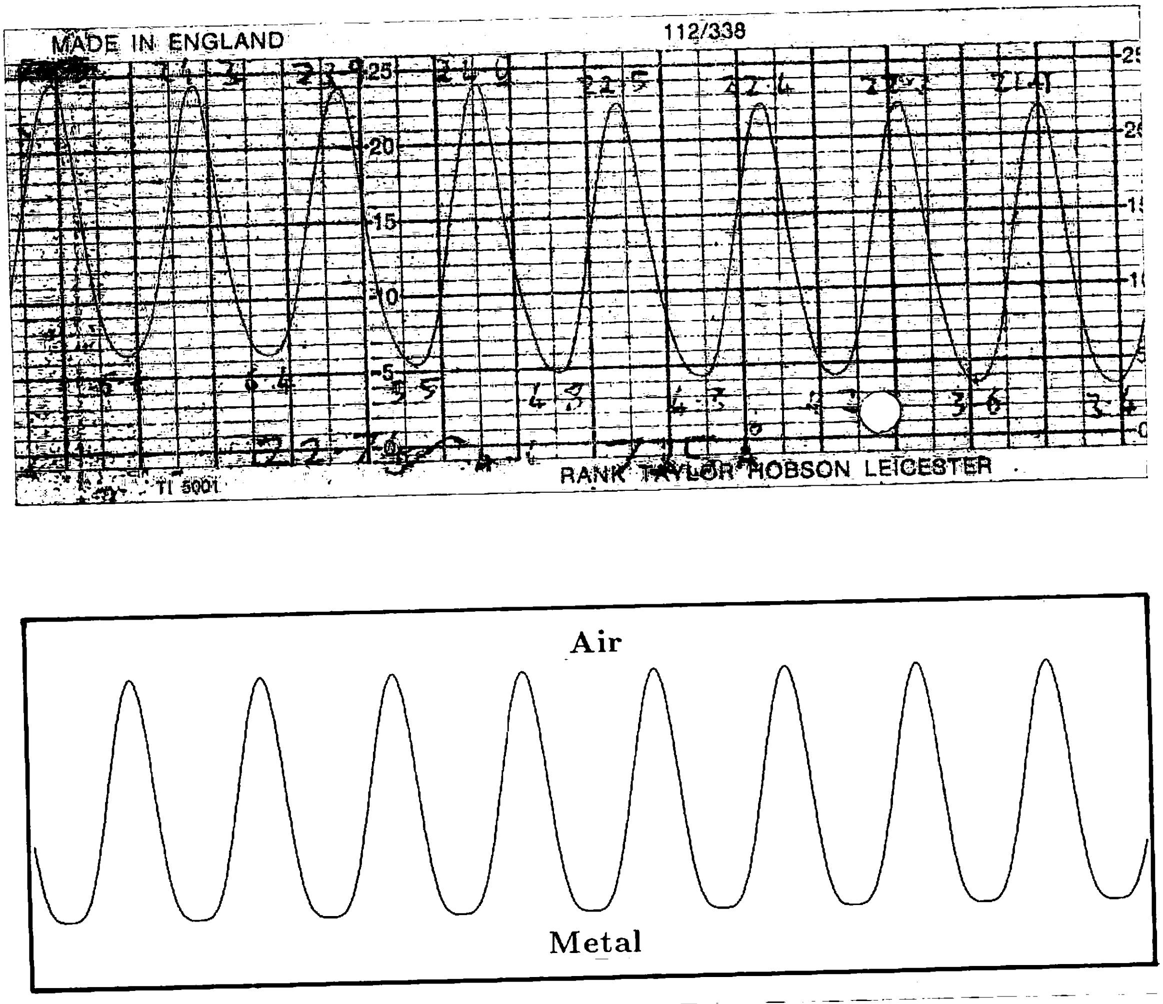

Figure 4.14: Comparison of groove profiles obtained from (a) Talystep measurements and (b) fitting to SPP resonance.

each effect.

4.6 Summary

In this chapter, several important properties of SPPs on gratings have been discussed. Differential grating theory has been used to compare parameters obtained from grating-coupled SPPs with those found from prism-coupled SPPs. Problems in fitting grating data for deep gratings have been solved by distorting the sinusoidal profile used in the theory and has produced much better results than those obtained by previous authors.

Chapter 5

Coupled Surface Plasmons on Silver Coated Gratings

5.1 Introduction

In the previous chapter we dealt with SPPs excited on the surface of thick metal films. If the films are now made thinner ($< 12.0nm$) and bounded by non absorbing dielectrics of equal refractive index then SPP modes on both the top and bottom metal interface can be excited and will interfere to produce coupled modes (discussed fully in section 1.5).

Figure 5.1 shows theoretically generated reflectivity scans for different thicknesses of metal film. The film is silver ($\epsilon = -17.12 + 0.7i$) bounded by dielectrics of equal index ($\epsilon = 2.1217$) on a grating with a pitch of $800.0nm$ and a groove depth of $28.5nm$. The film thickness is varied from $10.0nm$ to $50.0nm$ in steps of $10.0nm$. The two thickest films show the SRSP as well as the LRSP but for thinner films the propagation wavevector of the SRSP becomes too large for it to be excited within a suitable angle range (as explained in section 1.5). As the film becomes thinner, the LRSP coupling depth stays roughly constant but its half width becomes narrower due to decreasing damping of this mode with film thickness (see section 1.5). The off-resonance reflectivity drops with decreasing film thickness because the films allow significant transmission of light as well as reflection. For thicker films the SRSP and the LRSP will eventually merge to form the single interface SPP. For silver at $\lambda = 632.8nm$ the $1/e$ penetration depth of the SPP into the film is $\sim 20.0nm$ and so coupled modes are still seen for films that are $100.0nm$ thick.

Figure 5.2 shows theoretically generated reflectivity scans for different grating groove depths. The parameters are as with figure 5.1 with the metal thickness set at $50.0nm$. The groove depth is varied from $10.0nm$ to $70.0nm$ in steps of $10.0nm$. Both the LRSP and the SRSP show movement to higher angles with groove depth in a similar manner to SPPs in figure 4.1 . The background level drops with groove

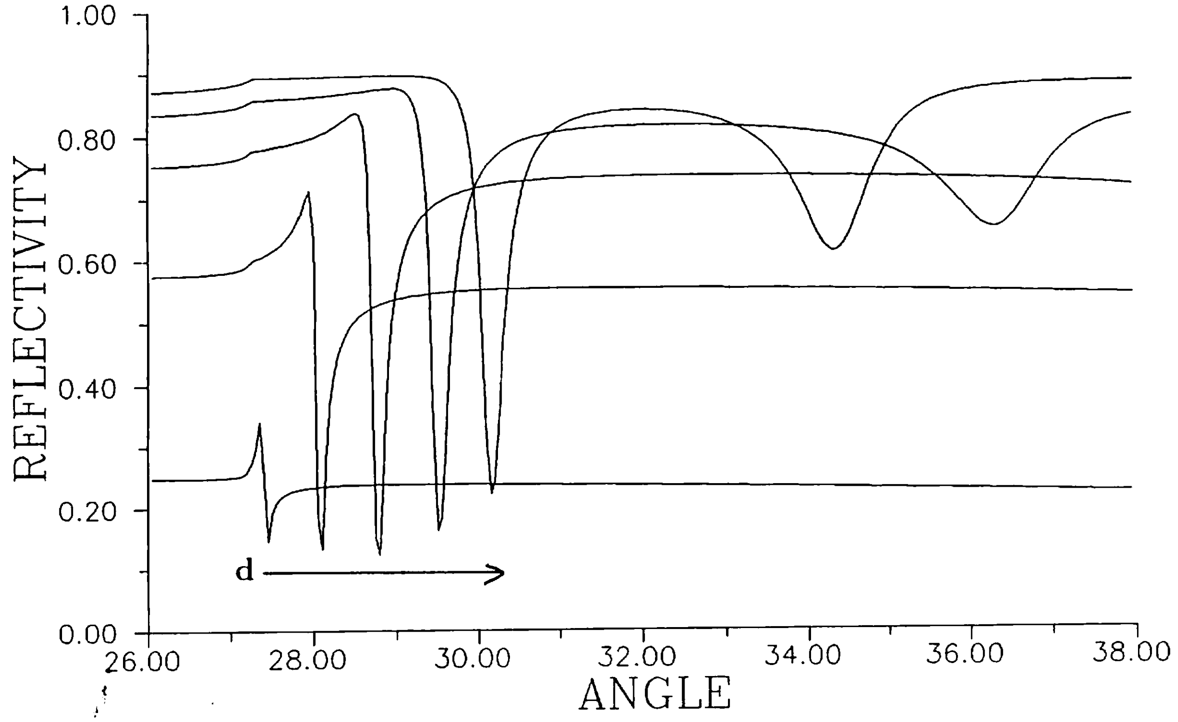

Figure 5.1: Theoretically generated reflectivity scans showing LRSPs and SRSPs for various thicknesses of silver films. Thicknesses varied from 10.0nm to 50.0nm in steps of 10.0nm.

depth due to an increased percentage of light scattered into diffracted beams. The maximum groove depth used is at the limit of accuracy for the differential method and yet the LRSP does not ever become perfectly coupled. This is surprising considering that the SPP achieves maximum coupling at a groove depth of only $\sim$ 34.0nm (see section 4.1)

5.2 Experimental Technique

Experimental observations of coupled modes have been carried out by Y Kuwamura *et al* (1983) and JC Quail *et al* (1983) who used prism coupling to thin silver films. Difficulty in fitting theory to data was encountered which may be attributed to finite laser beam divergence and the use of bulk silver parameters

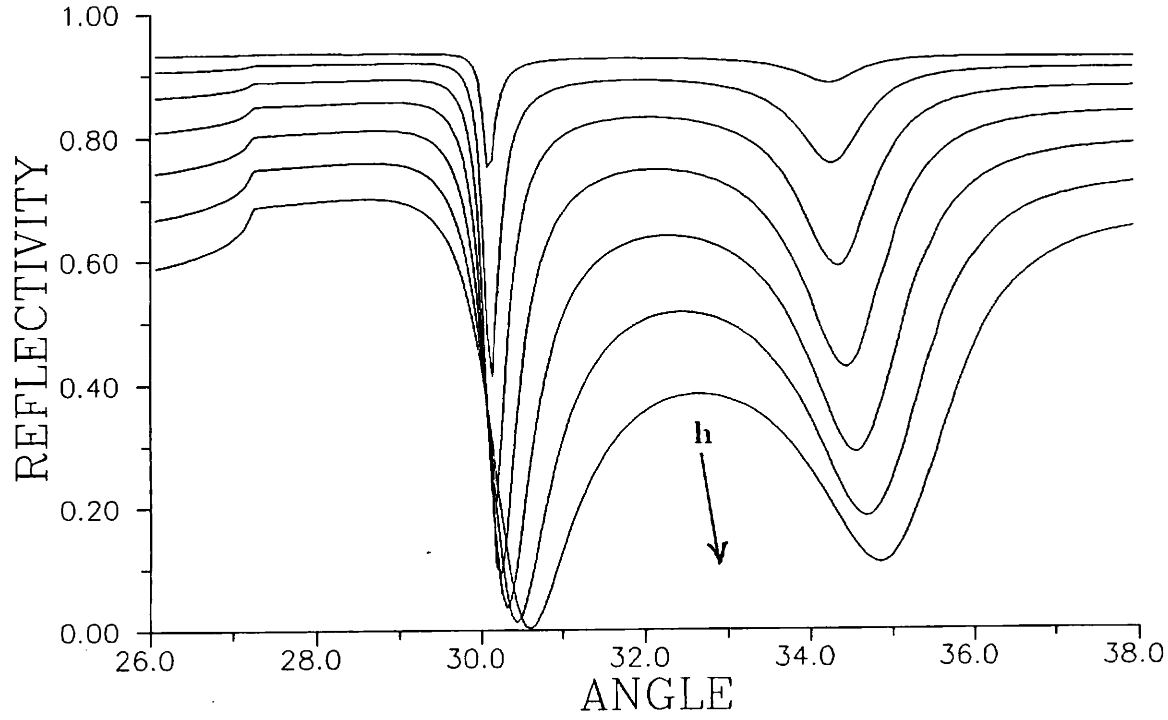

Figure 5.2: Theoretically generated reflectivity scans showing the effect of varying the grating groove depth on the LRSP and the SRSP. The metal layer is 50.0nm thick and the groove depth is varied from 10.0nm to 70.0nm in steps of 10.0nm.

for thin films.

T Inagaki *et al* (1985) succeeded in producing free standing corrugated silver films and demonstrated grating coupling to coupled modes using photoacoustic detection. It was found that the mode angles and half widths followed closely theoretical dispersion curves, being slightly displaced due to the grating perturbation on the eigenmodes. Z Chen *et al* (1988) took reflectivity measurements from a silver coated grating at 1.06μm and attempted to fit the data to theory developed using a Rayleigh approach. A fairly good fit was obtained for a 52.0nm film showing both the LRSP and the SRSP. However for thinner films (23.0nm) the fits were poor, which like the earlier results for prism coupling was also probably due to beam divergences and incorrect silver parameters.

In this work, coupled modes have been examined using gratings and theory has been fitted to the reflectivity data using the thin metal layer parameters as

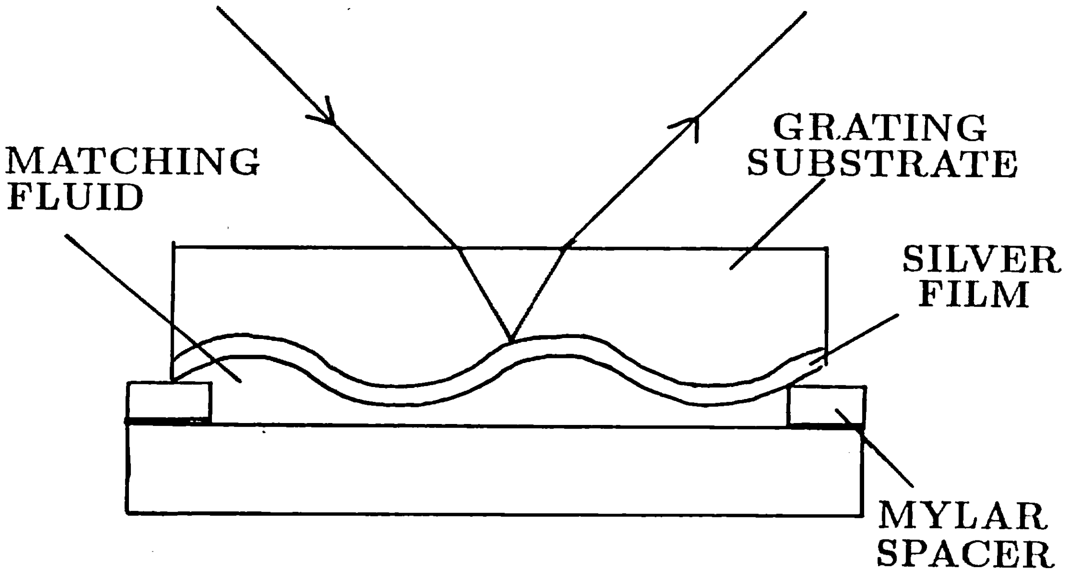

Figure 5.3: Configuration of experimental cell.

variables in a least squares fitting procedure.

As with the previous chapter, the grating used in this chapter was ion beam etched to allow cleaning and recoating with metal films of different thicknesses. This grating has a sinusoidal profile with a pitch of $800.0nm$ and a peak to trough groove depth of $25nm$. Talystep measurements showed the latter to vary by less than $1nm$ across the whole substrate. Silver films are deposited by vacuum evaporation of 99.999% pure silver in a pressure of 2×10^{-5} Pa at a rate of $\sim 1nm/s$. A typical sample cell is constructed with a thick ($100\mu m$) layer of matching fluid held in place by a mylar ring and a silica flat as shown in figure 5.3. The fluid is made by mixing octanol (n=1.42) with methyl benzoate (n=1.51) until the refractive index of the mixture is the same (at the wavelength of study) as the silica substrate (n=1.456). These fluids are chosen as they are sufficiently non-volatile, optically non-absorbing and do not chemically attack the silver films. Figure 5.4(a) shows the configuration used to measure fluid index. A sapphire prism of known index (n=1.766) and angles is clamped to a fluid chamber and sealed to it with an o-ring. A reflectivity scan from this sample gives a critical angle θ_c as shown

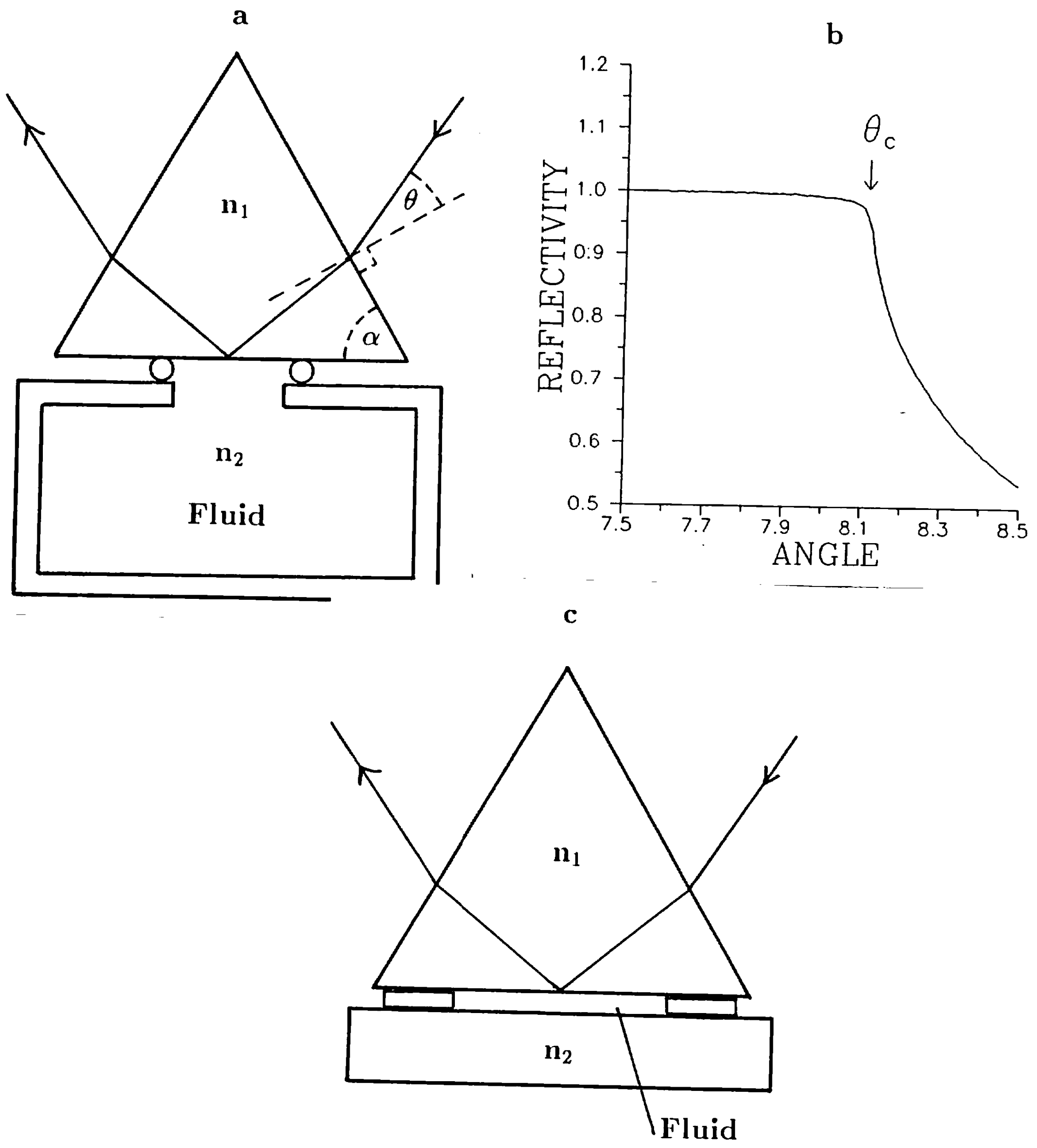

Figure 5.4: Configurations for measuring (a) the fluid index and (c) the grating substrate index. A typical reflectivity scan from configuration (a) is plotted in (b) showing the 'critical angle' used in the determination of the fluid index.

in figure 5.4(b). The refractive index of the fluid (n_2) is then given by;

$$n_2 = n_1 \sin\left\{ \alpha - \sin\left[(\frac{1}{n_1}) \sin \theta_c \right] \right\}$$

The grating substrate index is found using a similar configuration, shown in figure 5.4(c). The flat surface of the substrate is spaced from a characterised prism by thick ($100\mu m$) mylar spacers. The gap is then filled with a fluid whose index is known to be between n_2 and n_1 (its exact value is unimportant). A reflectivity scan will then give a 'critical angle' as before and n_2 (the grating substrate index) can now be found. The error on the indices found by these methods is ± 0.005.

The coupled mode configuration was constructed within 15 minutes of the removal of the silver film from the evaporator to prevent significant silver sulphide formation (GJ Kovacs (1978) showed this to be $< 0.1nm$ per day in normal laboratory conditions). The zeroth order (specular) beam reflectivity versus exterior angle was recorded for p-polarised (TM) radiation from a HeNe laser ($\lambda = 632.8nm$). A spatial filter and a collimating lens were used to reduce beam divergence to $0.02°$, while maintaining a spot size of $2mm$ diameter. Reflectivity data were taken for several different silver film thicknesses using the same grating. For all experiments, the grating was orientated with its grooves perpendicular to the plane of incidence ($\phi = 0°$). The reflectivity data in the form of normalized reflectivity verses external angle was then converted into the form of internal angle against reflectivity from the silver by taking into account reflection and refraction at the top substrate surface. This simplified theoretical comparison as the bounding dielectrics could then be assumed to be semi-infinite in thickness.

5.3 Results

The grating was first coated with a thick silver film ($150.0nm$) and a reflectivity scan was taken (with $\lambda = 632.8nm$) to give the air/silver surface plasmon resonance. By fitting theory to this curve the bulk relative permittivity of the silver film was obtained which in this case was $\epsilon = -17.12 + 0.636i$. The grating was then coated with a thin film of silver ($52.8nm$) and an index matched system was constructed as shown in figure 5.3. The corrected data from this sample is shown as crosses in figure 5.5. The solid line is the theoretical comparison to the

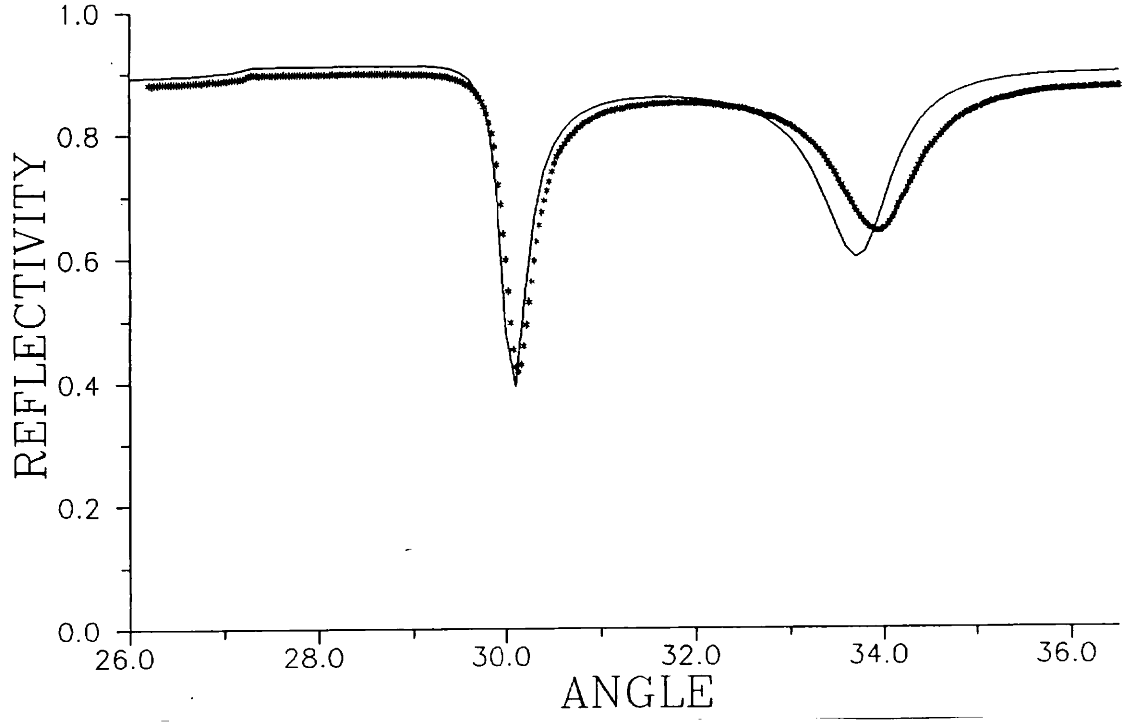

Figure 5.5: Reflectivity verses internal angle for a thin silver film (52.8nm). Points are data and the solid line is theory calculated using the bulk silver value for ϵ. The fit to the data is fairly good.

data calculated using the silver parameters obtained from the thick film and fits the data fairly well. Figure 5.6 shows data from a thinner film (14.4nm) and in this case the theory fails to fit to the data. However, if the relevant parameters are allowed to vary then a better fit is of course obtained.

Figure 5.7 shows all the results obtained for different silver thicknesses on the same grating. The angle scans for the two thickest films (D and E) show two resonant modes, the LRSP at lower angles and the SRSP at higher angles. The LRSP in curve D is sharper than in E due to the decrease in damping of this mode with decreasing metal thickness. Conversely, the SRSP becomes shallower and for C it can no longer be excited within the available angle range. The off-resonance reflectivity level is seen to drop significantly with decreasing metal thickness. This is due to the increasing transmission that occurs through the thinner films. The 'critical angle' at 27.22° is due to the 'falling off' of a diffracted beam from the

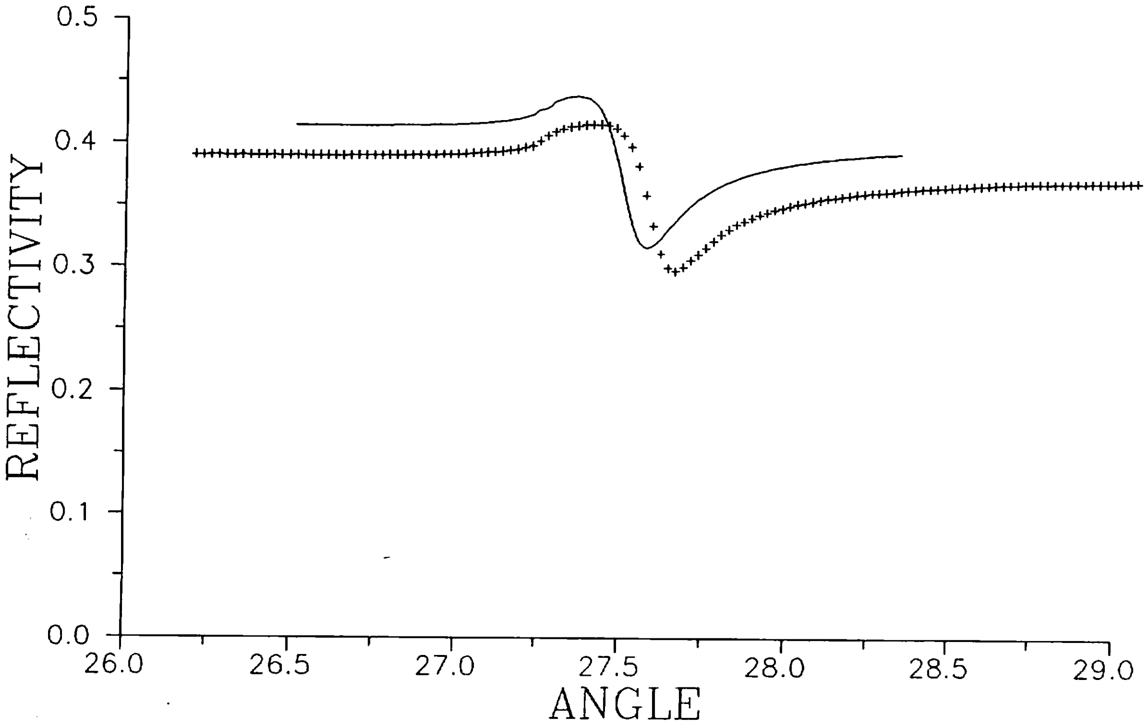

Figure 5.6: Reflectivity verses internal angle for a very thin silver film (14.4nm). Points are data and the solid line is theory calculated using the bulk silver value for ϵ. The theory fails to fit the data.

incident side of the grating.

The theory (solid line) was fitted to data by allowing the computer to vary parameters automatically, progressively reducing the sum of squares difference. This process was repeated until the sum of squares error between the data and theory was an acceptable value. On each fit as well as the silver thickness (d), and ϵ, the grating groove depth was allowed to vary within tight bounds. This is to allow for small variations of groove depth that occur across the grating substrate (It was impractical to position the laser spot to sample exactly the same region of the grating during different scans). The fluid index was also allowed to vary slightly. The parameters obtained from the fits are listed in table 5.1.

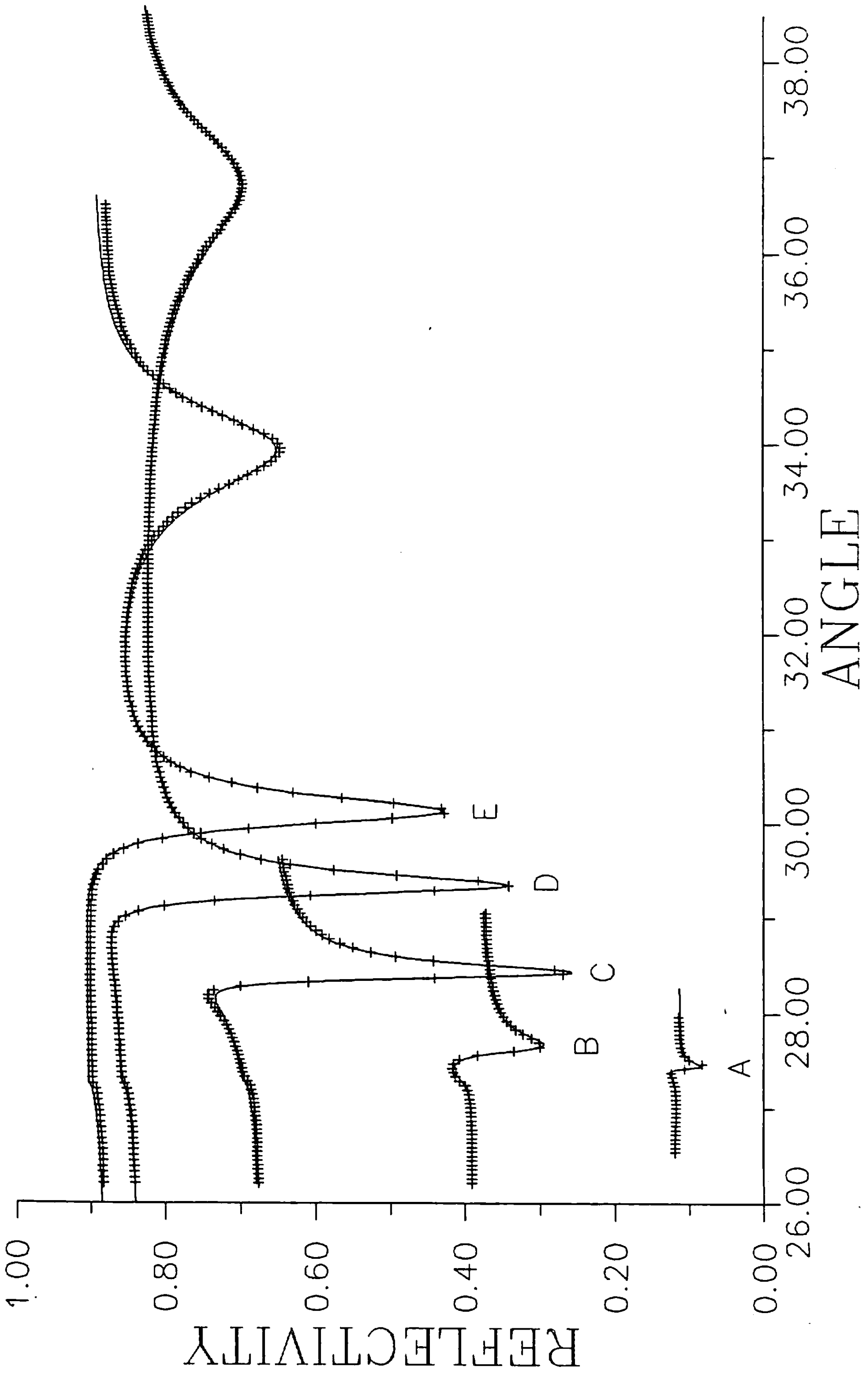

Figure 5.7: Experimental and theoretical (solid lines) curves showing reflectivity versus internal angle of incidence for different metal thicknesses. Curves A, B, C, D, E correspond to d= $8.5, 14.4, 25.0, 42.2, 52.8 nm$ respectively.

Table 5.1: Values of ϵ_r, ϵ_i, silver film thickness and groove depth obtained from fitting theory to reflectivity data.

Film thickness (nm)	ϵ_r	ϵ_i	Groove depth (nm)
52.8	-16.72	0.779	25.8
42.2	-15.42	0.775	25.2
25.0	-16.42	1.547	25.0
14.4	-16.93	1.643	25.4
8.5	-12.83	7.477	25.3

5.4 Discussion

Figure 5.7 shows clearly that the data are well fitted by the theory (continuous lines) indicating that the differential method for modelling gratings is satisfactory. The grating used in our study had a groove depth to pitch ratio of only 0.03 (well within the limit of accuracy of the differential method) and so a good fit is expected.

With such good fits we obtain the parameters of the silver film and the grating groove depth. The fitted values for the grating groove depth agree with talystep measurements and confirm that the groove depth variation was less than $1nm$. However the parameters obtained for the silver film show that there is a reduction in $|\epsilon_r|$ for the thinnest film. Also the values of ϵ_i obtained are clearly seen to increase with decreasing metal thickness, with the thinnest sample showing a substantially increased value. This behaviour in thin silver films has been previously noted using ATR prism coupling in the Kretschmann configuration (T Inagaki *et al*, 1986 and M Fukui *et al*, 1988) but not in grating coupling. These ATR studies found an increase in ϵ_i with decreasing metal thickness, and ϵ_r was also seen to become less negative for thinner films. This second observation is only seen clearly in our results for the 8.5nm thick film.

Of the previous studies on silver films, the latter explained the variations of ϵ with thickness in terms of the formation of small silver islands which tend to occur for very thin films. These islands of silver and the air (or fluid) between them lead to an effective ϵ for the thin layer which is substantially different to the value for bulk, continuous, films. The effective ϵ can be modelled approximately using Maxwell Garnet theory (JC Maxwell Garnet, 1904). However the degree of islandisation was found to depend on deposition conditions. In our samples, faster deposition leads to thinner films remaining continuous and so only the 8.5nm thick film showed a large change in ϵ_r and ϵ_i from bulk values. It is probable that the smaller changes in the thicker films are associated with the increased influence of surface scattering on the electron scattering time as the films become, in thickness, of the order of the electron mean free path at room temperature. This implies that even if the films are made continuous at much lower thicknesses, the increased ϵ_i arising from surface scattering has a marked influence on the ability to create a long range surface plasmon.

5.5 Summary

To summarise, we have used differential grating theory to fit to reflectivity data from thin silver films bounded by matched dielectrics. This is the first time that LRSPs excited on gratings have been fitted by grating theory to yield results on ϵ and d for silver. The variation of ϵ_r and ϵ_i with d shows the danger in using bulk values of ϵ for thin films, and highlights a need for caution for those working on LRSPs. The metal used in this study (silver) has traditionally been a good material to use for study of coupled modes in the visible and infra red. Its small ϵ_i compared to ϵ_r leads to smaller mode damping than other metals and hence the LRSP excited on a silver sample has a small angular half width. However in the next chapter we show that a thin film with a large ϵ_i and a small positive ϵ_r is also capable of supporting a long range mode with a small half width.

Chapter 6

Long Range Surface Exciton Polaritons on Chromium Films

6.1 Introduction

As discussed in the last chapter, coupled surface plasmon polariton modes have been studied by many workers. It has previously been considered that a thin layer with a large negative ϵ_r is needed to support long range coupled surface modes. However Fuzi *et al* (1990) have recently shown that a long range mode may exist on a thin layer having a large ϵ_i and a small ϵ_r. In this case the material may be almost any type, for example it could be an excitonic dielectric, or a metal at a frequency close to a strong interband transition. As this coupled mode needs a relatively large ϵ_i, it has been labelled the long range surface exciton polariton (LRSEP). The only experimental observation of the LRSEP so far has been by Fuzi *et al* (1990) who used a thin film of vanadium at a wavelength of $3.391\mu m$ (prism coupling to the LRSEP was used).

In this study we extend the observations on the LRSEP to thin films of chromium, which at the observation wavelength of $1.52\mu m$ also behaves like an excitonic dielectric. Also for the first time we have used grating coupling to this mode as well as the more readily modelled prism coupling. The grating coupling is examined because it may have advantages in possible device applications.

At this point it is worth discussing why some materials support plasmon-type resonances and some support exciton-type resonance. Hence we need to know what processes in a material dictate the value of ϵ. (Many texts have been published on dielectric constants such as ED Palik (1985), F Wooten (1972) and AV Sokolov (1966)).

The simplest method used to relate the ϵ to the microscopic parameters of a solid is to consider an atom with electrons bound to a nucleus. The motion of such an electron can be modelled as a Lorentz oscillator i.e.;

$$m\frac{d^2\mathbf{r}}{dt^2} + m\Gamma\frac{d\mathbf{r}}{dt} + m\omega_0^2\mathbf{r} = -e\mathbf{E}_{loc} \tag{6.1}$$

where m and e are the mass and charge of the electron, ω_0 is the resonant frequency and $\mathbf{E}_{loc}$ is the local field acting on the electron. The second term in equation 6.1 is a damping term and the third term is the restoring force. If equation 6.1 is solved for **r** and we introduce Maxwell's equations then the polarisability of a single electron atom can be written as;

$$\alpha = \frac{e^2}{m} \frac{1}{(\omega_0^2 - \omega^2) - i\Gamma\omega}$$

but the polarisability is linked to ϵ by;

$$\epsilon = 1 + 4\pi N\alpha$$

where N is the number of atoms per unit volume and therefore;

$$\epsilon = 1 + \frac{4\pi N e^2}{m} \frac{1}{(\omega_0^2 - \omega^2) - i\Gamma\omega} \tag{6.2}$$

Figure 6.1 shows the frequency dependencies of the two components of ϵ in equation 6.2.

Equation 6.2 describes the effect of bound electrons on the ϵ of a material, but it may be applied to the case of metals (free electrons) by simply setting the restoring force in equation 6.1 to zero. Equation 6.2 now becomes;

$$\epsilon = 1 - \frac{4\pi N e^2}{m} \frac{1}{\omega(\omega + i\Gamma)} \tag{6.3}$$

The damping factor Γ now represents the scattering of electrons and can be described by a characteristic $\tau = 1/\Gamma$.

$$\epsilon = 1 - \frac{4\pi N e^2}{m} \frac{\tau}{\omega(i + \omega\tau)} \tag{6.4}$$

Equation 6.4 is identical to the well known Drude formulae;

$$\epsilon_r = 1 - \frac{\omega_p^2 \tau^2}{(1 + \omega^2 \tau^2)} \qquad \epsilon_i = \frac{\omega_p^2 \tau}{\omega(1 + \omega^2 \tau^2)}$$

where ω_p is the plasma frequency, given by

$$\omega_p^2 = \frac{4\pi N e^2}{m}$$

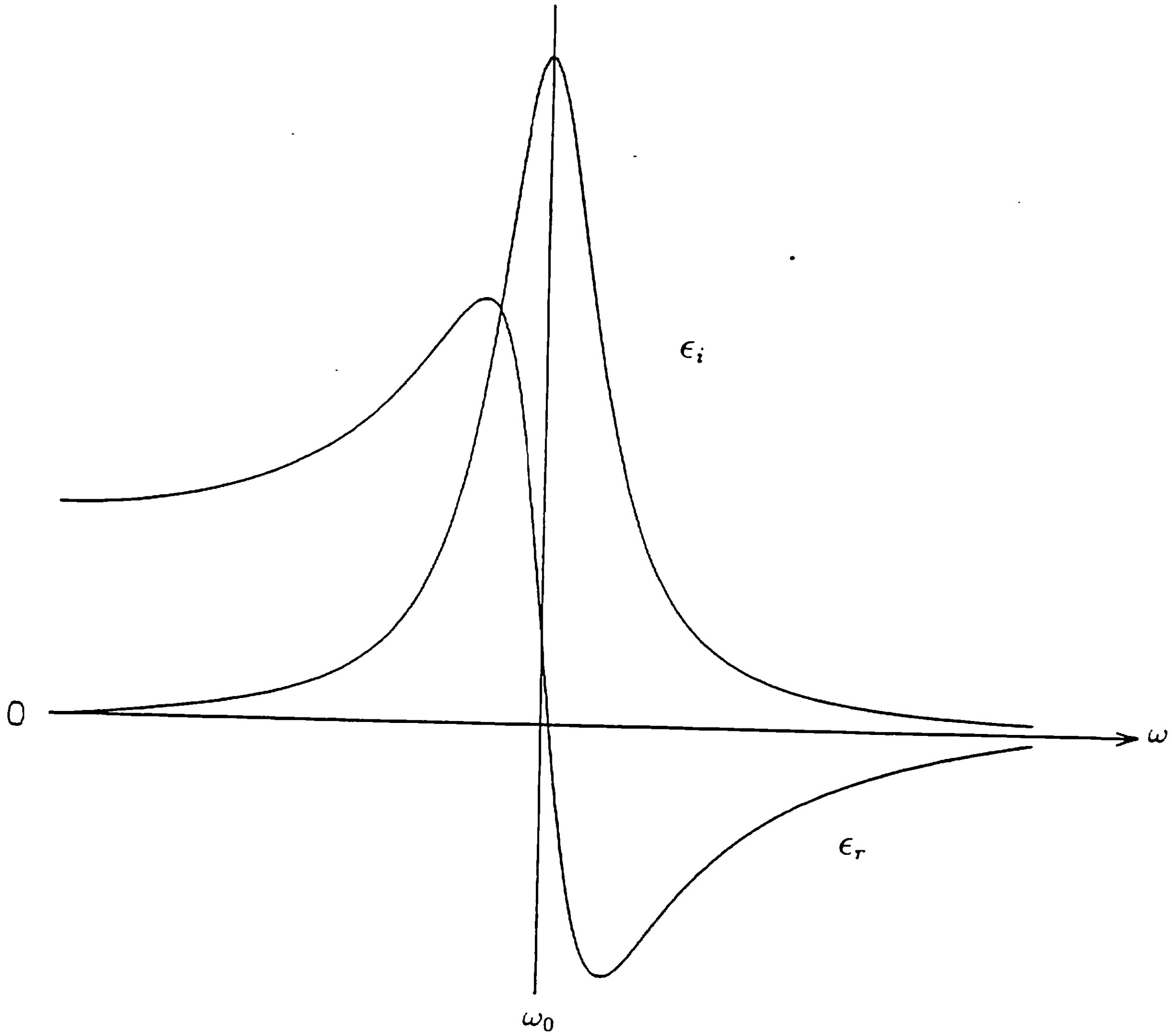

Figure 6.1: The frequency dependence of the dielectric constants of a solid modelled as a Lorentz oscillator.

In real metals, ϵ can be considered to be made up of two components given by equations 6.2 and 6.3. The former is the bound (Lorentz) component which arises from electron transitions between energy bands (called interband transitions) and the latter arises from electron transitions from energies below the Fermi edge to empty states above it (intraband transitions).

The simplistic approach shown above only describes single electron atoms with spherical Fermi surfaces. It does however clearly highlight two ways in which electrons contribute to the ϵ of a metal. Sodium is very free electron-like and closely follows the Drude formulae in the visible. Silver is free electron-like in the visible but has an interband transition in the near UV. The metal studied in this chapter (chromium) has a strong interband transition in the near IR and so we expect it to have a positive ϵ_r and a large ϵ_i in this wavelength region (as shown in figure 6.1). Hence thin films of chromium should support LRSEPs.

The LRSEP and its short range counterpart the SRSEP behave differently to the LRSP and SRSP with respect to film thickness. Figures 6.2 (a, b) are mode dispersion curves showing the real and imaginary components of propagation wavevectors versus film thickness. The curves are theoretically generated for the LRSEP and the SRSEP on a typical excitonic thin film (in this case vanadium at $\lambda = 3.391\mu m$). These curves are similar to those shown in section 1.5 for gold. Figure 6.2(a) shows that the SRSEP always propagates with $k_r < k$ hence the mode is leaky and too broad to excite. However the LRSEP changes from being leaky to non leaky when the thickness (d) is reduced below $360nm$ and so it may be excited below this thickness. For small d the LRSEP mode tends towards k with a quadratic dependence on d (as was found for the LRSP). Figure 6.2(b) shows that k_i for the LRSEP decreases with decreasing film thickness and suggests that the narrowest modes are obtained for very thin films. As with k_r, k_i also has a quadratic dependence on thickness for small thicknesses. However all these curves neglect coupling effects from the grating or prism and only represent unperturbed solutions to Maxwell's equations for the two interface system. In practice coupling to the mode always causes mode broadening (increased k_i) and shifts the mode to higher k when grating-coupled and lower k when prism-coupled. The shift due to grating coupling was clearly seen in the previous chapter for the LRSP (figure 5.2). Notice that the k scale in figure 6.2(b) is much larger than that in figure 1.5 which shows that LRSEP modes are usually much broader than LRSP modes.

In this section we experimentally examine only the LRSEP as the SRSEP is a broad leaky mode which cannot be excited with any significant efficiency.

6.2 Experimental Techniques

Both prism and grating coupling techniques are used for the excitation of LRSEPs on chromium films. The grating configuration is the same as that used in the previous section (see figure 5.3). The matching fluids used are tetrachloroethy-

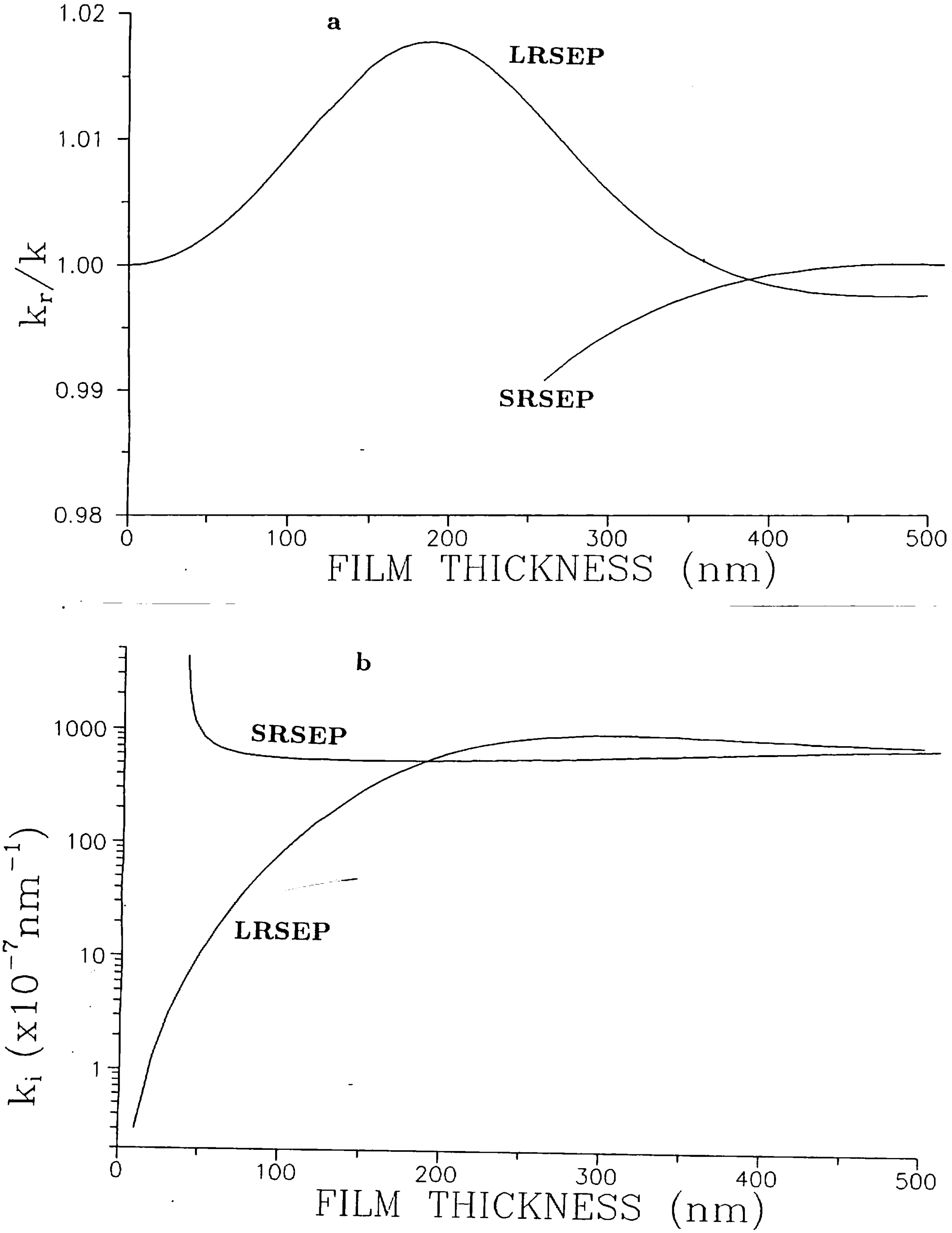

Figure 6.2: Mode dispersion curves showing (a) the real and (b) the imaginary components of the wavevectors verses film thickness for the LRSEP and the SRSEP on a typical excitonic thin film.

lene and propanone which are mixed and tested in the same way as before so that they matched the index of the grating substrate (n=1.445 at $\lambda = 1.52\mu m$). The gratings used have a sinusoidal profile with a pitch of $800.8nm$ and groove depths ranging from 25.0 to $65.0nm$.

The prism configuration is shown in figure 6.3(a). A silica glass disc coated with the thin chromium layer is mounted parallel to an equilateral sapphire prism. The matching fluid in the gap has the same index as the silica glass (n=1.502). In this configuration the coupling strength is varied by varying the fluid gap but this must be done without introducing any wedging in the gap which would cause problems in fitting theory to the data. To avoid wedging problems a specially designed sample holder is used which allows very fine adjustment of the silica glass substrate. The gap is set parallel by using a visible laser beam expanded and then focused in one plane onto the prism as shown in figure 6.3(b). The reflected beam contains Fabry-Perot mode lines excited in the air gap (carried out before the matching fluid is added). Two fine threaded screws are carefully adjusted until the mode lines appear parallel and correctly spaced. The laser beam is then moved from position 1 to position 2 and the fringes in the opposite direction are viewed. When both positions give fringes that appear the same and have no slants then the gap is parallel in both planes. The number of modes viewed in a given angle gives a rough estimate of the initial gap width. A micrometer screw (not shown) can then be used to adjust this gap without introducing a wedge.

Chromium is coated onto the gratings and silica glass flats by evaporation in a vacuum of 10^{-4}Pa at a deposition rate of $0.3nm$ per second. (Removal of chromium films to allow recoating is easily achieved using electrolysis. The sample is slowly dipped into a solution of HNO_3, HCL and glycerol in a ratio of 1:2:3, with the sample being held at +10V compared to the solution). Once a sample is fabricated (of either type) reflectivity as a function of angle is taken for p polarised light from a HeNe laser operating at $\lambda = 1.52\mu m$. Laser beam divergence cannot be reduced by a spatial filter and lens in the same way as in the visible and so it is allowed for in the theory fitting program (only prism coupled data has been reliably fitted). Both prism and grating data was corrected to obtain reflectivity verses internal angle.

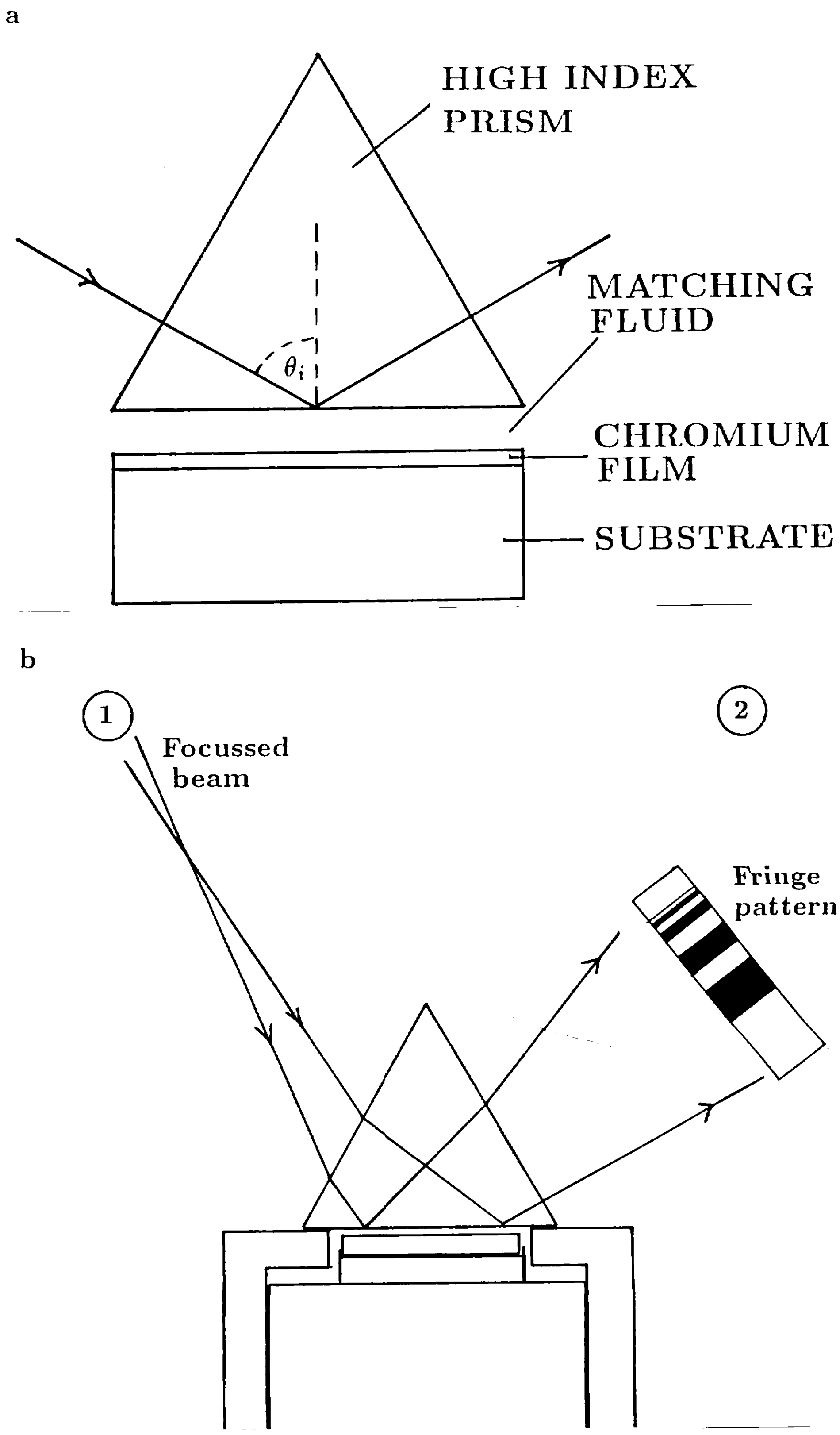

Figure 6.3: (a)Experimental configuration used for coupling to the LRSEP via a prism. (b) Configuration used to set up the prism gap to be accurately parallel by viewing Fabry-Perot modes in the air gap.

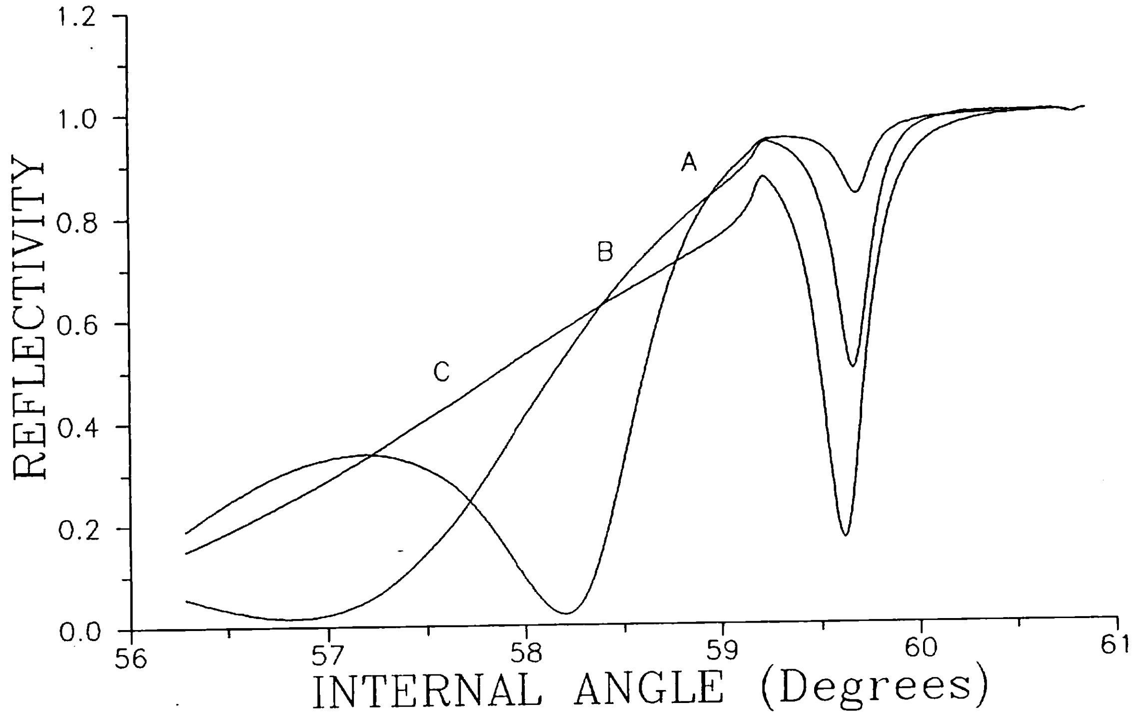

Figure 6.4: Measured p polarised reflectivity from prism configuration with $33.6nm$ of chromium for different fluid gaps: A, $3.95\mu m$; B, $2.76\mu m$; C, $1.97\mu m$.

6.3 Results

6.3.1 Prism-coupled LRSEP

We first consider results obtained by prism coupling. In figure 6.4 we illustrate a set of results for three fluid layer thicknesses for prism coupling to a chromium layer of $33.6nm$ thickness (d). A 'critical angle' θ_c for the system is visible at 59.25°. For $\theta < \theta_c$ a propagating photon beam exists below the prism and for $\theta > \theta_c$ the beam is evanescent (not to be confused with a grating critical angle which occurs when a difffracted beam ceases to propagate). For angles below θ_c there is a dip in the reflectivity corresponding to the excitation of a leaky guided mode in the fluid (this feature yields the fluid gap thickness). As the gap is increased the first mode reflectivity minimum moves progressively closer to the critical angle.

By contrast with this the sharp resonance, recorded at an angle above θ_c, remains largely unchanged in angle by the variation of coupling gap thickness, its primary change is in depth due to the change of coupling strength. In this situation this long range surface exciton-polariton has maximum coupling at the minimum fluid layer thickness obtained ($1.97\mu m$). Note that the resonance also broadens slightly as it deepens due to the increased influence of the coupling prism, even then it is still remarkably narrow with a half width of less than 0.25°. This half width is expected on theoretical grounds to reduce approximately quadratically with decrease in film thickness (for small thicknesses) if all other parameters remain the same (as discussed in section 6.1). Further, the displacement of the LRSEP from θ_c is also expected to be quadratic in film thickness. For the shallowest resonance (least perturbed by the prism), $\theta_{LRSEP} - \theta_c \approx 0.50°$.

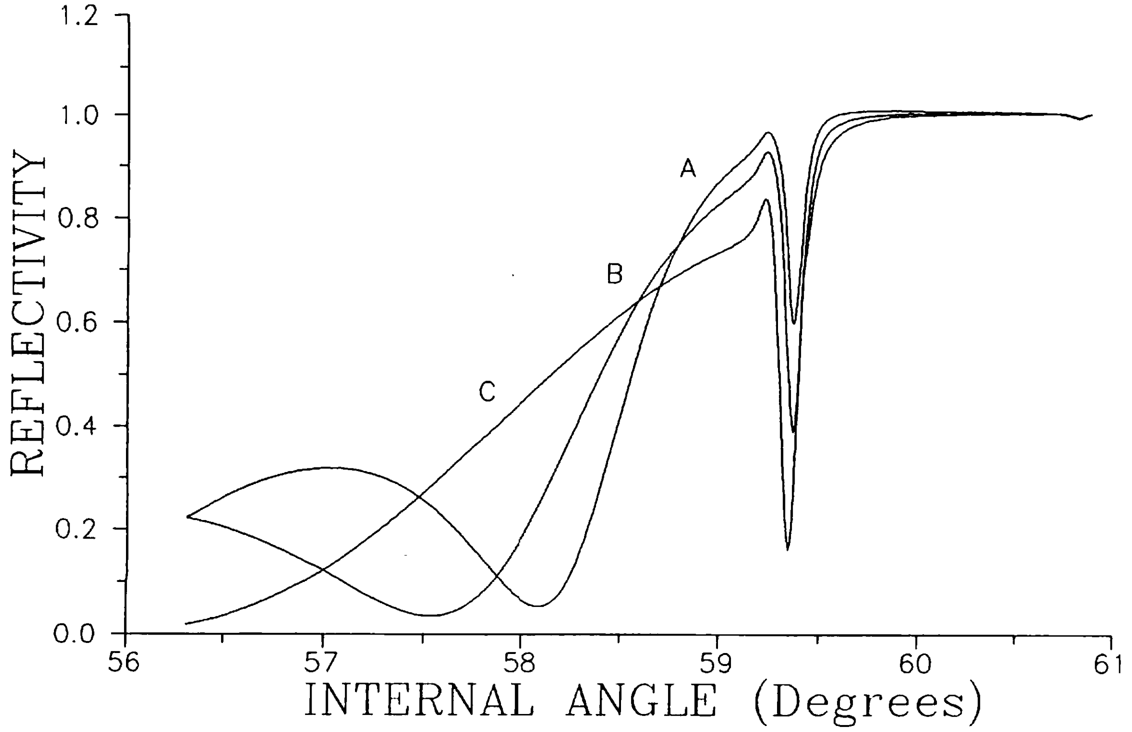

Figure 6.5: Measured p polarised reflectivity from prism configuration with $20.9nm$ of chromium for different fluid gaps: A, $4.13\mu m$; B, $3.47\mu m$; C, $2.74\mu m$.

In figure 6.5 we show results for a $20.9nm$ film of chromium where once again the best coupling to the LRSEP is obtained with the thinnest fluid layer, now $2.74\mu m$. In this case the half width of the deepest resonance is 0.09°, which agrees very well with the 0.097° predicted from a simple quadratic dependence on thickness. Also $\theta_{LRSEP} - \theta_c$ is 0.16° while a quadratic dependence in thickness would give 0.19°.

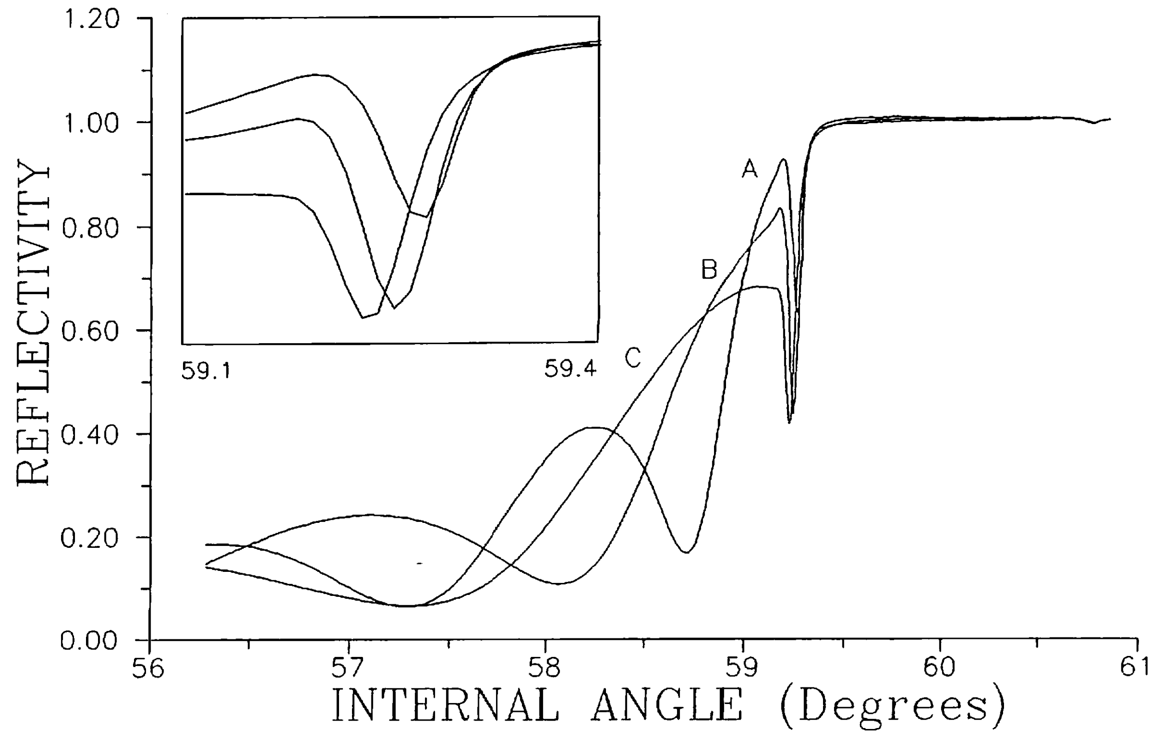

Figure 6.6: Measured p polarised reflectivity from prism configuration with $11.2nm$ of chromium for different fluid gaps. A, $5.85\mu m$; B, $4.19\mu m$; C, $3.40\mu m$. Insert shows the region of the LRSEP in detail.

The thinnest sample studied, $11.2nm$, produced a very sharp LRSEP resonance as shown in figure 6.6. Now the LRSEP has become so sharp that the laser beam angle spread is playing a significant role. Further it has moved so close to the critical angle that even for fluid gaps as large as $3.40\mu m$ the mode is distorting. Measuring the half width of the LRSEP for the $4.19\mu m$ fluid gap gives 0.06°. Not too surprisingly this does not conform to the quadratic dependency expected, largely because of the distortion due to the proximity of the critical angle. It is

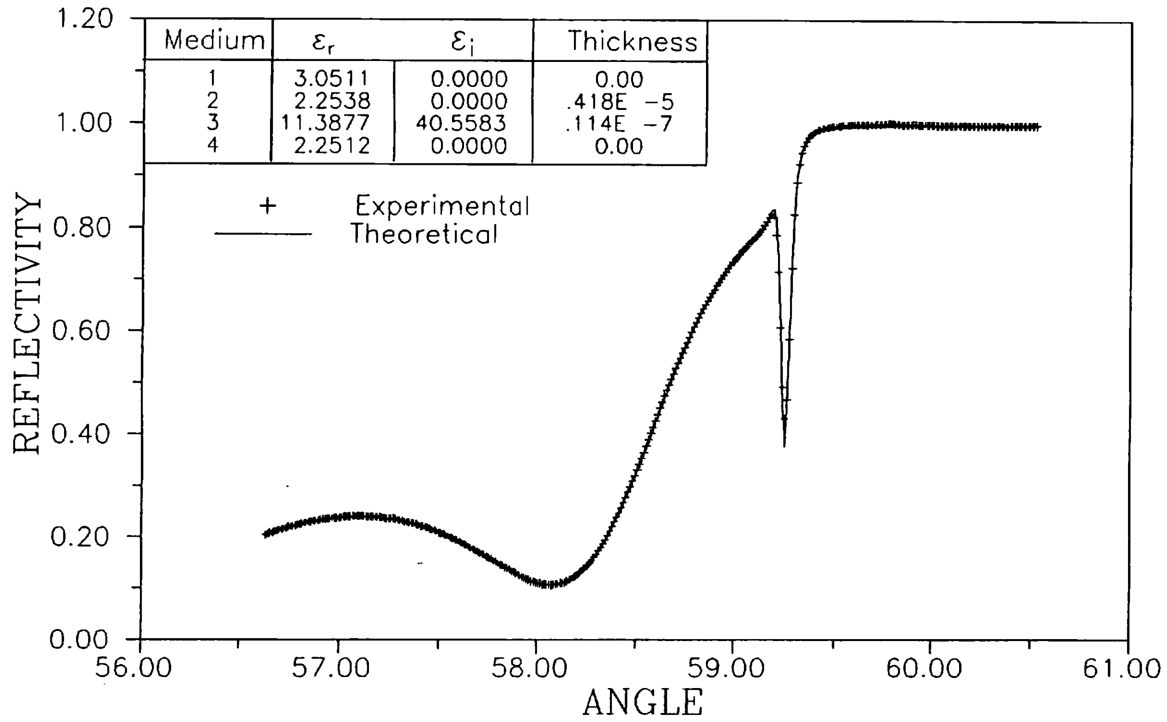

Figure 6.7: Theoretical fit to curve B from figure 6.6.

also extremely sensitive to small differences in ϵ between the fluid and the prism.

The dielectric constants, the chromium layer thickness and the fluid layer thickness were all obtained by carefully fitting the predictions of Fresnel theory to the reflectivity results. A typical fit of theory to experiment is shown in figure 6.7 for the thinnest sample studied (curve B of figure 6.6). The quality of comparison of theory with experiment is excellent. In table 6.1 we present all the fitted data parameters for the three films. A beam divergence of 0.06° has been taken into account in the theoretical comparison. There is a significant range in ϵ_r for all the films, particularly the thickest. Although further contributing factors are possibly the roughness and unknown oxidised state of the chromium layer. It is however apparent that for all the films studied there is no 'metallic' behaviour, that is ϵ_r is not negative. Further ϵ_i is bigger, or of the order of ϵ_r, which is typical excitonic-like or in this case interband-resonance behaviour. Thus this prism-coupled data confirms the predictions that a thin layer having apparently inappropriate dielectric constants may support a very sharp resonance.

Table 6.1: Parameters obtained from fitting Fresnel theory to prism data.

Figure	Curve	Fluid gap (μm)	ϵ_r (Chromium)	ϵ_i (Chromium)	Cr Thickness (nm)
6.4	A	3.95	10.3	20.1	32.4
6.4	B	2.76	18.5	17.1	33.7
6.4	C	1.97	29.8	20.3	35.3
6.5	A	4.13	7.6	38.1	20.9
6.5	B	3.47	9.3	34.5	20.8
6.5	C	2.74	12.1	46.5	21.1
6.6	A	5.85	13.9	37.5	11.2
6.6	B	4.75	9.1	43.5	11.1
6.6	C	3.40	10.7	43.0	11.1

6.3.2 Grating-coupled LRSEP

As mentioned earlier the discs used for the prism configuration were coated with their chromium layer at the same time as the gratings. Reflectivity verses angle of incidence was then recorded for the grating using p polarised light. Unfortunately when this data was taken, theory was not available for fitting and the need to normalise data was not seen. Allowing the data normalisation to vary as a fitting parameter leads to divergent behaviour and so in almost all cases a good fit was not obtained. Also the method now used for fitting grating data cannot take laser beam divergence into account. Hence virtually all the grating data is shown unfitted with an arbitrary reflectivity scale. The influence of the chromium thickness on the grating coupled LRSEP is shown in figure 6.8. Each chromium film was evaporated on the same grating (pitch=800.8nm, depth=40.4nm) at the same time as each of the films used for the prism experiment. The films thicknesses quoted on these films are therefore those found from the prism data fitting. For these resonances, the angle of the minimum is given by ;

$$nk \sin \theta_{int} = G - k_{lrsep}$$

Where n is the refractive index of the fluid (or grating substrate). Therefore increasing the angle of coupling is equivalent to decreasing k_{lrsep}.

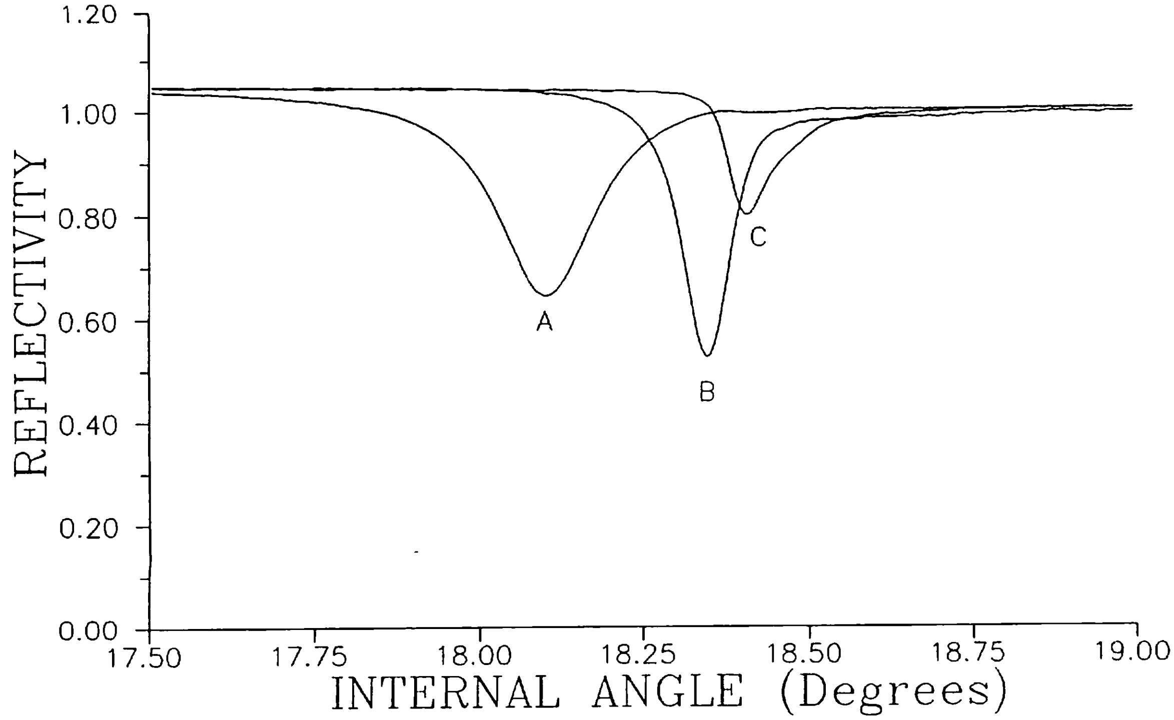

Figure 6.8: Measured p polarised reflectivity (arbitrary units) from a grating (pitch= 800.8nm, depth= 40.4nm) for different chromium thicknesses: A, 33.6nm; B, 20.9nm; C,11.2nm.

When $k_{lrsep}/nk = 1$ a 'critical angle' occurs. This cannot be seen clearly in figure 6.8 but it does exist at $\theta = 18.54°$. For the grating case we may still anticipate that k_{lrsep} increases rapidly (approximately quadratically) with d and this is born out by the data shown in figure 6.8 (the mode moves away from the critical angle as the thickness is increased). Likewise we expect the resonance width to increase approximately quadratically with d were it not for the perturbing influence of the grating, and this is approximately confirmed by the results. Note that the resonance for the thinnest film is rather broader than may be expected and it is clearly by no means optimally coupled to by this choice of grating amplitude. Indeed the coupling strength appears to go through a maximum somewhere between sample A and C in thickness.

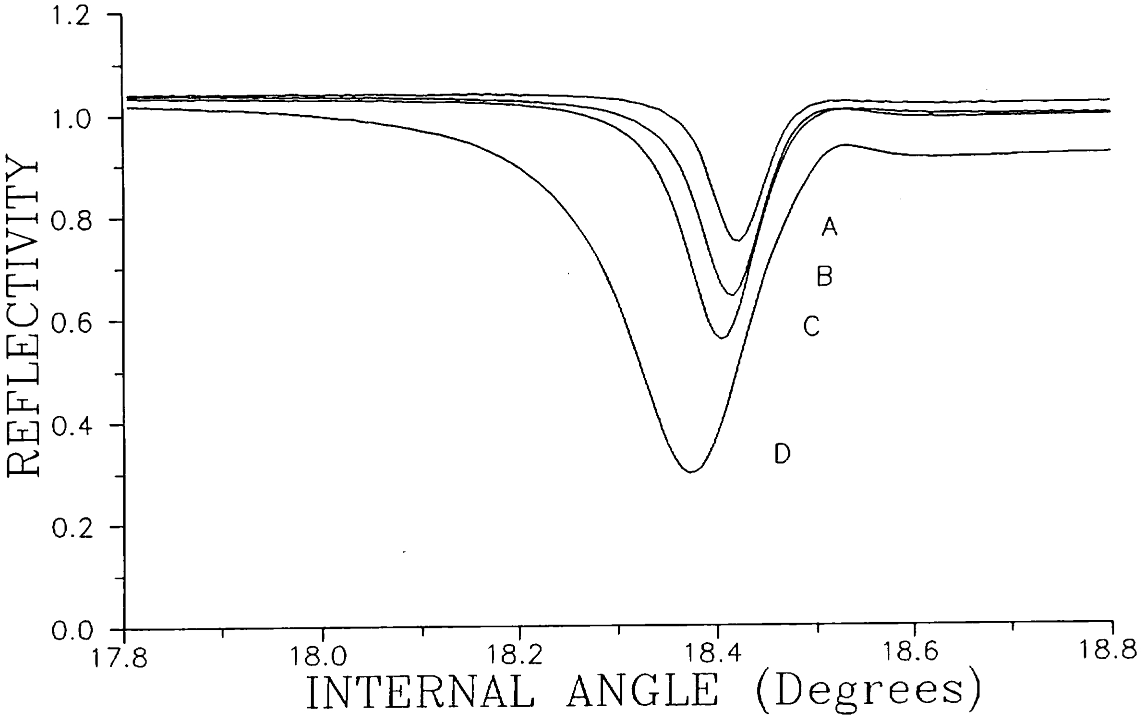

Figure 6.9: Measured p polarised reflectivity (arbitrary units) from gratings coated with 22.6nm of chromium for different groove depths: A, 25.0nm; B, 31.1nm;C, 40.4nm;D, 64.2nm.

The coupling strength can also be adjusted by varying the amplitude of the grating. Figure 6.9 shows results for four gratings coated simultaneously with 22.6nm of chromium. For this thickness, progressively improved coupling is achieved by increasing the grating amplitude. Indeed it is apparent that even with a grating depth of 64.2nm, the coupling has not reached 100%. However it is also obvious that the resonance broadens as a consequence of the increased grating perturbation. Further the resonance shifts to a lower angle corresponding to *increased* k_{LRSEP}. This is the opposite of the result achieved with decreasing gap thickness in the prism coupled case where, although the resonance deepens and broadens, it decreases in k_{LRSEP}. This perturbation of surface modes by increasing groove depth is well known for surface plasmons (see section 4.1) but the depth to pitch ratio needed to give full coupling to the LRSEP is larger than anticipated from experiments on grating coupling to surface plasmons. The deepest resonance in figure 6.9 did compare well with theory as shown in figure 6.10 but the parameters obtained are not accurate due to laser beam divergence effects. The chromium parameters obtained from the grating fit are $\epsilon = 8.69 + 29.18i$ with a thickness of $22.6nm$ whereas a fit to prism data from a sample evaporated simultaneously gives $\epsilon = 6.36 + 38.28i$ with a thickness of $17.9nm$.

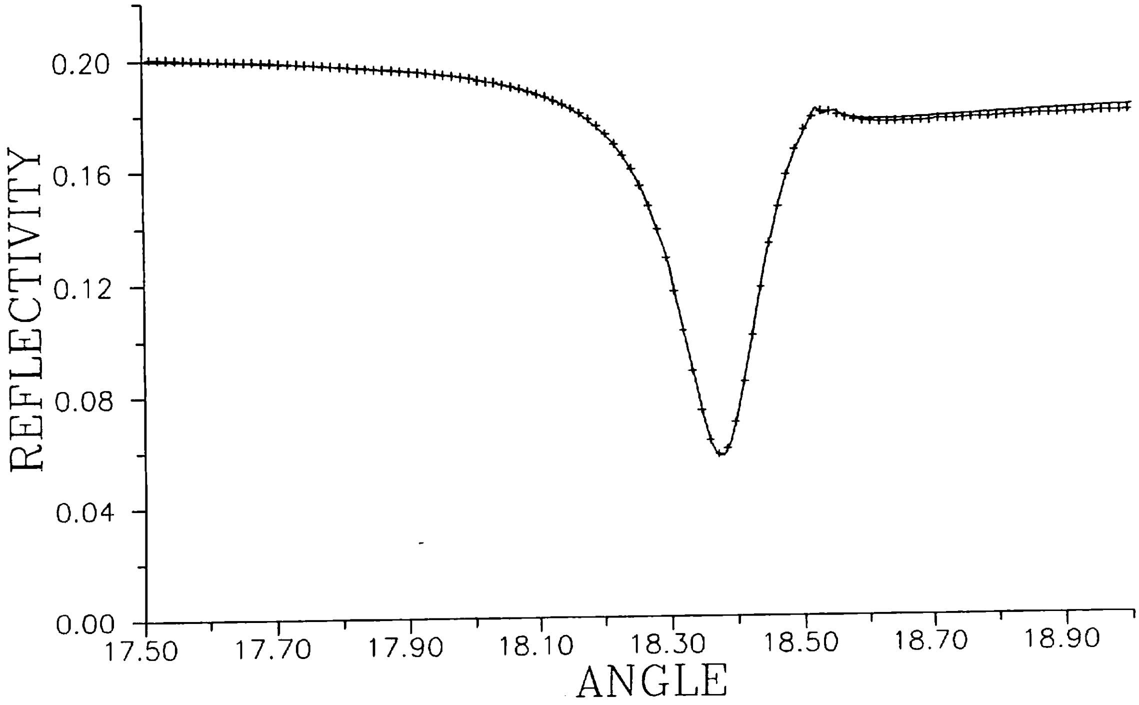

Figure 6.10: Theoretical fit to grating data taken from a deep grating (groove depth = $64.2nm$). The data has been automatically scaled by the fitting procedure.

One other variable that is easy to change for the grating coupled situation is the fluid index. This can be achieved without changing any other parameters. Figure 6.11 shows the influence of varying the fluid index from 1.4298 to 1.4599

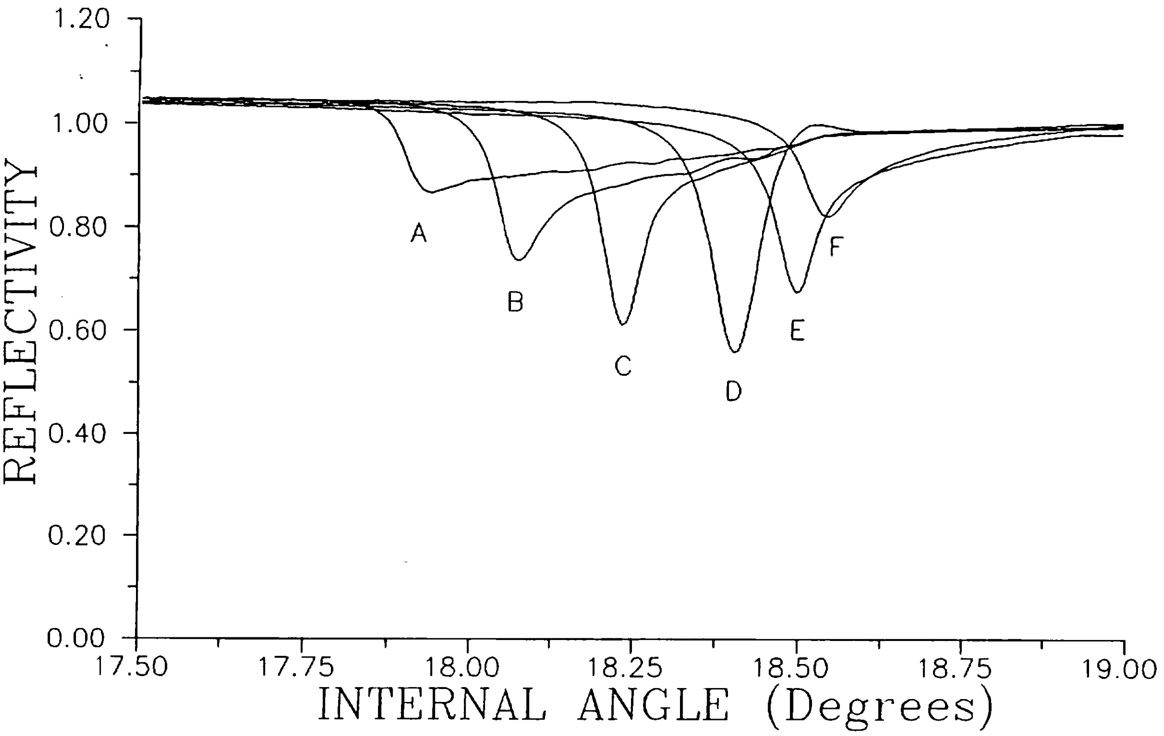

Figure 6.11: Measured p-polarised reflectivity (arbitrary units) from a grating (groove depth= $40.4nm$) with a chromium thickness of $22.6nm$ for different fluid indices. A, 1.4599; B, 1.4550; C, 1.4500; D, 1.4447; E, 1.4348; F, 1.4298. Substrate index is 1.4448.

(the substrate index being 1.4448). These results, once again for a $22.6nm$ film with a grating groove depth of $40.4nm$ show both variations in resonance angle and width as well as coupling strength. Further note that the mode has almost disappeared for curve A (for which the fluid index is 1.4599). Formal theory (Y Fuzi *et al* , 1990) for an unperturbed planar system suggests that the mode should be destroyed when ;

$$\epsilon_1 - \epsilon_3 \geq k^2 d^2 {\epsilon_3}^2 \frac{(\epsilon_1 - \epsilon_{r2})^2 + \epsilon_{i2}^2}{{\epsilon_{r2}}^2 + {\epsilon_{i2}}^2}$$

Where ϵ_1, ϵ_2 and ϵ_3 are the dielectric constants of the fluid, chromium and substrate respectively. This gives a limit $\epsilon_1 - \epsilon_3$ value of 0.034 corresponding to a fluid index of 1.457, somewhat smaller than the value of 1.4599 used to give curve A. The difference in these values is probably due to effects of grating-coupling to the mode i.e. the presence of the grating is sustaining the mode for a larger mismatch of indices than is predicted.

6.4 Discussion

Coupling of radiation to the LRSEP has been demonstrated using both prism and grating coupling techniques. The results for prism coupling fit well to Fresnel theory but the variation in metal parameters required for different fits is disappointing. A previous study (PB Johnson *et al*, 1974) has given $\epsilon = -3.5 + 30i$ for thicker chromium films, but it was found that films below $40nm$ in thickness show an increase in both ϵ_r and ϵ_i (i.e. ϵ_r becoming less negative). This is indeed what is seen in our data although the ϵ_r values appear somewhat more positive than expected.

The grating data has shown the variation of the LRSEP with metal thickness and groove depth. The only parameters obtained from fitting theory to grating data (figure 6.10) show a large discrepancy compared to the parameters obtained from a fit to prism data. It is unlikely that this is due solely to beam divergence effects. The surface quality of the gratings and the silica glass discs prior to evaporation may be sufficiently different to affect the roughness of the chromium film and so cause the difference in parameters. The grating results also show that a large groove depth to pitch ratio is required for good coupling of radiation to the LRSEP compared to the LRSP. The sensitivity of the LRSEP to surrounding ϵ values has been demonstrated with the mode being almost destroyed for a difference of only 0.05 (in ϵ).

6.5 Summary

In this chapter the microscopic origin of the ϵ of a material has been discussed. From this it has been shown that a free electron (plasmon) type material may become excitonic in nature in the region of an interband transition. For such a metal there is the possibility of a symmetric coupled surface mode in the region of strong absorption, the LRSEP. The properties of a typical LRSEP have been investigated using both prism and grating coupling of radiation to thin chromium films at $\lambda = 1.52\mu m$. This is only the second time that the LRSEP has been seen experimentally and is also the first time that the values of ϵ for chromium have been obtained by exciting a resonant mode.

In chapters 5 and 6, results have shown a plasmon type resonance on silver films at $\lambda = 632.8nm$ and an exciton type resonance on chromium films at $\lambda = 1.52\mu m$. In the next chapter we deal with palladium at $\lambda = 632.8nm$ which shows a resonance which is in between plasmon and exciton type in nature.

Chapter 7

Coupled Surface Plasmons on Palladium Coated Gratings

7.1 Introduction

In chapters 5 and 6, results were presented for LRSPs excited on silver coated gratings and LRSEPs excited on chromium coated gratings. Silver films supported a plasmon type resonance and had dielectric constants such that $-\epsilon_r \gg \epsilon_i$. In the case of chromium films ($|\epsilon_r| < \epsilon_i$) the resonance was excitonic in nature. In this chapter we discuss results taken using palladium films for which $-\epsilon_r \sim \epsilon_i$. We therefore expect palladium to support modes which are between plasmon and exciton type in nature.

Optical characterisation of palladium has previously been carried out by reflection and transmission measurements (PB Johnson *et al*, 1974) and also by ellipsometry (BT Sullivan, 1990). J Lafait *et al* (1978) used reflectivity measurements in the wings of an SPP resonance, but to our knowledge, fitting to a resonance minimum has never previously been used for the optical characterisation of Pd.

In this chapter, LRSP resonances taken from Pd samples are fitted to give the optical constants of Pd at a wavelength of $632.8nm$. Optical measurements were carried out on several thicknesses of palladium and resistivity measurements were also taken as a further indication of film quality.

7.2 Experimental Technique

The grating used in these experiments is ion beam etched with a pitch of $800.8nm$ and a groove depth of $25.3nm$. Palladium films are deposited onto this grating by vacuum evaporation with electron beam bombardment using 99.999% pure Pd in a vacuum of 6.6×10^{-4} Pa at a rate of $\sim 0.7nm/s$. The evaporation is carried out through a mask which had an appropriate shape for four probe re-

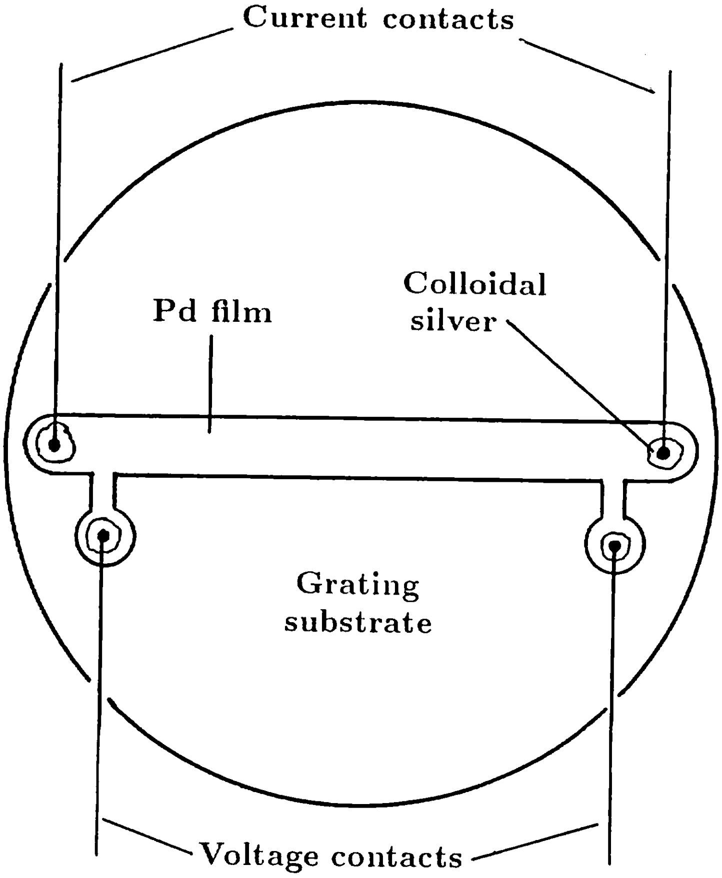

Figure 7.1: Shape of palladium film to allow resistance measurements.

sistance measurements (shown in figure 7.1). After removal from the evaporator, electrical contacts are made to the film using thin wires and colloidal silver. Once the colloidal silver has dried, resistance measurements are made using a Hewlett Packard constant current source, a Keithley 617 electrometer and a Keithley 195A multimeter. Measurements are carried out at room temperature using low enough currents to avoid heating the film. The electrical contacts are removed by dissolving the colloidal silver in 4-methyl-2-pentanone and an experimental cell is then constructed (similar to that shown in figure 5.3). As in chapter 5 the matching fluid is made from an appropriate mixture of octanol and methyl benzoate. Reflectivity verses angle is then recorded using p polarised light from a HeNe laser (632.8nm).

This procedure was repeated for different thicknesses of palladium and in each case the optical measurement was taken using the middle of the Pd strip to avoid the region that may have been contaminated by the colloidal silver. The need for speed in carrying out measurements under lab conditions is not important in the case of Pd as it has been shown that oxide formation occurs at the rate of about one monolayer every three weeks (BT Sullivan, 1990).

7.3 Results

Figures 7.2(a) and (b) show reflectivity (R_{pp}) from two Pd films with optical thicknesses of 33.4nm and 16.7nm respectively. The thicker film shows a very broad and shallow resonance which is well fitted by the theory considering the highly enlarged reflectivity scale. The off resonance reflectivity of ~ 0.41 is much lower than that found for similar thickness silver films and demonstrates the reduced reflectivity of Pd compared to Ag. The thinner film (figure 7.2(b)) shows a much sharper resonance and has a lower off resonance reflectivity level (~ 0.215). In this case the theoretical fit to data is good and the deviations at low and high angles are due to a slight slant in the data caused by spot movement across the photodiode detector. (These slants are not usually seen but they are enhanced here by the expanded reflectivity scale). The increase in resonance width as the thickness is increased from 16.7nm to 33.4nm shows that very thick ($> 100nm$) Pd films would support a surface mode with a very broad resonance which would be very difficult to fit accurately.

The results from two thinner films are shown in figure 7.3. These curves show further drops in off resonance reflectivity and also show that the resonance is still becoming sharper with decreasing metal thickness. The theoretical fits to figure 7.3(a) is very good but in (b) the shape of the 'critical angle' was impossible to fit accurately.

One final set of data from a very thin Pd film is shown in figure 7.4. In this case the off resonance reflectivity is only $\sim 1\%$ and the theoretical fit is not very good. This poor agreement is probably due to stray light or diffuse scatter in the vicinity of the sample which would significantly perturb the very low specular reflectivity. The parameters obtained from all the theoretical fits are shown in

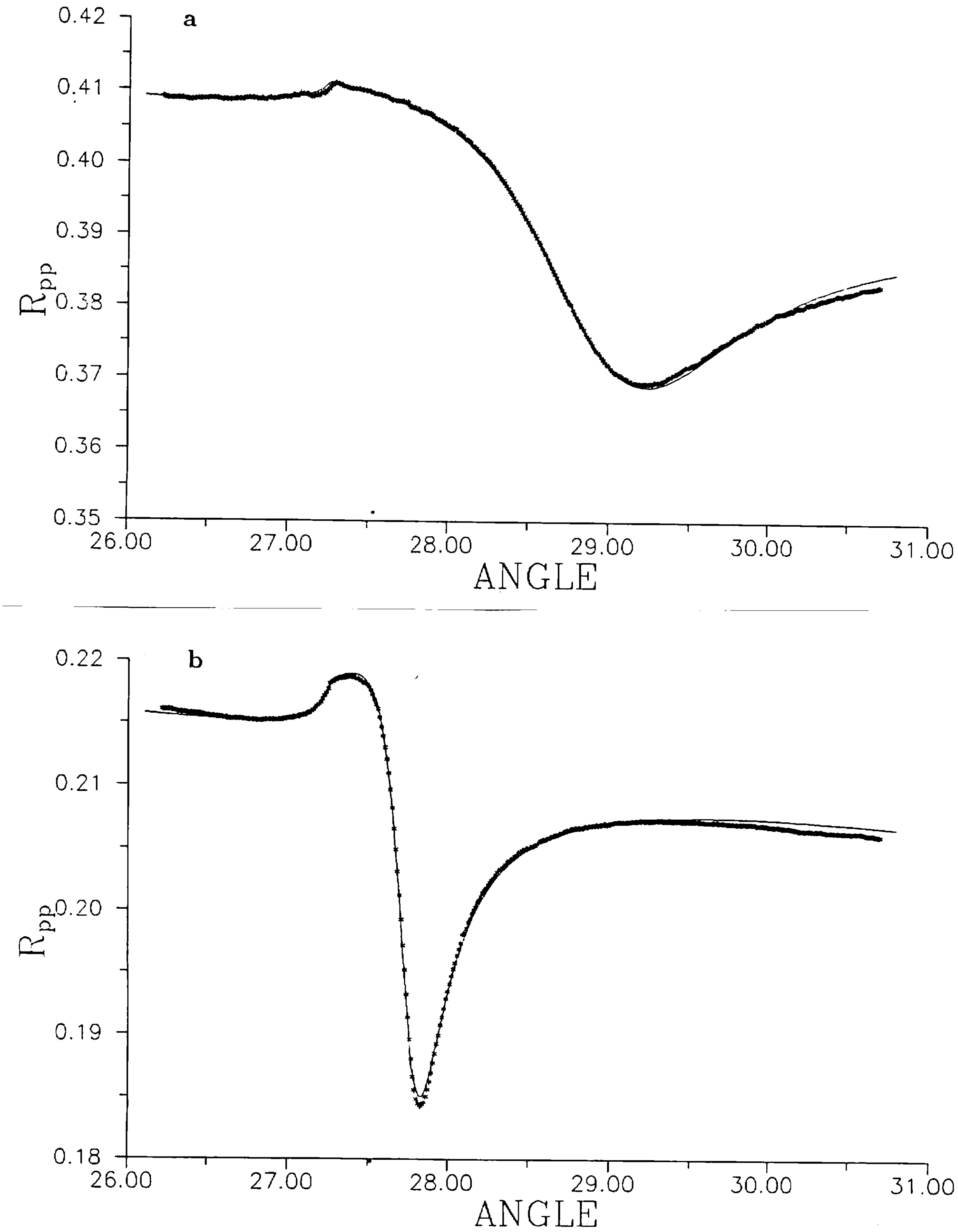

Figure 7.2: Reflectivity verses internal angle from (a) 33.4*nm* of Pd and (b) 16.7*nm* of Pd. Points are data and solid lines are theory.

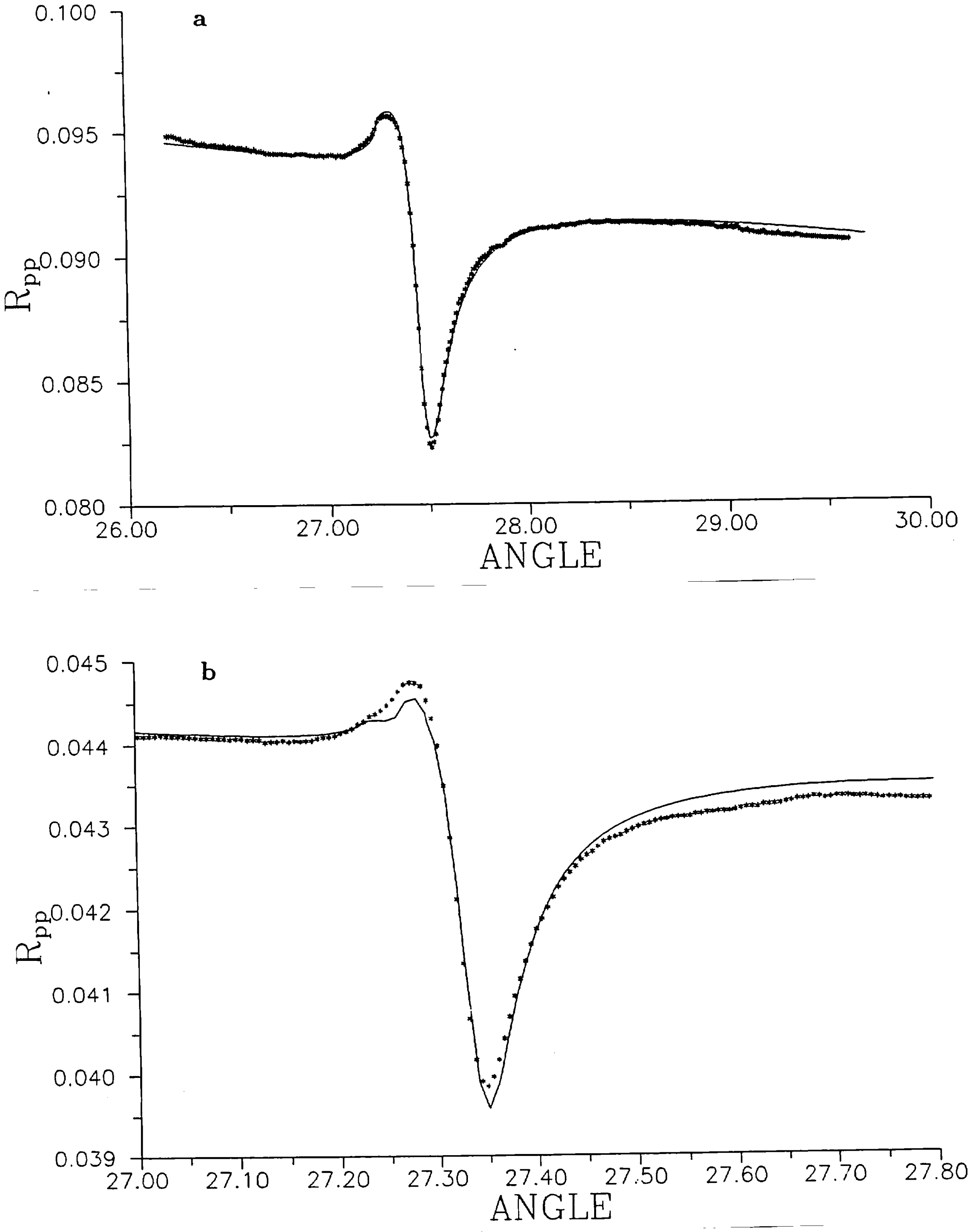

Figure 7.3: Reflectivity verses internal angle from (a) 11.1nm of Pd and (b) 7.3nm of Pd. Points are data and solid lines are theory.

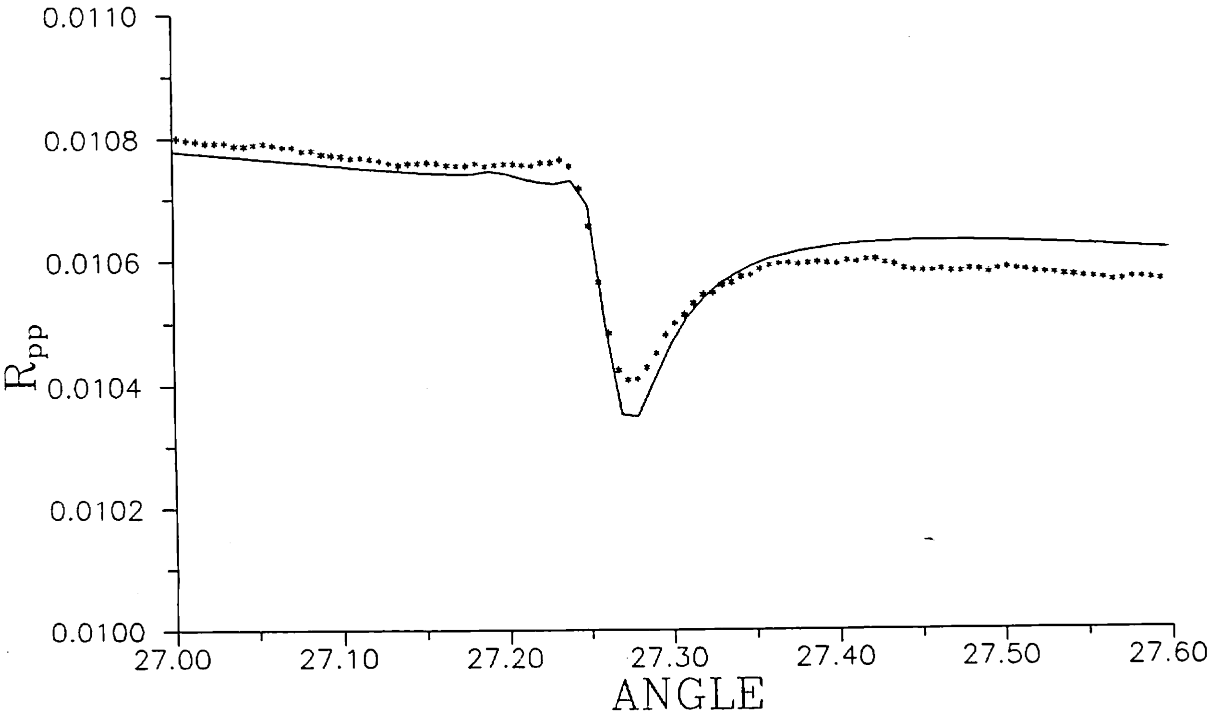

Figure 7.4: Reflectivity verses internal angle from 6.2*nm* of Pd. Points are data and the solid line is theory.

table 7.1. The errors in the parameters obtained from the good fits are similar to those given in chapter 4 (for the SPP) but the bad fit (from the thinnest Pd film) will lead to larger errors and so those parameters must be treated with caution. For each film the resistivity is also quoted (calculated from the resistance using accurate film dimensions and the optical thickness). The mass thickness was not used as the crystal oscillator deposition monitor was found to have an inconsistent calibration.

7.4 Discussion

Before analysing the optical results from the Pd films, we may use the resistivity results to give us an alternative indication of film quality. For high quality (fully dense) thin films, resistivity is increased compared to the bulk value due

Table 7.1: Parameters obtained from fitting data taken from Pd samples along with their measured resistivities.

Thickness (nm)	ϵ_r	ϵ_i	Groove depth (nm)	Resistivity (Ωm)
33.4	-9.19	12.07	25.3	4.21×10^{-7}
16.7	-7.75	12.40	25.1	8.91×10^{-7}
11.1	-2.77	12.49	26.2	3.42×10^{-6}
7.3	1.43	12.65	24.5	2.17×10^{-5}
6.2	5.00	6.02	25.3	8.12×10^{-3}

to surface scattering of conduction electrons. This surface scattering is significant when the film thickness is comparable with the electron mean free path. If our observed resistivity is greater than the value predicted using surface scattering theories then we may conclude that our films may not be fully dense.

There are many theories that describe resistivity as a function of thickness. These are based on different microscopic quantities but all have an approximate 1/d dependence (discussed by G Wedler *et al*, 1980). One of these (P Wiβmann *et al*, 1975) uses the expression

$$\rho = \rho_0 \left\{ 1 + (\mathrm{ZA_s} + \mathrm{Z^*A_s^*})\frac{\mathrm{l_0}}{\mathrm{d}} \right\}$$

where ρ_0 is the bulk resistivity, d is the film thickness and $\mathrm{l_0}$ is the electron mean free path. Z and Z* are the numbers of scattering centres per square metre at the surfaces and grain boundaries respectively and A and A* are the mean scattering cross sections at the surface and the grain boundaries respectively. If ρ is plotted against 1/d then a straight line should be obtained with an intercept of ρ_0 and a gradient of $(\mathrm{ZA_s} + \mathrm{Z^*A_S^*})l_0$. Figure 7.5 shows such a plot for 3 of our data points. For comparison, a straight line is also plotted which uses the gradient and intercept found by G Wedler *et al* (1980) for high quality annealed Pd films.

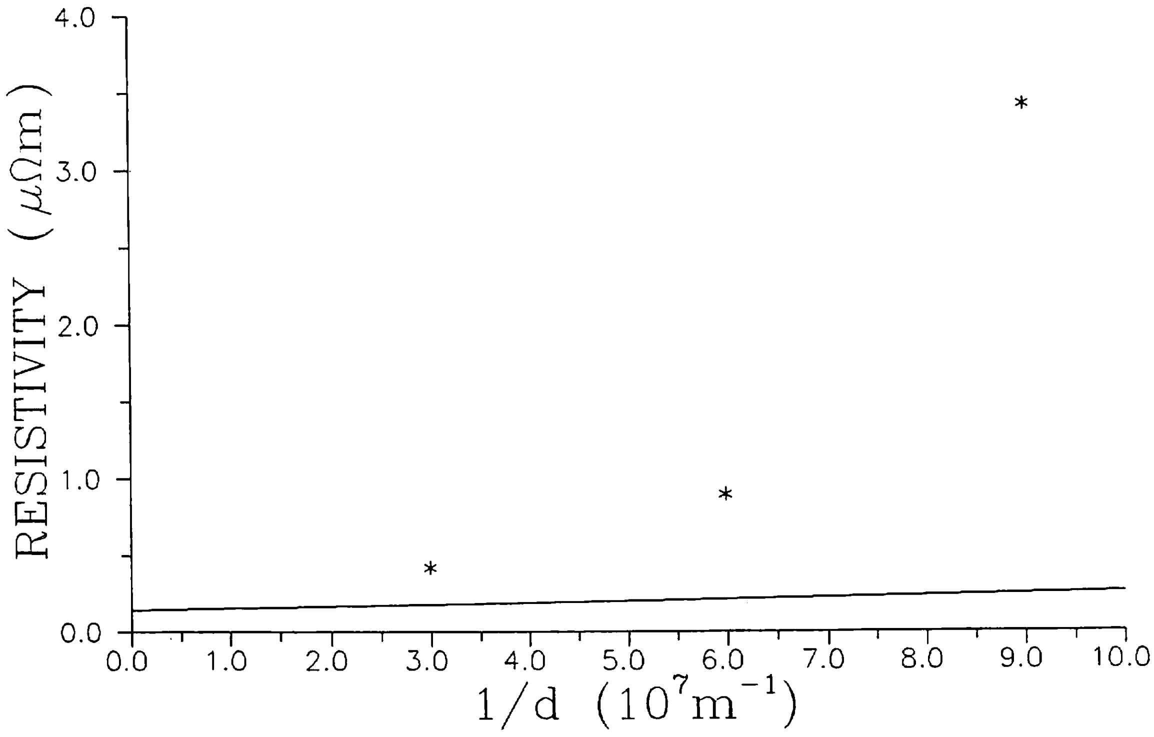

Figure 7.5: Film resistivity verses reciprocal film thickness. Points are data and the solid line shows previous results.

The plotted data points show an increasing deviation from this line as the film thickness is decreased. The data from the thinnest samples ($7.3nm$ and $6.2nm$) are not plotted but were found to be greater than the line by factors of 62.6 and 2×10^4 respectively. Therefore none of our films are fully dense and the level of porosity appears to increase with decreasing metal thickness. For the thinnest film, the very large ρ is probably indicative of small islands of Pd with only a few interconnections. The poor quality of our films is perhaps to be expected as they were not prepared in ultra high vacuum and were not annealed. Also our evaporation rate of $0.7nm/s$ is much higher than that used by Wedler *et al* (1nm/minute) which may lead to increased film roughness.

The optical results in table 7.1 show a substantial variation in ϵ_r with film thickness. Palladium appears to change from a metal ($\epsilon_r < 0$) to a dielectric ($\epsilon_r > 0$) as the film thickness is reduced. The ϵ_i values remain approximately constant and a decrease is only seen for the thinnest film (which has a large associated error). Previous values obtained for Pd at 632.8nm include $\epsilon = -15.29 + 15.19i$ by PB Johnson *et al* (1974), $\epsilon = -15.96 + 18.06i$ by BT Sullivan *et al* (1990) and $\epsilon = -15.91 + 28.85i$ by J Lafait *et al* (1978) (i.e. all show a similar ϵ_r but there is a large variation in ϵ_i). Our ϵ values show a reduction in both $|\epsilon_r|$ and ϵ_i compared to these values, but the disagreement may be explained in terms of the film porosity.

When a metal film is not fully dense, lattice cavities exist which are then filled with air (or matching fluid in our case). This then produces a film with an effective ϵ that is modified compared to the metal ϵ. Two simple theories are available to calculate the effective ϵ. These are applicable in different regimes but may both be described by

$$\frac{\epsilon - \epsilon_{\mathrm{h}}}{\epsilon + 2\epsilon_{\mathrm{h}}} = \mathrm{f_a}\frac{\epsilon_{\mathrm{a}} - \epsilon_{\mathrm{h}}}{\epsilon_{\mathrm{a}} + 2\epsilon_{\mathrm{h}}} + \mathrm{f_b}\frac{\epsilon_{\mathrm{b}} - \epsilon_{\mathrm{h}}}{\epsilon_{\mathrm{b}} + 2\epsilon_{\mathrm{h}}} \qquad (7.1)$$

where ϵ_a, ϵ_b and f_a, f_b are the dielectric constants and the volume fractions of the two constituents in the film. ϵ is the effective value and ϵ_h is the host dielectric constant which is assigned different values according to the theory. In the theory of JP Maxwell Garnet (1904), a or b is considered as the host medium hence $\epsilon_h = \epsilon_a$ or ϵ_b and one of the right hand side terms in equation 7.1 disappears. The theory of DAG Bruggemann (1935) is obtained by setting $\epsilon = \epsilon_h$, hence the left hand side of equation 7.1 disappears. These two theories are applicable in different regimes of f. The Maxwell Garnet theory considers spheres of one material completely surrounded by the host, hence it is applicable when f is near 1 or 0. The Bruggeman theory describes a random or aggregate configuration of both constituents and hence is applicable when $\mathrm{f}_a \sim \mathrm{f}_b$. For each theory, the real and imaginary components of ϵ may be extracted from equation 7.1. These are plotted against f_a in figure 7.6 (a) and (b) for the Maxwell Garnet expression and the Bruggemann expression respectively. We have set $\epsilon_a = -15.72 + 20.70i$ (the average of the three Pd values found by previous workers) and $\epsilon_b = 2.1240 + 0.000i$ to represent the matching fluid used in our case.

The theory of Maxwell Garnet (figure 7.6(a)) appears to show the best qualitative agreement with our data. To explain, we may assume that in our experiments, the volume fraction of the metal increases monotonically with film thickness (shown by resistivity results). Therefore if our thickest film has f$\sim$ 0.85 and our thinnest film has f$\sim$ 0.8 then the trends in our data follow those in figure 7.6(a).

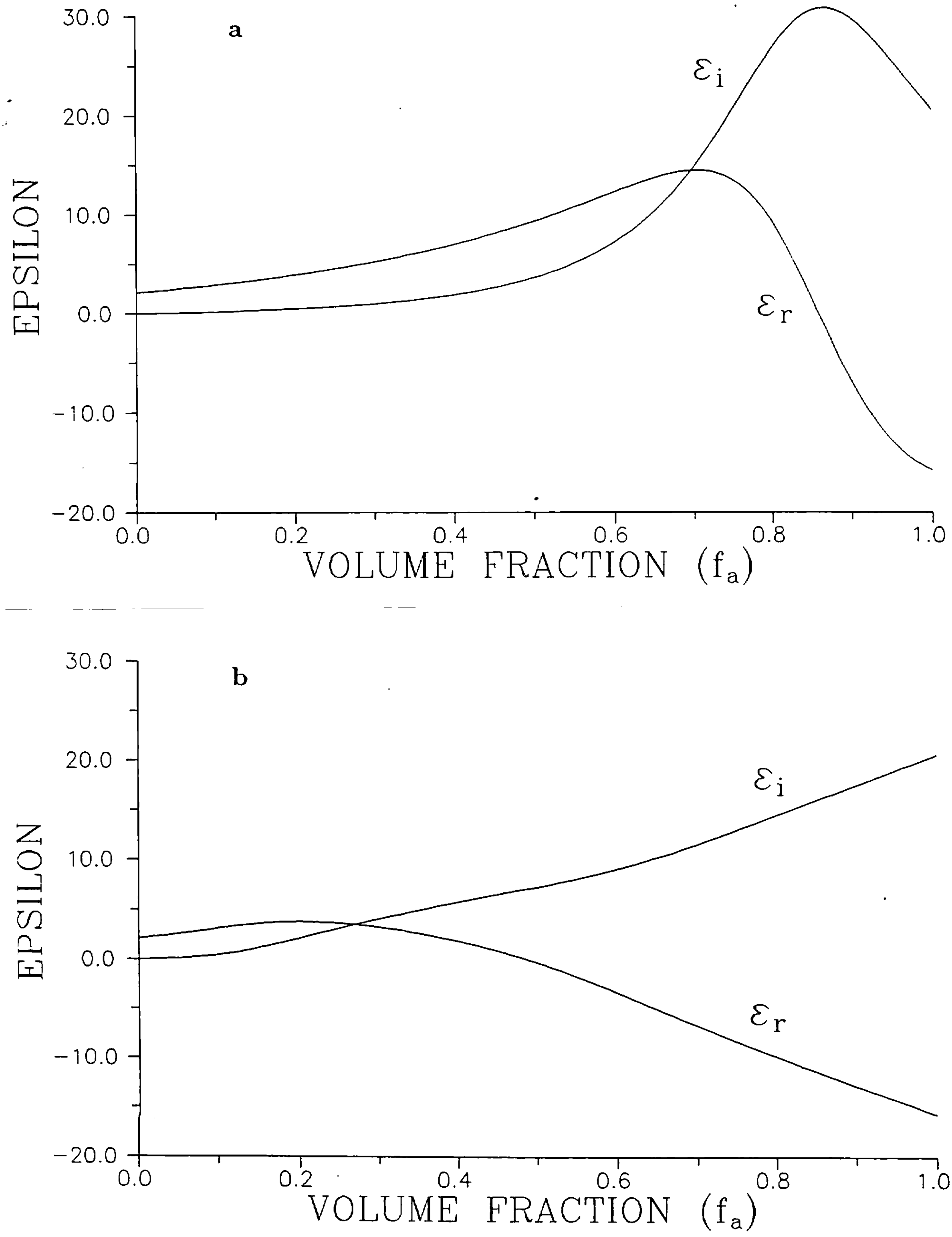

Figure 7.6: Real and imaginary parts of ϵ verses the volume fraction of Pd (in matching fluid) using (a) Maxwell Garnet theory and (b) Bruggemann theory.

However in this region of f, the Bruggemann theory is also partially valid. This theory predicts that both $|\epsilon_r|$ and ϵ_i are reduced compared to values at $f_a=1$ (as seen in figure 7.6(b)), hence it explains why even our thickest sample showed reduced epsilon values compared to previous result for high quality films.

7.5 Summary

In this chapter it has been demonstrated for the first time that thin palladium films may support a long range coupled surface mode, which cannot strictly be called a LRSP or a LRSEP. Resistivity measurements at room temperature have shown that all the films studied were porous with a level of porosity that increases with decreasing film thickness. Qualitative modelling of the variation in optical ϵ also shows that the porosity increases with decreasing metal thickness. The volume fraction of Pd in our films was approximately 0.8 and so both Maxwell Garnet and Bruggemann theories are partially applicable.

Chapter 8

p to s Conversion via Optical Modes on Gratings

8.1 Introduction

In section 4.2 the effect of azimuthal orientation on the coupling of radiation to the SPP was discussed. When $\phi > 0°$ the coupling of p polarised radiation to the SPP is diminished compared to coupling at $\phi = 0°$. It was recently discovered (GP Bryan-Brown *et al*, 1990) that this reduction in coupling is accompanied by the conversion of radiation polarisation from p to s. The effect called p to s conversion occurs with a large efficiency in the vicinity of the SPP resonance with up to $\sim 66\%$ of the incident light being converted to s polarisation for deep gratings. This new effect is studied in detail in this chapter for SPPs and also LRSPs and resonant guided modes which also cause significant p to s conversion.

8.2 p to s Conversion Via SPPs

8.2.1 Experimental Procedure

A batch of 10 holographic gratings were made for this study with the same pitch ($842.3nm \pm 0.5nm$) but with a range of groove depths. It is not necessary to ion beam etch these gratings as they do not need to be used for different coatings (also no problems exist in evaporating silver directly onto photoresist). Some of the data was taken using ion beam etched gratings which were also used for studies in previous chapters.

Silver is used to coat all the gratings as it produces the narrowest SPP in the visible and so should give the highest p to s conversion efficiency. The gratings are coated in a vacuum of 10^{-4}Pa at a rate of $\sim 6nm$ per second using 99.999% pure silver. All experiments are conducted within 30 minutes after removal of the sample from the evaporator to ensure that overlayer contamination is negligible.

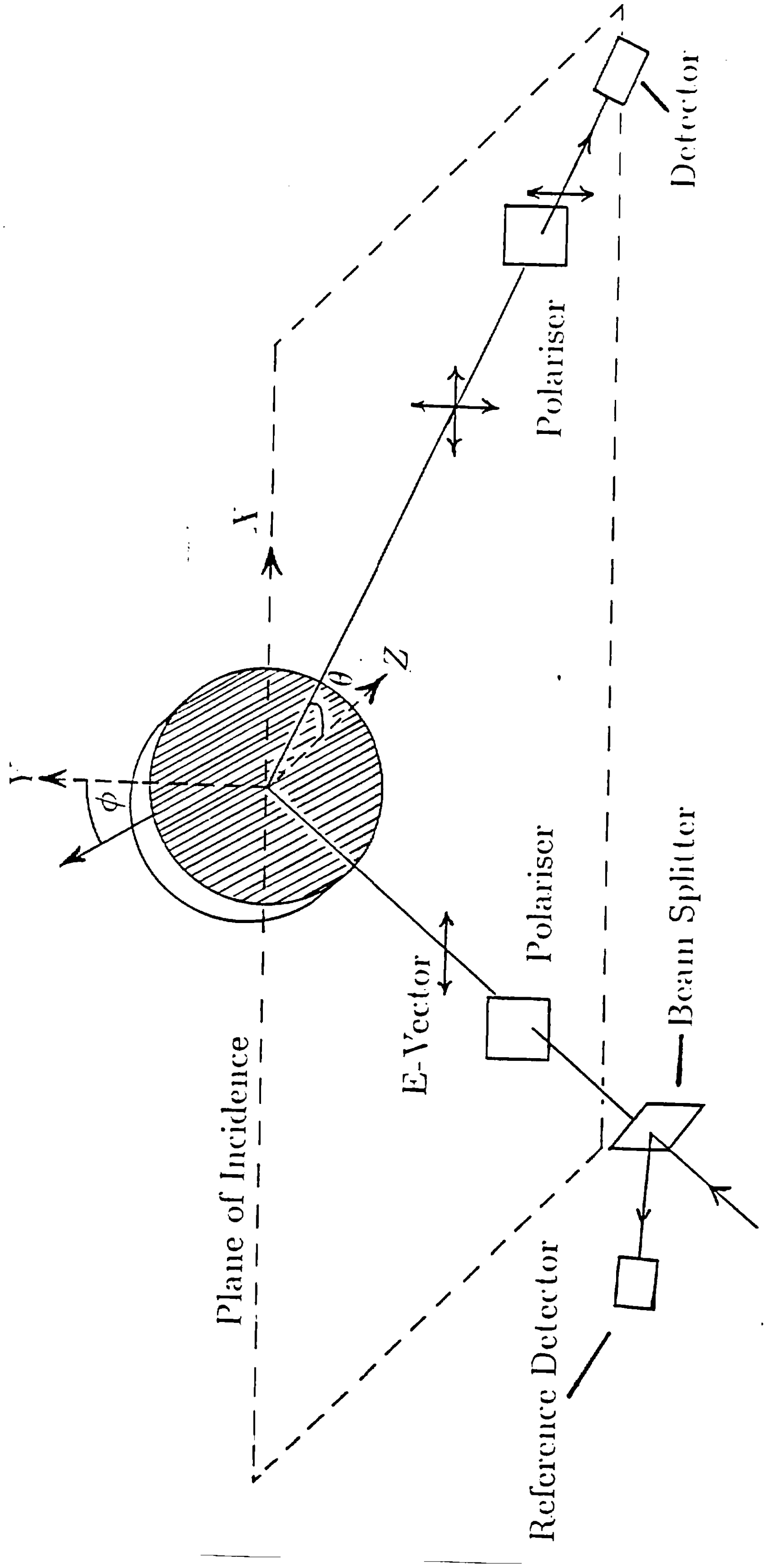

Figure 8.1: Experimental arrangement used to study p to s conversion.

The experimental arrangement used to record data is shown schematically in figure 8.1. This set up is identical to those used to record data in previous sections but now the second polariser (in front of the detector) is set with its transmission plane orthogonal to the first so that only the s polarised component of the reflected light is detected. The sample is mounted on a holder allowing adjustment of the azimuthal angle with an accuracy of $\pm 0.1°$. Absolute magnitudes of R_{ps} (p incident, s detected) are obtained by comparing data with the signal measured directly from the input beam with the second polariser set to transmit p polarisation. This study was carried out using a visible HeNe laser ($\lambda = 632.8nm$).

8.2.2 Dependence of conversion on azimuthal angle

Figure 8.2(a) shows a typical SPP resonance on a silver coated grating (the crosses are data and the solid line is theory). For this data, the grating is orientated with $\phi = 0°$ and R_{pp} is measured. If this grating is now rotated to $\phi = 45°$ then the scans shown in figure 8.2(b) are obtained for R_{pp} and R_{ps}. The R_{pp} scan shows that the coupling of radiation to the SPP has diminished and that the SPP has moved to a higher angle (see section 4.2). The R_{ps} scan now shows a resonance peak that occurs at very nearly the same angle as the R_{pp} minimum and has the same half width. In this case the maximum conversion efficiency is only 8.8% but the grating used does have shallow grooves (groove depth $= 25.0nm$, pitch $= 800.8nm$). The off-resonance p to s conversion is negligible ($< 10^{-3}\%$) and demonstrates that the enhancement is solely due to the excitation of the SPP. The solid theory lines have been generated using the new conical diffraction theory described in section 2.3 and are in excellent agreement with the experimental data points.

R_{ps} scans were taken on a deeper grating for a range of ϕ values as shown in figure 8.3. For $\phi = 0°$ and $90°$, R_{ps} is negligible for all angles of incidence as expected. The movement of SPP resonance angle with ϕ can clearly be seen in this diagram. In figure 8.4(a), the maximum value of R_{ps} is shown as a function of ϕ. As might be expected the maximum conversion occurs at $\phi = 45°$ and in this case the maximum efficiency is 44.4%. The solid line in this diagram is simply $\sin^2 2\phi$ and seems to fit well to the data. This dependence may be explained on a simplistic level by considering electric field components. The polarised incident

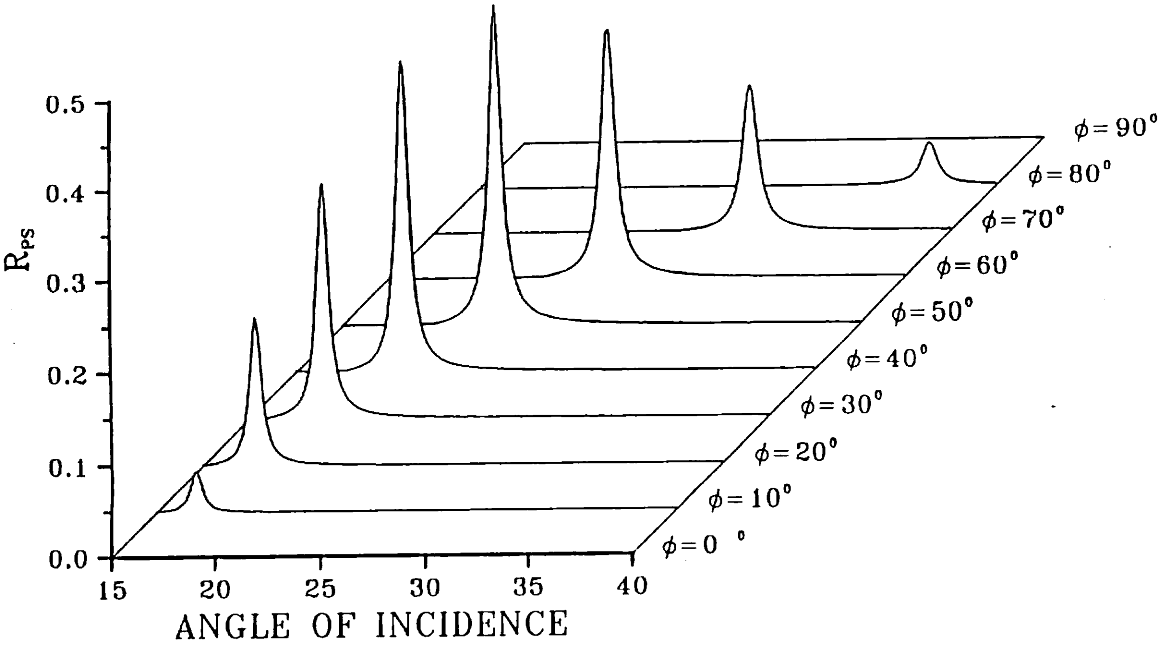

at different ϕ for a grating with a groove depth of $57.0nm$ and a pitch of $842.3nm$.

radiation has a component of its electric field vector which is perpendicular to the grooves and which varies as $\cos\phi$. This in turn has a component perpendicular to the incident polarisation which varies as $\sin\phi$. The product of these components is then squared to give the intensity i.e. a $\sin^2 2\phi$ dependence. It must be stressed that the the above argument is far from rigorous and although it fits very well to the data we would expect the conical differential grating theory to produce a more realistic fit to data. Figure 8.4(b) shows a similar scan to 8.4 (a) but this time the data is taken using a shallow ion beam etched silver coated grating which has been well characterised. The crosses are data and the solid line is generated using rigorous grating theory with the following parameters;

$$\text{Groove depth} = 25.5\text{nm}$$

$$\epsilon_{silver} = -16.85 + 0.6735i$$

All the above parameters are realistic for this silver coated grating (at $\lambda = 632.8nm$).

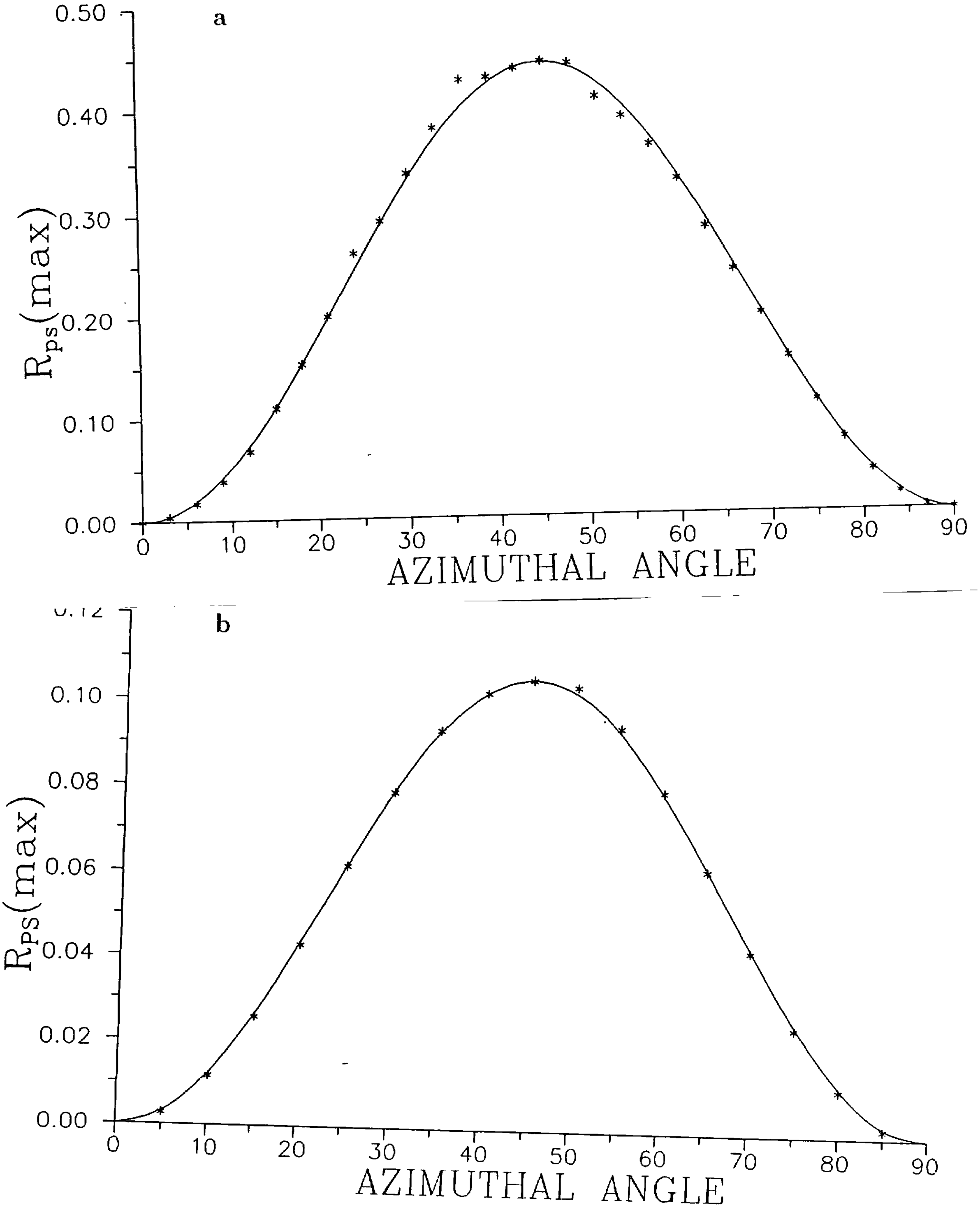

Figure 8.4: R_{ps} peak height as a function of angle ϕ for two silver coated gratings. In (a) the grating is the same as used to obtain figure 8.3 and in (b) the grating has a groove depth of 25.5nm and a pitch of 800.0nm. The line in (a) has a $\sin^2 2\phi$ dependence and the line in (b) is generated from rigorous grating theory.

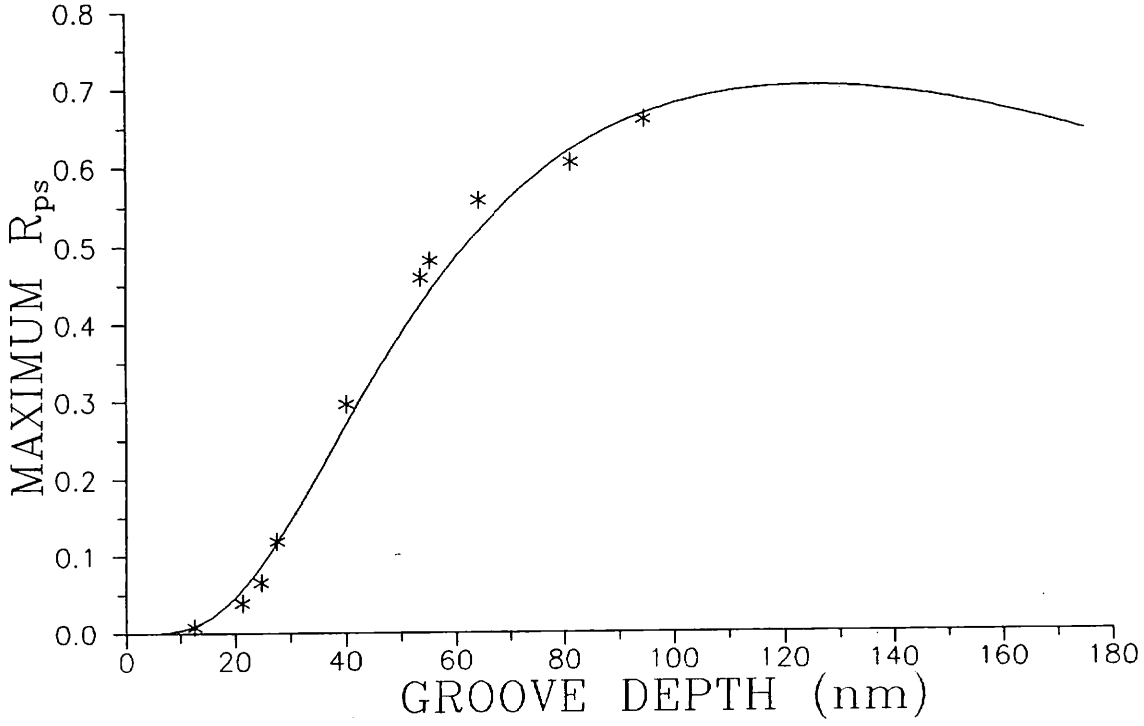

Figure 8.5: Maximum p to s conversion (R_{ps}) at $\phi = 45°$ as a function of groove depth. Points are experimental data and the solid line is calculated from theory.

8.2.3 Dependence of conversion on groove depth and pitch

A batch of 10 photoresist gratings (pitch=842.3nm) were each coated with a thick layer of silver. Reflectivity scans were than taken to find the maximum p to s conversion (at $\phi = 45°$) for each grating. The results are shown as crosses in figure 8.5. The maximum p to s conversion found in these scans was 66.1% obtained from a grating with a groove depth of 94.7nm. The SPP that produced this mixing has a half width which is greatly perturbed by the deep grating and is about 15 times broader than an SPP excited on a shallow ($<$ 10.0nm) grating. The solid line in figure 8.5 is generated from theory using $\epsilon = -15.5 + 0.58i$ (this ϵ was obtained by fitting R_{pp} data taken from one of the gratings used in this experiment). The theory fits the data fairly well and the differences are probably due to the variation in silver parameters which will occur between different evaporations. The theory line has been extended to 175nm and shows that the conversion goes through a maximum of 70.4% at a groove depth of $125nm$. The theory used (differential method) is only accurate for groove depths less than $60nm$ (for this pitch) but it still gives approximate predictions up to $170nm$ and so the existence of an optimum groove depth for p to s conversion is almost certainly a real feature.

It is interesting to know whether conversion efficiency depends only on the ratio of groove depth to pitch or whether each parameter has an independent functional dependance. To answer this, the maximum R_{ps} is calculated for a silver coated grating with a groove depth of $104.8nm$ and a pitch of $1811.4nm$ (again using $\epsilon = -15.5 + 0.58i$ for silver). This grating has a depth to pitch ratio of 0.0579 and gives a maximum p to s conversion of 31.63%. The corresponding depth for a pitch of $842.3nm$ is $48.7nm$ (to give a ratio of 0.0579) and using the solid line in figure 8.5 this produces 37.38% conversion. Hence gratings with a smaller pitch require a smaller depth to pitch ratio to give the same conversion as a coarser grating (using the same coating and wavelength). Note that in all these experiments R_{sp} was found to be the same as R_{ps}.

8.2.4 Dependence of conversion on material parameters

Most metals have a better conductivity at infra red (IR) frequencies than at optical frequencies. This leads to an increase in $\mid \epsilon_r \mid$ compared to ϵ_i. The imaginary part of the propagation wavevector (k_i) of a SPP contains a term $\propto \epsilon_i/{\epsilon_r}^2$ (equation 1.10). Therefore k_i and hence the SPP half width (and loss) decreases for most metals in the IR compared to the visible. This leads to very sharp SPP resonances which should give a bigger p to s conversion.

Figure 8.6 shows R_{pp} and R_{ps} generated for scans at $\phi = 45°$ at a wavelength of $3.391\mu m$ (IR HeNe laser line) for a grating with a pitch of $3.0\mu m$ and a groove depth of $100nm$. A value of $\epsilon = -420 + 68.3i$ (B Dold *et al*, 1965) is used for silver at this wavelength. The SPP is closer to the critical angle compared to the SPP shown in figure 8.2(b) and also has a much smaller half width. A maximum p to s conversion of 16.6% is obtained in this case which shows a definite enhancement compared to the visible (for a grating of a similar depth to pitch ratio).

An analogous curve to figure 8.5 can then be plotted for a range of groove depths with the pitch, wavelength and ϵ as above. This is shown in figure 8.7. This curve does not have an optimum groove depth even though the depth scale

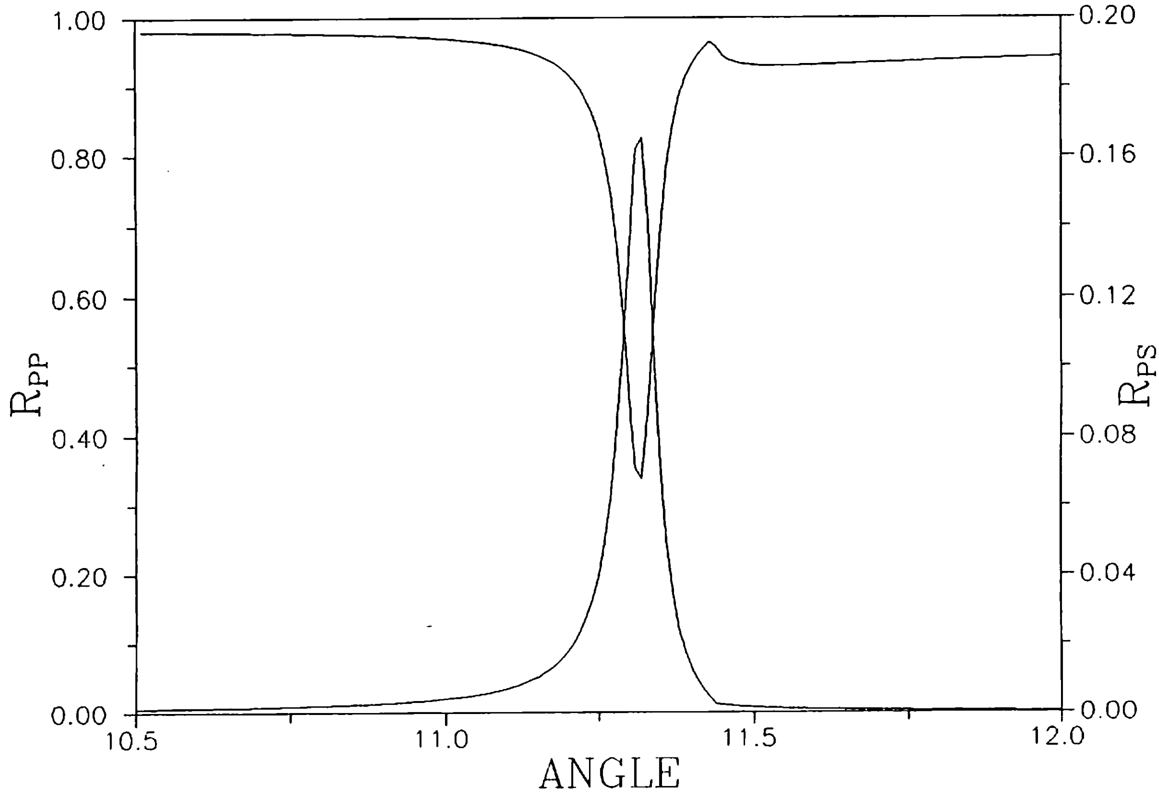

generated reflectivity scans at $\phi = 45$ for a silver coated grating at a wavelength of 3.391μm.

extends as far as in figure 8.5 (in terms of depth to pitch ratio). The maximum conversion in this case is 83.19% which is an increase on the visible case. Perhaps more significant is the fact that the SPP which gives this mixing is at least 5 times narrower than that encountered in the visible. This is an important factor when considering device applications.

8.2.5 Dependence of conversion on wavelength

In the last subsection, we looked at variation of conversion due to changing both the wavelength and the grating parameters. It is also of interest to study a single grating across a range of wavelengths. To do this, a monochromator was used as a radiation source as described in section 3.3.

Figure 8.8 shows typical results taken from a silver coated grating (pitch = 842.3nm) in the wavelength range of 400nm to 800nm. The SPP can be seen

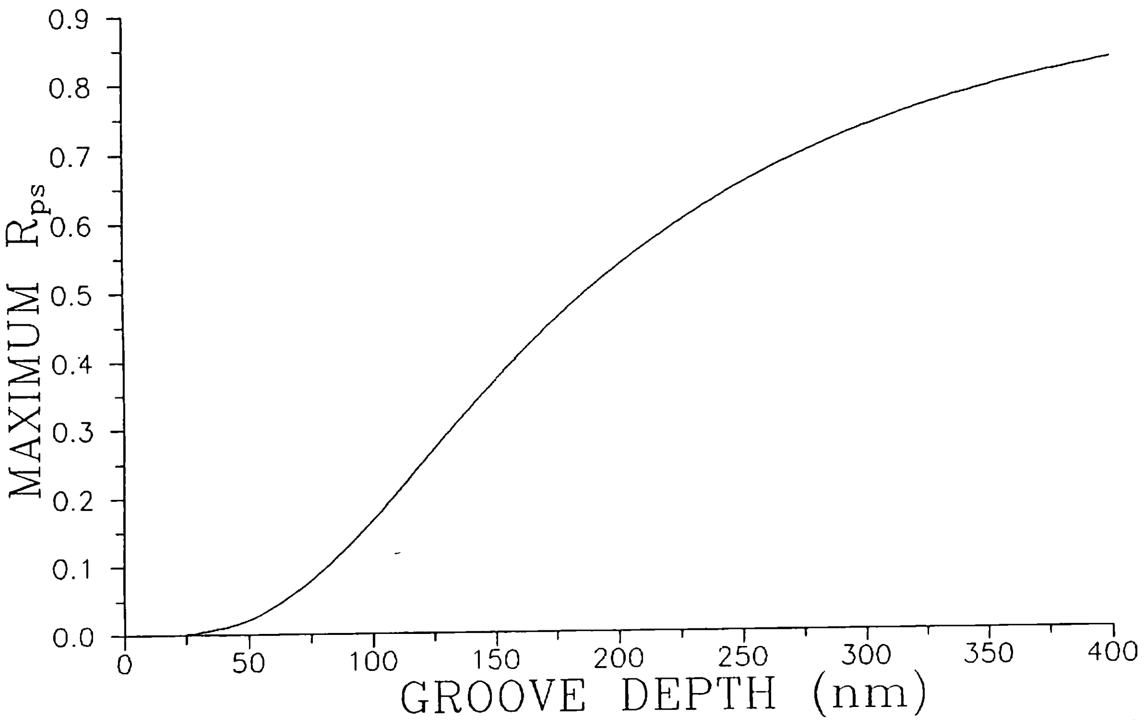

Figure 8.7: Maximum p to s conversion at $\phi = 45^\circ$ as a function of groove depth for a silver coated grating at $\lambda = 3.391\mu m$.

to broaden substantially with decreasing wavelength due to decreasing silver conductivity. It can also be seen that θ_{spp} is dependent on wavelength as described by equation 4.2. The grating pitch was carefully chosen to give SPPs at convenient angles of incidence for the entire wavelength range obtainable with the monochromator.

Results from more detailed experiments are shown in figure 8.9 for two gratings with groove depths of $64.2nm$ and $94.7nm$ (both with a pitch of $842.3nm$). Both sets of data show a decrease in conversion towards $\lambda = 400nm$ as expected. However they also show a decrease towards $800nm$. This is not due to the silver as it has no interband transitions in this region. It is instead dependent on the grating and seems to produce a decrease in efficiency as θ_{spp} moves closer to 0°. When θ_{spp} is close to 0°, a minigap between 2 counterpropagating SPPs is formed (D Heitmann *et al*, 1987) which probably causes the observed decrease in efficiency. The minima at $\sim 560nm$ are again due to the gratings and occur when

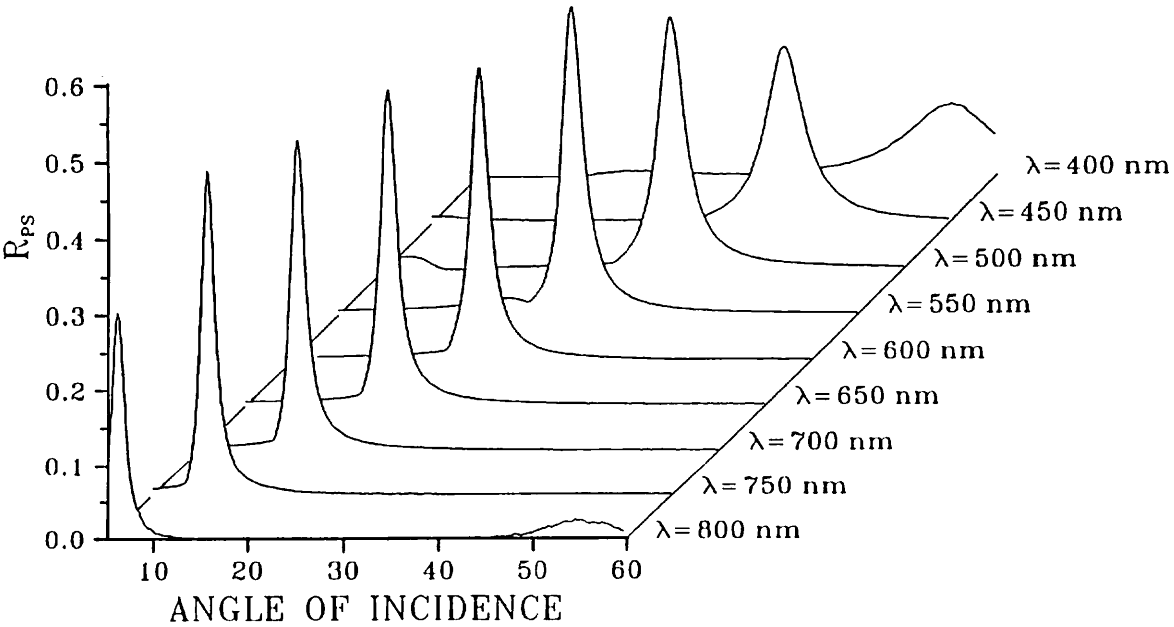

Figure 8.8: p to s conversion as a function of wavelength.

$2\lambda = 3\lambda_g$. No further explanation for this can be given at present as this equality has no geometric significance in this experimental configuration (The data points also show a smaller minima at $\sim 700nm$ when $5\lambda = 4\lambda_g$).

Figure 8.9 has shown that to achieve high conversion efficiency, one must avoid wavelengths (or grating pitches) that give a small θ_{spp} and also minima such as those seen at 560 and $700nm$ should be avoided.

8.2.6 p to s conversion via coupled SPPs

In section 1.5 it was stated that a long range surface plasmon (LRSP) has reduced damping (k_i) compared to a single interface SPP. This is clearly shown in figure 1.5(b). The effect of SPP damping on p to s conversion efficiency has already been discussed and it would seem that the reduced damping of the LRSP would lead to enhanced conversion efficiency.

Figure 8.10 shows R_{ps} data taken from a grating coated with thin silver layers and constructed as shown in figure 5.3 (the grating used has a pitch of $554.5nm$ and a groove depth of $29.0nm$). The data taken with a $42.0nm$ layer of silver (a) shows

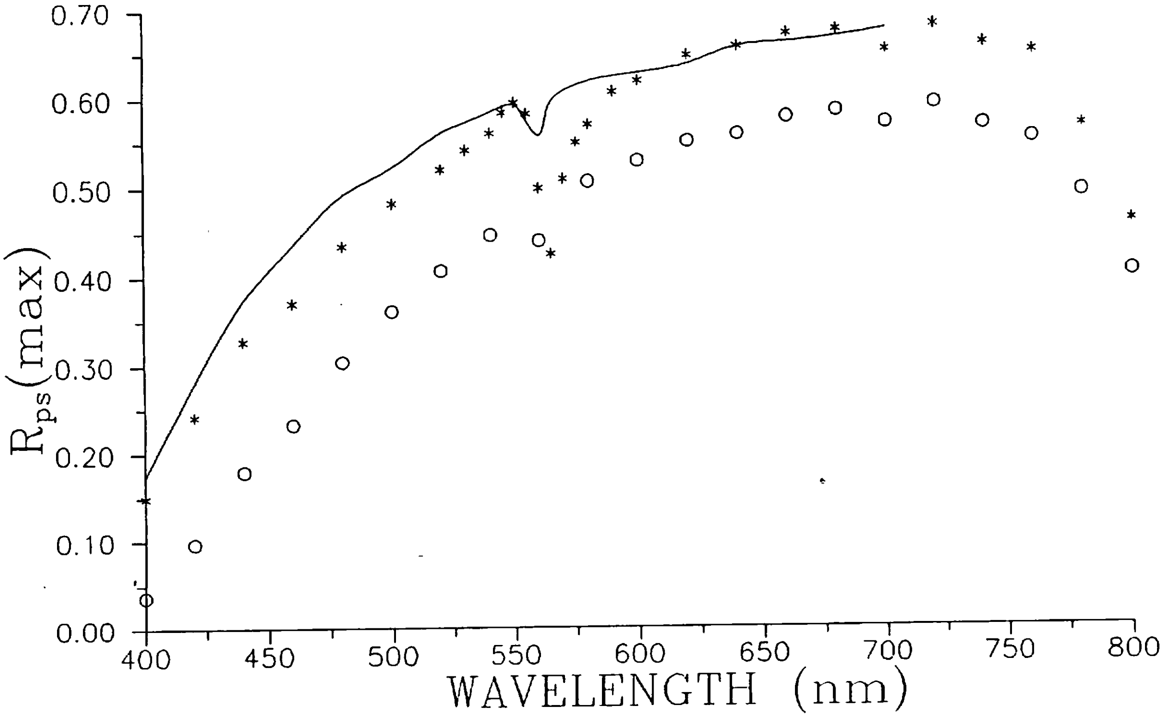

94.7nm (crosses). The solid line is calculated from theory.

a LRSP at 19.23° and a SRSP at 24.73°. The LRSP only produces a conversion of 4.27% and for the 30.0nm silver film (b) this is further reduced to 1.36%. A thick layer of silver (120nm) on the same grating produced 17.96% conversion via a SPP and so instead of enhancing the conversion efficiency, using thin films to excite coupled SPPs has drastically reduced it. This result is probably due to the fact that LRSP modes are not as well coupled to by radiation compared to SPP modes for the same groove depth (as demonstrated in figure 5.2). Also when the metal layer is thin, significant transmission occurs which will cause a reduction in the reflected R_{ps} signal.

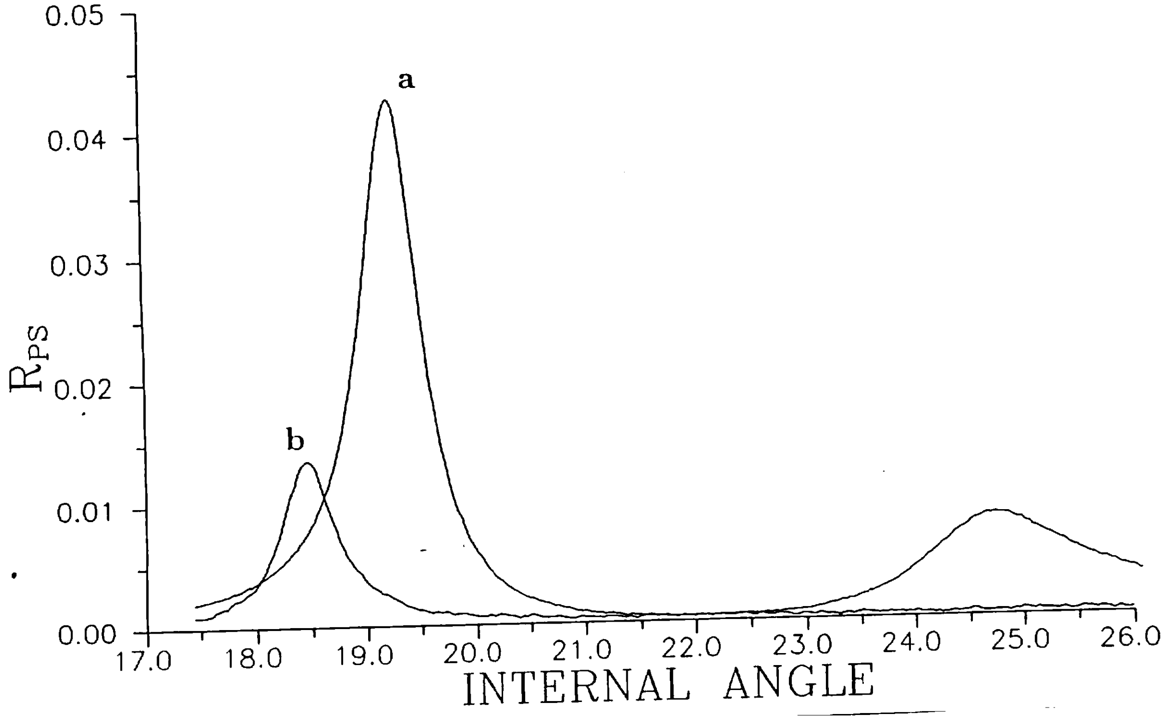

8.3 p to s Conversion via Guided Modes

8.3.1 Introduction

Resonant guided modes may exist in a dielectric layer with a thickness greater than $\sim \lambda/4n$ as discussed in section 1.6. In an air/dielectric/metal system (metal clad waveguide) these modes will almost always propagate with less loss than SPPs as their associated fields are contained mainly in the non-absorbing dielectric rather than the metal. Hence coupling to these modes via a prism or grating will produce reflectivity minima with angular half widths much less than those of SPPs. Guided modes are therefore of interest with respect to p to s conversion.

A guided mode structure may be constructed on a grating by depositing a thick metal film ($> 150nm$) followed by a guiding layer of appropriate thickness. Such guiding layers can be deposited via spinning, thermal evaporation or sputtering (Only the first two were available to us). Spinning of photoresist on a metallised grating was found to give reproducible guided modes but slight absorption in the photoresist caused these modes to be broader than was expected. Thermal evaporation of guiding layers was tried for MgF_2, CaF_2 and Na_3AlF_6 (cryolite). The latter two were found to give porous films which lead to difficulty in fitting theory and they also showed optical anisotropy. MgF_2 evaporation produced fully dense isotropic films and so was used to obtain all the results presented in this section.

8.3.2 Results

The first sample was made by depositing $324.5nm$ of MgF_2 onto a silver coated grating (pitch=$800.8nm$, depth=$20.3nm$). Figure 8.11(a) shows R_{pp} and R_{ss} data taken from this sample at $\phi = 0°$ (with $\lambda = 632.8nm$). The SPP resonance can be seen at 41.4°. It is at a much higher angle than the uncoated silver SPP and hence has a larger propagation wavevector. This is because the evanescent SPP field is decaying into MgF_2 (n=1.38) rather than air (n=1.0003). The mode at 12.98° is the first transverse magnetic (TM_0) guided mode. Probing the sample with s radiation reveals the first transverse electric (TE_0) guided mode at 24.11°. A TE mode will always have a larger propagation wavevector than the corresponding TM mode (in this configuration) due to different phase matching at the dielectric/metal interface. The solid theory line in figure 8.11(a) has been fitted to the R_{pp} data to reveal the optical constants of the waveguide and silver;

$$\epsilon_{wg} = 1.897 + 0.00033i$$

$$\epsilon_{Silver} = -17.12 + 0.683i$$

If this grating is now rotated to $\phi = 45°$ then an R_{ps} scan shows enhanced p to s conversion via the guided modes and the SPP (figure 8.11(b)). Both the TM and TE modes are now excited by p polarised radiation and so are no longer strictly p or s in nature (they are now called mixed modes). At $\phi = 45°$ they give 11.5% and 32.6% conversion respectively, whereas the SPP on this grating gives only 3.3% (a similar value to an SPP on an uncoated grating of this groove depth). R_{sp} scans on this sample shows the same mixing as obtained above.

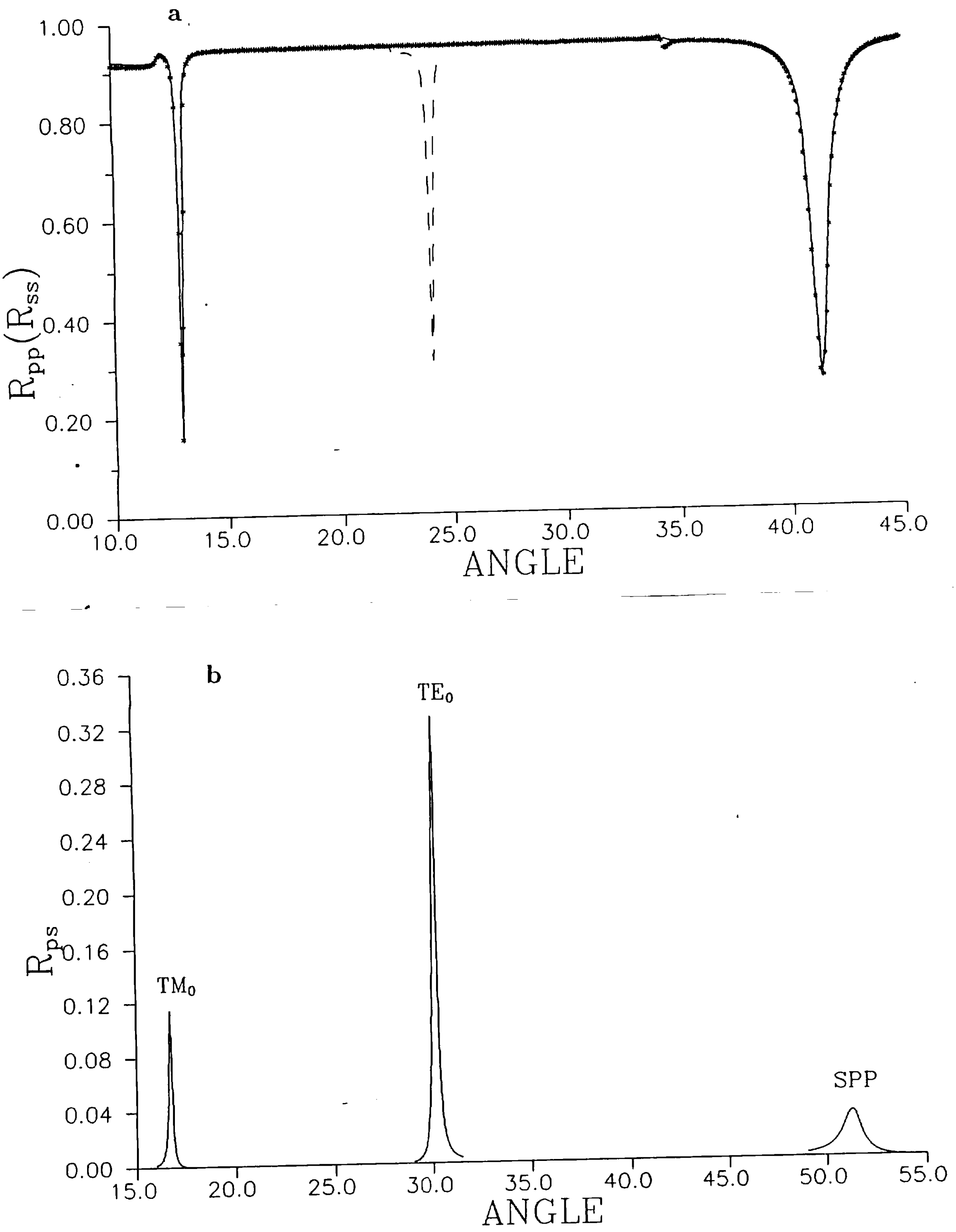

Figure 8.11: (a) R_{pp} and R_{ss} data taken from an air/MgF$_2$/silver waveguide on a grating at $\phi = 0°$. The crosses are R_{pp} data, the solid line is fitted theory and the dashed line is R_{ss} data. (b) R_{ps} data taken at $\phi = 45°$.

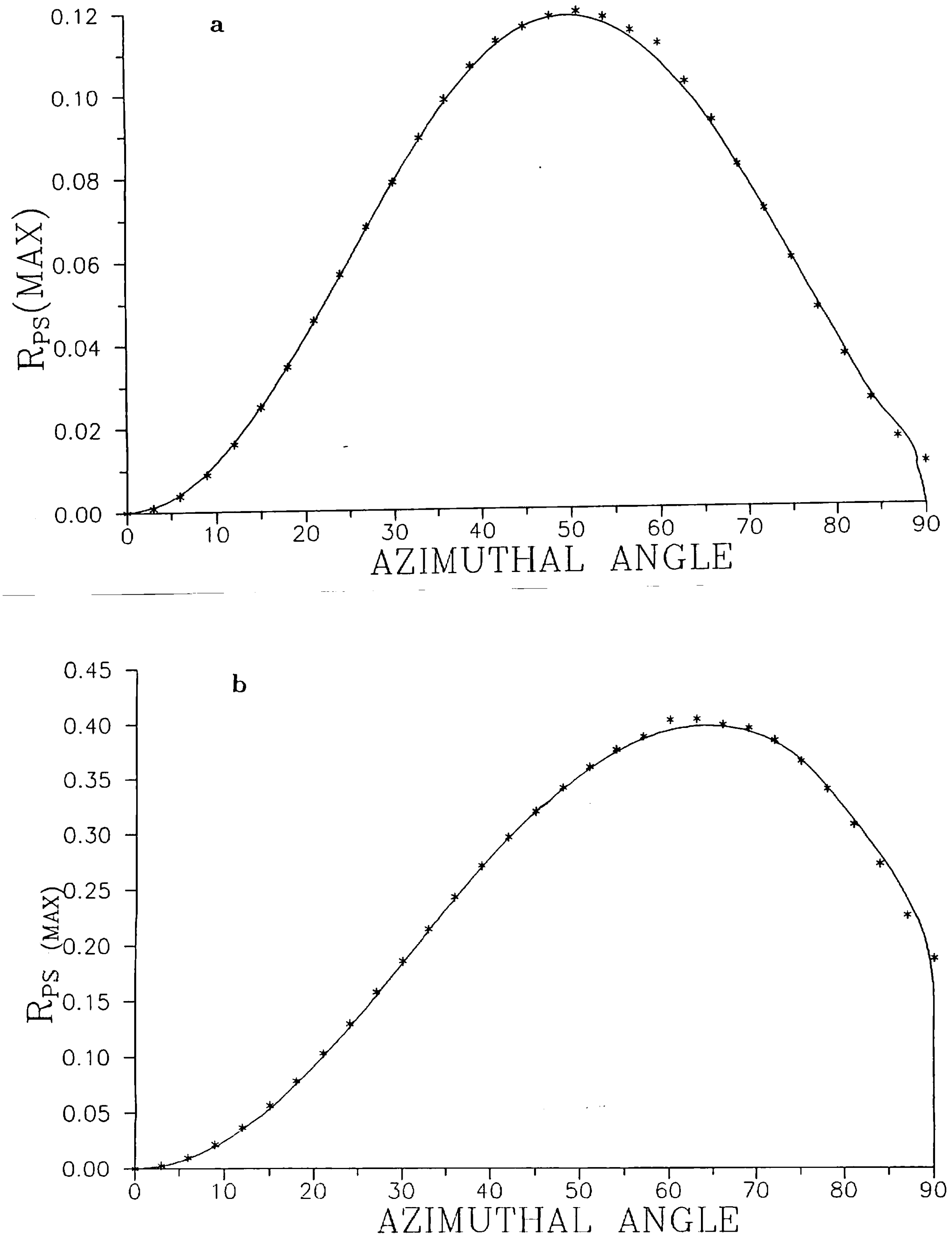

Figure 8.12: p to s conversion as a function of azimuthal angle for (a) the TM_0 mode and (b) the TE_0 mode. Crosses are data and the solid lines are theory.

Figure 8.12 shows the effect of varying ϕ on the conversion efficiency of the two guided modes. These points differ from figure 8.4 (for the SPP) in two important ways. Firstly they do not fall to zero at $\phi = 90°$ and secondly the azimuthal angle found to give maximum conversion is shifted from 45°. The maximum conversion now occurs at $\phi = 49°$ for the TM mode and at $\phi = 64°$ for the TE mode. The azimuthal shift in maximum conversion is curious as both the new angles have no obvious geometric significance. The solid lines in each graph are calculated from theory using the parameters obtained from the fit in figure 8.11(a). These differ from the data as they both fall to zero at $\phi = 90°$. However the theory only drops off sharply between 89.93° and 90° and so zero p to s conversion is never seen in practice due to the laser beam divergence of 0.06° and also the limited accuracy in setting the azimuthal angle (±0.05°). It is perhaps reassuring that the theory does fall to zero at 90° as there would be no explanation for p to s conversion in the absence of any broken symmetry. At $\phi = 90°$, two modes merge to the same excitation angle (see figure 8.13(a)) and in this case each has a half width of $\sim 0.15°$. Therefore the sharp drop in p to s conversion only occurs when these two modes have almost fully merged. This suggests that the effect is due to more than just destructive interference between the modes especially as an R_{pp} scan still shows a well coupled mode at $\phi = 90°$.

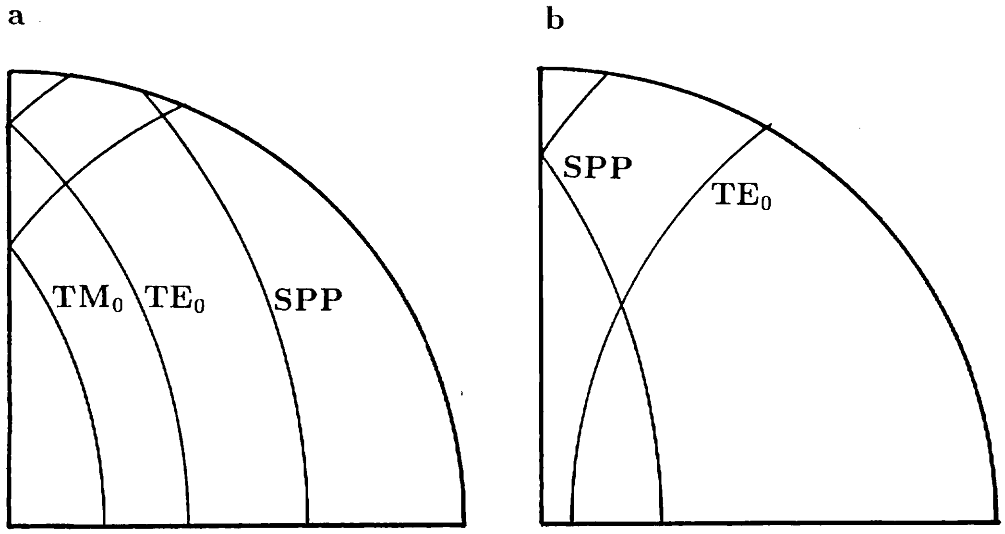

Figure 8.13: k space diagrams for the two samples studied in this section (coated with (a) 324.5nm of MgF_2 and (b) 213.5nm of MgF_2).

The modes studied in the first sample lie on the k space diagram as shown in figure 8.13(a). In this case k_{mode} >G for both the guided modes and the SPP. It is interesting to study the ϕ dependence of a guided mode where k_{mode} <G as shown in figure 8.13(b). This was achieved by evaporating a thinner layer of MgF_2 (213.5nm) onto a silver coated grating with a finer pitch (the one used has a pitch of 551.1nm and a groove depth of 28.0nm). Reflectivity scans were taken from this sample at $\phi = 0°$ for p and s incident radiation as shown in figure 8.14(a).

p incident radiation reveals a SPP resonance at 16.14° and a 'critical angle' at 8.50°. The latter is the reverse sense to those seen previously as it is now due to a diffracted beam 'passing on' (or changing from an evanescent to a propagating beam. An R_{ss} scan shows the TE_0 guided mode at 3.75°. The p to s conversion from this TE_0 was measured as a function of ϕ as shown in figure 8.14(b). In this case the data points and the theory line show good agreement for all ϕ. The maximum azimuthal angle for the existence of this mode is ~ 70° as shown in figure 8.13(b) hence the p to s conversion can only be measured for this limited range. The data shows a maximum conversion of 30.4% at $\phi = 42°$ i.e. the maximum now occurs at $\phi < 45°$ (as opposed to the modes shown earlier which peaked at $\phi > 45°$). Again this angle has no obvious geometric significance. It is surprising that this TE mode gives less mixing than the TE mode on the first sample as this mode is excited on a deeper grating with a smaller pitch. This suggests that guided mode conversion is also dependent on its propagation wavevector magnitude i.e. its k space separation from the critical angle. The TE mode on this second sample has a wavevector of 1.083k whereas the same mode on the first sample has a wavevector of 1.198k. Therefore p to s conversion via a guided mode appears to increase with mode wavevector.

Further experiments were carried out to test the dependence of guided mode conversion on groove depth. Two gratings (pitch= 800.8nm, groove depths = 40.4nm, 64.2nm) were coated with silver followed by 324.5nm of MgF_2. These gave modes similar to those shown in figure 8.11(a) i.e. a TM_0 mode, a TE_0 mode and a SPP. The p to s conversion from these modes was then measured at $\phi = 45°$ for each grating. Table 8.1 shows the p to s conversion results from all three gratings with the only variable being the grating groove depth (the guiding layer thickness and ϵ were approximately the same for each sample). For all three gratings, the guided modes both show higher conversion than the SPP. The biggest

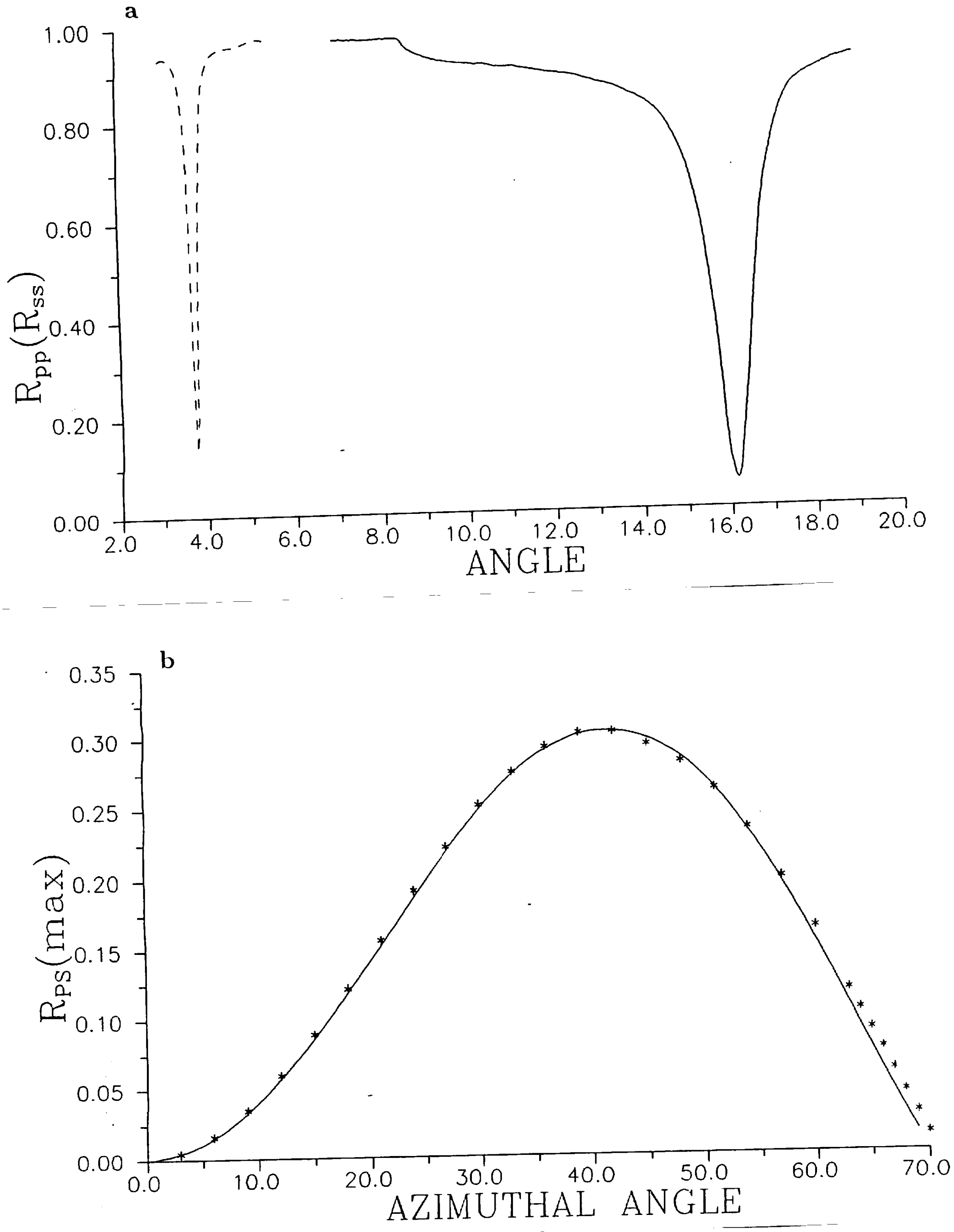

Figure 8.14: (a) R_{pp} (solid line) and R_{ss} (dashed line) scans taken from a silver coated grating with a 213.5nm overlayer of MgF$_2$. (b) p to s conversion as a function of ϕ for the TE$_0$ mode on this grating.

difference is for the shallowest grating where the TE$_0$ mode gives 9.9 times the conversion of the SPP. For the deepest grating the SPP conversion is diminished compared to the uncoated silver case and the TE$_0$ mode conversion seems to have almost saturated as it only shows an increase in $R_{ps}(\text{max})$ of 0.063 compared to the $40.4nm$ grating. If the conversion of this mode at $\phi = 45°$ is extrapolated using figure 8.12(b) then a maximum conversion of $\sim$ 71% is predicted at $\phi = 64°$.

Table 8.1: p to s conversion at $\phi = 45°$.

GROOVE DEPTH (nm)	TM_0	TE_0	SPP
20.3	0.115	0.326	0.033
40.4	0.359	0.496	0.159
64.2	0.508	0.559	0.277

8.3.3 Dependence of p to s conversion on material parameters

We now look at the effect of varying parameters associated with the guided mode configuration in a similar way to section 8.2.5 (for SPPs). The two parameters that have the largest effect on conversion efficiency are ϵ_{iwg} and $\epsilon_{isilver}$. The effect of varying these is shown in figure 8.15(a) and figure 8.15(b) respectively. The mode studied here is the TE$_0$ mode shown in figure 8.11(a) with azimuthal angle set at $\phi = 45°$ (all other parameters are as before). Figure 8.15(a) shoes the effect of setting ϵ_{iwg} to 0.00, 0.00001, 0.0001, 0.001, 0.01. The difference between a perfectly non-absorbing film ($\epsilon_i = 0.00$) and a film with very small absorption ($\epsilon_i = 0.00001$) is negligible but a further increase in ϵ_i causes a significant decrease in conversion efficiency. Thermally evaporated dielectrics typically have ϵ_i values which range from 0.0001 to 0.001 which for this mode give conversions of 34.5% and 22.5% respectively (in the first experimental sample an ϵ_{iwg} of 0.0003 gave a conversion of 32.6%). Using sputtering to deposit dielectric films such as SiO$_2$ can

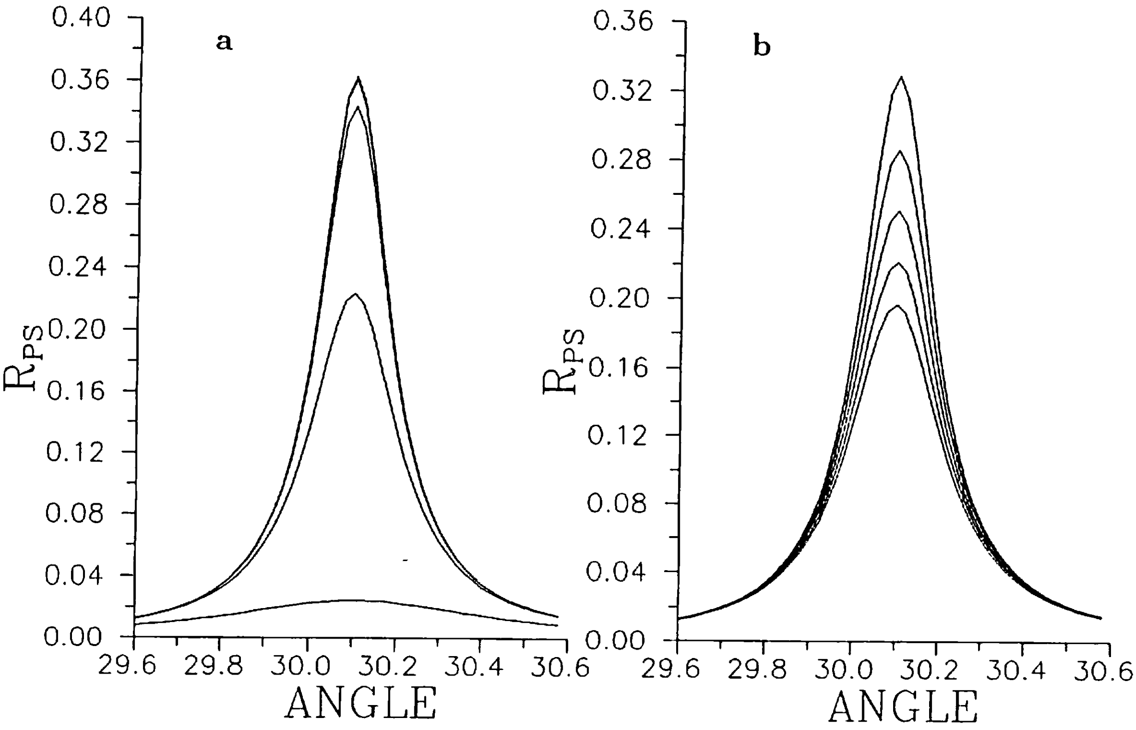

Figure 8.15: p to s conversion via a TE guided mode showing the effect of varying (a) ϵ_{iwg} and (b) $\epsilon_{isilver}$.

give $\epsilon_i < 0.0001$ which would give a conversion of $\sim 35\%$ i.e. using sputtered films only gives a small improvement over thermally evaporated films. In figure 8.15(b) the effect on the mode of varying ϵ_i of the metal layer is shown. This parameter is varied from 0.1 to 0.9 in steps of 0.2 (with ϵ_{iwg} fixed at 0.001). This variation of ϵ_i (while keeping ϵ_r fixed) is equivalent to varying the metal absorption which occurs for all metals when the wavelength is varied. When $\epsilon_i = 0.7$ a conversion maximum of 22.1% is calculated whereas with $\epsilon_i = 0.1$ this is increased to 33.0% i.e. a metal clad waveguide at IR wavelengths may produce 1.5 times more p to s conversion than a similar structure in the visible (but the actual conversion obtained will also depend on waveguide thickness).

The experiment on the deepest grating in the last subsection predicted a maximum conversion of 71% and it would seem possible with the above arguments that a sample could be optimised to give nearly 100% conversion via a guided mode in the infra-red.

8.4 Summary

In this chapter the newly discovered effect of p to s conversion via optical modes has been studied in detail both experimentally and theoretically. In section 8.2 we studied p to s conversion via SPPs and showed that maximum conversion occurs when the grating is orientated at $\phi = 45°$. A maximum conversion efficiency of 66% was found experimentally and theory showed that in the IR a sample may produce up to $\sim$ 83% conversion. LRSPs were found to give disappointingly low conversion which was explained in terms of coupling efficiency to these modes and the existence of significant transmission. Section 8.3 showed that resonant guided modes are the best optical modes for producing p to s conversion. The optimum azimuthal angle for these modes is found to be dependent on the mode wavevector and occurred at angles both above and below that found for the SPP. The conversion efficiency via guided modes was found to be enhanced compared to the SPP especially for shallow gratings.

In the next chapter it is shown that scanning a p to s conversion maximum rather than a reflectivity minimum has many advantages with respect to device applications.

Chapter 9

Applications of p to s Conversion

9.1 Introduction

The electric field associated with a SPP resonance decays away from the surface with a typical decay length of a few hundred nanometers into air. The SPP is therefore very sensitive to changes occurring close to the metal surface and it is this property that has been exploited in SPP gas sensors and biosensors.

In this chapter a new SPP technique for SPP sensing is described which is based on the detection of a resonance maximum (via p to s conversion) instead of the traditionally used SPP minimum. This detection of a large signal on a weak background yields a far improved signal to noise ratio over measurement of a resonant minimum on a strong background signal. It also allows wavelength dispersive detection which has advantages over angular dispersive detection with respect to remote gas sensing. This new technique can also be applied to gas sensing via guided modes which are sensitive to both refractive index change and thickness change in the guiding layer.

Much work has been previously carried out by detecting resonant mode minima. K Matsubara *et al* (1988) used a prism coupled SPP to detect ethanol dissolved in water (in direct contact with the metal layer). They found a limiting sensitivity of 1 part in 10^4 ethanol by weight. C Nylander *et al* (1982) coated a silver surface with a thin layer ($40.0nm$) of silicon glycol copolymer and used a prism coupled SPP to detect halothane gas absorption into this thin layer. The minimum concentration of this gas that could be detected was found to be 10ppm (in N_2) and it was concluded that the limiting factor on sensitivity was the signal to noise ratio of the photodetecter. B Liedburg *et al* (1983) demonstrated that a SPP resonance may be used for biosensing. They coated silver with a monolayer ($\sim 5.0nm$) of an antibody called human γ-globulin. When a weak solution of antihuman γ-globulin was entered into the cell antibodies were found to bind to the monolayer. This binding was irreversible and specific i.e. the antigen-antibody reaction does not occur significantly for unrelated antibodies. A measurable shift was recorded for an antibody concentration as low as 20ppm (in water). Another reaction was also studied in which the binding was found to be reversible. W Lukosz *et al* (1988) examined waveguide sensitivity and concluded that changes in thickness of $0.04nm$ or changes in refractive index of 2×10^{-5} can be measured for monomode waveguides provided that the guide refractive index is much larger than the substrate refractive index.

9.2 Sensing via p to s Conversion

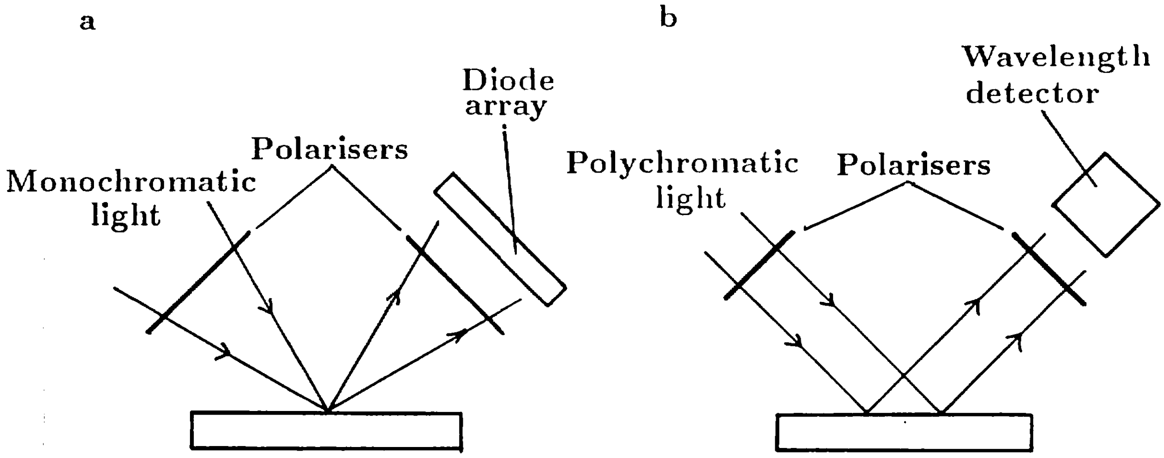

Figure 9.1: Experimental configurations for (a) angular dispersive measurements and (b) wavelength dispersive measurements.

As mentioned earlier p to s conversion allows angular dispersive or wavelength dispersive measurements to be made. These are shown schematically in figure 9.1. In the former case (figure 9.1(a)) a monochromatic beam from a laser is expanded and then focussed through a polariser onto the metallised grating surface. The range of angles in this beam is chosen to include a SPP resonance, so that after passing through a second polariser (set to be crossed with respect to the first) the beam consists only of light converted by the excitation of the SPP. The position (hence angle) of the SPP peak is then measured by a linear diode array. Any change in SPP environment will cause the peak reflectivity to shift to a different pixel on the array. The second configuration (figure 9.1(b)) uses a parallel polychromatic light source (eg. an LED). This time the reflected beam after passing through the second polariser contains a small spread of wavelengths due to SPP conversion. The mean wavelength in this beam is then detected with a wavelength detector. For a fixed input angle, a change in SPP environment will now cause a change in peak wavelength of the reflected beam. Hence the two methods show that changes in the SPP wavevector can be detected as either angle changes or wavelength changes as is clear from equation 4.1.

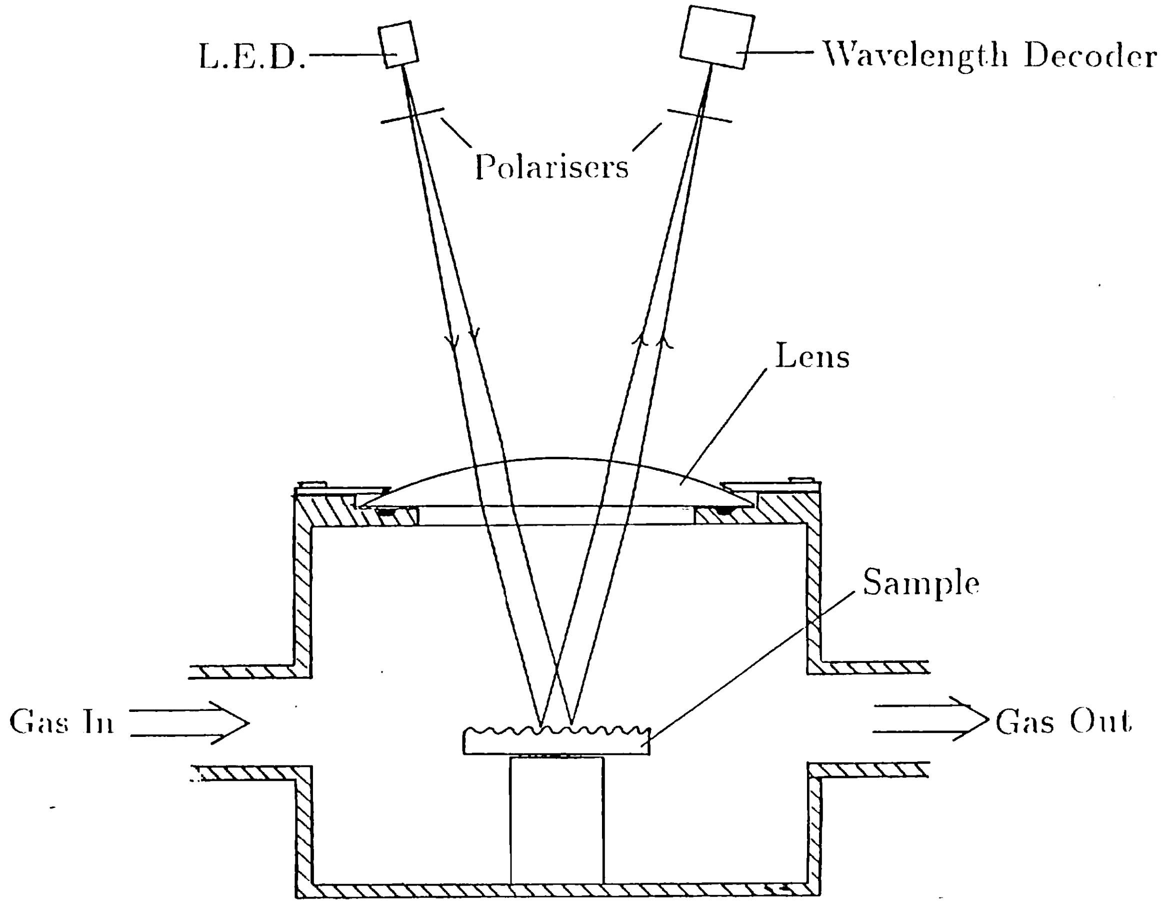

Figure 9.2: A prototype gas sensor employing p to s conversion.

A prototype gas sensor employing p to s conversion was constructed as shown in figure 9.2. The purpose of this experiment was to test that the principle worked, and in this case we merely examined condensation of isopropyl alcohol (IPA) onto a silver coated grating. A red LED is used as the light source which produced radiation in the range of $600 - 700nm$ (it was slightly modified to give a point source of light). The focussing lens also acts as a chamber window and collimates the light from the LED. After reflection from the sample the light passes back out of the chamber through a second polariser and into a wavelength detector. Conventional spectroscopic methods for wavelength detection tend to be bulky, expensive and provide more information than is really necessary for the present application. In this case we merely need to know the centre of gravity of the wavelength spectrum. This can be achieved by using a pair of photodiodes which have different spectral responses. We used a wavelength detector made by Plessey for NPL (see MC Hutley *et al*, 1986). It has an output which varies monotonically between 0 and 2.5V as the wavelength varies between $600nm$ and $1\mu m$. The device is fairly insensitive to input intensity when used in the range of 100nW to 10μW (radiation power) and typically a factor of 30 change in the intensity causes a 1% change in output. The grating sample shown in figure 9.2 is orientated at $\phi = 45°$ to give maximum p to s conversion.

The sample chamber was initially evacuated to a pressure of ~1 Pa and then slowly returned to room pressure. During this procedure no change in output was measured from the wavelength decoder. This showed that o-ring compression below the lens was not realigning the input beam. The chamber was then evacuated once more and then isolated from the pumping system. IPA was carefully injected into the chamber via a needle valve while the wavelength decoder output was being monitored. Figure 9.2 shows a typical trace of detector output verses time. When the inlet valve is opened IPA is condensed on the grating surface and causes a rise in output. Pumping on the chamber now causes the IPA to evaporate from the surface causing the detector output to drop back to its original value. During this cycle, the chamber pressure did not rise above ~ 100Pa. Further experiments have shown that this system can detect wavelength changes as small as $\sim 0.1nm$ which corresponds to an IPA overlayer less than one monolayer thick. However it will be possible to detect much smaller wavelength shifts using better electronics and more rigid apparatus. Experiments using different sample layers are presently

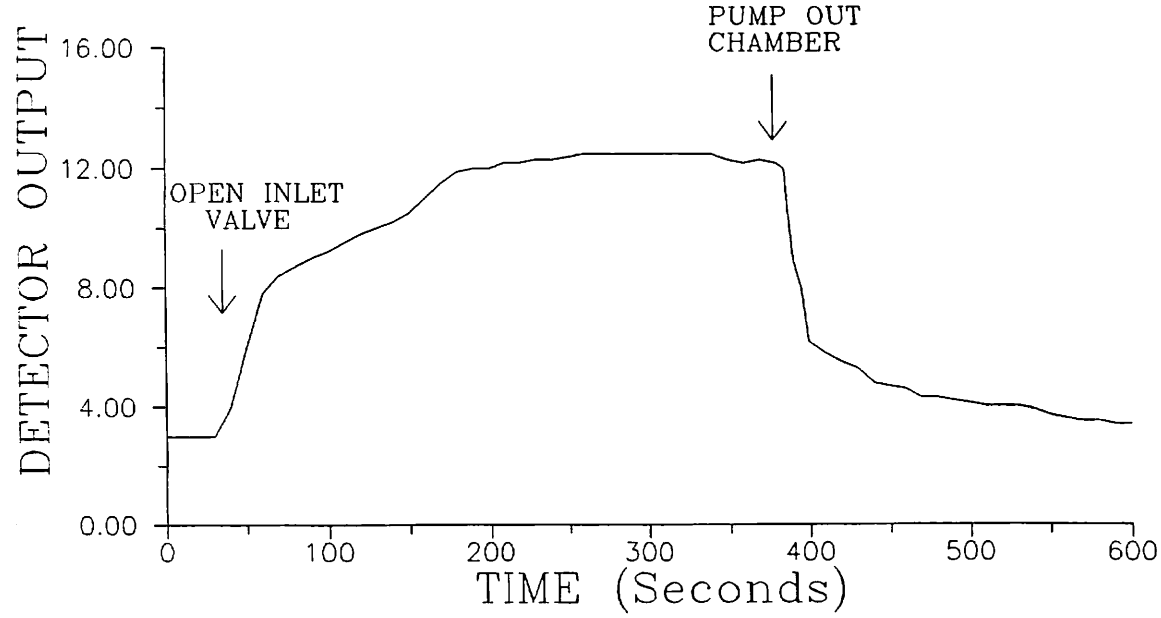

Figure 9.3: Experimental data showing wavelength decoder output verses time during condensation and evaporation of IPA on silver.

being carried out.

To demonstrate typical sensitivities of SPPs and guided modes to changes in environment a few calculations were carried out. In the first we take a silver coated grating at $\lambda = 632.8nm$ (groove depth=$25.4nm$, pitch=$800.8nm$) and scan angle with $\phi = 45°$ as shown in figure 9.4. The effect of adding very thin overlayers of IPA (n=1.37) on the silver surface can clearly be seen. (A scan of wavelength at constant angle would give a similar graph). For a $1.0nm$ thick overlayer, the SPP has shifted from 17.93° to 18.03°. It is of interest to link this result with the wavelength dispersive experiment shown earlier. A 0.1° shift in angle in figure 9.4 is equivalent to a $1.36nm$ shift in wavelength using the wavelength dispersive experiment. The limit on sensitivity so far found is $0.1nm$ and therefore using the wavelength experiment we can presently measure wavelength shifts corresponding to angle shifts of 0.007°. Using the results in figure 9.4, the thinnest layer of IPA that may presently be detected with the wavelength dispersive experiment is therefore $0.07nm$ (less than 1 monolayer).

If the silver is now coated with a thin non absorbing dielectric, for example a

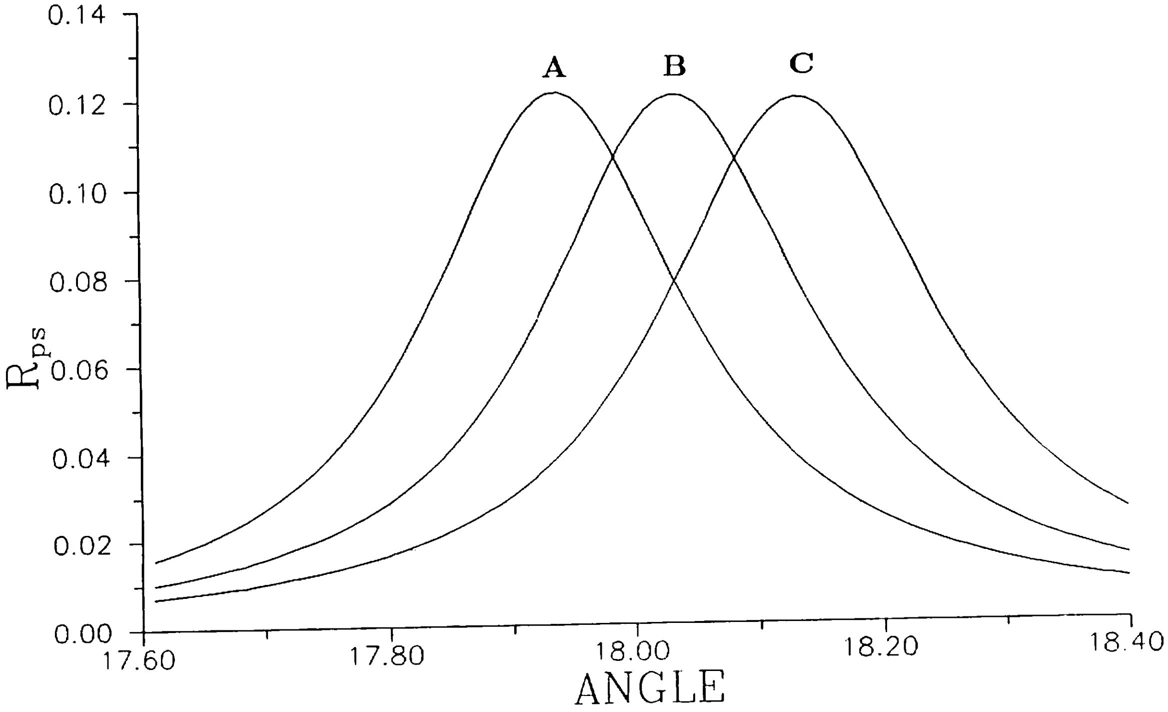

Figure 9.4: Theoretically generated reflectivity scans showing the effect on the SPP of adding very thin IPA overlayers: A, bare silver; B, 1.0*nm* IPA overlayer; C, 2.0*nm* IPA overlayer.

5.0*nm* layer with n=1.38, then the SPP should now be sensitive to both changes in thickness and n of this layer. The smallest thickness change that can be detected is still ~ 0.07*nm* but the smallest index change is 0.008. The latter is disappointingly insensitive and shows that any chemical being absorbed in a thin overlayer must change the layer thickness in order to be well detected using SPPs. To achieve good sensitivity to changes in refractive index, one must use much thicker layers which have the added advantage of being able to support guided modes.

Figure 9.5(a) shows the effect on a TE_0 mode of changing the refractive index of a 600*nm* thick waveguide by steps of 0.004 (the waveguide has n=1.38 initially and is on a silver coated grating with a groove depth of 20.0*nm* and a pitch of 800.8*nm*). A change in index from 1.380 to 1.384 causes the mode to shift from 38.814° to 39.145° (a shift of 0.271°) hence an angle shift of 0.007° corresponds to an index change of $\sim 8.5 \times 10^{-5}$. The waveguide parameters are by no means

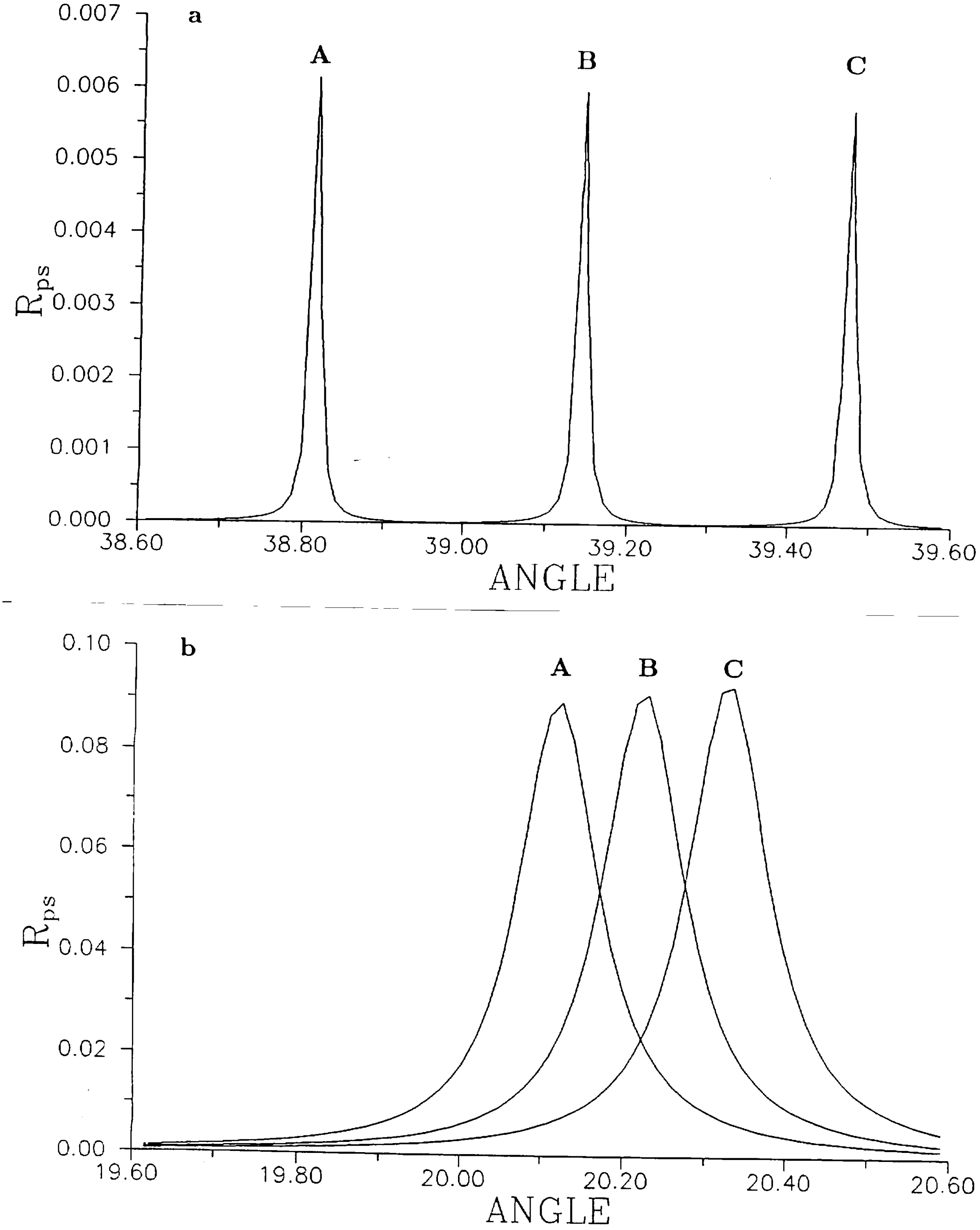

Figure 9.5: Theoretically generated reflectivity curves showing the effect on a TE_0 mode of (a) varying the guide index (A, 1.380; B, 1.384; C, 1.388) and (b) varying the guide thickness (A, 200*nm*; B, 201*nm*; C, 202*nm*).

optimised and yet this guide shows a sensitivity 94 times larger than that found earlier using the SPP. The sensitivity found here (8.5×10^{-5}) is similar to the value found by W Lukosz *et al* for dielectric clad waveguides. Changing the waveguide thickness also has a large effect on mode angle. Figure 9.5(b) shows a TE_0 excited in a $200nm$ waveguide (n=1.38) on the same silver coated grating as above. When the thickness is increased from $200nm$ to $201nm$ the mode position shifts from 20.12° to 20.22° (a shift of 0.10°), hence an angle shift of 0.007° corresponds to a thickness change of $0.07nm$. This sensitivity to thickness is the same as that found earlier for a thin overlayer detected via a SPP. The TE_0 modes in figure 9.5(a, b) have wavevectors of $1.311k$ and $1.061k$ respectively because the waveguide thickness is different. These thicknesses have been chosen because guided modes with large wavevectors are more sensitive to index change and those with small wavevectors are more sensitive to thickness change. In fact for a guided mode there are two different optimum thicknesses for maximum sensitivity to index change and thickness change (W Lukosz *et al*, 1988).

To summarise, sensing using optical modes has many advantages over other techniques. It offers in situ measurement, non destructive sensing, no moving parts, instantaneous response and good sensitivity. In addition to these, using p to s conversion via gratings gives an enhanced signal to noise ratio and allows wavelength dispersive detection which has a few advantages over angular dispersive detection. Detecting wavelength leads to an experimental configuration which is much cheaper than angle detection, is much easier to miniaturize and is much more applicable to remote sensing because only one optic fibre is needed to receive the reflected colour.

The smallest detectable wavelength shift using p to s conversion and wavelength detection $(0.1nm)$ has been converted to an angle shift to allow limits of sensitivity to be calculated for various configurations. Better apparatus will allow detection of much smaller wavelength shifts (by a factor of maybe 100) and so increase the quoted sensitivities by two orders of magnitude.

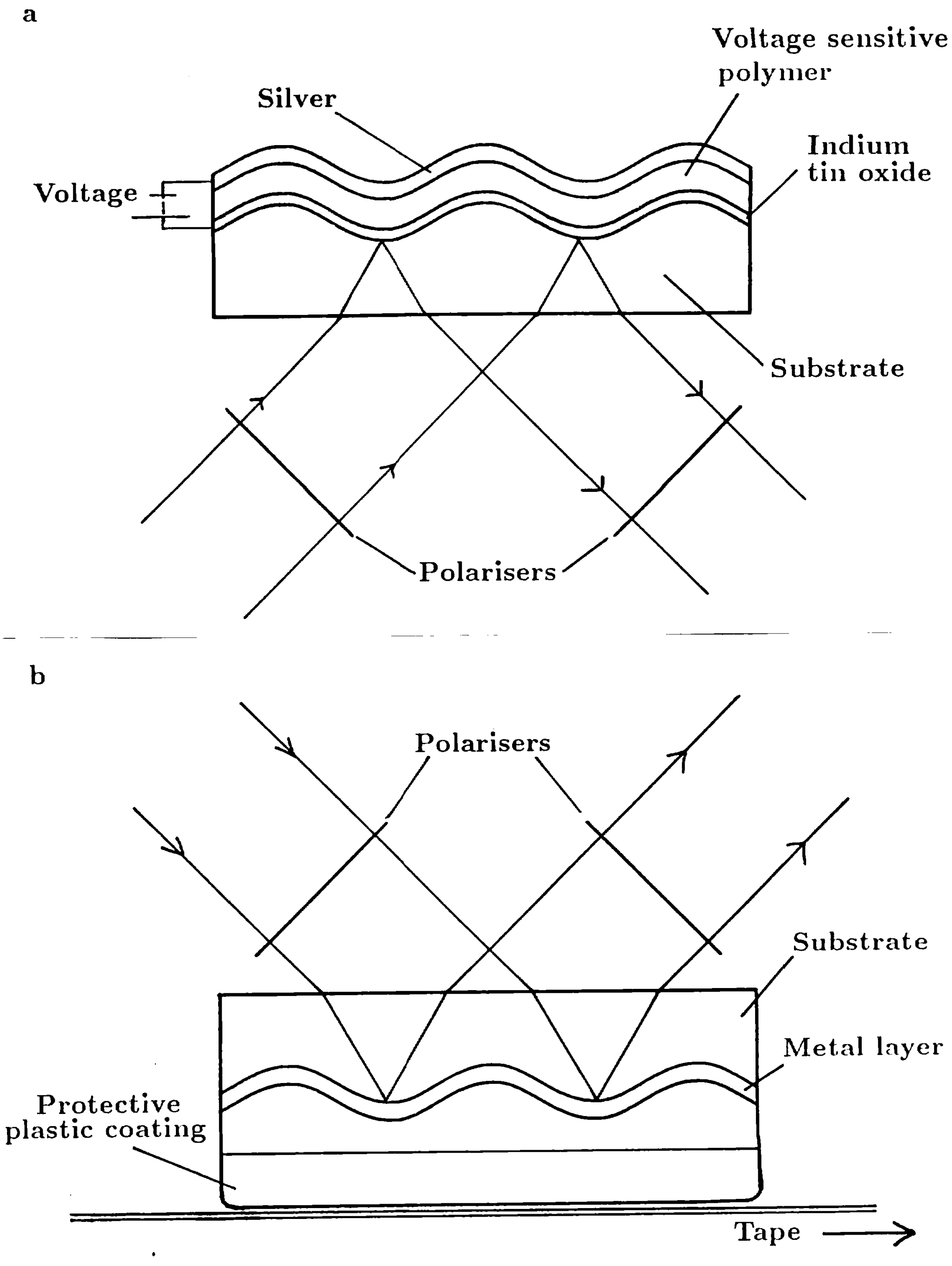

Figure 9.6: Two other applications of p to s conversion; (a) a tunable monochromator (b) an optical decoder of magnetic information.

9.3 Other Applications

Other than gas sensing, p to s conversion has a few other potential applications. Two of these are shown in figure 9.6. The first is a tunable monochromator; a grating is coated with a thin layer of indium tin oxide (transparent conducting layer), followed by a voltage sensitive polymer and finally an opaque layer of silver. As long as the polymer has a refractive index higher than the grating substrate then it may support guided modes. If a parallel polychromatic beam is incident on the sample (at $\phi = 45°$), then the reflected beam after passing through the second polariser will only contain wavelengths converted by the guided modes. Altering the voltage across the polymer will change its refractive index and hence the wavevectors of allowed guided modes. This causes the output to change wavelength and so act as a tunable monochromator. Throughput efficiencies of 60% should be achievable with resolution limited only by beam divergence and guided mode half width. Experiments are currently being carried out using a liquid crystal instead of a voltage sensitive polymer.

The second potential application is an optical reader for magnetically stored information (shown in figure 9.6(b)). A grating substrate is coated with a thin metal layer followed by a matching dielectric and finally a protective dielectric coating. Either the metal layer or the matching dielectric needs to be magnetically active so that the movement of the magnetic tape causes a change in optical properties. This change perturbs the LRSP (or LRSEP) on the metal layer and so changes the wavelength of the output (via p to s conversion). Hence magnetic information in the tape is converted to a wavelength modulation (or an angle modulation if required). The sensitivity of such a device is at present unknown but if highly magnetically active materials can be found then this very useful device will work well.

9.4 Summary

In this chapter the use of p to s conversion for gas sensing has been discussed. The new configurations give improved signal to noise compared to previous detection methods involving detection of resonant minima. The present limits on sensitivity predict detection of a thickness change of 0.07nm (using a SPP) and a refractive index change of 8.5×10^{-5} (using a guided mode with a large wavevector). Better apparatus should allow an improvement of maybe two orders of magnitude. Two other applications of p to s conversion have been outlined and these are currently receiving attention.

The new experimental configurations discussed in section 9.2 and 9.3 are the subject of a patent (JR Sambles and GP Bryan-Brown, No. 8916764.7) which was filed with the assistance of BTG.

Chapter 10

Conclusions

10.1 Summary of Thesis

The aims of the work presented in this thesis have been twofold. Firstly to use optical modes to characterise polycrystalline metal films and secondly to study the optical modes themselves. In chapter 4 it was shown that grating coupled SPPs were as reliable as prism coupled SPPs in the determination of the optical constants of Ag, Al and Au. Difficulties in fitting data from deep gratings prompted the use of a distorted sine wave profile as a description of the grating surface. This new profile was found to model the nonlinearity in photoresist sensitivity far more accurately than previously used models.

In chapter 5 it has been shown for the first time that coupled surface plasmons on gratings may be fitted accurately by theory to reveal the optical constants of thin silver films. Islandisation of very thin silver films lead to a deviation in optical constants from the thick film (bulk) values and explained why earlier studies had failed to show good theoretical agreement with data. In chapter 6 both prism coupling and grating coupling were used to show that highly absorbing chromium films could support a long range coupled mode, the LRSEP. Theoretical fitting to prism data revealed that the optical constants of chromium were dependent on film thickness. A comparison of fitted prism results and fitted grating results suggest that the optical constants and hence film quality are very sensitive to the quality of substrate used. Results using the grating configuration also show that the LRSEP is very sensitive to changes in index of one of the bounding media. In chapter 7, thin palladium films were also shown to support a long range coupled mode. Fitting of theory to these resonances revealed the optical constants of Pd at 632.8nm and resistivity measurements were also carried out as a further indication of film quality. The resistivity of our Pd films was compared to previous results for annealed Pd films and suggested that all our films were porous with a level of of porosity that increased with decreasing film thickness. The optical constants obtained for all the Pd films were found to be significantly different from previous results. However the trends in ϵ_r and ϵ_i were explained qualitatively in terms of effective medium theories. These implied that the film porosity was increasing with decreasing film thickness and hence backed up the deductions made from resistivity measurements.

In chapter 8, the newly discovered phenomenon of p to s conversion via optical modes was studied in detail for SPPs, LRSPs and resonant guided modes. Data was compared to theory which had been extended (chapter 2) to the regime of conical diffraction. Conversion via SPPs was found to reach efficiencies as high as 66% which is at least 10^4 times larger than the off-resonance value. LRSPs showed disappointingly small conversion which was attributed to finite transmission and a reduction in coupling efficiency. Resonant guided modes were found to produce higher conversion efficiencies than SPPs especially for shallow gratings and theoretical modelling suggested that efficiencies close to 100% could be achieved using a suitable waveguide at infra-red wavelengths.

Chapter 9 discussed the applications of p to s conversion to gas sensing and showed results from a prototype configuration. The novel detection of a resonance maximum instead of a minimum enhanced the signal to noise and so allowed detection of submonolayers of condensed liquid using a very simple (and inexpensive) set up. Theoretical modelling was used to find out which configurations would be best suited for detection of thickness change and/or refractive index change. Two other applications of p to s conversion were also briefly mentioned.

The application of grating-coupled modes to nonlinear optics is discussed in appendix A for various sample configurations.

10.2 Future Work

The use of grating-coupled SPPs to characterise metal films (chapter 4) can be extended to study a wide range of interesting materials. Sodium, for example, is a very free electron like metal and could be studied by melting Na onto the grating substrate in a vacuum and then recording the substrate/sodium SPP (on an interface which is protected from oxidation). This method could also be used to study lithium, potassium, gallium and even mercury (at suitable wavelengths). Chapter 4 also shows that fitting theory to SPP resonances is an excellent method of accurately determining the grating groove depth and profile. Well defined microscopic surface standards are currently in high demand for calibration of Talysteps, scanning electron microscopes, scanning tunneling microscopes and optical tunneling microscopes. Hence gratings are currently being characterised for this purpose.

Chapters 5, 6 and 7 have shown that long range coupled modes may be used in the characterisation of three very different metals. By using suitable wavelength sources this technique can be applied to a very wide range of metals and also excitonic dielectrics which exhibit very interesting dispersion. The effect on thin films of deposition temperature, deposition rate and annealing can also be studied accurately using this method. The experiments on Pd also pose the interesting question of how thin a metal film can be before it can no longer support a mode. Reflectivity scans carried out on ultra thin films of a low absorbing metal (deposited by molecular beam deposition) could perhaps show an optical mode on a film as thin as $2nm$ i.e. a few molecules thick.

The precise origin of p to s conversion is still unknown and detailed modelling of field profiles and power flow distributions is probably required to produce a full picture of the photon processes that occur on the grating surface. The azimuthal dependance of guided mode conversion along with the minima found in the conversion verses wavelength experiments do not appear to follow any obvious geometric form. A full explanation of this is therefore also required. Theoretical modelling of p to s conversion predicts high efficiencies for materials in the infra red and so future experiments should be carried out in this region. Modelling should also be extended to see whether blazed gratings or crossed gratings are more attractive with respect to p to s conversion.

The use of p to s conversion for gas sensing is now well understood in terms of the required optical apparatus and so future improvements must concentrate on finding new materials to incorporate in the grating configuration. These materials must be suitable for thin film deposition and should also be chemically or biologically specific. They should also undergo a reversible reaction which can be detected by a change in refractive index or thickness. The applications of p to s conversion in the construction of monochromators and the optical decoding of magnetic information are also reliant on suitable materials.

In the area of nonlinear optics, there are a large number of very interesting physical effects (thermal or electronic) which may be studied using optical modes and work is currently being carried out with this aim.

10.3 Publications

- *Polarisation conversion through the excitation of surface plasmons on a metallic grating*
  G P Bryan-Brown, J R Sambles and M C Hutley.
  Journal of Modern Optics **37** (1990) 1227
- *Prism and grating coupling to long range coupled surface exciton-polaritons*
  G P Bryan-Brown, Fuzi Yang, G W Bradberry and J R Sambles.
  Accepted by Journal of the Optical Society of America B
- *Comparison of metal parameters obtained from prism and grating coupling to surface plasmon polaritons*
  G P Bryan-Brown, S J Elston and J R Sambles.
  Accepted by Journal of Modern Optics
- *Coupled surface plasmons on silver coated gratings*
  G P Bryan-Brown, S J Elston and J R Sambles.
  Accepted by optics communications
- *Surface resonance polarisation conversion mediated by brocken surface symmetry*
  S J Elston, G P Bryan-Brown, T W Preist and J R Sambles.
  Submitted to Physical Review Letters
- *Polarisation conversion from diffraction gratings*
  S J Elston, G P Bryan-Brown and J R Sambles.
  Submitted to Physical Review B
- *Surface plasmon resonance on gratings as a novel means for gas sensing*
  P S Vukusic, G P Bryan-Brown and J R Sambles.
  Submitted to Sensors and Actuators

References

Ashwell GJ, Dawnay JC, Kuczynski AP,···	1990	J. Chem. Soc. Faraday. Trans. **86** 1117
Ashwell GJ, Sambles JR, Martin AS, ···	1990a	J. Chem. Soc. Chem. Comm. **19** 1374
Blodgett KB and Langmuir I	1937	Phys. Rev. **51** 964
Brueck SRJ, Diadiuk V, Jones T and Lenth W	1985	Appl. Phys. Lett. **46** 915
Bruggemann DAG	1935	Ann. Phys. **24** 636
Campbell RJ, Mathew JGH, Smith SD and WAlker AC	1989	J. Mod. Opt. **36** 323
Celli V and Tran P	1988	Phys. Rev. B **32** 9089
Chandezon J, Dupuis MT, Cornet G and Maystre D	1982	J. Opt. Soc. Am. **72** 839
Chen Z and Simon HJ	1988	J. Opt. Soc. Am. **B5** 1396
Chow YT, Wherrett BS, Stryland E Van,···	1986	J. Opt. Soc. Am B **3** 1535
Chuang SL and Kong JA	1983	J. Opt. Soc. Am. **73** 669
Coutez JL, Nevière M, Pic E and Reinisch R	1985	Phys. Rev. B **32** 2227
Cullen TJ, Ironside CW, Seaton CT and Stegeman GI	1986	Appl. Phys. Lett. **49** 1403
Dannberg P, Possner T, Braüer and Bartuch U	1980	Phys. Stat. Sol. **150** 873
Decher G, Tieke B, Bosshard C and GünterP	1989	Ferroelectrics **91** 193
Depine RA and Simon JM	1987	J. Opt. Soc. Am. A **4** 834
Dneproskii VS, Furtichev AI, Klimov VI, Shen Li,···	1988	Phys. Stat. Sol. **150** 839
Dold B and Mecke R	1965	Optik **22** 435

Ehrlich JE, Assanto G, and Stegeman GI	1990	Opt. Comm. **75** 441
Elston SJ, Sambles JR and Clark MG	1989	J. Mod. Opt. **36** 1019
Fukui M and Oda K	1988	Surf. Sci. **33** 882
Feldman A, Horowitz D and Waxler RM	1973	IEEE J. Quan. Elect. **9** 1054
Fuzi Yang, Bradberry GW and Sambles JR	1987	J. Mod. Opt. **36** 1405
Fuzi Yang, Sambles JR and Bradberry GW	1990	Phys. Rev. Lett. **64** 559
Fuzi Yang, Sambles JR and Bradberry GW	1990a	Phys. Rev. B To be published
Garaev RA, Vlasov DV and Koroblin VV	1982	Sov. J. Quan. Elect. **12** 100
Greffet JJ and Maassarani Z	1990	J. Opt. Soc. Am. A **7** 1483
Gribkovskii VP, Zimin LG, Gaponenko SV, $\cdots$	1988	Phys. Stat. Sol. **150** 761
Gruhlke RW and Hall DG	1989	Phys. Rev. B **40** 5367
Gupta SD, Varada GV and Agarwal GS	1987	Phys. Rev. B **36** 6331
Halevi P and Mata-Méndez O	1989	Phys. Rev. B **39** 5694
Harada T, Taira H, Kita T and Itou M	1987	SPIE **815** 118
Heitmann D, Kroo N, Schultz C and Szentirnay Z_s	1987	Phys. Rev. B **35** 2660
Hessel A and Oliner AA	1965	Appl. Opt. **4** 1275
Hickernoll RK and Sarid D	1986	J. Opt. Soc. Am. B **3** 1059
Hutley MC	1982	*Diffraction Gratings* (Acedemic Press, London)
Hutley MC and Maystre D	1976	Opt. Comm. **19** 431
Hutley MC, Stevens RF and Putland DE	1986	J. Opt. Sens. **1** 153

Inagaki T, Goudonnet JP and Arakawa ET	1986a	J. Opt. Soc. Am. **B3** 992
Inagaki T, Goudonnet JP, Royer P and Arakawa ET	1986b	Appl. Opt. **25** 3635
Inagaki T, Motosuga M, Arakawa ET and Goudonnet JP	1985	Phys. Rev. B **32** 6238
Innes RA and Sambles JR	1987	J. Phys. F : Met. Phys. **17** 277
Johnson PB and Christy RW	1974	Phys. Rev. B **9** 5056
Kar AK and Wherrett BS	1986	J. Opt. Soc. Am. B **3** 345
Knoll W, Philpott MR, Swalen JD and Girlando A	1982	J. Chem. Phys. **77** 2254
Kolinsky PV and Jones RJ	1989	GEC Jnl. Res. Inc. Marconi rev. **1** 46
Koteles ES, Chen YT, Sonek GJ and Bollantyne JM	1984	J. de Phys. **4** 213
Kovacs GJ	1978	Surf. Sci. **78** 245
Kretschmann E and Kröger E	1975	J. Opt. Soc. Am. **65** 150
Kretschmann E and Raether H	1968	Z. Natur. **23a** 2135
Kuwamura Y, Fukui M and Tada O	1983	J. Phys. Soc. Jpn. **52** 2350
Lafait J, Abelès F Theye ML and Vuye G	1978	J. Phys. F. **8** 1597
Liedburg B, Nylander C and Lundström I	1983	Sens. and Actu. **4** 299
Lloyd AD, Janossy I, Mackenzie HA and Wherrett BS	1987	Opt. Comm. **61** 339
Lukosz W and Tiefenthaler K	1988	Sens. and Actu. **15** 273
Matsubara K, Kawata S and Minami S	1988	Appl. Opt. **27** 1160
Marvin A, Toigo F and Celli V	1975	Phys. Rev. B **11** 2777
Maxwell Garnet JC	1904	Phil. Trans. **203** 385
Maystre D	1978	J. Opt. Soc. Am. **68** 490
Maystre D, Nevière M, Reinisch R and Coutaz JL	1988	J. Opt. Soc. Am. B **5** 338

NevièreM, Vincent P, Maystre D, Reinisch R and Coutez JL	1988	J. Opt. Soc. Am. B **5** 330
Nevière M, Vincent P and Petit R	1974	Nouv. Rev. Opt. **5** 65
Numata H	1982	J. Phys. Soc. Jpn. **51** 2575
Nylander C, Liedburg B and Lind T	1982	Sens. and Actu. **3** 79
Otto A	1968	Z. Phys. **216** 398
Otto A	1969	Z. Phys. **219** 227
Palik ED	1985	*Handbook of Optical constants of Solids* (Acedemic Press, New York)
Patela S, Jerominek H, Delisle C and Trembley R	1986	J. Appl. Phys. **60** 1591
Petit R (Editor)	1980	*Electromagnetic Theory of Gratings* (Springer-Verlag, Berlin)
Petit R and Tayeb G	1987	SPIE **815** 11
Pockrand I	1976	J. Phys. D:Appl. Phys. **9** 2423
Pockrand I and Raether H	1976	Opt. Comm. **18** 395
Popov E, Tsonev L and Maystre D	1990	J. Mod. Opt. **37** 379
Popov E, Tsonev L and Maystre D	1990a	J. Mod. Opt. **37** 367
Quail JC, Rako JG and Simon HJ	1983	Opt. Lett. **8** 377
Raether H	1982	Opt. Comm. **42** 217
Raether H	1988	*Surface Plasmons* (Springer-Verlag, Berlin)
Rosengart EH and Pockrand I	1977	Opt. Lett. **1** 194
Sarid D	1981	Phys. Rev. Lett. **47** 1927
Sarid D, Deck RT, Craig AE, Hickernell RK, ⋯	1982	Appl. Opt. **21** 3993
Schroder U	1981	Surf. Sci. **102** 118

Seymour RJ, Krupezak JJ, and Stegeman GI	1984	Appl. Phys. Lett. **44** 373
Simon HJ, Huang C, Quail JC, and Chen Z	1988	Phys. Rev. B **38** 7408
Sokolov AV	1965	*Optical properties of metals* (Blackie, London)
Stegeman GI, Burke JJ and Hall DG	1982	Appl. Phys. Lett. **41** 906
Sullivan BT	1990	Appl. Opt. **29** 1964
Svensson BC, Seaton CT, Gibson UJ and Stegeman GI	1988	Appl. Phys. Lett. **53** 941
Tien PK	1977	Rev. Mod. Phys. **49** 361
Tillin MD and Sambles JR	1988	Thin Solid Films **167** 73
Tillin MD and Sambles JR	1989	Thin Solid Films **172** 27
Trendgold RH	1987	Thin Solid Films **152** 223
Wedler G and Alshorachi G	1980	Thin Solid Films **74** 1
Wendler L and Haupt R	1986	J. Appl. Phys. **59** 3289
Williams VS, Olbright GR, Fluegel BD, ···	1988	J. Mod. Opt. **35** 1979
Wiβmann P and Höhler G	1975	*SpringerTracts* ··· vol. 77 (Springer, Berlin)
Wood RW	1902	Proc. Phys. Soc. **18** 396
Wooten F	1972	*Optical Properties of Solids* (Acedemic Press, New York)
Yueh HA, Shin RT and Kong JA	1988	J. Appl. Phys. **64** 1657

Appendix A

Nonlinear Studies of Optical Modes on Gratings

A.1 Introduction

Optical modes excited on gratings have two properties that make them applicable for use in nonlinear optics. Firstly by using resonant absorption of light, one can concentrate 100% of the incoming laser beam power into a very small area causing local heating and hence a change in optical properties (thermal nonlinearity). Secondly an optical mode has an associated field enhancement which will enhance nonlinear electron dynamics within appropriate materials (electronic nonlinearity). In this chapter, we discuss experiments which utilise both of the above effects. Namely, a thermal nonlinearity in ZnSe and electron nonlinearities in semiconductor doped glass and Langmuir Blodgett films.

When light passes through a substance, its associated electric field causes redistribution of weakly bound electrons surrounding each atom. This leads to an induced electronic dipole in each atom and hence we can define a polarisation **P**, which is the induced dipole moment per unit volume. This is proportional to the applied field **E** for small values of this field, hence

$$\mathbf{P} = \epsilon_0 \chi^{(1)} \mathbf{E} \qquad (A.1)$$

where ϵ_0 is the permittivity of free space and $\chi^{(1)}$ is the linear electric susceptibility (see PV Kolinsky *et al*, 1989). The dipole oscillators in turn affect the propagation of light through the medium and hence affect the refractive index (n). In fact

$$\mathrm{n}^2 = 1 + \chi^{(1)} \qquad (A.2)$$

When **E** is no longer small equation A.1 must be modified to include higher order terms

$$\mathbf{P} = \epsilon_0 (\chi^{(1)} \mathbf{E} + \chi^{(2)} \mathbf{E}^2 + \chi^{(3)} \mathbf{E}^3 + \cdots) \qquad (A.3)$$

Equation A.2 now becomes

$$\mathrm{n}^2 = 1 + \chi^{(1)} + (\chi^{(2)} \mathbf{E} + \chi^{(3)} \mathbf{E}^2 + \cdots) \qquad (A.4)$$

$\chi^{(2)}$ and $\chi^{(3)}$ are the quadratic and cubic susceptibilities respectively and are the origin of nonlinear behaviour. $\chi^{(2)}$ is the term responsible for second harmonic generation which can easily be seen by substituting $\mathbf{E} = \mathbf{E}_0 \cos(\omega t)$ into equation A.3. However in this chapter we are interested in the $\chi^{(3)}$ term which is the origin of intensity dependent phase shift. This nonlinear susceptibility is a very complicated quantity which is usually a fourth rank tensor. It is therefore convenient to simplify equation A.4 and define a nonlinear refractive index n_2, such that

$$n = n_0 + n_2 \mathbf{E}^2 \qquad (A.5)$$

Where n_0 is the zero intensity refractive index, and n_2 is the macroscopic nonlinearity dependent on $\mathbf{E}^2$ (or intensity). There are four microscopic contributions to n_2; electronic, vibrational, electrostrictive and thermal. Each of these have different response times, different magnitudes and may have different signs (A Feldman *et al*, 1973 and RA Garaev *et al*, 1982). The electronic and vibrational response times are 10^{-15} and 10^{-13} seconds respectively (obtained from the frequencies of optical transitions involving bound electrons and lattice vibrations). The electrostrictive response time is dictated by the time taken for an acoustic deformation to travel across the diameter of the optical beam ($\sim 10^{-8}$ seconds for a focused laser beam). The thermal response time depends on the thermal inertia of the sample configuration and is usually in the range of 10^{-6} to 10^{-3} seconds. The different response times allow each effect to be isolated by using different probing times.

Experiments can either involve probing the bulk material directly or can employ some form of field enhancement via a Fabry-Perot cavity, a prism-coupled optical mode or a grating-coupled optical mode. It is the third configuration that is used in the following studies.

A.2 Nonlinear Semiconductor Waveguides

Bulk semiconductors such as ZnSe and ZnS have well defined band gaps (at 2.58eV and 3.54eV respectively). When probed with photons possessing an energy less than the band gap, these materials appear transparent. However, when photon energies are greater than the band gap, valence electrons are excited across the gap and the photons are absorbed. Therefore these materials act as high pass (in wavelength) filters. The band gaps and corresponding wavelengths are listed in table A.1 for a few important semiconductors.

Table A.1: Semiconductor band gaps and corresponding cut-off wavelengths.

Semiconductor	Band gap (eV)	Wavelength (μm)
InSb	0.16	7.750
Ge	0.67	1.851
Si	1.11	1.117
GaAs	1.35	0.918
CdS	2.42	0.512
ZnSe	2.58	0.481
ZnS	3.54	0.350

Heating the semiconductor reduces the band gap and so shifts the absorption edge to a higher wavelength (AK Kar *et al*, 1986). For wavelengths near the band gap, heating will cause a change in both the refractive index and the absorption. This thermal nonlinearity may be very large (dn/dt$\sim$ 4×10^{-4} K^{-1} for ZnSe at $475nm$). An electronic nonlinearity also exists for these semiconductors but for most CW experiments its contribution to n_2 is negligible. If a 500mW laser beam ($\lambda = 514.5nm$) is focused to a radius of 10^{-4}m and completely absorbed in a ZnS waveguide then the thermal nonlinearity dominates over the electronic nonlinearity by a factor of $\sim$ 2000 (assuming a temperature rise of $\sim$ 80K). This estimate ignores the field enhancement that occurs in the waveguide. If this enhancement is as large as 44.7 ($\sqrt{2000}$), then the nonlinearities would be the same (and would cancel as they are opposite in sign).

Optical nonlinearities have been studied in bulk ZnSe (VP Gribkovskii *et al*,

1988) and CdS (VS Dneprovskii *et al*, 1988) but most studies involve the use of resonant modes. In particular, nonlinear Fabry-Perot cavities have attracted a lot of interest from many workers. These cavities have the structure $[HL]^p[HH]^q[LH]^P$, where the notation [HL] implies a quarter wave thickness of high index material followed by a quarter wave thickness of a low index material. The structure is therefore a cavity sandwiched between two dielectric stack mirrors. L is usually MgF_2, ThF_4 or cryolite and H is the nonlinear material (ZnSe or ZnS etc.). Using ZnSe at 514nm, a highly nonlinear Fabry-Perot has been constructed which exhibits bistability with a laser power of only 16mW (30μm beam diameter) (YT Chow *et al*, 1986). However the bistable loop was found to drift during the experiment and eventually narrowed and disappeared. This instability was explained in terms of the porous nature of the evaporated films which leads to adsorption of water. An improvement in stability was found by using films deposited by molecular beam deposition (MBD) carried out under ultra high vacuum. These films gave reproducable bistability with a required switching power of 30mW (30μm beam diameter). It has been recently suggested (RJ Campbell *et al*, 1989) that ZnSe instability is due to both thermal annealing and high irradiance levels within the cavity. These effects are still under investigation. Using metal layers as reflecting mirrors, a Fabry-Perot has been constructed which exhibits a different form of bistability called 'butterfly' bistability (AD Lloyd *et al*, 1987). These cavities may be filled with a variety of liquids to give switching powers less than those found for ZnSe filters (a Glenfiddich whiskey cavity was found to switch at 2.2mW). Butterfly bistability has also been observed by using grating coupling to an InSb waveguide at a wavelength of 10μm. Switching was observed for laser powers greater than 3.0W and was found to be thermal in nature (JE Ehrlich *et al*, 1990). By using prism and grating coupling to a ZnS waveguide, a beam from an Ar^+ laser was coupled to the TE_0 mode and was used to control the output angle of a beam from a HeNe laser coupled to the TE_1 mode. An angle shift of 0.24° was observed as the input power varied from 0 - 2.5W (BC Svensson *et al*, 1988).

In this section results are presented from experimental studies carried out on ZnS and ZnSe waveguides.

The first configuration tried used a 300nm layer of ZnS evaporated onto silver coated grating (groove depth =550.8nm, pitch =28.0nm). A beam from an Ar^+

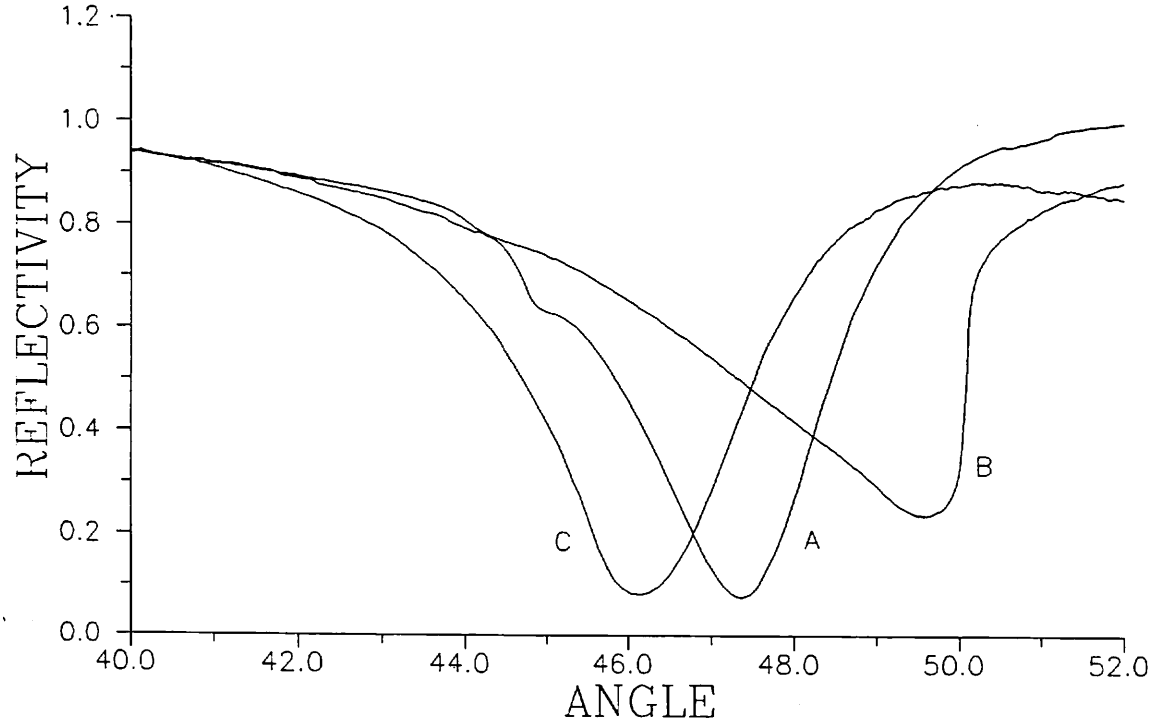

Figure A.1: Reflectivity (arbitrary units) verses angle showing the effect of laser intensity on the position and shape of a TE_2 guided mode resonance:A, low intensity ; B, 260mW; C, low intensity.

laser of $\lambda = 514.5nm$ was used to probe the sample. Figure A.1 shows how coupling of s radiation into a guided mode (TE_2) is affected by laser beam intensity. (As a thermal nonlinearity was being studied, these scans are carried out without a chopper or PSDs, as chopping would reduce sample heating. Instead, the scans are taken with 'D.C.' detectors fed directly into the computer A-to-D. The signal to noise ratio obtained is still fairly good due to internal stabilisation in the Ar^+ laser). Using low laser powers the mode minimum occurs at 47.38° (curve A). When the beam intensity is increased to 260mW ($80\mu m$ beam radius), this mode shifts to 49.56° and is clearly distorted (curve B). As light is coupled into the mode, heating occurs which raises the ZnS refractive index and hence shifts the mode to a higher wavevector (angle). When there is no further increase in temperature the high mode angle can no longer be sustained as coupling into the mode decreases which cools the film, which in turn shifts the mode back to its low intensity position. This causes rapid decoupling of radiation as can be seen on the high angle side of the high intensity mode resonance. A final low intensity scan shows that the sample has been permanently changed by the intense laser power. This change is due to water desorption, structural changes and maybe also a reaction of ZnS with the silver. Using planar mode theory (i.e. the prism- coupled counterpart), the refractive index change in the film can be estimated from the angle shift. The difference in angle between curve A and B in figure A.1 corresponds to an index change of 0.0348 which implies a temperature rise of $348°C$ (assuming dn/dt=1×10^{-4} $°C^{-1}$). This is rather large and much less heating is likely to cause reaction between the silver and the ZnS, hence the sample is bound to give irreproducable results. Protecting the silver with a thin layer of SiO before coating with ZnS produced similar results to the above and adding another layer of SiO on top of the ZnS to prevent water absorption also failed to produce a stable sample.

In a further effort to protect the ZnS from atmospheric effects a sample was made with a reversed structure i.e. grating-ZnS-MgF-Ag (The MgF layer was added instead of SiO). With the laser beam entering through the grating substrate a scan was obtained for s polarised light as shown in figure A.2(a). This scan shows a surprisingly sharp guided mode at 21.9°. After adding a 30cm lens to focus the beam, a low power and a high power (126mW) run was taken on the sharp guided mode as shown in figure A.2(b). The shift is disappointingly small, but this very sharp mode probably has an associated field enhancement which is large enough to provide a significant electronic nonlinearity and so negate the thermal nonlinearity (a pulsed laser was not available at this time to resolve the two nonlinearities).

The next configuration tried used a $455nm$ thick ZnS layer on an aluminium coated grating (as Al should be more stable than Ag). The sample still shows drift in mode position but after about 10 high power scans the drift became very small. Figure A.3 shows the low intensity and high intensity (137mW) scans using this 'annealed' sample. The shift from 15.95° to 17.90° corresponds to an index change of 0.0207 which would correspond to a temperature rise of of $207°C$ if it was all thermally induced.

Figure A.1 and A.3 both show nonlinearity but no bistability i.e. a high intensity scan from high angle to low angle shows the same mode as a scan from low angle to high angle. In order to try to obtain bistability, ZnSe was used instead

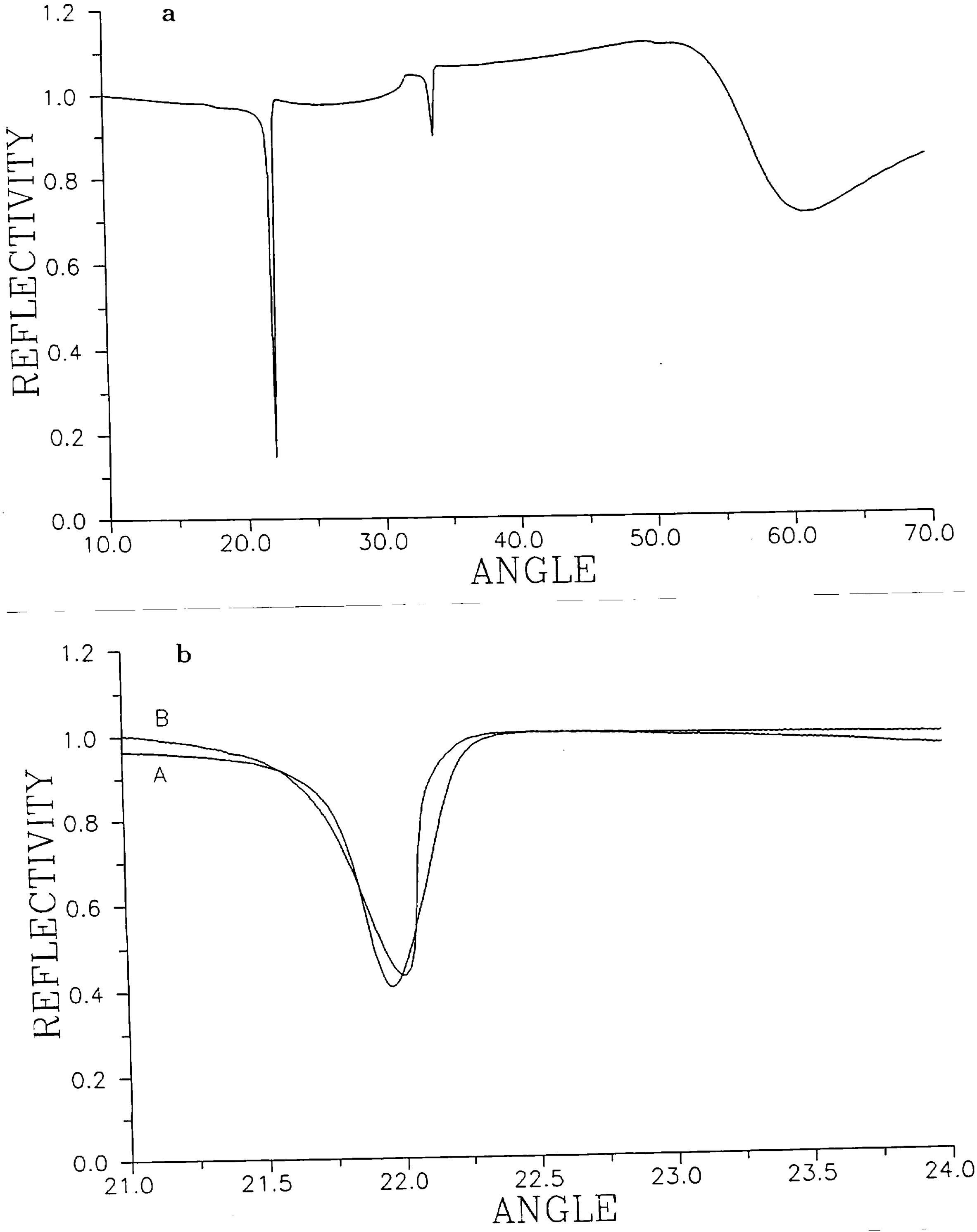

Figure A.2: Reflectivity (arbitrary units) verses angle from a sample consisting of grating-ZnS-MgF-Ag. The scans in (b) are taken for:A, low laser power; B, 126mW.

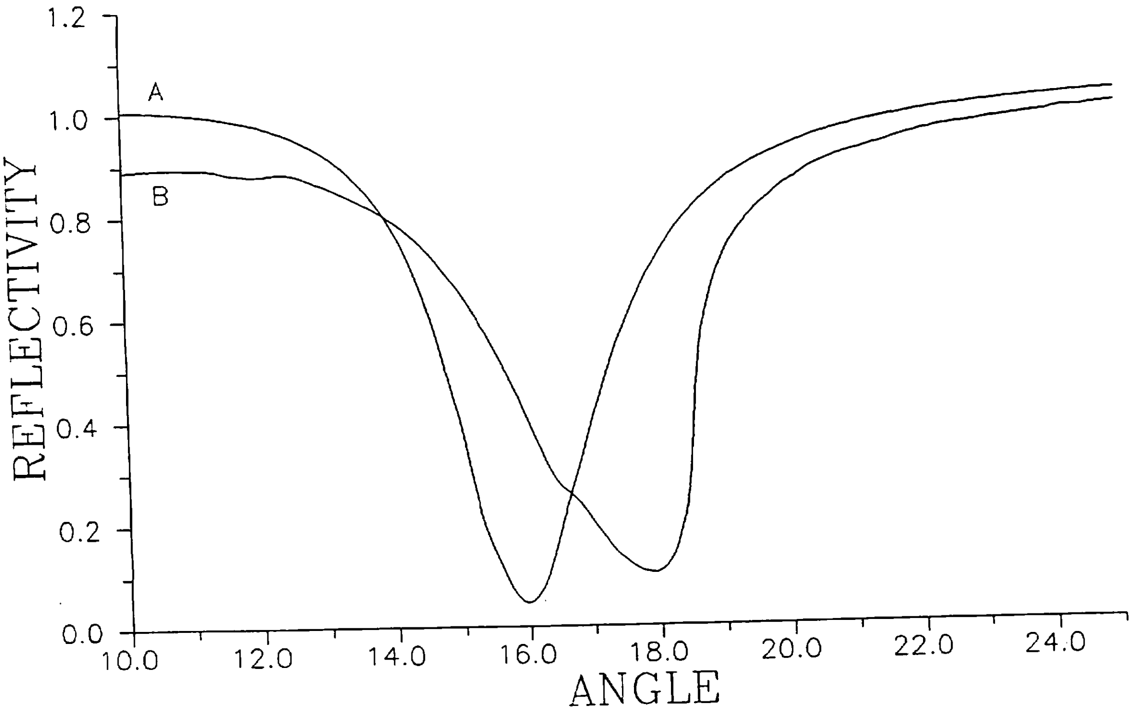

Figure A.3: Reflectivity (arbitrary units) verses angle for a sample consisting of ZnS-aluminium-grating:A, low power; B, 137mW.

of ZnS as its nonlinearity is at least twice as large. However, thermally evaporated ZnSe films showed a large amount of absorption. This is due to the different sticking coefficients of Zn and Se which leads to ZnSe films with small grain size and many interstitials. Better ZnSe films are obtained by molecular beam deposition (MBD). Hence a $1\mu m$ ZnSe film was deposited on an aluminium coated grating using MBD (at RSRE, Malvern). Figure A.4 shows the affect of changing the beam power on an s guided mode from the MBD sample using s polarised light (this mode could not be clearly identified but is probably the TE_8 mode). Using a beam power of only 66.4mW ($150\mu m$ beam radius) causes the mode to shift from 28.4° to 36.1°. This corresponds to an index change of 0.0690 which would imply a temperature rise of $345°C$ (assuming dn/dt=2×10^{-4} $°C^{-1}$). The final low power scan shows that the sample has not been permanently damaged by a large amount but a small change is still observed which is probably due to slight water desorption. The dip in the low angle wing of the TE mode (at 25.48°) is a TM like mode which is

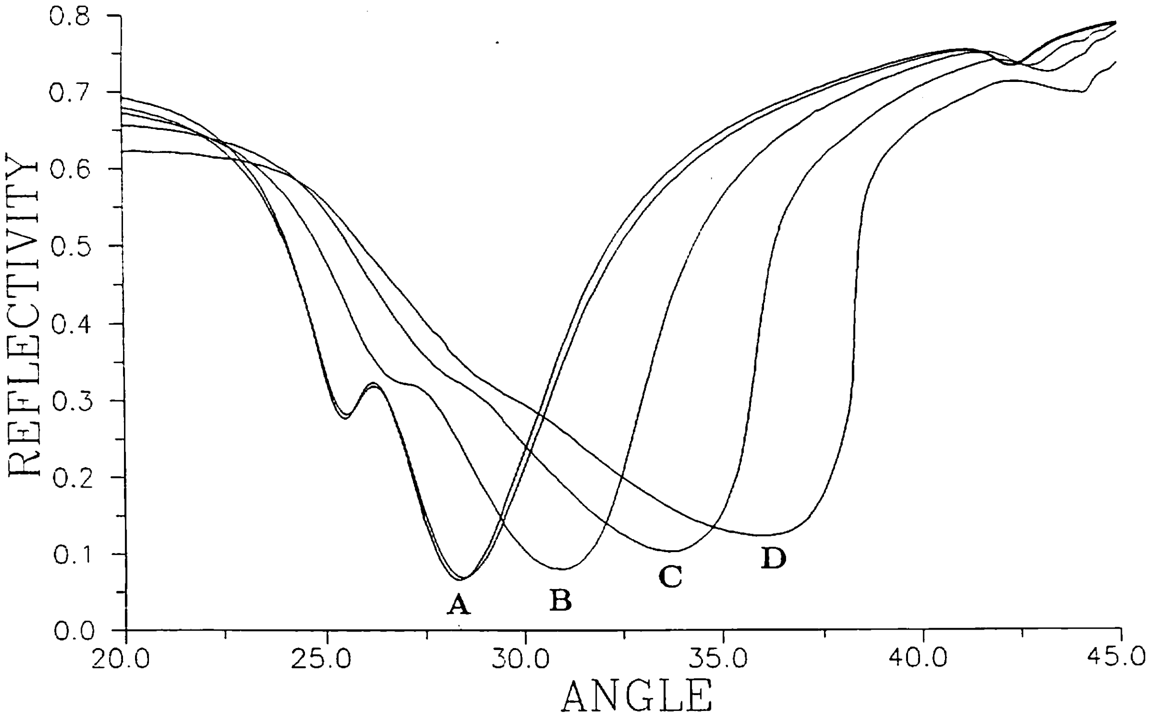

Figure A.4: Reflectivity (absolute units) verses angle using a sample consisting of ZnSe-aluminium-grating for different laser intensities:A, low power; B, 26.7mW; C, 47.2mW; D, 66.4mW.

coupled to via film anisotropy. This coupling to a TM like mode via a TE mode has also been seen in liquid crystal cells (SJ Elston *et al*, 1989). It is surprising to observe anisotropy in MBD ZnSe (which should be polycrystalline) and even more surprising is the fact that this is reduced by heating the film. Figure A.4 also shows that the mode broadens and shallows when the film is heated. This implies that the film absorption is increasing with temperature which is the opposite to that seen using nonlinear Fabry-Perot cavities (RJ Campbell *et al*, 1989). Optical bistability was still not seen using angle scans and any attempt to raise the beam power too high (> 80mW) resulted in permanent damage to the film. Hence this sample shows reversible changes in refractive index and adsorption at lower beam powers followed by irreversible sample destruction at high beam powers. The large width of the mode is indicative of large film absorption and suggests that the ZnSe in not fully dense. Therefore improvement is still required to obtain good quality

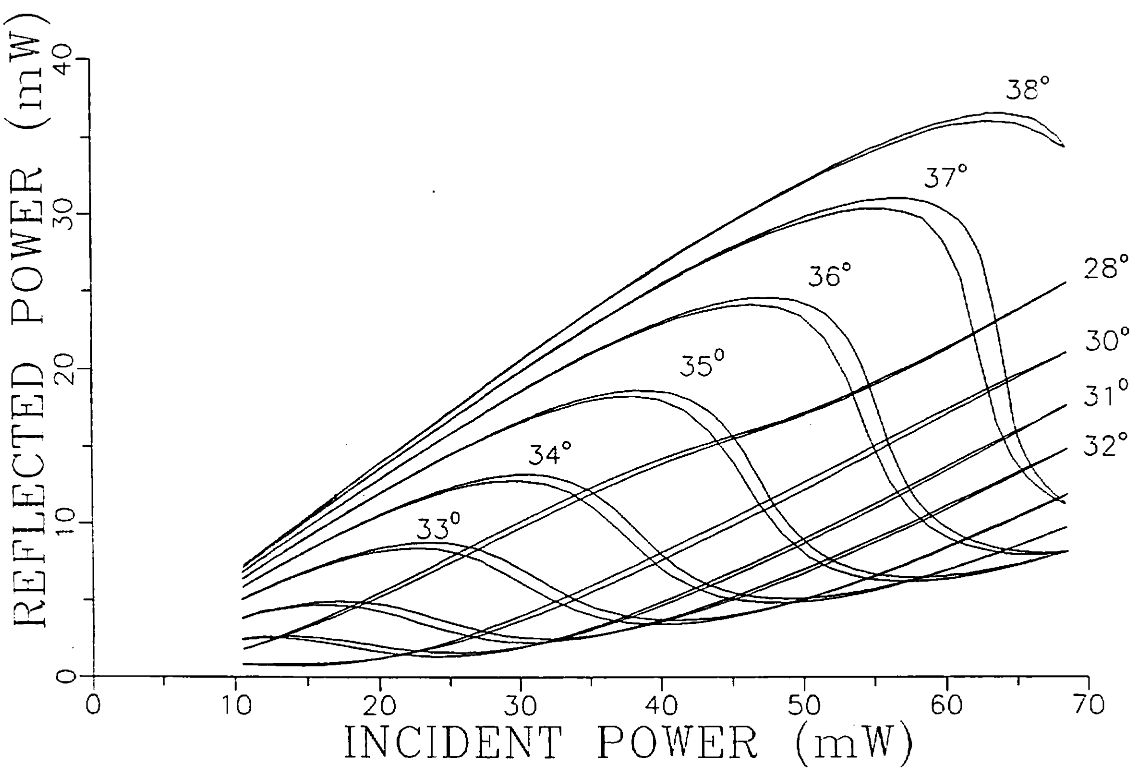

Figure A.5: Power scan results taken using the MBD ZnSe sample for a variety of incident angles.

films.

As well as scanning angle, nonlinearity can be observed by fixing angle and then ramping the beam intensity. This is achieved by passing the laser through an acousto-optic modulator. Typical results are shown in figure A.5 for a selection of incident angles in the vicinity of the TE_8 guided mode (scan time is 67 seconds in each case). With no nonlinearity present these scans would merely show straight lines of various gradients. However in this case there is clearly nonlinearity and all the scans show small bistable loops.

To achieve significant bistability at low powers, guided modes are required which possess a small half width and a large sensitivity (angle shift) to refractive index change. Theoretical modelling has shown that these requirements are optimised by using high order modes with large propagation wavevectors. Also TE modes were found to be better than TM modes.

To summarize, thermal nonlinearity in thin films has been studied by using laser beam absorption into guided modes. This is the first time to our knowledge that metal clad waveguides have been used to produce nonlinearity in ZnS and ZnSe. This configuration has the advantage over dielectric clad waveguides in that 100% of the incident light may be coupled into the waveguide. The presence of the metal does however lead to broader guided modes. Evaporated ZnS films showed large nonlinear shifts but suffered from instability even when probed with moderate beam intensities. A MBD grown ZnSe film showed far more stable operation but the data still suggests that further improvement in deposition is possible. Theoretical modelling also suggests that further optimisation is easily achievable.

A.3 Semiconductor Doped Glass

In this section we describe results obtained by using grating coupling to resonant modes excited on semiconductor doped glass diffraction gratings.

The nonlinear processes occurring in semiconductor doped glass (SDG) have been of interest to many workers because of possible applications to optical signal processing (reviewed by VS Williams *et al*, 1988). Our SDG consists of CdS_xSe_{1-x} microcrystals of radius 10 to 100nm embedded in glass. The doping level is usually about 1% by volume and so most physical properties such as density and thermal expansion are defined by the host glass. The optical properties however are dominated by the microcrystals and SDG acts as a high (wavelength) pass optical filter. The cut off wavelength corresponds to a photon energy equal to the semiconductor band gap which may be adjusted by varying the doping ratio x. When $x > 0.8$ the cut off occurs in the yellow region of the spectrum and when $x < 0.2$ the cut off is in the red region. The absorption edge is about 3 times broader than in bulk CdS_xSe_{1-x} due to spread in microcrystal sizes and also a spread in doping ratio ($\Delta x \sim 0.04$) between microcrystals. The nonlinearity in SDG occurs in the vicinity of the cut-off wavelength and is mainly due to band filling of photoexcited electron hole plasma that leads to a power dependent absorption and refractive index. The nonlinearity has the same magnitude in SDG as in the bulk semiconductor but the relaxation time in SDG is about 10 times faster than in the bulk and has been measured to be ~ 10ps. Negative index changes are observed at wavelengths corresponding to energies below the bandgap and positive index changes are observed at energies above the band gap. Most studies have observed a nonlinear susceptibility ($\chi^{(2)}$) in the range of 10^{-12} to 4×10^{-11} m^2/V^2. P Dannberg *et al* (1980) fabricated an ion exchanged waveguide in SDG and used prism coupling to observe a shift in the TE_0 mode angle as a function of laser pulse energy (using a Nd:YAG laser). The maximum shift corresponded to an index change of 10^{-4} and a thermal nonlinearity ($n_2^{(th)} = 6 \times 10^{-4} m^2/W$) was also measured using a continuous wave beam from an Ar^+ laser. S Patela *et al* (1986) studied prism coupled guided modes in glass waveguides deposited on SDG using a beam from an Ar^+ laser and found a maximum index change in the SDG of 0.002. This change is also a thermal nonlinearity as there is no significant field enhancement in the SDG waveguide cladding (the origin of this large thermal nonlinearity was not explained).

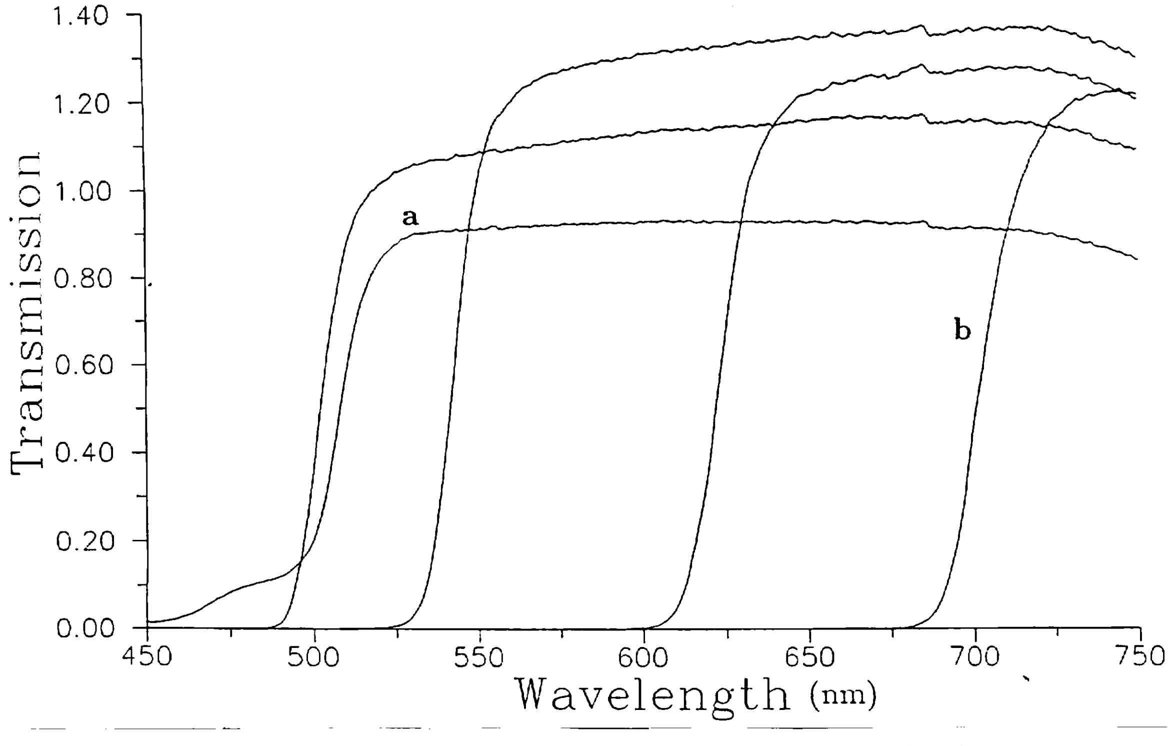

Figure A.6: Transmission (arbitrary units) verses wavelength (nm) scans taken through the SDG grating substrates used in this section.

In this section, we discuss results obtained from cw and pulsed experiments carried out using SDG gratings in various experimental configurations chosen to enhance the electromagnetic field in the grating substrate and therefore study the electronic and thermal nonlinearities in SDG. Gratings of suitable pitch were manufactured on SDG substrates by using holographic exposure followed by ion beam etching. Several different glasses were used with cut-off wavelengths as shown in figure A.6.

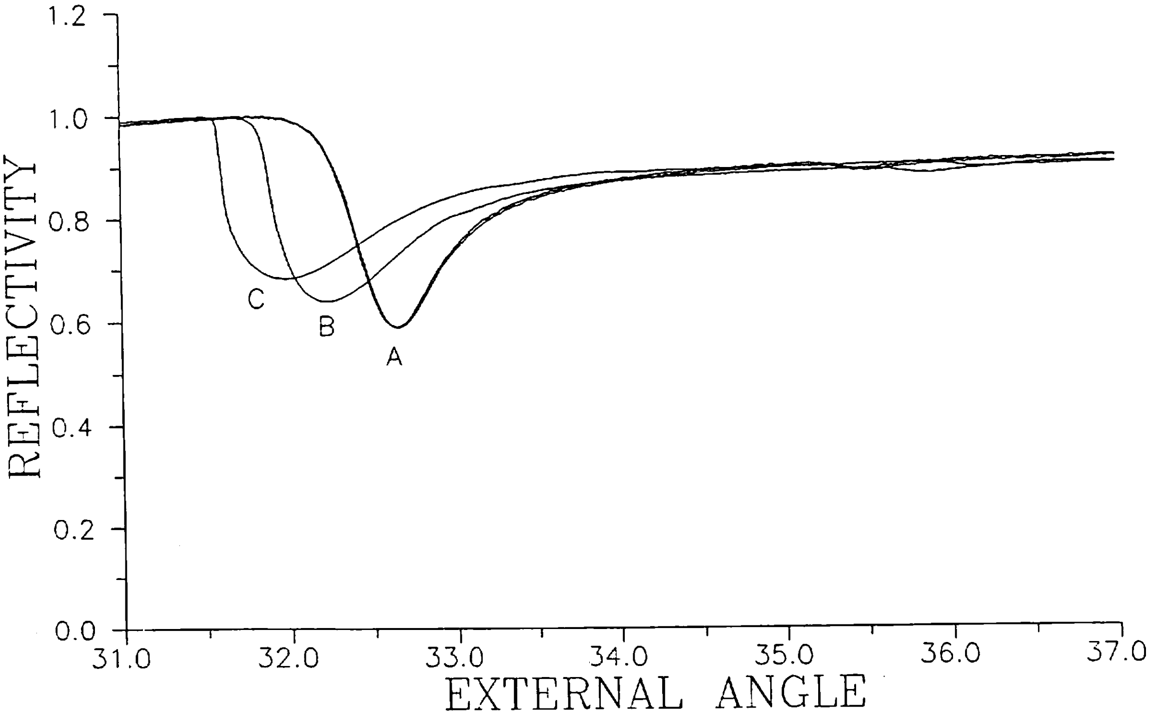

Figure A.7: Reflectivity (arbitrary units) verses external angle taken from a SDG sample showing a LRSP. The scans were taken for different laser beam intensities: A, low power; B, 75mW; C, 150mW.

The first experiment used the sample which produced curve (a) in figure A.6. A sinusoidal grating was etched into this sample with a pitch of $500nm$. The purpose of the experiment was to induce a nonlinearity in the SDG by using it as one of the bounding dielectrics in a LRSP configuration. The sample (n=1.533) was coated with $20nm$ of silver and index matched with chlorobenzene (n=1.532).

Using p polarised light from an Ar^+ laser ($514.5nm$), angle scans were taken with various beam intensities. Figure A.7 shows the LRSP obtained from four scans carried out in the sequence: low power-75mW-150mW-low power ($230\mu m$ beam radius). The two low power scans are almost identical showing full recovery of the sample. Unfortunately the impressive shift in the LRSP is almost solely due to thermal nonlinearity in the chlorobenzene (confirmed by comparing with an LRSP sample on a silica grating). Further experiments of this type were therefore not carried out as the matching fluid heating always dominated the observed nonlinearity. However this problem can be overcome by using a pulsed laser as the fluid would then not have time to warm up and only the fast electronic nonlinearity in the SDG would be seen.

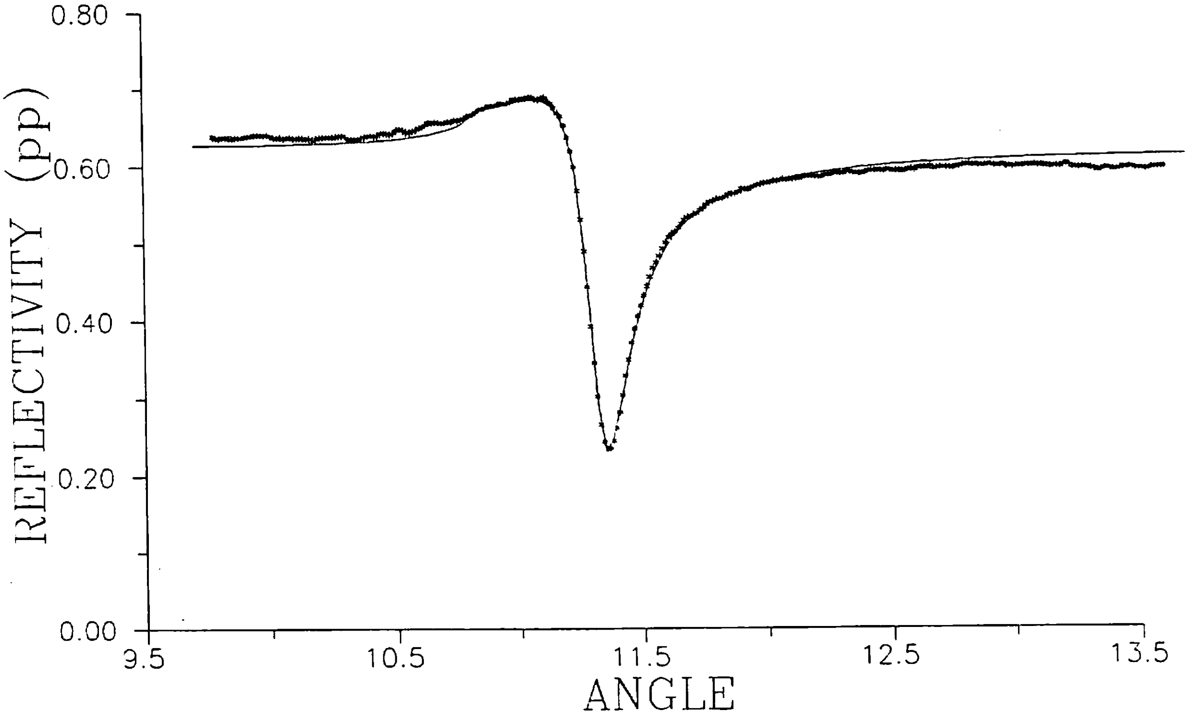

Figure A.8: Fitted reflectivity data from a LRSP configuration using a SDG grating substrate.

A pulsed ruby laser ($\lambda = 694.3nm$) was used to test this hypothesis. SDG with a suitable cut off wavelength (curve b in figure A.6) was used as the grating substrate (pitch =560.7nm, groove depth =25.8nm). This sample was coated with 19.4nm of silver and then index matched with an appropriate mixture of methyl benzoate and octanol. A low power (linear) angle scan was taken at $\lambda = 694.3nm$ using p polarised light from a monochromator as shown in figure A.8 (the theory fits the data fairly well). The pulsed ruby laser was then fired at the sample with the incident angle set to 11.27°. This angle was chosen to be at the maximum gradient of the left hand wing of the LRSP so that any change in mode position would cause a change in reflectivity. The pulse intensity was then ramped up and down to observe the nonlinearity. However the maximum index change of 10^{-4} found by P Dannberg *et al* corresponds to an angle shift of only 0.002° in our experiment. At 11.27° this would produce a reflectivity change of only 0.0073. This was not seen due to bad signal to noise in the pulse detectors. However with better pulse stability and improved detectors, this configuration would reveal the SDG nonlinearity and therefore demonstrate a new use of LRSPs in nonlinear optics. (To our knowledge LRSPs have never yet been used to observe an intensity dependent phase shift in SDG).

In the next configuration, a silver/SDG SPP was excited by a beam from an Ar^+ laser entering through the SDG substrate coated on its grating face with thick silver. Increasing the beam power caused a shift in the SPP angle and coupling strength. Using the same configuration on a silica substrate showed a similar angle shift hence we can conclude that thermally induced index changes in SDG are mainly due to the host glass and that absorption changes are due to the semiconductor microcrystals. These appear to get 'bleached out' by the intense laser power and do not recover completely (this bleaching effect has been previously seen by LG Zimin *et al*, 1988). Further experiments would be required to accurately quantify the observed bleaching effect.

Nonlinear coupling to ion exchange waveguides in SDG was also attempted. These waveguides are fabricated on the grating surface by immersing the sample in potassium nitrate at 340°C for a few hours. During this time Na^+ ions in the glass are replaced by K^+ ions resulting in an index change of ~ 0.009 at the surface (TJ Cullen *et al*, 1986). Prism coupling with a very small Otto gap was then used to locate the modes. Three modes were found for a sample immersed in KNO_3 for 1 hour 40 minutes and eight modes were found after an immersion time of 20 hours 48 minutes. These waveguides (in SDG) were then coated with thick silver and probed with a HeNe beam entering through the sample substrate (the SDG chosen was transparent at these wavelengths). Scans of the sample showed no grating coupled guided modes. This was in fact not too surprising as the small Otto gap required to prism couple to these modes implies a large groove depth in the grating case. Hence for efficient grating coupling to ion exchanged waveguides the samples must be etched with much deeper grating grooves (this has not yet been done). Using guided modes to study nonlinearities is preferable to LRSPs as theoretical modelling has shown them to posses superior sensitivity (angle shift) to index change (studied in detail in chapter 9 for sensing applications).

To summarize, this work has shown that pulsed experiments are required to separate the electronic SDG nonlinearity from the thermal nonlinearity associated with the host glass. The best grating configuration for this purpose involves the excitation of guided modes. These modes are superior to SPPs and LRSPs by virtue of their sensitivity to index change and also their large associated field enhancement.

A.4 Langmuir Blodgett Films

In this section we discuss the use of organic molecules in nonlinear optics and show that waveguide structures of suitable molecules may be constructed using the Langmuir Blodgett (LB) technique (KB Blodgett *et al*, 1937).

Organic materials have received a lot of interest due to their large second and third order susceptibilities ($\chi^{(2)}$ and $\chi^{(3)}$), ultrafast response times and high damage thresholds. Many studies have used non- centrosymmetric molecules to produce second harmonic generation (SHG) with an efficiency much greater than found using inorganic crystals such as KTP or KDP (G Decher *et al*, 1989 and PV Kolinsky *et al*, 1989). These materials contain side group molecules which when attached to benzene rings form electron acceptors and donors. Hence the molecule has a permanent dipole which leads to a large value of $\chi^{(2)}$. If the molecules form a centrosymmetric structure then the dipoles cancel out and lead to no macroscopic $\chi^{(2)}$ and hence no SHG. Therefore extra side groups are added to the molecule to encourage it to form a non-centrosymmetric structure. In this section we are only interested in the large $\chi^{(3)}$ of organic molecules (which is the origin of an intensity dependent refractive index). This nonlinearity is different to those found in semiconductors in that it may remain significant across a wide range of wavelengths.

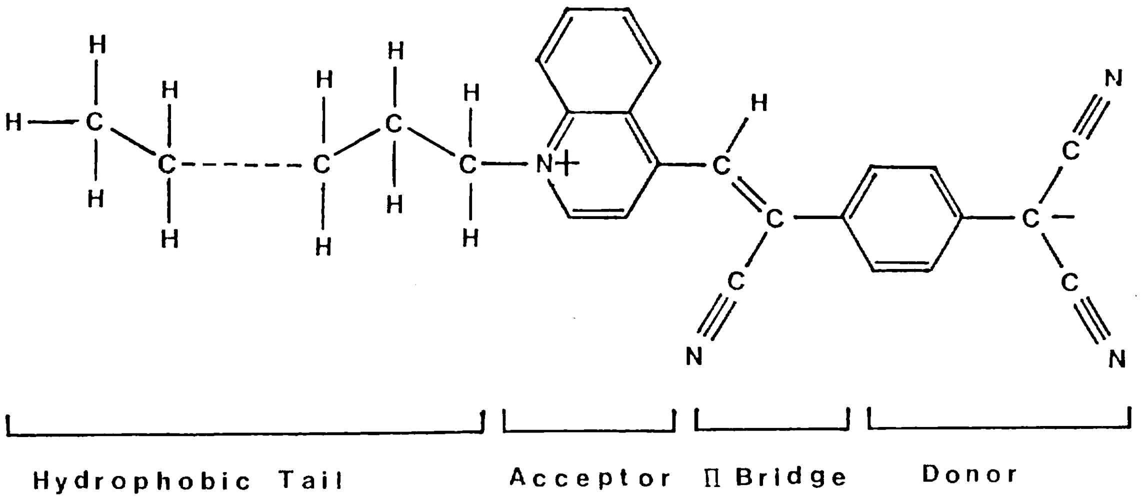

Figure A.9: The structure of $C_{16}H_{33}$-Q3CNQ.

In our experiments we used a molecule called Z-β-(1-hexadecyl-4-quinolinium)-α-cyano-4-styryldicyanomethanide or $C_{16}H_{33}$-Q3CNQ (the structure is shown in figure A.9). This molecule consists of a hydrophobic hydrocarbon chain attached to a donor and acceptor group separated by a π bridge. It therefore has a permanent dipole and hence when organised as a LB film in which dipoles align it has a large nonlinearity. This molecule has been previously used to obtain strong SHG (GJ Ashwell *et al*, 1990) and has also shown asymmetric electrical conductivity (GJ Ashwell *et al*, 1990a). The SHG study showed that this molecule when deposited in an LB film forms a non- centrosymmetric structure (i.e. the SHG intensity was found to increase with the number of molecular layers).

To deposit films, a PTFE trough of ultra clean ($> 25\mathrm{M}\Omega\mathrm{cm}^{-1}$) water was used as the subphase. 1mg of the material was dissolved in 100ml of dichloroethane. The solution was then carefully spread on the water surface and was left for 30 minutes to allow the solvent to evaporate leaving a monolayer of the organic molecule. This layer was then compressed by two PTFE barriers until a surface pressure of $25\mathrm{mNm}^{-1}$ was reached (measured with a Wilhelmy plate). After a further

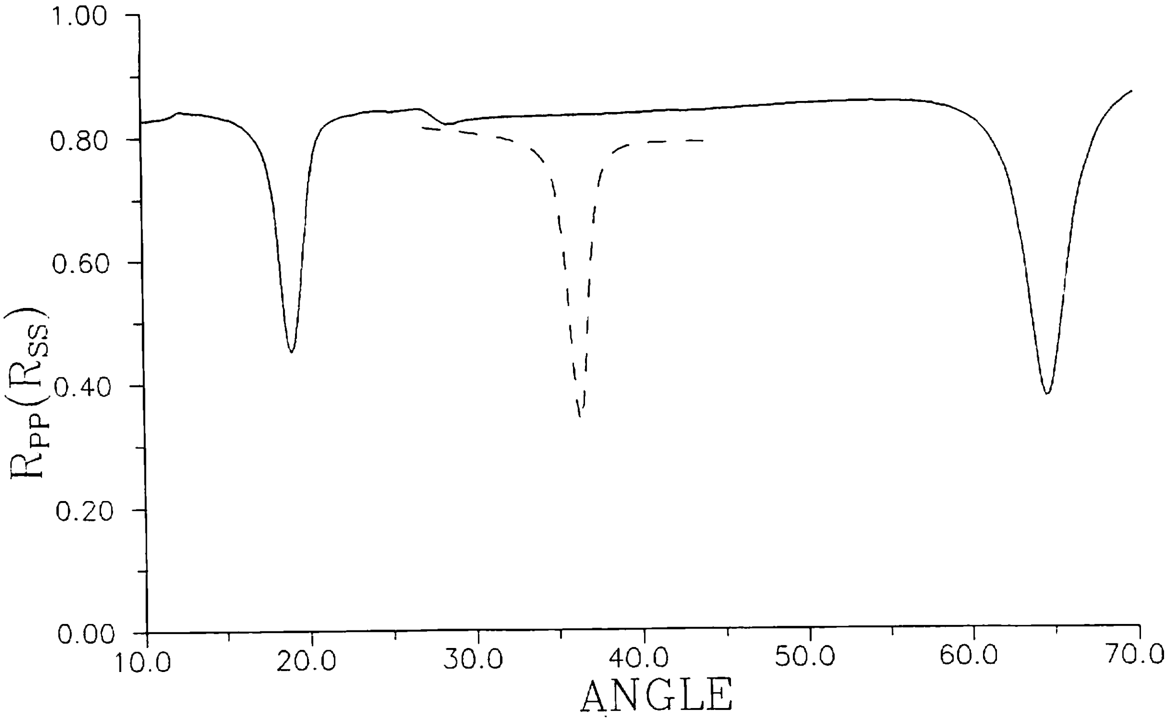

Figure A.10: Reflectivity verses angle obtained from an LB waveguide on a silver coated grating. The solid line is R_{pp} reflectivity and the dotted line is R_{ss}.

30 minutes a silver coated grating was lowered through the water surface at a rate of 0.1mm/s and then withdrawn at the same speed. On the upstroke a monolayer was transferred from the water surface onto the grating (the barriers were then automatically adjusted to maintain the surface pressure). This process was repeated and it was found that material was only deposited on each upstroke. The LB film was therefore non-centrosymmetric (Z-type). It was estimated that 120 layers would be needed for a waveguide structure supporting a TM_0 mode and a TE_0 mode. However this number of layers resulted in a dark blue film which was too absorbing to support guided modes (the colour is due to photon absorption via charge oscillation between the donor group and the accepter group). However, a further dipping attempt produced a yellow film which did support guided modes as shown in figure A.10. The R_{pp} scan shows the TM_0 guided mode and the SPP while the R_{ss} scan shows the TE_0 guided mode (taken using a HeNe laser). Unfortunately this film showed no nonlinearity when probed with a pulsed ruby

laser and it was later concluded that the LB material only forms yellow (non-absorbing) films as a result of metal ion contamination from the dipping trough. These ions attach to the donor group, destroying the permanent dipole and hence the nonlinearity. Therefore this material only possesses a significant nonlinearity when the LB film is blue and so nonlinear coupling to guided modes is impossible in the visible (waveguiding in the infra red may still be possible).

Other LB materials have shown much less absorption (RH Trendgold, 1987) and construction of nonlinear LB waveguides is an area of continued interest.

A.5 Summary

In this appendix we briefly described the nonlinear processes occurring in semiconductor films, semiconductor doped glass and organic molecules. ZnSe films deposited by MBD showed large nonlinear effects that are thermal in origin. Further optimisation of these structures should yield bistability. The experiments using SDG showed a difficulty in separating thermal and electronic nonlinearities, but pulsed experiments using waveguides in SDG should reveal the ultrafast nonlinearity associated with the microcrystals. Organic LB molecules are also good candidates for fast nonlinearity but new materials must be found with low absorption at suitable operation wavelengths.

A great deal has been learned from the experiments carried out so far and the large amount of current interest in optical nonlinearity warrants the need for further experiments using grating configurations.